Dissertation

Measurement of WWW production and search for supersymmetric particles in multi-lepton final states in pp collisions at $\sqrt{s} = 8$ TeV with the ATLAS detector at the LHC

Martina Javůrková
geb. Pagáčová

Fakultät für Mathematik und Physik
Albert-Ludwigs-Universität Freiburg

Measurement of WWW production and search for supersymmetric particles in multi-lepton final states in pp collisions at $\sqrt{s} = 8$ TeV with the ATLAS detector at the LHC

Dissertation

vorgelegt von

Martina Javůrková
geb. Pagáčová

Prof. Dr. Gregor Herten

Fakultät für Mathematik und Physik
Albert-Ludwigs-Universität
Freiburg im Breisgau

March 2017

Dekan:	Prof. Dr. Gregor Herten
Betreuer der Arbeit:	Prof. Dr. Gregor Herten
Referent:	Prof. Dr. Gregor Herten
Koreferent:	Prof. Dr. Marc Schumann
Prüfer:	Prof. Dr. Stefan Dittmaier
	Prof. Dr. Markus Schumacher
	Prof. Dr. Gregor Herten

Datum der mündlichen Prüfung: 24.05.2017

Abstract

The results presented in this thesis use the full dataset collected in 2012 by the ATLAS experiment from the LHC proton-proton collisions at $\sqrt{s} = 8$ TeV, corresponding to an integrated luminosity of 20.3 fb^{-1}. The first part is devoted to the search for the $W^{\pm}W^{\pm}W^{\mp}$ production in the decay channel where each W boson decays leptonically (excluding leptonic τ decays). Upper limits are placed on the production cross-section in the fiducial phase space. The results are also interpreted in terms of the total cross-section when combined together with the semi-leptonic decay channel. In addition, limits on anomalous quartic gauge boson couplings in an effective field theory approach are extracted. The second part presents a search for supersymmetry in events with multiple jets, two leptons of identical charges or three leptons (electrons or muons). The absence of any excess in the signal regions with respect to the Standard Model expectations is interpreted in terms of limits in the parameter space of 14 supersymmetric models and one mUED model.

Zusammenfassung

Die Ergebnisse, die in dieser Arbeit vorgestellt werden, beinhaten den kompetten Datensatz von LHC Proton-Proton Kollisionen bei $\sqrt{s} = 8$ TeV, der vom ATLAS Detektor im Jahre 2012 aufgezeichnet wurde. Dies entspricht einer totalen integrierten Luminosität von 20.3 fb^{-1}. Der erste Teil dieser Arbeit beschäftigt sich mit der Messung des WWW Prozesses, bei dem jedes W Boson leptonisch zerfällt (der Zerfall in τ Leptonen wird hierbei nicht berüksichtigt). Es konnten hierbei obere Grenzen für den messbaren Wirkungsquerschnitt dieses Prozesses berechent werden. Kombiniert mit den Resultaten aus dem semi-leptonischen Zerfallkanal konnten auch Angaben bezüglich des totalen Wirkungsquerschnitts gemacht werden. Ebenfalls konnten Ausschlussgrenzen bezüglich anormalen Kopplungen zwschen vier Vektorbosonen bestimmt werden. Der zweite Teil der Arbeit widmet sich der Suche nach Supersymmetrie in Ereignissen mit mehreren Jets, zwei Leptonen gleicher Ladung oder drei Leptonen. Es wurden keine signifikanten Abweichungen von den Vorhersagen des Standardmodells in der Signalregionen festgestellt und Auschlussgrenzen in 14 verschiedenen supersymmetrischen Modellen (und einem mUED Modell) konnten bestimmt werden.

CONTENTS

LIST OF FIGURES

LIST OF TABLES

INTRODUCTION

The theoretical and experimental progress made since the 1930s has lead to a better understanding of the fundamental structure of matter. The Standard Model (SM) of particle physics, developed in the early 1970s, provides the most accurate description of all known elementary particles and their interactions. It has explained almost all experimental data over the last decades and predicted many phenomena that were later observed experimentally. Despite these successes, many important questions remain unanswered. The SM is thus widely regarded as an effective theory of a more fundamental one. Furthermore, there are still unexplored kinematic domains within the SM itself.

This thesis investigates these open issues by looking for an electroweak process which is predicted by the SM but has not been observed so far, particularly the $W^{\pm}W^{\pm}W^{\mp}$ production, and by looking for signs of supersymmetry in multi-lepton final states. Triple gauge boson production at the LHC is an important test of the electroweak sector of the SM. The search for $W^{\pm}W^{\pm}W^{\mp}$ production in the fully-leptonic decay channel is one of the first probing the quartic gauge $WWWW$ coupling directly at a collider. Any deviations from the SM prediction would indicate possible new physics processes at higher energy scales. The presented analysis allows therefore to study the existence of anomalous quartic gauge couplings (aQGCs) using an effective field theory approach. To increase the sensitivity, two decay channels ($WWW \to \ell\nu\,\ell\nu\,\ell\nu$ and $WWW \to \ell\nu\,\ell\nu\,jj$

with $\ell = e, \mu$) are statistically combined. The results are interpreted in terms of 95% confidence level upper limits on the $W^{\pm}W^{\pm}W^{\mp}$ production cross-section as well as on the aQGC parameters. An interesting candidate for physics beyond the SM is supersymmetry (SUSY). It naturally solves the hierarchy problem and provides a possible candidate for dark matter. The search for SUSY particles presented in this thesis uses events with multiple energetic jets and either two same-sign leptons (e or μ) or at least three leptons. This signature is sensitive to a wide class of SUSY models, mainly involving strong production processes. No significant excess in data over the SM prediction is observed and constraints are placed on the visible cross-section for new physics processes. Furthermore, new or more stringent exclusion limits at the 95% confidence level are set on the supersymmetric particle masses in the context of scenarios with simplified mass spectra.

The thesis is structured as follows. Firstly, a comprehensive introduction to the theoretical framework of the SM is given in Chapter 1. A particular emphasis is placed on the description of the electroweak sector. Motivated by the limitations of the SM, a supersymmetric extension providing possible solutions is introduced. The Large Hadron Collider and the ATLAS detector are outlined in Chapter 2. The computing grid is briefly reviewed as the author developed monitoring tools used by the ATLAS production system and helped to streamline workflow of the physics validation process. Chapters 3, 4 and 5 present physics analyses where the author has made considerable contributions. Chapter 3 describes a measurement of the $W^{\pm}W^{\pm}W^{\mp}$ production in the fully-leptonic final state. Focus is given to a data-driven technique used to estimate the background events with at least one mis-identified lepton, entirely performed by the author. Given that these processes represent the dominant contribution in the most sensitive signal region, this is a particularly challenging aspect of the analysis. Afterwards, the statistical framework is introduced in details, since the author has contributed to the statistical interpretation of the experimental results in all three analyses. In Chapter 4, a combination with a similar analysis carried out by the ATLAS collaboration in the semi-leptonic final state is performed and presented. Chapter 5 is dedicated to the search for the supersymmetric particles in events with two same-sign or three isolated leptons. Here the focus lies on

the background processes with prompt leptons. The author was responsible for the determination of their theoretical systematic uncertainties and the validation of their estimates. Finally, Chapter 5.10 is devoted to the conclusions and perspectives.

CHAPTER 1

THEORETICAL OVERVIEW

1.1 Introduction

This chapter introduces the Standard Model (SM) that is, as of today, the best theoretical model of elementary particle physics. Within Section 1.2, firstly the particle content is reviewed and then three fundamental forces of nature are outlined. Particular emphasis is given to the electroweak sector which describes the $W^{\pm}W^{\pm}W^{\mp}$ production. Despite a number of SM predictions that have been experimentally confirmed with outstanding precision, the SM is an incomplete theory. One of the most appealing possible extensions is supersymmetry, introduced in Section 1.3. Section 1.4 describes an alternative framework for probing physics beyond the SM, the effective field theory. Section 1.5 gives an overview of the basics of the description and simulation of proton-proton collisions.

Throughout this thesis, the system of natural units, defined such that the speed of light (c) and the reduced Planck constant ($\hbar$) are set to unity, is used. Energy, momentum and mass are thus all expressed in electronvolt (eV).

1.2 The Standard Model of Particle Physics

The Standard Model of particle physics is a relativistic quantum field theory describing the elementary particles of matter and the forces that govern their interactions. It is a combination of non-Abelian gauge theory of the strong interactions proposed by Gross, Wilczek and Politzer [1–3], called quantum chromodynamics, and the unified weak and electromagnetic interactions developed by Glashow, Weinberg and Salam [4–6]. The imposition of local gauge invariance on the quantized fields representing the fundamental particles leads to the emergence of massless gauge fields. It is the mechanism introduced by Goldstone [7] and completed by Brout, Englert [8], Higgs [9] and Guralnik, Hagen, Kibble [10] which allows to construct a renormalizable theory with massive weak vector bosons. This so-called Higgs mechanism breaks the electroweak symmetry and predicts the existence of a scalar particle, the Higgs boson. The complete symmetry group structure of the SM is given through:

$$SU(3)_C \otimes SU(2)_L \otimes U(1)_Y \tag{1.1}$$

where $SU(3)_C$ represents the symmetry of the strong interactions that acts on particles that bear the *colour charge*. The gauge group of the unified electroweak theory is $SU(2)_L \otimes U(1)_Y$ where the associated charges are the *weak isospin* and the *weak hypercharge*. It also contains the subgroup $U(1)_Q$ which describes the electromagnetic interactions acting on particles with the *electric charge*.

1.2.1 Fundamental Particles and Interactions

The elementary particles can be classified according to their spin. *Fermions* have half-integer spin and obey Fermi statistics while *bosons* have integer spin and are characterized by Bose-Einstein statistics.

The fermions are subdivided into *leptons*, which do not interact strongly as they have no colour charge, and *quarks*, which have fractional electric charge and participate in the electroweak as well as the strong interactions. Each of these fermions has a corresponding antiparticle with the same mass but opposite ad-

ditive quantum numbers (e.g. charge). Both, quarks and leptons, are organized into three generations with increasing masses. The heavier fermions subsequently decay to the first-generation fermions, which explains why the observed matter in the universe is composed of the electrons and the up and down quarks. The neutrinos are electrically neutral leptons participating exclusively in the weak interactions. Whereas they are treated as massless within the SM, the experimental evidence of neutrino oscillations [11, 12] indicates non-vanishing masses. Their unique feature compared to other fermions is that they could possibly be their own antiparticles, so-called Majorana fermions. Table 1.1 lists some of their properties.

Particle		Flavour	Symbol	m [MeV]	Q [e]
Leptons	I	electron	e	0.511	-1
		electron neutrino	ν_e	$< 2 \times 10^{-6}$	0
	II	muon	μ	105.7	-1
		muon neutrino	ν_μ	< 0.19	0
	III	tau	τ	1777	-1
		tau neutrino	ν_τ	< 18.2	0
Quarks	I	up	u	2.2	2/3
		down	d	4.7	-1/3
	II	charm	c	1.27×10^3	2/3
		strange	s	96	-1/3
	III	top	t	173.21×10^3	2/3
		bottom	b	4.18×10^3	-1/3

Table 1.1: Fermions of the SM, their electric charge and approximative mass, organized by the generation (I, II, III). The u, d and s quark masses are given as so called "current quark masses" in a mass-independent $\overline{\text{MS}}$ renormalization scheme. The c and b quark masses are the running masses in the $\overline{\text{MS}}$ scheme. The top-quark mass is given as the pole mass. The limits on the electron neutrino and tau neutrino masses are set at a 95% confidence level while the muon neutrino limits are set at a 90% confidence level. Mass values are taken from Reference [13].

The interactions are mediated by the exchange of gauge bosons of spin one, summarised in Table 1.2. The massless photon is the mediator of the *electromagnetic* force which has infinite range and couples to the electrically charged particles. It is neutral and it is its own antiparticle. The *weak* interaction acts on

all fermions but it is sensitive to their chirality, which is defined as the projection of the spin on the direction of the momentum. The short range of this force implies that it is mediated by massive $W^{\pm}$ and Z^0 gauge bosons. The W^+ boson is the antipartner of the W^- boson and vice versa while the Z^0 boson is its own antiparticle. The *strong* interaction is mediated by eight electrically neutral and massless gluons and couples to the particles with colour charge. It is a short-range interaction due to the confinement phenomenon, as discussed later. The gluon is its own antiparticle. In addition to the gauge bosons, the SM includes also one neutral massive spin-zero particle, the Higgs boson.

Interaction	Associated charge	Group	Boson	m [GeV]
Strong	colour	$SU(3)_C$	8 gluons g	0
Electromagnetic	electric charge	$U(1)_Q$	photon γ	0
Weak	weak isospin	$SU(2)_L$	$W^{\pm}$	80.4
			Z^0	91.2

Table 1.2: Gauge bosons in the SM with corresponding interactions, gauge symmetry and approximate mass. Masses taken from Reference [13]. In the SM, the electromagnetic and weak interactions are unified into the electroweak interaction, described in Section 1.2.4. The corresponding gauge group is $SU(2)_L \otimes U(1)_Y$ and the associated charges are the weak isospin and weak hypercharge.

The fourth fundamental interaction, gravitational, is not yet incorporated in the SM since no consistent renormalizable theory of quantum gravity exists up to date. However, its strength is negligible at current high energy physics experiments.

1.2.2 Quantum Electrodynamics

Quantum electrodynamics (QED) is the first formulation of a quantum field theory (QFT), where the incorporation of the principles of quantum mechanics and special theory of relativity is achieved. It is based on the well known gauge invariance of electromagnetism, which is mathematically described by the *Abelian* $U(1)$ symmetry group. Free fermions with non-zero mass, m, are described as

four-component complex spinor, $\psi(x)$, which satisfy the following equation of motion:

$$(i\partial\!\!\!/ - m)\psi(x) = 0 \tag{1.2}$$

Here γ^μ with $\mu = 0, 1, 2, 3$ are the 4×4 Dirac gamma matrices and $\partial\!\!\!/ \equiv \gamma^\mu \partial_\mu$ denotes the contraction with them. This is the famous *Dirac equation*[1]. The gamma matrices must satisfy the Clifford algebra. The *quantized* free Dirac field $\psi(x)$ is represented by a local spinor operator in the Fock space which obeys canonical anticommutation relations. As this field is also *relativistic*, it has a well defined transformation property under Lorentz transformations. Finally, the Lagrangian density of a non-interacting Dirac field can be written as[2]:

$$\mathcal{L}_D = \bar{\psi}(x)(i\partial\!\!\!/ - m)\psi(x) \tag{1.3}$$

where $\bar{\psi}$ is the adjoint Dirac field. This Lagrangian is invariant under global gauge transformations, defined as $U(1)_Q$ phase rotations, which implies the conservation of electric charge Q. However, it is not invariant under local phase rotations i.e. transformations depending on the x coordinates:

$$\psi(x) \to \psi'(x) = e^{i\alpha(x)}\psi(x) \tag{1.4}$$

The local gauge invariance is restored by introducing a gauge vector field $A_\mu(x)$ that interacts with the Dirac field $\psi(x)$ through the covariant derivative $\mathcal{D}_\mu$:

$$\partial_\mu \to \mathcal{D}_\mu = \partial_\mu + ieA_\mu(x) \tag{1.5}$$

where e determines the strength of the interaction and will be interpreted as the electric unit charge. The gauge field can be identified with the photon field with the well known gauge transformation property of electrodynamics:

$$A_\mu(x) \to A'_\mu(x) = A_\mu(x) - \frac{1}{e}\partial_\mu\alpha(x) \tag{1.6}$$

[1] For the massless spin-1/2 particles, the Dirac equation reduces to the Weyl equation.
[2] The Euler-Lagrange equation yields the Dirac equation.

Adding a term describing its dynamics, the Lagrangian of QED reads:

$$\mathcal{L}_{QED} = \bar{\psi}(i\not{D} - m)\psi - \frac{1}{4}F_{\mu\nu}F^{\mu\nu} \tag{1.7}$$

$$= \bar{\psi}(i\not{\partial} - m)\psi - e\bar{\psi}\gamma_\mu\psi A^\mu - \frac{1}{4}F_{\mu\nu}F^{\mu\nu} \tag{1.8}$$

where $F_{\mu\nu} \equiv \partial_\mu A_\nu - \partial_\nu A_\mu$ is the electromagnetic field strength tensor and $-e\bar{\psi}\gamma_\mu\psi$ can be interpreted as the current j_μ produced by the Dirac particles which is conserved.

1.2.3 Quantum Chromodynamics

In order to classify the dozens of strongly interacting particles discovered by the end of 1950s, Gell-Mann [14] and Zweig [15] proposed the *quark model*, which assumed that hadrons are composite particles of fundamental constituents, called quarks. The model was based on the flavour $SU(3)$ symmetry structure of the three lightest quarks: up, down and strange. Later, the deep inelastic scattering data [16, 17] confirmed the hypothesis and indicated that the proton is composed of three charged spin-1/2 particles. Even though it was very successful in providing an understanding of many aspects of baryon (qqq) and meson ($q\bar{q}$) spectroscopy, it did not describe the interactions which hold the quarks together in hadrons. Another shortcoming was the discovery of the Δ^{++} baryon which violated the Pauli exclusion principle. A solution was proposed by Greenberg [18] who introduced an additional degree of freedom, known as a *colour charge*. The concept of colour became the fundamental ingredient of the theory of strong interactions, quantum chromodynamics (QCD) [1–3]. It describes the dynamics of all three quark families, including the later discovered charm [19, 20], bottom [21] and top [22, 23] quarks, as well as gluons [24].

QCD is the gauge theory whose structure is entirely fixed by the requirement of invariance under *non-Abelian* local $SU(3)_C$ rotations in the colour (C) space. As already outlined, each quark field appears in three colour states which are conventionally called red (r), green (g) and blue (b):

$$\Psi(x) \equiv \begin{pmatrix} \psi_r(x) \\ \psi_g(x) \\ \psi_b(x) \end{pmatrix} \tag{1.9}$$

and transforms as:

$$\Psi(x) \to \Psi'(x) = e^{i\alpha^a(x)T^a}\Psi(x) \tag{1.10}$$

where the sum in the exponent runs over eight generators T^a of the $SU(3)_C$ symmetry group and the phase factors α^a depend on the space-time coordinates. The generators are the 3×3 hermitian and traceless matrices which satisfy:

$$T^a = \frac{\lambda^a}{2} \tag{1.11}$$

$$[T^a, T^b] = if^{abc}T^c \tag{1.12}$$

Here λ^a are so-called *Gell-Mann matrices* and f^{abc} are the antisymmetric $SU(3)$ structure constants. Similarly as in QED, the local invariance is recovered by introducing eight gauge vector fields $G^a_\mu(x)$ and replacing the normal derivative in the free Lagrangian 1.3 by the covariant one:

$$\partial_\mu \to \mathcal{D}_\mu = \partial_\mu - ig_s G^a_\mu(x)T^a \tag{1.13}$$

$$G^a_\mu(x) \to G^{a\prime}_\mu(x) = G^a_\mu(x) + \frac{1}{g_s}\partial_\mu\alpha^a(x) - \alpha^b(x)f^{abc}G^c_\mu \tag{1.14}$$

where g_s is the strong coupling constant. The gauge fields correspond to the gluon, which can exist in eight independent colour states with different combinations of one colour and one anticolour charge. Finally, the gauge invariant QCD Lagrangian for a quark flavour q can be formulated as:

$$\mathcal{L}_{QCD} = \bar{\Psi}(i\not{\mathcal{D}} - m_q)\Psi - \frac{1}{4}G^a_{\mu\nu}G^{a,\mu\nu} \tag{1.15}$$

$$= \bar{\Psi}(i\not{\partial} - m_q)\Psi + g_s\bar{\Psi}\gamma^\mu T^a\Psi G^a_\mu - \frac{1}{4}G^a_{\mu\nu}G^{a,\mu\nu} \tag{1.16}$$

The strength tensor of the gluon field a is defined as[1]:

$$G^a_{\mu\nu} \equiv \partial_\mu G^a_\nu - \partial_\nu G^a_\mu + g_s f^{abc} G^b_\mu G^c_\nu \tag{1.17}$$

The non-Abelian structure of $SU(3)$ results in an additional interaction term in 1.17 which describes the triple and quartic gluon coupling vertices. This gives rise to special features of QCD, such as confinement and asymptotic freedom, discussed in more details in Section 1.2.6.2.

1.2.4 Electroweak Theory

The first quantitative theory of weak interactions was formulated by Fermi in 1934 [25]. He interpreted the beta decay of the neutron in terms of a four-fermion interaction vertex. In 1956, Lee and Yang proposed the parity violation in the weak interactions [26] which was experimentally confirmed by Wu [27] one year later. Afterwards, the available experimental data showed that the parity is violated maximally. This gave rise to the V-A theory [28, 29], in which the total current is an equal mixture of vector (V) and axial (A) vector currents. In order to mitigate the high energy behaviour of the pointlike Fermi-type interaction, the massive intermediate vector (IVB) bosons, $W^\pm$, have been introduced[2]. However, it turned out that the scattering amplitudes in this, so-called IVB, theory still violated unitarity. The electroweak theory of Glashow, Salam and Weinberg [4–6] was born through the attempts to unify the electromagnetic and weak interactions as well as to eliminate the problem of quadratic divergences. It required the existence of a neutral particle carrying the weak fundamental force, Z^0 boson, which was discovered in the Gargamelle bubble chamber at CERN in 1973 [30]. Another triumph of the electroweak theory was the first direct observation of the massive vector bosons, $W^\pm$ and Z^0, by the UA1 experiment at CERN in 1983 [31, 32].

The electroweak theory is a gauge field theory with a symmetry group of

[1] Using Equation 1.12 and an alternative representation $G_\mu \equiv G^a_\mu T_a$, the strength tensor can be rewritten as $G_{\mu\nu} \equiv \partial_\mu G_\nu - \partial_\nu G_\mu - ig_s[G_\mu, G_\nu]$. The last term is absent in QED because the Abelian generators of the $U(1)$ gauge symmetry generators commute.

[2] These vector bosons were not true gauge bosons yet.

$SU(2)_L \otimes U(1)_Y$. The subscript L refers to the fact that only the left-handed fermions (and right-handed antifermions) take part in the charged weak interactions. The main idea is to split the fermion fields into the left-handed and right-handed components:

$$\psi = \psi_L + \psi_R = \mathcal{P}_L\psi + \mathcal{P}_R\psi = \frac{1}{2}(\mathbb{1} - \gamma^5)\psi + \frac{1}{2}(\mathbb{1} + \gamma^5)\psi \tag{1.18}$$

where ψ is the 4-component Dirac field, $\mathbb{1}$ denotes the 4×4 unity matrix, $\mathcal{P}_{L/R}$ are the chirality projection operators, and then to assign them different transformation properties. In particular, the left-handed fermions form doublets in the space of *weak isospin* ($I = 1/2$ with $I_3 = \pm 1/2$), while the right-handed fermions are singlets ($I = I_3 = 0$):

$$\Psi_L \equiv \begin{pmatrix} \psi_{\,1/2} \\ \psi_{\text{-}1/2} \end{pmatrix} = \begin{pmatrix} \nu_e \\ e \end{pmatrix}_L, \begin{pmatrix} \nu_\mu \\ \mu \end{pmatrix}_L, \begin{pmatrix} \nu_\tau \\ \tau \end{pmatrix}_L, \begin{pmatrix} u \\ d \end{pmatrix}_L, \begin{pmatrix} c \\ s \end{pmatrix}_L, \begin{pmatrix} t \\ b \end{pmatrix}_L \tag{1.19}$$

$$\Psi_R \equiv \quad \psi_0 \quad = \; e_R,\; \mu_R,\; \tau_R,\; u_R,\; d_R,\; c_R,\; s_R,\; t_R,\; b_R \tag{1.20}$$

Under the *non-Abelian* local $SU(2)_L$ rotations, $\Psi_L(x)$ transforms as a doublet while $\Psi_R(x)$ transforms as a singlet:

$$\begin{aligned} \Psi_L(x) &\to \Psi'_L(x) = e^{i\alpha^i(x)\tau^i}\Psi_L(x) \\ \Psi_R(x) &\to \Psi'_R(x) = \Psi_R(x) \end{aligned} \tag{1.21}$$

where α^i are the parameters and τ^i are three generators of the group satisfying:

$$\tau^i = \frac{\sigma^i}{2} \tag{1.22}$$

$$[\tau^i, \tau^j] = i\epsilon^{ijk}\tau^k \tag{1.23}$$

Here ϵ^{ijk} is the antisymmetric Levi-Civita symbol and σ^i are the 2×2 *Pauli matrices* that are hermitian, unitary and traceless. Meanwhile, the *Abelian* subgroup $U(1)_Y$ introduces a new conserved quantum number known as *hypercharge* Y. It relates the electric charge Q and the third component of the weak isospin I_3 via

the following relation:

$$Y = Q - I_3 \tag{1.24}$$

The Lagrangian 1.3 is invariant under the local $SU(2)_L \otimes U(1)_Y$ group if a triplet of gauge fields W_μ^i associated to the weak isospin subgroup is introduced together with a single gauge field B_μ which corresponds to the weak hypercharge subgroup. The covariant derivative then reads:

$$\mathcal{D}_\mu = \partial_\mu - ig\tau^i W_\mu^i - ig' Y B_\mu \tag{1.25}$$

where two independent coupling constants for $SU(2)_L$ and $U(1)_Y$ are denoted as g and g', respectively. As defined in Equations 1.21 and 1.22, $\tau^i = \sigma^i/2$ for the left-handed fermions and $\tau^i = 0$ for the right-handed fermions. In addition, the non-Abelian W_μ^i and Abelian B_μ gauge fields should transform as:

$$W_\mu^i(x) \to W_\mu^{i\prime}(x) = W_\mu^i(x) + \frac{1}{g}\partial_\mu \alpha^i(x) - \alpha^j(x)\epsilon^{ijk}W_\mu^k \tag{1.26}$$

$$B_\mu(x) \to B'_\mu(x) = B_\mu(x) + \frac{1}{g'}\partial_\mu \beta(x) \tag{1.27}$$

where β is a parameter of the $U(1)_Y$ transformation which is similar to that in QED. Finally, after adding gauge invariant contributions involving the kinetic terms of the vector fields, one gets the electroweak Lagrangian in the form:

$$\mathcal{L}_{EW} = i\bar{\Psi}_L \not{\mathcal{D}} \Psi_L + i\bar{e}_R \not{\mathcal{D}} e_R - \frac{1}{4} W_{\mu\nu}^i W^{i,\mu\nu} - \frac{1}{4} B_{\mu\nu} B^{\mu\nu} \tag{1.28}$$

where only the first generation of leptons is considered. The respective strength tensors are given by:

$$W_{\mu\nu}^i \equiv \partial_\mu W_\nu^i - \partial_\nu W_\mu^i + g\epsilon^{ijk} W_\mu^j W_\nu^k \tag{1.29}$$

$$B_{\mu\nu} \equiv \partial_\mu B_\nu - \partial_\nu B_\mu \tag{1.30}$$

The last term in Equation 1.29 represents the self-interactions of the electroweak gauge fields. To reproduce the properties of quantum electrodynamics, the photon and Z boson fields (A_μ and Z_μ) are recognized as a linear combination of the

corresponding neutral gauge fields (B_μ and W^3_μ):

$$\begin{pmatrix} Z_\mu \\ A_\mu \end{pmatrix} = \begin{pmatrix} \cos\theta_W & -\sin\theta_W \\ \sin\theta_W & \cos\theta_W \end{pmatrix} \begin{pmatrix} W^3_\mu \\ B_\mu \end{pmatrix} \tag{1.31}$$

Here θ_W is the weak mixing angle which is related to the weak (g) and hypercharge (g') coupling constants as well as to the electric unit charge e:

$$\sin\theta_W = \frac{g'}{\sqrt{g^2 + g'^2}}, \quad \cos\theta_W = \frac{g}{\sqrt{g^2 + g'^2}}, \quad e = g\sin\theta_W \tag{1.32}$$

Moreover, this angle also relates the masses of the W and Z gauge bosons:

$$\cos\theta_W = \frac{m_W}{m_Z} \tag{1.33}$$

After identifying A_μ and Z_μ among the gauge fields, the charged weak gauge bosons are determined by:

$$W^\pm_\mu = \frac{1}{\sqrt{2}}(W^1_\mu \mp iW^2_\mu) \tag{1.34}$$

Given the orthogonal transformations 1.31 and 1.34, the kinetic terms in the Lagrangian 1.28 can be rewritten directly as:

$$\mathcal{L}^{kin.}_{gauge} = -\frac{1}{2}W^-_{\mu\nu}W^{+\mu\nu} - \frac{1}{4}A_{\mu\nu}A^{\mu\nu} - \frac{1}{4}Z_{\mu\nu}Z^{\mu\nu} \tag{1.35}$$

where the strength tensors are defined similarly as in Equation 1.30. The terms containing the interactions of the gauge fields with themselves are:

$$\mathcal{L}^{int.}_{gauge} = -\frac{1}{2}g\epsilon^{ijk}(\partial_\mu W^i_\nu - \partial_\nu W^i_\mu)\, W^{j,\mu}W^{k,\nu} \tag{1.36}$$

$$-\frac{1}{4}g^2\epsilon^{ijk}\epsilon^{ilm}\, W^j_\mu W^k_\nu\, W^{l,\mu}W^{m,\nu} \tag{1.37}$$

By employing again 1.31 and 1.34, one can identify two trilinear (WWZ, $WW\gamma$) and four quadrilinear ($WWWW$, $WWZZ$, $WWZ\gamma$ and $WW\gamma\gamma$) couplings. Finally, the terms giving rise to the charged-current interactions, which are of particular interest for this thesis, have the following form for the first family of

leptons:

$$\mathcal{L}^{e}_{CC} = \frac{g}{2\sqrt{2}}\,\bar{\nu_e}\gamma^{\mu}(1-\gamma_5)e\,W^{+}_{\mu} + \text{h.c.} \tag{1.38}$$

where h.c. denotes the hermitian conjugate. The third component of the weak isospin changes by one unit and thus the $W^{\pm}$ bosons have $I = 1$ with $I_3 = \pm 1$.

Table 1.3 shows all fundamental fermions together with the quantum numbers associated with the electroweak interactions. Note that the right-handed massless neutrinos have zero charges and that is why they are absent in 1.20. Actually, they are singlets under all gauge groups of the SM and therefore they do not participate in any of the interactions.

	I	II	III	I_3	Y	Q
Leptons	$\begin{pmatrix}\nu_e\\ e\end{pmatrix}_L$	$\begin{pmatrix}\nu_\mu\\ \mu\end{pmatrix}_L$	$\begin{pmatrix}\nu_\tau\\ \tau\end{pmatrix}_L$	1/2 -1/2	-1/2 -1/2	0 -1
	$\nu_{e,R}$	$\nu_{\mu,R}$	$\nu_{\tau,R}$	0	0	0
	e_R	μ_R	τ_R	0	-1	-1
Quarks	$\begin{pmatrix}u\\ d\end{pmatrix}_L$	$\begin{pmatrix}c\\ s\end{pmatrix}_L$	$\begin{pmatrix}t\\ b\end{pmatrix}_L$	1/2 -1/2	1/6 1/6	2/3 -1/3
	u_R	c_R	t_R	0	2/3	2/3
	d_R	s_R	b_R	0	-1/3	-1/3

Table 1.3: Classification of fermions into three generations (I, II, III) and electroweak multiplets. The gauge quantum numbers are the third component of the weak isospin I_3, weak hypercharge Y and electric charge Q.

The introduction of any term in the Lagrangian 1.28 of the form $-\frac{1}{2}M^2A_\mu A^\mu$, which would give a mass M to a vector field A_μ, violates the gauge invariance. Nevertheless, experimental observations have shown that the $W^{\pm}$ and Z bosons are massive. Moreover, the chiral components Ψ_L and Ψ_R of the fermion fields transform differently under the weak isospin $SU(2)_L$ gauge transformations. Therefore, a fermion mass term of the form $m\bar{\Psi}\Psi = m(\bar{\Psi}_L\Psi_R + \bar{\Psi}_R\Psi_L)$ breaks the chiral symmetry as well and is thus forbidden[1]. The mechanism that incorporates massive fermions and gauge bosons, while preserving the gauge invariance of the

[1]The gauge symmetry is not violated in the QED and QCD models since the gauge bosons (photon and gluons) are massless and the left- and right-handed components transform identically under the corresponding gauge transformations.

Lagrangian, is known as *Higgs mechanism*. It describes a spontaneous breaking of the electroweak $SU(2)_L \otimes U(1)_Y$ symmetry group into the $U(1)_Q$ symmetry group and is further discussed in the following section.

1.2.5 Electroweak Symmetry Breaking

The idea behind spontaneous symmetry breakdown (SSB) is that a system described by a Lagrangian which is invariant under a given symmetry group can evolve into a ground state which is not. The symmetry of the theory is thus no longer manifest in the physical spectrum. This mechanism predicts the existence of a fundamental scalar boson [8–10], the *Higgs boson*, and allows particles to acquire mass by interacting with it. Such a boson was discovered by the ATLAS [33] and CMS [34] collaborations in 2012. Moreover, it unitarizes the $W_L W_L \to W_L W_L$ scattering process (W_L being the longitudinal component of W bosons)[1].

A basic ingredient of the SSB is an introduction of a new isospin doublet Φ of two complex scalar fields, corresponding to four real degrees of freedom, into the theory:

$$\Phi \equiv \begin{pmatrix} \phi^+ \\ \phi^0 \end{pmatrix} \tag{1.39}$$

Its weak hypercharge is equal to 1/2, so that ϕ^+ and ϕ^0 carry charges +1 and 0, respectively. The following kinetic and potential terms describing the dynamics of this new field can be added to the electroweak Lagrangian 1.28, as they are invariant under the corresponding symmetry group:

$$\mathcal{L}_{Higgs} = (\mathcal{D}_\mu \Phi)^\dagger (\mathcal{D}^\mu \Phi) + \mu^2 \Phi^\dagger \Phi - \lambda (\Phi^\dagger \Phi)^2 \tag{1.40}$$

where $\mathcal{D}_\mu$ represents the covariant derivative defined in Equation 1.25. Recalling that $\mathcal{L} = T - V$, the above Lagrangian has the potential $V(\Phi)$ which includes the self-interaction of Φ:

$$V(\Phi) = -\mu^2 \Phi^\dagger \Phi + \lambda (\Phi^\dagger \Phi)^2 \tag{1.41}$$

[1] This section follows Reference [35].

The shape of the potential depends on the parameters μ^2 and λ. The parameter λ is a dimensionless coupling constant which is required to be positive in order to ensure that the energy density is bounded from below. The parameter μ has the dimension of a mass. For $\mu^2 > 0$, the potential has a local maximum for vanishing values of Φ, and an absolute minimum for:

$$\Phi_0^\dagger \Phi_0 = \frac{v^2}{2} \quad \text{with} \quad v = \frac{\mu}{\sqrt{\lambda}} \tag{1.42}$$

This means that the Φ_0 values minimizing the energy density lie on a circle in the complex plane with radius $v/\sqrt{2}$ which is also known as *vacuum expectation value* (VEV). The energy minimum is thus continuously degenerate, what reflects the spontaneous breakdown of the $SU(2)_L \otimes U(1)_Y$ symmetry. In order to preserve the electromagnetic $U(1)_Q$ symmetry of the vacuum[1], only the neutral component of Φ can acquire a non-vanishing VEV. Moreover, given that the ground state of the considered system is described by a non-zero constant field, Φ can be expanded around this stable vacuum state using an exponential parametrization:

$$\Phi(x) = \frac{1}{\sqrt{2}} \exp\left(i \frac{\pi^i(x)}{v} \tau^i\right) \begin{pmatrix} 0 \\ v + H(x) \end{pmatrix} \tag{1.43}$$

where τ^i denote the Pauli matrices, the "angular" fields $\pi^i(x)$ represent three spin-zero massless particles, *Goldstone bosons*. The factor $1/v$ is introduced to ensure the dimension of mass. The "radial" shift defines the Higgs field $H(x)$ which is a scalar field with zero VEV corresponding to the physical Higgs boson. Furthermore, the gauge is fixed[2] such that the Goldstone bosons do not manifest explicitly in the physical spectrum. The field Φ in this so-called *unitary gauge* becomes:

$$\Phi_U(x) = \frac{1}{\sqrt{2}} \begin{pmatrix} 0 \\ v + H(x) \end{pmatrix} \tag{1.44}$$

[1] This requirement is mandatory since the photon is massless.

[2] It is actually the local $SU(2)_L$ invariance of the Lagrangian which allows to "rotate away" any dependence on the angular fields $\pi^i(x)$ from Φ. This rotation is thus formally equivalent to a gauge fixing.

and the Lagrangian of the system 1.40 can be rewritten as:

$$\begin{aligned}\mathcal{L}^{U}_{Higgs} = &\frac{1}{2}(\partial_\mu H)(\partial^\mu H) - \lambda v^2 H^2 - \lambda v H^3 - \frac{1}{4}\lambda H^4 \\ &+ \frac{1}{8}(v+H)^2\left[2g^2 W^-_\mu W^{+\mu} + \frac{g^2}{\cos^2\theta_W} Z_\mu Z^\mu\right]\end{aligned} \tag{1.45}$$

The mass terms for the W and Z gauge bosons as well as the Higgs boson can be directly identified, and the following relations are found:

$$m_W = \frac{gv}{2}, \quad m_Z = \frac{gv}{2\cos\theta_W}, \quad m_H = \sqrt{2\lambda}v \tag{1.46}$$

Furthermore, one can recognize the interactions of these massive electroweak vector bosons with the Higgs field, namely the trilinear (WWH, ZZH) and quadrilinear ($WWHH$, $ZZHH$) couplings. Finally, the Lagrangian 1.45 also contains cubic (HHH) and quartic ($HHHH$) self-couplings of the Higgs boson.

The fermion masses can also be generated through appropriate interactions with the Higgs doublet. In order to preserve the renormalizability and gauge invariance of the SM Lagrangian, new terms are added in the form of so-called *Yukawa couplings*. Considering only leptons of the first family, one can write:

$$\mathcal{L}^{e}_{Yukawa} = -h_e \, \bar{L}^e \Phi \, e_R + \text{h.c.} \tag{1.47}$$

$$= -\frac{1}{\sqrt{2}} h_e (v+H)\,(\bar{e}_L e_R + \bar{e}_R e_L) + \text{h.c.} \tag{1.48}$$

where h_e is a coupling constant, L^e denotes the left-handed doublet of the electron type, e_R is the right-handed electron singlet and Φ represents the Higgs doublet in unitary gauge 1.44. It contains an electron mass term with

$$m_e = \frac{1}{\sqrt{2}} h_e v \tag{1.49}$$

and an interaction term with a coupling strength proportional to the electron mass. Given that the flavour changing charged currents (FCCC) have been observed experimentally in the quark sector, the electroweak interaction eigenstates have to be superpositions of the physical quark mass eigenstates. The relevant

Yukawa interactions can be thus written as:

$$\begin{aligned}\mathcal{L}^{quark}_{Yukawa} = &- h_{1i}\,\bar{U}_{0L}\Phi\,d^i_{0R} - h_{2i}\,\bar{C}_{0L}\Phi\,d^i_{0R} - h_{3i}\,\bar{T}_{0L}\Phi\,d^i_{0R} \\ &- \tilde{h}_{1i}\,\bar{U}_{0L}\tilde{\Phi}\,u^i_{0R} - \tilde{h}_{2i}\,\bar{C}_{0L}\tilde{\Phi}\,u^i_{0R} - \tilde{h}_{3i}\,\bar{T}_{0L}\tilde{\Phi}\,u^i_{0R} + \text{h.c.}\end{aligned} \tag{1.50}$$

where h_{ji} with $i,j \in \{1,2,3\}$ are arbitrary dimensionless coupling constants. The left-handed $SU(2)_L$ doublets corresponding to three generations of quarks are denoted as $\bar{U}_{0L}$, $\bar{C}_{0L}$ and $\bar{T}_{0L}$. The right-handed $SU(2)_L$ singlets are represented by $u^i_{0R} \in \{u_{0R}, c_{0R}, t_{0R}\}$ and $d^i_{0R} \in \{d_{0R}, s_{0R}, b_{0R}\}$. The subscript '0' indicates the unphysical nature of the quark fields participating in these interactions. The charge conjugate of Φ is equal to $\tilde{\Phi} = (\frac{1}{\sqrt{2}}(v+H), 0)^T$. The mass terms can be rewritten in a compact form:

$$\mathcal{L}^{quark}_{mass} = -\,\bar{Q}^{dsb}_{0L}\mathcal{M}\,Q^{dsb}_{0R} - \bar{Q}^{uct}_{0L}\tilde{\mathcal{M}}\,Q^{uct}_{0R} + \text{h.c.} \tag{1.51}$$

Here $Q^{dsb}_{0R/L}$ and $Q^{uct}_{0R/L}$ are the right-/left-handed down- and up-type quarks, respectively. Introducing similar notation for the physical fields, one defines:

$$Q^{dsb}_{0L} = \begin{pmatrix} d_{0L} \\ s_{0L} \\ b_{0L} \end{pmatrix} \quad Q^{uct}_{0L} = \begin{pmatrix} u_{0L} \\ c_{0L} \\ t_{0L} \end{pmatrix} \quad Q^{dsb}_{L} = \begin{pmatrix} d_{L} \\ s_{L} \\ b_{L} \end{pmatrix} \quad Q^{uct}_{L} = \begin{pmatrix} u_{L} \\ c_{L} \\ t_{L} \end{pmatrix} \tag{1.52}$$

The quark fields are redefined through unitary transformations:

$$\begin{aligned} Q^{dsb}_L &= \mathcal{U}\,Q^{dsb}_{0L} \qquad & Q^{dsb}_R &= \mathcal{V}\,Q^{dsb}_{0R} \\ Q^{uct}_L &= \tilde{\mathcal{U}}\,Q^{uct}_{0L} \qquad & Q^{uct}_R &= \tilde{\mathcal{V}}\,Q^{uct}_{0R} \end{aligned} \tag{1.53}$$

The matrices $\mathcal{M}$, $\tilde{\mathcal{M}}$ can be diagonalized by means of biunitary transformations:

$$\mathcal{M} = \mathcal{U}^\dagger\mathfrak{M}\mathcal{V} \qquad \tilde{\mathcal{M}} = \tilde{\mathcal{U}}^\dagger\tilde{\mathfrak{M}}\tilde{\mathcal{V}} \tag{1.54}$$

The $\mathfrak{M}$ and $\tilde{\mathfrak{M}}$ matrices are thus diagonal and positive, $\text{diag}\{m_d, m_s, m_b\}$ and $\text{diag}\{m_u, m_c, m_t\}$. The Lagrangian 1.51 takes the simple final form:

$$\mathcal{L}^{quark}_{mass} = -\,\bar{Q}^{dsb}_{L}\mathfrak{M}\,Q^{dsb}_{R} - \bar{Q}^{uct}_{L}\tilde{\mathfrak{M}}\,Q^{uct}_{R} + \text{h.c.} \tag{1.55}$$

Finally, one can write the charged-current interaction in terms of the unphysical as well as the physical quark fields in the following form:

$$\mathcal{L}_{CC}^{quark} = \frac{g}{2\sqrt{2}}\,\bar{Q}_0^{uct}\gamma^\mu(1-\gamma_5)\,Q_0^{dsb}\,W_\mu^+ + \text{h.c.} \tag{1.56}$$

$$= \frac{g}{2\sqrt{2}}\,\bar{Q}^{uct}\gamma^\mu(1-\gamma_5)V_{\text{CKM}}\,Q^{dsb}\,W_\mu^+ + \text{h.c.} \tag{1.57}$$

The transformation to the physical basis has been performed according to 1.53 and $\tilde{\mathcal{U}}\mathcal{U}^\dagger$ is called Cabibbo-Kobayashi-Maskawa (CKM) matrix [36, 37], V_{CKM}. It is non-diagonal matrix and therefore describes three level FCCC between the different quark generations. Given that $\mathcal{U}\mathcal{U}^\dagger$ is a unit matrix, it is clear that within the considered three-generation scheme the flavour changing neutral currents (FCNC) are not allowed at three level in the SM. In addition, the CKM matrix is unitary and complex, which can be parametrized by means of three rotation angles θ_1, θ_2, θ_3 and one complex phase δ. This non-zero phase is a source of $\mathcal{CP}$ violation in the quark sector.

In the SM extension including neutrino masses, they propagate in the mass eigenstates that are linear combinations of the weak interaction eigenstates. An analogue flavour-mixing mechanism thus occurs, known as neutrino oscillations, which is described by Pontecorvo-Maki-Nakagawa-Sakata (PMNS) matrix [38].

In summary, the SM is a renormalizable theory with the Lagrangian:

$$\mathcal{L}_{SM} = \mathcal{L}_{QCD} + \mathcal{L}_{EW} + \mathcal{L}_{Higgs} + \mathcal{L}_{Yukawa} \tag{1.58}$$

It is invariant under local gauge transformations of the $SU(3)_C \otimes SU(2)_L \otimes U(1)_Y$ symmetry group and can be used to perturbatively calculate processes at the currently accessible energy scales. The SM has a number of parameters whose values are not specified by the theory and have to be measured experimentally. Since neutrinos are treated as massless within the SM, the total number of these parameters is 18. Namely, the SM incorporates nine Yukawa couplings for the fermion masses excluding neutrinos, the Higgs boson mass m_H and the vacuum expectation value v, three coupling constants g_s, g and g' corresponding to the gauge groups $SU(3)_C$, $SU(2)_L$ and $U(1)_Y$, respectively, and four parameters of the CKM matrix.

1.2.6 From Lagrangian to Cross-section

Given the Lagrangian of an interacting theory, one can derive the cross-section for any process of interest. The initial state $|i\rangle$ evolves to a final state $|f\rangle$ under a Hamiltonian which is obtained through the Legendre transformation of the corresponding Lagrangian[1]. The scattering processes are represented by Feynman diagrams and calculated using Feynman rules. This section introduces the most important concepts and techniques in quantum field theories, such as perturbation expansion, dimensional regularization and renormalization.

1.2.6.1 Perturbation Theory

In the quantum field theory, the N-particle Hilbert space is known as the *Fock space*. The creation and annihilation operators, $a_i^\dagger$ and a_i, act on a multi-particle state and add or remove a particle in the ascribed quantum state i. All the particles of a given species are then described as a field operator defined at each space-time point x in terms of a and $a^\dagger$. The bosonic $\phi(x)$ and fermionic $\psi(x)$ field operators are quantized with the canonical commutation and anticommutation relations, respectively. When calculating scattering amplitudes in particle physics, one presumes that the interacting field is related to the free field describing the incoming and outgoing partons by a unitary transformation. Since the momenta of the incoming particles are generally known, it is convenient to do the calculation in the momentum space:

$$\langle f \,|\, S \,|\, i \rangle = \lim_{t\to\infty} \langle \vec{p}_1, \ldots, \vec{p}_m \,|\, U(t,-t) \,|\, \vec{p}_{m+1}, \ldots, \vec{p}_n \rangle \tag{1.59}$$

$$= \langle \vec{p}_1, \ldots, \vec{p}_m \,|\, \mathcal{T} \exp[-i \int \mathcal{H}_{\text{int}}(x)\, \mathrm{d}^4 x\,] \,|\, \vec{p}_{m+1}, \ldots, \vec{p}_n \rangle \tag{1.60}$$

where the unitary operator S is known as the *S-matrix*[2] and $\mathcal{H}_{\text{int}}(x)$ is the interaction Hamiltonian density. The integration goes over the whole space-time.

This is the key expression for the *perturbation theory*. The coefficient of the

[1] In a case of non-derivative coupling, the interaction Hamiltonian density $\mathcal{H}_{\text{int}}(x)$ coincides up to a sign with the interaction Lagrangian density $\mathcal{L}_{\text{int}}(x)$.

[2] Another approach in QFT is to describe the time evolution between the initial and final states of particles created simultaneously at certain positions using the *Green's functions* which are time-ordered correlation functions of fields at different space-time points.

interaction terms is assumed to be small enough, so that it can be used as an expansion parameter. It is a good approximation for electroweak as well as high energy QCD processes. The perturbative expansion is given a graphical representation in terms of *Feynman diagrams*. So-called loop diagrams correspond to higher orders of the perturbation theory. The scattering amplitude is then given by the sum of each possible interaction over all possible intermediate particle states. It is directly related to physical quantities, such as cross-sections and decay rates.

1.2.6.2 Renormalization

Beyond tree level, many fundamental loop diagrams give rise to divergent integrals in the UV i.e. at very short distances. However, it has been found that they are finite if the integration is performed in $4 - \epsilon$ dimensions. One can thus consider the analytic continuation of the amplitude to $4 - \epsilon$ dimensions where the infinities of perturbation theory manifest as poles for $\epsilon = 0$. This is known as the *dimensional regularization*, devised by 't Hooft and Veltman [39, 40], which respects gauge as well as Lorentz symmetries. These UV poles are then subtracted in a *renormalization* scheme by properly adjusting the coefficients of the theory. Formally, the "bare" Lagrangian is split into a "renormalized" Lagrangian, defined in terms of the physical parameters and the physical fields, and a counterterm Lagrangian. The divergent parts are cancelled by the counterterms. Specifically, the charge renormalization absorbs the higher order contributions involving loops in the propagator. It can be physically interpreted as the fact that the elementary particles are "dressed" by a cloud of virtual particles.

In QED, the electron charge can be defined via the electron-electron scattering amplitude. It is related to the fine-structure constant by $\alpha = e^2/4\pi$. The corrections to the photon propagator are due to the polarization of the vacuum, i.e. the creation of virtual electron-positron pairs. A renormalized coupling constant can be expressed in terms of a quantity measured at a specific kinematic point with the energy characteristic for the experiment, called the *renormalization scale* μ_R. By taking μ_R as a reference, any dependence on the cut-off scale is eliminated. The invariance of physical quantities under a change of μ_R is ensured

by the renormalization group [41]. This scaling behaviour, encoded by so-called beta-functions, can be translated into the momentum-dependent *running coupling constant*:

$$\alpha(Q^2) = \frac{\alpha(\mu_R^2)}{1 - \frac{\alpha(\mu_R^2)}{3\pi} \ln\left(\frac{Q^2}{\mu_R^2}\right)} \tag{1.61}$$

where Q^2 is the momentum transfer. It describes the effect of the electron charge *screening* due to quantum vacuum polarization which can be treated as a virtual dipole. The unscreened bare charge is logarithmically divergent.

In QCD, there are two additional graphs arising from the self-interaction of gluons. The running strong coupling constant α_s, related to the coupling g_s by $\alpha_s = g_s^2/4\pi$, is then given by:

$$\alpha_s(Q^2) = \frac{\alpha_s(\mu_R^2)}{1 + (33 - 2n_f)\frac{\alpha_s(\mu_R^2)}{12\pi} \ln\left(\frac{Q^2}{\mu_R^2}\right)} \tag{1.62}$$

where n_f is the number of quark flavours. It describes the *antiscreening* of colour charge by virtual gluon pairs in the vacuum. As a consequence, an effective colour charge becomes small at short distances (high energies) and large at large distances (low energies). The behaviour at high Q^2 is referred to as *asymptotic freedom* since the quarks appear as free particles and can be treated perturbatively. At sufficiently low Q^2, the coupling constant becomes of order unity and the physics becomes nonperturbative. This leads to the *confinement* of quarks and gluons inside hadrons. The energy needed to isolate two quarks is so large that it becomes more energetically favourable to create a new quark-antiquark pair out of the vacuum, which then again confines within colourless boundstates. This process is known as *hadronisation* and results in the experimentally observable spray of hadrons called *jet*. The value at which this occurs is called the intrinsic *QCD scale*, Λ_{QCD}, and is at about 200 MeV:

$$\Lambda_{QCD}^2 = \mu_R^2 \exp\left[\frac{-12\pi}{(33 - 2n_f)\alpha_s(\mu_R^2)}\right] \tag{1.63}$$

Now $\alpha_s(Q^2)$ can be rewritten in terms of Λ_{QCD}^2:

$$\alpha_s(Q^2) = \frac{12\pi}{(33 - 2n_f)\ln\left(\frac{Q^2}{\Lambda^2_{QCD}}\right)} \tag{1.64}$$

At low energy scales ($Q^2 < \Lambda^2_{QCD}$), the theory is predicted using either numerical (lattice QCD) or phenomenological techniques.

1.2.7 Limitations of the Standard Model

The Standard Model of particle physics is an exceptionally predictive theory which has been experimentally verified to a high degree of precision over a wide range of energy and processes. Despite these successes, there are still several questions within the SM which remain unanswered. They provide hints for new physics beyond the SM (BSM) and some of them are discussed below.

The so-called *hierarchy problem* stems from the large difference between the electroweak scale $M_{EW} \sim \mathcal{O}(10^2$ GeV) and the Plank scale $M_P \sim \mathcal{O}(10^{19}$ GeV). While the electroweak symmetry breaking occurs at M_{EW}, the gravitational force becomes comparable to the other forces at M_P. This problem can be interpreted as the unnaturalness of the weak scale scalar mass. The physically observed mass of the Higgs boson is expected to have large contributions from loop diagrams involving virtual particles, in particular the top quark. These quantum corrections diverge quadratically with the ultraviolet cut-off scale Λ_{UV}, introduced to regulate the loop integrals. Assuming that the SM is valid up to the Plank scale ($\Lambda_{UV} \sim M_P$), the bare Higgs boson mass appearing in the Lagrangian needs to be fine-tuned by 10^{17} orders of magnitude.

Another unexplained phenomenon within the SM is the *matter-antimatter asymmetry*. The visible universe consists of significantly less antimatter than matter. It can be explained by the presence of $\mathcal{CP}$ violating processes. Although the CKM matrix contains a $\mathcal{CP}$ violating phase, it is not big enough to describe the observed asymmetry in the universe.

Cosmological and astrophysical measurements indicates that only about 5% of the overall matter-energy density in the universe can be accounted for by the ordinary matter [42]. The so-called *dark matter* corresponds to about 27% of the

total density. It is defined as matter which is massive, stable on cosmological scales and has very weak couplings to the electromagnetic sector. Its nature still remains unknown. The remaining 68% of the universe is thought to be dark energy which is even less understood than dark matter.

As already discussed, the SM includes only left-handed massless neutrinos. However, measurements of neutrino oscillations [11, 12] imply that the *neutrinos have non-zero masses*. These could be incorporated into the SM by two relatively simple extensions which treat neutrinos as Majorana [43] or Dirac [44] particles. In addition, the extreme smallness of neutrino masses can be elegantly explained by the seesaw mechanism [45–47] which requires an extension of the SM by adding one heavy right-handed neutrino per family.

The electroweak force successfully combines the weak and electromagnetic forces. This indicated that there might be a *grand unification theory* (GUT) which unifies all three gauge interactions of the SM. By embedding the $SU(3)_C \otimes SU(2)_L \otimes U(1)_Y$ group into a larger symmetry group, for example $SU(5)$ or $SO(10)$, the number of independent coupling constants can be reduced to only one at the unification scale [48]. However, evolving the couplings towards high energies shows that the SM alone is not sufficient to ensure this convergence.

1.3 Supersymmetry

Several theories beyond the SM have been proposed in order to solve some of the shortcomings discussed in the previous section. Supersymmetry (SUSY) [49–57] is often regarded as one of the most attractive and thoroughly formulated extensions of the SM. It introduces a new fundamental space-time symmetry which maps bosons into fermions, and vice versa. In 1975, Haag, Lopuszanski and Sohnius [58] showed that *supersymmetry* is the unique extension of the Poincaré space-time symmetry[1] and internal symmetries (such as gauge symmetries) of the scattering matrix i.e. of the particle interactions. They evaded the famous "no-go" Coleman-Mandula theorem [59], which prohibits any additional non-trivial symmetries,

[1] The Poincaré group is the full symmetry group of any relativistic field theory. Its elements can be written as $\{(\Lambda, a)\}$ where Λ parametrizes transformations of the Lorentz group (rotations and boosts) and a parametrizes translations.

by allowing for *fermionic generators* satisfying anticommutation relation. The generators of the SUSY transformations are thus defined as:

$$\mathcal{Q}\,|\text{boson}\rangle = |\text{fermion}\rangle \qquad \mathcal{Q}\,|\text{fermion}\rangle = |\text{boson}\rangle \tag{1.65}$$

and obey the following algebra relations:

$$\{\mathcal{Q}_a, \mathcal{Q}_b^\dagger\} = 2(\sigma^\mu)_{ab} P_\mu \qquad \{\mathcal{Q}_a, \mathcal{Q}_b\} = \{\mathcal{Q}_a^\dagger, \mathcal{Q}_b^\dagger\} = 0 \tag{1.66}$$

where $\mathcal{Q}$ and its hermitian conjugate $\mathcal{Q}^\dagger$ are two-component complex spinor operators which carry spin angular momentum $1/2$, a and b are the spinor indices, P_μ is the four-momentum generator of space-time translations and $\sigma^\mu = (\mathbb{1}, \vec{\sigma})$. The former shows that two successive SUSY transformations preserve the spin but generate a space-time translation and therefore illustrates the entanglement of the SUSY and the space-time symmetry. In addition, the generators $\mathcal{Q}$ and $\mathcal{Q}^\dagger$ commute with P_μ:

$$[\mathcal{Q}_a, P_\mu] = [\mathcal{Q}_a^\dagger, P_\mu] = 0 \tag{1.67}$$

This implies the invariance of the SUSY transformations under the translations i.e. they are independent on the space-time position.

Irreducible representations of the Poincaré superalgebra[1], also known as SUSY algebra, are called *supermultiplets*. Each supermultiplet contains an equal number of fermionic and bosonic degrees of freedom. All particles within the same supermultiplet have degenerate masses since the squared mass operator P^2 is the Casimir operator of SUSY algebra. Moreover, $\mathcal{Q}$ and $\mathcal{Q}^\dagger$ also commute with the generators of the $SU(3)_C \otimes SU(2)_L \otimes U(1)_Y$ gauge group corresponding to the internal symmetries. Therefore, all states in one supermultiplet have the same quantum numbers of electric charge, weak isospin and colour.

Besides being a mathematically elegant theory, the weak-scale supersymmetry provides a natural solution to the hierarchy problem. Each SUSY scalar loop

[1]The Poincaré superalgebra is defined by the relations 1.66 and 1.67 which are to be combined with the usual Poincaré algebra.

contributes to the Higgs boson mass with opposite sign than the corresponding SM fermionic loop. Therefore, the quadratic dependence on the cut-off scale is cancelled. In addition, the three SM coupling constants do not meet in a single point after their extrapolation to the GUT scale. This is shown in Figure 1.1a where the evolution of the inverse couplings as a function of the logarithm of the energy is depicted. This behaviour changes when including the particles predicted by SUSY. If the SUSY masses are of the order of TeV a perfect unification is achieved at $\sim 10^{16}$ GeV, as shown in Figure 1.1b. Some SUSY models can also provide a suitable candidate for dark matter, a weakly interacting particle not present in the SM.

1.3.1 Minimal Supersymmetric Standard Model

The minimal supersymmetric Standard Model (MSSM) is the supersymmetric extension of the SM with a minimal particle content. Each SM particle is placed within either a gauge or chiral supermultiplet together with a superpartner that differs by half a unit of spin.

The fermions represent one component in a chiral supermultiplet. The corresponding spin-0 superpartners are denoted with a tilde and a prefix "s", for example the superpartner of the quark is called a *squark* ($\tilde{q}$). The gauge bosons form alongside with their spin-1/2 superpartners a gauge supermultiplet. They are labelled with a tilde and a suffix "ino", and are altogether referred to as the *gauginos*. Since the left-handed and right-handed components of the fermions have different transformation properties, they have separate scalar partners. The gauge interactions for $\tilde{q}_L$ and $\tilde{q}_R$ are then the same as for q_L and q_R, respectively. The subscript refers only to the chirality of the SM partner. On the other hand, the gauge transformations of the left-handed and right-handed components of the gaugino fermions are the same.

The Higgs boson resides in a chiral supermultiplet. The MSSM requires two electroweak Higgs doublets in order to restore anomaly cancellation and to give masses to the up-type as well as the down-type quarks. The MSSM Higgs sector has thus eight degrees of freedom. Three of them are absorbed by the $W^{\pm}$ and Z gauge fields as in the SM and remaining five form the following physical

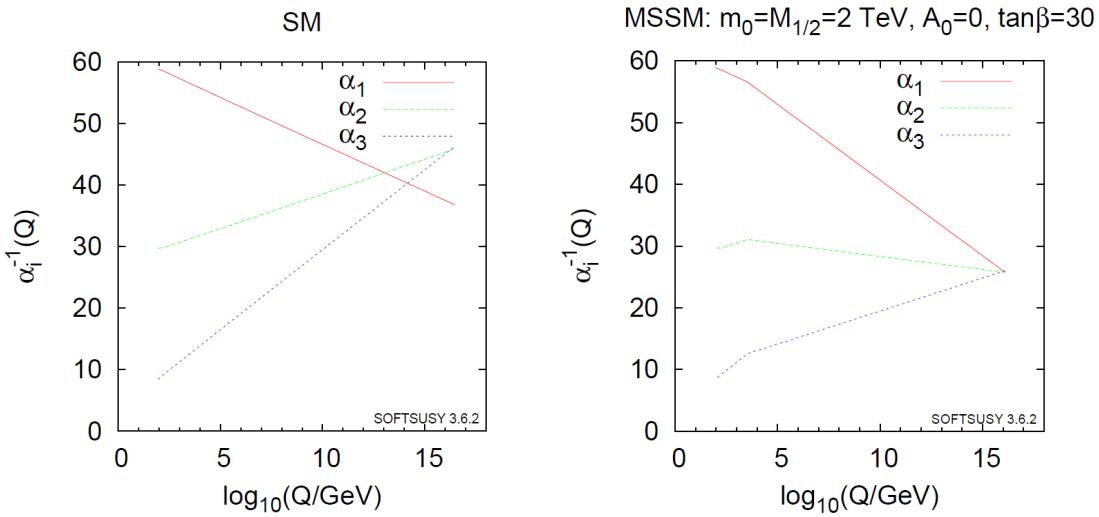

(a) (b)

Figure 1.1: Evolution of the inverse gauge coupling constants in the SM (a) and the MSSM (b) with the energy scale for the electromagnetic force (α_1) the weak force (α_2) and the strong force (α_3) using two-loop renormalization group evolution. The SUSY threshold at 2 TeV is clearly visible. Figure taken from Reference [13].

particles: h^0, H^0, A^0 and $H^\pm$. The $\mathcal{CP}$-even neutral Higgs bosons are denotes as h^0, H^0 with $m_{h^0} \leq m_{H^0}$, A^0 is the $\mathcal{CP}$-odd neutral Higgs boson and $H^\pm$ is a pair of charged Higgs bosons that are the charge conjugates of each other. Their fermionic counterparts are called *higgsinos*.

After the electroweak symmetry breaking and the SUSY breaking (discussed in Section 1.3.1.1), the superpartners with equal gauge quantum numbers mix and the mass eigenstates are obtained by diagonalizing the mass matrices in the Lagrangian. The physical states called *charginos* and *neutralinos* are linear combinations of the charged and neutral gauginos and higgsinos, respectively. The mixing also occurs in the sfermion sector. As it is proportional to the mass of the corresponding SM partner, it is non-negligible only for third generation sfermions. A summary of the MSSM particle content together with these mixings is shown in Table 1.4.

Particle group	Spin	Gauge eigenstates	Mass eigenstates
Higgs bosons	0	H_u^0, H_d^0, H_u^+, H_d^-	h^0, H^0, A^0, $H^\pm$
Neutralinos	1/2	$\tilde{B}^0$, $\tilde{W}^0$, $\tilde{H}_u^0$, $\tilde{H}_d^0$	$\tilde{\chi}_1^0$, $\tilde{\chi}_2^0$, $\tilde{\chi}_3^0$, $\tilde{\chi}_4^0$
Charginos	1/2	$\tilde{W}^\pm$, $\tilde{H}_u^+$, $\tilde{H}_d^-$	$\tilde{\chi}_1^\pm$, $\tilde{\chi}_2^\pm$
Gluinos	1/2	$\tilde{g}$	$\tilde{g}$
Squarks	0	$\tilde{u}_L$, $\tilde{d}_L$, $\tilde{u}_R$, $\tilde{d}_R$	$\tilde{u}_L$, $\tilde{d}_L$, $\tilde{u}_R$, $\tilde{d}_R$
		$\tilde{s}_L$, $\tilde{c}_L$, $\tilde{s}_R$, $\tilde{c}_R$	$\tilde{s}_L$, $\tilde{c}_L$, $\tilde{s}_R$, $\tilde{c}_R$
		$\tilde{t}_L$, $\tilde{b}_L$, $\tilde{t}_R$, $\tilde{b}_R$	$\tilde{t}_1$, $\tilde{b}_1$, $\tilde{t}_2$, $\tilde{b}_2$
Sleptons	0	$\tilde{e}_L$, $\tilde{\nu}_{e,L}$, $\tilde{e}_R$	$\tilde{e}_L$, $\tilde{\nu}_{e,L}$, $\tilde{e}_R$
		$\tilde{\mu}_L$, $\tilde{\nu}_{\mu,L}$, $\tilde{\mu}_R$	$\tilde{\mu}_L$, $\tilde{\nu}_{\mu,L}$, $\tilde{\mu}_R$
		$\tilde{\tau}_L$, $\tilde{\nu}_{\tau,L}$, $\tilde{\tau}_R$	$\tilde{\tau}_1$, $\tilde{\nu}_{\tau,L}$, $\tilde{\tau}_2$

Table 1.4: The particle content in the MSSM. It is assumed that the sfermion mixing for the first and second generation is negligible. The neutralinos and charginos are ordered by increasing mass i.e. $m_{\tilde{\chi}_1^0} \leq m_{\tilde{\chi}_2^0} \leq m_{\tilde{\chi}_3^0} \leq m_{\tilde{\chi}_4^0}$ and $m_{\tilde{\chi}_1^\pm} \leq m_{\tilde{\chi}_2^\pm}$.

1.3.1.1 Supersymmetry breaking

As already mentioned, all particles within a supermultiplet have the same mass. Since there is no experimental evidence for SUSY (so far), if this symmetry is realised in nature, it has to be broken. The mechanism which breaks the symmetry such that the superpartners are more massive than the corresponding SM particles is unknown. Nevertheless, the solution of the hierarchy problem can still be maintained if the SUSY breaking terms in the Lagrangian are *soft* i.e. their mass dimension is less than four and their mass scale at TeV. As it is very difficult to introduce the MSSM soft terms arising from tree-level renormalizable couplings, they are assumed to arise rather indirectly or radiatively (loops). The idea is that the SUSY breaking occurs, irrespective of a specific mechanism, in a *hidden sector*. It is then communicated to the *visible sector* through some interactions, either gravity or gauge interactions, and as a result the soft breaking terms appear in the MSSM Lagrangian. In the supergravity mediated models (SUGRA), the hidden sector is near the Plank scale. In the gauge-mediated SUSY breaking

scenario (GMSB), the soft terms come from the loop diagrams involving some *messenger* particles with SM gauge quantum numbers and the SUSY breaking scale can be as low as $\sim 10^4$ GeV.

1.3.1.2 R-parity

In general, it is possible to add to the MSSM Lagrangian also terms which are consistent with the symmetries of the SM as well as the supersymmetry but allow for tree-level proton decay processes, such as $p \to e^+\pi^0$. A lower limit on the proton lifetime in this decay channel has been set to 1.29×10^{34} years by the Super-Kamiokande collaboration [60]. This implies that the coupling constant of such a process should be inconceivably small. In order to avoid these baryon (B) and lepton (L) number violating terms, a new symmetry is imposed in the MSSM, called *R-parity*. It is a multiplicatively conserved quantum number defined for a particle of spin s as:

$$R = (-1)^{3(B-L)+2s} \tag{1.68}$$

All SM particles have even R-parity ($R = +1$) while all sparticles have odd R-parity ($R = -1$). Its conservation in all interactions has several important phenomenological consequences. Firstly, sparticles can only be produced in pairs at the LHC. Afterwards, each of them decays to an odd number of lighter SUSY particles. The lightest supersymmetric particle (LSP) of the decay chain is thus stable. Given that no such particle has been observed, the LSP must be neutral and very weakly interacting, and therefore represents a good candidate for dark matter. Consequently, it escapes the detector, giving the missing transverse energy signature which is characteristic for all R-parity conserving (RPC) models. The MSSM, defined as the RPC theory, can be extended by including those R-parity violating (RPV) interaction terms which violate either B or L[1].

[1] As the proton decay violates both B and L, it is avoided in this model.

1.4 Effective Field Theory

In general, a search for new physics is conducted either directly, via the production of new particles, or indirectly, via new interactions of the SM particles. This section focuses on the latter method. The physics of these interactions can be described in a model-independent way. However, some features need to be incorporated in order to recover the SM at low energies and to respect the Lorentz invariance and the $SU(3)_C \otimes SU(2)_L \otimes U(1)_Y$ gauge symmetry of the theory. The unique way to do so is via an *effective field theory* (EFT) [61], in which the SM is extended by adding higher dimensional operators constructed out of the SM fields into the Lagrangian 1.58. While the operators in the SM Lagrangian are restricted to be of mass dimension four or less, these operators have a mass dimension higher than four. They have thus coefficients of inverse powers of the cut-off scale Λ which is assumed to be large compared with the experimentally accessible energies but smaller than the Planck mass M_P. The EFT is hence a low-energy approximation to the physics beyond the SM and its Lagrangian has the following form:

$$\mathcal{L}_{\mathit{eff}} = \mathcal{L}_{SM} + \sum_{n>4} \sum_{i} \frac{c_i^{(n)}}{\Lambda^{n-4}} \mathcal{O}_i^{(n)} \tag{1.69}$$

where $\mathcal{L}_{SM}$ represents the renormalizable SM Lagrangian, Λ is the scale of the new physics, $\mathcal{O}_i^{(n)}$ are the gauge invariant dimension-n operators and $c_i^{(n)}$ are the corresponding dimensionless couplings that parameterize the strength with which the BSM physics couples to the SM particles. The sum over i is a sum over all operators of a given dimension which are invariant under the full symmetry of the SM. The new terms are suppressed by factors of $1/\Lambda$. The odd-dimensional operators are not considered because they violate lepton and/or baryon number. Since the dominant operators are those with the lowest dimensionality, only the dimension-6 and dimension-8 operators are taken into account:

$$\mathcal{L}_{\mathit{eff}} = \mathcal{L}_{SM} + \sum_{i} \frac{c_i^{(6)}}{\Lambda^2} \mathcal{O}_i^{(6)} + \sum_{j} \frac{c_j^{(8)}}{\Lambda^4} \mathcal{O}_j^{(8)} \tag{1.70}$$

While the dimension-6 operators predict new anomalous triple gauge coupling (aTGC) together with new anomalous quartic gauge coupling (aQGC) interactions, the dimension-8 operators predict only new aQGC interactions. A direct study of the trilinear and quadrilinear vector boson interactions can either confirm the SM or, in case of a deviation from the SM predictions, give some hints on the existence as well as the structure of new phenomena at higher scale.

In the presented work, only the quartic couplings are investigated assuming that the aTGC interactions appear at one-loop level and are thus suppressed w.r.t. the aQGC interactions. For the sake of simplicity, only the dimension-8 operators without derivatives of the gauge fields are considered. In a linear realisation of the spontaneous symmetry breaking, there are two independent operators contributing to the vertices with four gauge bosons [62]:

$$\mathcal{L}_{S,0} = \frac{f_{S,0}}{\Lambda^4}[(\mathcal{D}_\mu\Phi)^\dagger(\mathcal{D}_\nu\Phi)] \times [(\mathcal{D}^\mu\Phi)^\dagger(\mathcal{D}^\nu\Phi)] \tag{1.71}$$

$$\mathcal{L}_{S,1} = \frac{f_{S,1}}{\Lambda^4}[(\mathcal{D}_\mu\Phi)^\dagger(\mathcal{D}^\mu\Phi)] \times [(\mathcal{D}_\nu\Phi)^\dagger(\mathcal{D}^\nu\Phi)] \tag{1.72}$$

where $f_{S,0}$ and $f_{S,1}$ denote the corresponding coupling constants, $\mathcal{D}_\mu$ is the covariant derivative defined in Equation 1.25 and Φ is the Higgs field. These terms contain additional quartic interactions between the electroweak gauge bosons. Only those with four $W^\pm$ bosons are relevant for the studied process:

$$\mathcal{L}_{eff}^{WWWW} = \frac{v^4 g^4}{16}\left[\frac{f_{S,0}}{\Lambda^4} W_\mu^- W^{-\mu} W_\nu^+ W^{+\nu} + \frac{f_{S,1}}{\Lambda^4} W_\mu^- W^{+\mu} W_\nu^- W^{+\nu}\right] \tag{1.73}$$

where v is the Higgs vacuum expectation value ($v \approx 246$ GeV [13]). These are added to the SM $WWWW$ interaction term in Equation 1.37 and therefore enhance the predicted cross-section.

1.4.1 Unitarity Violation

By definition, the EFT is valid only up to a cut-off scale Λ, beyond which the tree-level unitarity may be violated. Given that the contributions from the dimension-8 operators rise rapidly with energy, the unitarity violation in scattering processes can occur already at energies accessible at the LHC. The standard procedure

to avoid this unphysical behaviour is to multiply the aQGC parameters by an energy-dependent form-factor [63]:

$$F(\hat{s}) = \frac{1}{(1 + \hat{s}/\Lambda_F^2)^n} \tag{1.74}$$

where $\hat{s}$ is the square of the partonic center-of-mass energy, n is an arbitrary exponent and Λ_F is the form-factor cut-off scale. In the full model, this would be achieved by the presence of new particles which have been integrated out in the EFT. Even though this approach is model-dependent, it requires relatively few assumptions about the BSM physics. The choice of these unitarization parameters for the WWW process is discussed in Section 3.2.4. Once the energy scale of new physics is reached, the EFT is not applicable. As the data always respect the unitarity bound, it has to be replaced by a new theory incorporating the new particles.

1.5 Proton-Proton Collisions

A brief overview of the Standard Model has been given in Section 1.2. To describe the phenomenology of proton-proton collisions, the SM alone is not sufficient. A complete description requires, along with the perturbative QCD calculations, various phenomenological methods which model the non-perturbative QCD effects. This section introduces some of the techniques implemented in the Monte Carlo simulations in order to obtain reliable predictions of scattering processes measured at the LHC.

1.5.1 Luminosity

The number of events from a given process in any collider experiment is proportional to the corresponding production cross-section σ and the integrated luminosity L:

$$N = \sigma \cdot L = \sigma \cdot \int \mathcal{L}\, \mathrm{d}t \tag{1.75}$$

where $\mathcal{L}$ is the instantaneous luminosity[1] which depends on the experimental parameters of the collider as well as of the beam. For a proton-proton collider with a revolution frequency f, it is given by:

$$\mathcal{L} = \frac{f n_b N_p^2}{4\pi \sigma_x^* \sigma_y^*} F \tag{1.76}$$

where N_p denotes the number of protons per bunch, n_b is the number of bunches which collide at a given interaction point (IP) and $\sigma_{x/y}^*$ are the beam widths in the transverse plane under the assumption of a Gaussian density profile at the IP. The factor F accounts for the geometrical correction due to the crossing angle at the IP. Assuming further that the beams are round and have the same parameters, it may be expressed as [64]:

$$\mathcal{L} = \frac{f n_b N_p^2 \gamma}{4\pi \epsilon_n \beta^*} F \tag{1.77}$$

where ϵ_n is the normalised transverse beam emittance, β^* is the value of the beta function at the IP and γ is the relativistic gamma factor. The integrated luminosity is a measure of how many data events can be collected by the experiment in a certain period of time and is usually given in units of inverse barns (for instance fb^{-1}) where $1\ \text{b} \equiv 10^{-24}\ \text{cm}^2$.

1.5.2 Parton Density Functions and Factorization

The inclusive cross-section for the production of the final state X in the collision of hadron A and B, illustrated in Figure 1.2, can be described using the *factorization theorem*[2] [66–68].

$$\sigma_{AB} = \sum_{a,b} \int_0^1 \mathrm{d}x_a \int_0^1 \mathrm{d}x_b \, f_{a/A}(x_a, \mu_F^2) \, f_{b/B}(x_b, \mu_F^2) \, \hat{\sigma}_{ab}(x_a p_A, x_b p_B, \mu_F^2, \mu_R^2) \tag{1.78}$$

[1] The luminosity is not constant over a physics run but decreases as a function of time.

[2] It was introduced by Drell and Yan in 1971 [65]. They adapted the parton distribution functions extracted from deep inelastic scattering to a process in hadron-hadron collisions - the production of a massive lepton pair by quark-antiquark.

where the function $f_{a/A}(x_a, \mu_F^2)$ is the parton density function (PDF) which describes the structure of the incoming hadron A giving the probability of finding a parton a of momentum $x_a p_A$ in a hadron A of momentum p_A at the effective energy scale μ_F^2. The PDFs are independent of the particular process. The cross-section for the hard scattering partonic process $\hat{\sigma}_{ab}$ is calculated at finite order of the perturbation theory, resulting in a dependence on the strong coupling constant and its renormalization scale μ_R. This is done by integrating the absolute square of the corresponding matrix element over the available phase space. The *factorization scale* μ_F is an arbitrary parameter which represents the scale separating the long-distance and short-distance physics. While partons with a transverse momentum less than μ_F are absorbed in the parton distribution functions, those with a large transverse momentum are regarded as a part of the hard scattering process and thus contribute to the short distance partonic cross-section. Finally, the hadron-hadron cross-section is obtained by integrating over the fractions of the hadron momentum x_i and by summing over all possible parton-parton scattering processes.

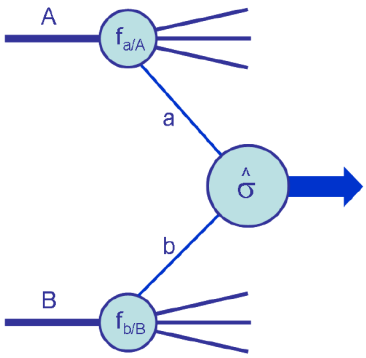

Figure 1.2: Schematic diagram of a generic hard scattering process. Taken from Reference [69].

The factorization is one of the fundamental properties of QCD. It enables to apply perturbative calculations to many important processes involving hadrons. In contrast to the naive parton model proposed by Feynman [70], the dynamics of partons inside a hadron is taken into account. The hadron structure has a non-perturbative nature and its dynamics is described by PDFs. All large loga-

rithms arising from gluons emitted collinear with the incoming partons[1], which would spoil the convergence of the perturbative expansion, can be absorbed in the renormalized distribution functions. It gives rise to a logarithmic violation of *scaling*[2] which is described by the Dokshitzer-Gribov-Lipatov-Altarelli-Parisi (DGLAP) evolution equations [76–78]. This system of the integro-differential equations is analogue to the renormalization group equation for the running coupling constants and gives the energy scale dependence of the PDFs used in the hard scattering calculations[3]:

$$\frac{\mathrm{d}\, q_i(x,\mu_F^2)}{\mathrm{d}\ln\mu_F^2} = \frac{\alpha_s}{2\pi}\int_x^1 \frac{\mathrm{d}y}{y}\Big[P_{qq}(x/y)\, q_i(y,\mu_F^2) + P_{qg}(x/y)\, g(y,\mu_F^2)\Big] \tag{1.79}$$

$$\frac{\mathrm{d}\, g(x,\mu_F^2)}{\mathrm{d}\ln\mu_F^2} = \frac{\alpha_s}{2\pi}\int_x^1 \frac{\mathrm{d}y}{y}\Big[\sum_{i=1}^{2n_f} P_{gq}(x/y)\, q_i(y,\mu_F^2) + P_{gg}(x/y)\, g(y,\mu_F^2)\Big] \tag{1.80}$$

where $q_i(x,\mu_F^2)$ and $g(x,\mu_F^2)$ denote the density functions for quark of flavour i and gluon summed over all colours inside the hadron, respectively. The sum runs over quarks and antiquarks of all flavours. The parent and daughter parton momenta are expressed in terms of fractions of the hadron momentum p as yp and xp, respectively. $P_{qq}(x/y)$, $P_{qg}(x/y)$, $P_{gq}(x/y)$ and $P_{gg}(x/y)$ represent the evolution kernels which describe the following splittings: $q \to q\,(g)$, $g \to q\,(\bar{q})$, $q \to g\,(q)$ and $g \to g\,(q)$, respectively. $P_{qq}(x/y)$ is diagonal in quark indices because a gluon is emitted without changing the flavour of a quark. When the quark masses are neglected, $P_{gq}(x/y)$ and $P_{qg}(x/y)$ do not depend on the index i because the probability of emitting a gluon is the same for all quark flavours and a gluon emits a $q\bar{q}$ pair with equal probability for all flavours, respectively. These splitting functions can be expanded in powers of the running couplings α_s:

[1] The soft and collinear divergences related to the outgoing particles are cancelled when summing over all degenerate final states as stated in the Kinoshita-Lee-Nauenberg theorem [71, 72].

[2] The scaling, also known as Bjorken scaling [73], refers to the independence of the characteristic scale and hence effectively the point-like nature of the hadron constituents. This is exactly true in the parton model. The approximate scaling behaviour was observed in the first SLAC data [74, 75].

[3] At higher Q^2, the energy dependence of the PDFs can be viewed as a higher resolution at which the hadron structure is probed.

$$P_{ab}(z,\alpha_s) = P_{ab}^{(0)}(z) + \frac{\alpha_s}{2\pi}P_{ab}^{(1)}(z) + \left(\frac{\alpha_s}{2\pi}\right)^2 P_{ab}^{(2)}(z) + \dots \tag{1.81}$$

where $z \equiv x/y$ is the momentum fraction which splits from a parent parton and zyp is thus the daughter parton momentum. At leading order, Equation 1.79 can be interpreted as the variation of the quark density at x given by the convolution of the quark density at a higher momentum fraction y times the probability of of emitting a quark with fraction z of the quark momentum plus the gluon density at y times the probability of emitting a quark with fraction z of the gluon momentum. Currently, the splitting functions are known up to the next-next-to-leading order [79, 80]. For consistency, the order of the expansion of the splitting functions should be the same as that of the partonic cross-section.

Since the PDFs cannot be calculated from first principles, they are extracted from a global fit to experimental data, especially from deep inelastic scattering experiments and hadron colliders. The recent results of the PDF fits are provided, among others, in the CTEQ [81], MSTW [82], NNPDF [83, 84] sets. The associated uncertainties include experimental uncertainties of the input data as well as theoretical uncertainties on the strong coupling constant and on the choice of parametrization. Figure 1.3 shows the proton PDFs at two different momentum transfer scales Q^2. While the up and down valence quarks dominate at large x, the gluons dominate at low x. At higher Q^2, the soft gluon and sea quark contributions are enhanced. The PDFs, measured at a specific Q_0^2, are then evolved up in Q^2 by means of the DGLAP equations.

Finally, the renormalization μ_R and factorization μ_F scales have been introduced to deal with the ultraviolet and collinear (infrared) singularities related to the short- and large-distance properties of the theory, respectively. The μ_R^2 and μ_F^2 dependence is exactly compensated by the scale dependence of the coupling constant $\alpha_s(\mu_R^2)$ and the PDFs $f_i(x,\mu_F^2)$. The cross-section calculated to all orders in perturbation theory is thus invariant under changes in these scales. The scale dependence is reduced as higher order corrections are included. Different

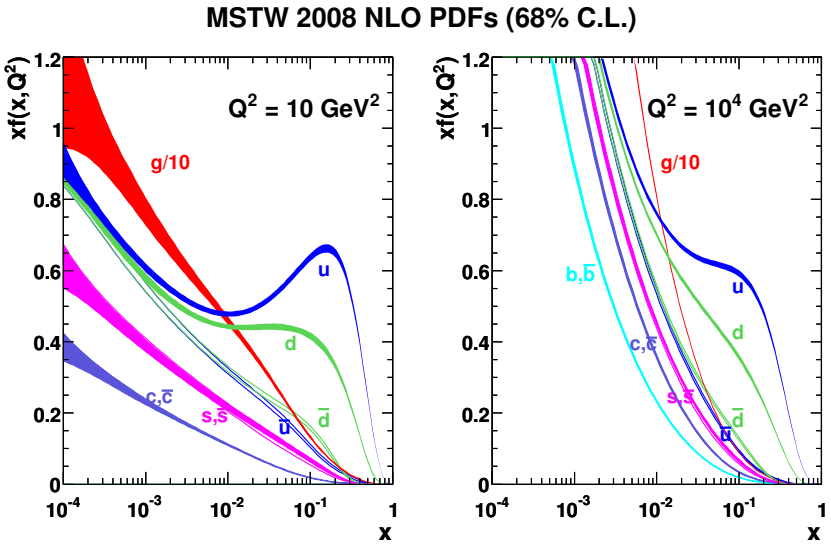

Figure 1.3: Parton densities as a function of x for $Q^2 = 10$ GeV^2 (left) and $Q^2 = 10^4$ GeV^2 (right) from the MSTW2008 PDF set [82]. The associated 68% confidence level uncertainty bands are shown.

choices of the two parameters yield different numerical results. The values are typically chosen of the order of the characteristic energy scale of the hard scattering process.

Figure 1.4 shows the predicted cross-sections for some important SM processes in $p\bar{p}$ and pp collisions as a function of center-of-mass energy, calculated using the above formalism. The inelastic pp interactions have a large total cross-section of about 100 mb for $\sqrt{s}$ =8 TeV at the LHC. One can see that the dominant contribution is the production of multiple jets by QCD processes. The cross-sections of the electroweak diboson production are found to be several orders of magnitude smaller. Given that the cross-section of the process of interest in this thesis, the WWW production, is expected to be around 0.2 pb, its measurement is very challenging[1].

[1]Three W bosons may occur in one out of $5 \cdot 10^{11}$ events.

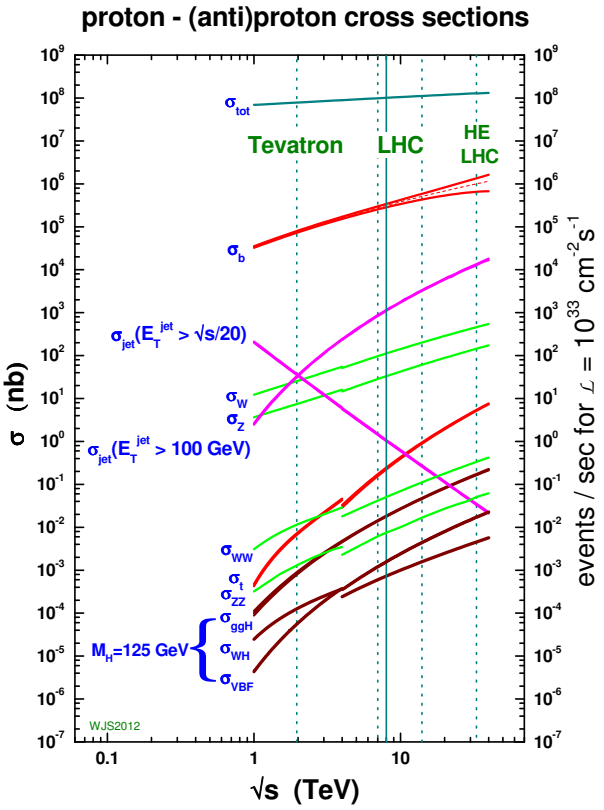

Figure 1.4: Predicted SM cross-sections (left axis) and production rates for $\mathcal{L} = 10^{33}$ cm^{-2}s^{-1} (right axis) for important processes at the Tevatron and the LHC colliders as a function of the centre-of-mass energy [85]. The vertical solid line represents the centre-of-mass energy of 8 TeV (data collected during this LHC operation are analysed in this thesis). The vertical dotted lines denote the center-of-mass energy of 1.96 GeV at the Tevatron, of 7 GeV and 14 GeV at the LHC and of 33 TeV at a prospective higher-energy LHC (HE-LHC) [86]. The discontinuity at $\sqrt{s} = 4$ GeV arises because the Tevatron, operating at lower energies, is a $p\bar{p}$ collider and the LHC is a pp collider.

1.5.3 Parton Shower

The parton showers implement higher order real-emission corrections, either in the initial state or in the final state, to the hard scattering process. The showering process relates a few partons produced in a hard scattering process to partons at an energy scale close to Λ_{QCD}. At this soft energy scale, QCD is no longer perturbative and non-perturbative models need to be employed to hadronize the obtained partons into colour-neutral hadron states which are observed experimentally. The probability for a parton to evolve from higher to lower scales without emitting a parton harder than some resolution scale is encoded by the so-called *Sudakov form factors* which obey the DGLAP equation. An ordered evolution of these probabilistic factors stops, once the *hadronization scale* is reached. It represents the lowest scale that can appear in the perturbative calculations and is typically around 1 GeV. The parton showers can be simulated as a Markov chain without a memory of individual past steps which locally conserve flavour and four-momentum.

Since the DGLAP equations are derived in the strict collinear limit, as discussed in Section 1.5.2, this description is formally correct only in regions which are dominated by the emission of soft and collinear extra partons. On the other hand, the matrix element calculation (fixed order pQCD) provides a better description of processes where partons become hard and widely separated. The combination of the two calculations is hence well motivated. However, a final state X with one additional parton emission is generated by both: the matrix element for the $X+1$ process and the parton shower with a real radiation starting from the $X+0$ parton state. The double counting in these overlapping kinematic regions is avoided by applying so-called *matching* schemes. The most widely used matching techniques are the Catani-Krauss-Kuhn-Webber (CKKW) [87] and the Michelangelo L. Mangano (MLM) [88] algorithms.

1.5.4 Hadronization

As already mentioned, the partons in the final state after the showering process hadronize due to the colour confining effect of QCD. Since such interactions happen at small momentum transfers which are beyond the perturbative regime

of QCD, phenomenological approaches have to be used to model it. There are two classes of the hadronization models: the string model and the cluster models.

In the former [89], the confinement between two colour charged partons is modelled with a linearly rising potential. Once it becomes energetically favourable, the string breaks and creates a quark-antiquark pair. This process proceeds until only stable and colourless hadrons remain, each hadron corresponding to a short string. The most widely used string model is the so-called Lund model [90] which is implemented in the PYTHIA code.

The latter hadronization model [91], used in HERWIG, arranges the partons nearby in the phase space in a colour neutral cluster. They are then fragmented into the hadrons. The produced hadrons may be instable and hence decay into hadrons with sufficiently large lifetimes to be considered as stable. Both approaches involve free parameters which need to be tuned to reproduce experimental data.

1.5.5 Structure of an event

At hadron-hadron colliders, the "primary" hard scattering interaction of the two incoming partons is accompanied by softer interactions from the remaining partons, called the *underlying event* (UE). Although these interactions are usually soft, the UE can have a hard partonic scattering component where multiple partons from the same proton take part in hard interactions. This is referred to as *multi-parton interactions* (MPI).

Another background to the hard process is *in-time pile-up*. It originates from interactions of protons in the same bunch-crossing as the hard process of interest. In addition, *out-of-time pile-up* occurs when signals from different bunch-crossing interfere with the current one. These interactions are dominated by the inelastic proton-proton scatterings which produce relatively soft particles in the final state. The number of overlaid pile-up events depends upon the beam conditions.

Finally, coloured or electrically charged particles in the initial or final state can radiate additional particles. This is known as *initial state radiation* (ISR) and *final state radiation* (FSR).

CHAPTER 2

THE ATLAS EXPERIMENT AT THE LHC

The Large Hadron Collider (LHC) [92] is a hadron accelerator located at the European Organization for Nuclear Research (CERN) in the northwest suburbs of Geneva on the Franco-Swiss border. The ATLAS experiment [93] is one of the four major experiments which study the collisions produced by the LHC. This chapter introduces the CERN accelerator complex in Section 2.1 and gives a brief description of the ATLAS detector in Section 2.2.

2.1 The Large Hadron Collider

The LHC collider was built in the 27 km long tunnel, approximately 100 m below ground level, which previously hosted the Large Electron-Positron Collider (LEP) until its shutdown in 2000. The accelerator is designed to provide proton-proton (pp) collisions up to unprecedented centre-of-mass energies of $\sqrt{s} = 14$ TeV and luminosities of more than 10^{34} cm^{-2}s^{-1}. Higher energies than at the LEP collider can be achieved because protons suffer less from synchrotron radiation than electrons[1]. The pp collisions are used to probe the fundamental interactions at very high energies as well as to search for new physics. In addition, the LHC can provide also heavy ion collisions, such as lead ion, for studies of strongly interacting matter under extreme conditions.

[1] The corresponding energy loss is proportional to $1/m^4$.

Before being delivered to the LHC, particles have to be accelerated by a chain of linear and circular accelerators, as shown in Figure 2.1. Protons, obtained from the ionization of hydrogen gas, are first injected in the linear accelerator LINAC 2 where they are accelerated to the energy of 50 MeV. The Proton Synchrotron Booster (PSB) followed by the Proton Synchrotron (PS) accelerate protons further to 1.4 GeV and 25 GeV, respectively, and adapt the beam structure used at the LHC. The protons are then sent to the Super Proton Synchrotron (SPS) which accelerates them to the injection energy of 450 GeV. Finally, the beams of proton bunches are sent to the two evacuated beam pipes of the LHC: one circulating clockwise while the other one anticlockwise. Each beam can be accelerated to up to 7 TeV.

The magnetic fields needed to bend the particle beams are provided by 1232 superconducting dipole magnets, which are cooled to a temperature of 1.9 K by liquid helium. Their field strength of up to 8.33 T limits the maximum beam energy. In addition to the dipole magnets, 392 quadrupole magnets are used to focus the beams toward the collision points inside the experiments. Eight radio-frequency (RF) superconducting resonating cavities, operating at a frequency of 400 MHz, are generating the electric fields which accelerate the particle beams each time they pass through[1]. They are supplied with an energy of about 485 keV per revolution during the acceleration phase. During colliding beam operation, the lifetime of the beam is limited mainly by the collision losses due to the high proton-proton cross-section.

The beam is arranged in the form of *bunch trains*. At design conditions, they consist of 72 bunches separated by a spacing of 25 ns and followed by empty buckets, which makes for 39 bunch trains in total 2808 filled bunches per beam. Each bunch contains about 10^{11} protons. There are several filling schemes defined for the LHC [94].

[1]This results in 3564 energetically favourable locations where bunches can sit, so called *RF buckets*.

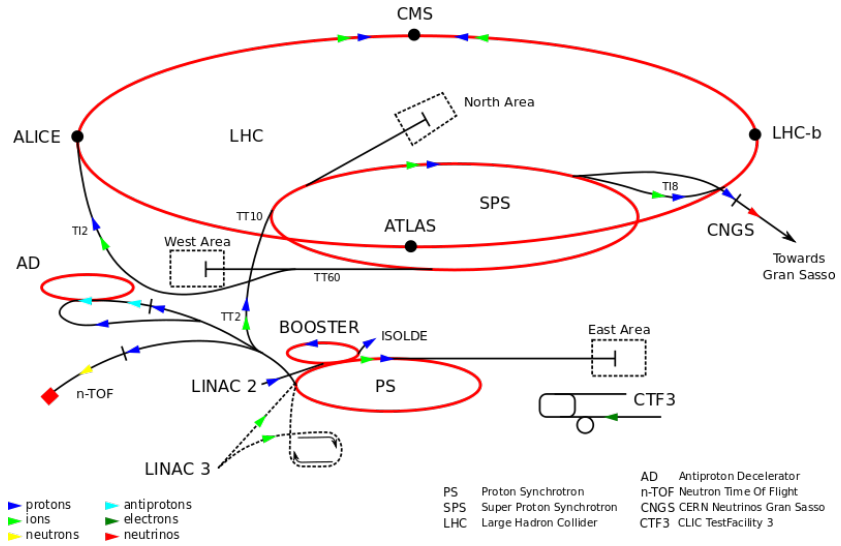

Figure 2.1: The CERN accelerator complex. The multi-stage system of accelerators used to boost the beams before delivering them to the LHC is shown [95].

2.1.1 LHC Experiments

The collisions provided by the LHC occur at four interaction points where the large experiments reside: ATLAS [93] (A Toroidal LHC ApparatuS), CMS [96] (Compact Muon Solenoid), LHCb [97] (LHC beauty) and ALICE [98] (A Large Ion Colliding Experiment). The ATLAS and CMS experiments are general-purpose detectors designed to explore all aspects of the LHC program. Studies of the Standard Model as well as direct searches for new particles are among their main objectives. ALICE is dedicated to heavy-ion physics and LHCb, an asymmetric detector with an excellent vertex resolution, is designed to measure precisely CP violation and rare decays of b-hadrons.

In addition, there are a few smaller experiments situated at the LHC. TOTEM [99] and LHCf [100] focus on forward physics phenomena and are located near CMS and ATLAS, respectively. While TOTEM measures the total pp cross-section and studies elastic and diffractive scattering, LHCf is specifically designed to study the very forward production cross-sections of neutral particles in pp collisions. The results from the latter provide information for the calibration of the hadron interaction models used in MC simulation. Finally, the MoEDAL experiment [101] searches for magnetic monopoles.

2.1.2 LHC Performance and Perspectives

The data-taking period from 2010 to 2012 is referred to as *Run1*. The LHC delivered pp collisions at $\sqrt{s} = 7$ TeV in 2010 and 2011, and $\sqrt{s} = 8$ TeV in 2012. The analyses presented in this thesis use the full 2012 dataset. During this run, the accelerator operated with the bunch spacings of 50 ns and high bunch intensity, reaching a peak luminosity of 7.7×10^{33} cm^{-2}s^{-1} which is more than half the design luminosity. Table 2.1 shows the design values of selected parameters of the LHC performance, along with the actual values achieved during Run1.

Parameter	**2011**	**2012**	**Design value**
Beam energy [TeV]	3.5	4	7
Number of bunches/beam	1380	1380	2808
Number of protons/bunch	1.45×10^{11}	1.7×10^{11}	1.15×10^{11}
Bunch spacing [ns]	75/50	50	25
Peak luminosity [cm^{-2}s^{-1}]	3.7×10^{33}	7.7×10^{33}	1.0×10^{34}
Max. $\langle\mu\rangle$	17	37	19
β^* [m]	1.0	0.6	0.55
ϵ_n [μm]	2.4	2.5	3.75

Table 2.1: Overview of the LHC parameters. The design values are compared with the values reached during the first years of the LHC operation [64]. The normalised transverse beam emittance ϵ_n and the beta function at the interaction point β^* are introduced in Section 1.5.1 and $\langle\mu\rangle$ denotes the mean number of interactions per bunch crossing.

The total luminosity delivered by the LHC during stable beam conditions in 2012 is shown in Figure 2.2a. Given the data acquisition (DAQ) inefficiency, the luminosity recorded by the ATLAS detector is slightly lower. Only a fraction of data passing the data quality (DQ) criteria is suitable for physics analysis. The luminosity relevant for this thesis is 20.3 fb^{-1}. The distributions of the mean number of interactions per bunch crossing in 2011 and 2012 are shown on Figure 2.2b. The pile-up activity raised to an average of 20.7 collisions in 2012 due to the increased peak luminosity.

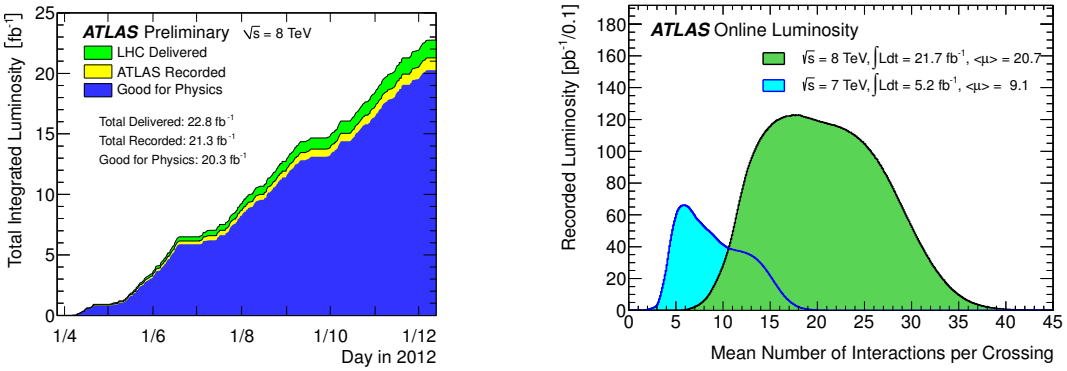

(a) (b)

Figure 2.2: (a) Total integrated luminosity delivered by the LHC (green), recorded by the ATLAS experiment (yellow) and selected as suitable for physics analysis (blue) as a function of time in 2012 [102]. (b) Mean number of interactions per bunch crossing for the 2011 and 2012 data [102].

After a very successful Run1, *Run2* data-taking resumed in 2015 and the LHC is currently recording pp collisions with an increased centre-of-mass energy of 13 TeV. The ATLAS detector is expected to collect an integrated luminosity of about 100 fb^{-1} by the end of 2018. *Run3* phase will start in 2021 aiming to deliver about 300 fb^{-1} at 14 TeV. The LHC will then undergo a major high-luminosity upgrade (HL-LHC) [103]. Starting in 2026, about 3000 fb^{-1} are expected to be collected over a ten year period. Afterwards, a logical successor to the LHC would be higher-energy LHC (HE-LHC) [86]. By putting more powerful dipole magnets in the same tunnel, much larger energy of 33 TeV can be achieved with minimal cost.

2.2 The ATLAS detector

The ATLAS detector[1] [93] is one of four main LHC experiments. It is a multi-purpose detector designed to explore a wide range of physics processes, from high precision measurements to searches for new phenomena. To achieve this versatility, ATLAS combines many different technologies in a layered design allowing

[1]The ATLAS collaboration has about 5000 members from 38 countries around the world.

for near-complete reconstruction and identification of the products of the hard scattering process in high pile-up conditions.

Figure 2.3 shows a three-dimensional illustration of the ATLAS experiment. It has a forward-backward symmetric cylindrical geometry with almost hermetic azimuthal coverage. Its dimensions are 25 m in height and 44 m in length and the overall weight is approximately 7000 tonnes. The detector consists of three different detecting subsystems built around the beam pipe: the inner detector, the electromagnetic and hadronic calorimeters and the muon spectrometer. The cylindrical layers built around the beam pipe form the *barrel*, while the discs perpendicular to the beam axis are referred to as the *end-caps*. ATLAS contains also a magnet system to measure the trajectory and momentum of charged particles and a multi-stage triggering system to select only the most interesting events. All these subsystems are described in more detail in the following sections.

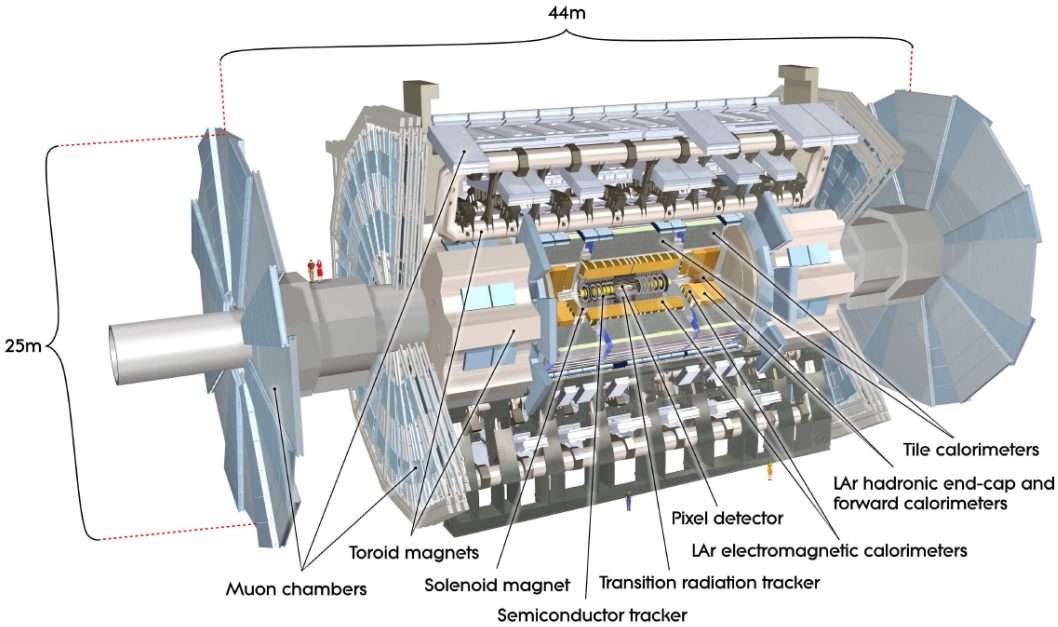

Figure 2.3: Schematic view of the ATLAS experiment with the various subdetectors and the magnet systems [93].

2.2.1 Coordinate System

The ATLAS coordinate system is a right-handed system with the origin in the interaction point. The z axis is defined as the beam axis and the $x-y$ plane is transverse to the beam line. The x axis points to the center of the LHC ring and the y axis points upwards. The azimuthal angle ϕ is measured around the beam axis, while the polar angle θ is the angle relative to the beam direction. The pseudorapidity η, commonly used instead of θ, is defined as follows:

$$\eta = -\ln \tan\left(\frac{\theta}{2}\right) \tag{2.1}$$

It is the zero-mass or high-energy approximation of the rapidity y which is invariant under longitudinal Lorentz boosts:

$$y = \frac{1}{2}\ln\left(\frac{E+p_z}{E-p_z}\right) \tag{2.2}$$

where E denotes the energy and p_z the component of the momentum along the beam axis. The angular distance between two objects in the $\eta-\phi$ coordinate space is described by a so-called cone size ΔR:

$$\Delta R = \sqrt{\Delta\eta^2 + \Delta\phi^2} \tag{2.3}$$

Quantities, such as transverse momentum p_{T} and transverse energy E_{T} are often defined in the $x-y$ plane, where momentum conservation can be applied.

2.2.2 Magnet System

The ATLAS magnet system is essential for precise momentum measurement and electric charge identification of charged particles from the curvature of their trajectories. As shown in Figure 2.4, it is composed of a central superconducting solenoid and three outer superconducting toroids. The solenoid magnet is aligned with the beam axis and provides the inner detector with a 2 T axial magnetic field bending charged particles in the ϕ direction. In order to reduce the material in front of the calorimetry, its radial thickness is minimized and it shares the

cryostat with the electromagnetic barrel calorimeter. The toroid system consists of one barrel ($|\eta| < 1.4$) and two end-cap ($1.6 < |\eta| < 2.7$) magnets arranged in an eight-fold azimuthal coil symmetry around the calorimeters. They produce a toroidal magnetic fields of approximately 0.5 T and 1 T for the muon detectors in the central and end-cap regions, respectively, which deflect particles in the η direction. In the transition region ($1.4 < |\eta| < 1.6$), the magnetic deflection is provided by a combination of toroid fields.

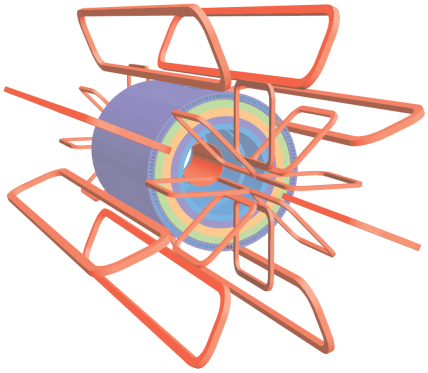

Figure 2.4: Schematic view of the ATLAS magnet system with the central solenoid inside the calorimeter volume, one barrel and two end-cap toroids [93].

2.2.3 Inner Detector

The inner detector (ID), embedded in a 2 T solenoidal field, is the subdetector located the closest to the interaction point. It is designed to reconstruct tracks of charged particles and to measure their momenta to very high precision over the pseudorapidity range of $|\eta| < 2.5$. This enables the reconstruction of both primary vertices from pp collisions and secondary vertices from long-lived particles, such as b-flavoured hadrons. Since operating in a high-occupancy and high-radiation environment, the fast readout electronics and good radiation resistance are needed to meet the design requirements. In addition, the amount of material in front of the calorimeter system is required to be minimized. The ATLAS tracking system comprises silicon sensors and drift-tube based detectors. The silicon sensors must be kept at a temperature of approximately $-5°$C to $-10°$C to suppress electronic noise. The transverse momentum of a track can be determined with a design resolution of $\sigma_{p_\mathrm{T}}/p_\mathrm{T} = 0.05\%\, p_\mathrm{T}\,[\mathrm{GeV}] \oplus 1\%$ [93]. A cut-away view of the ATLAS

ID is shown in Figure 2.5a. Figure 2.5b illustrates different subdetectors in the barrel region.

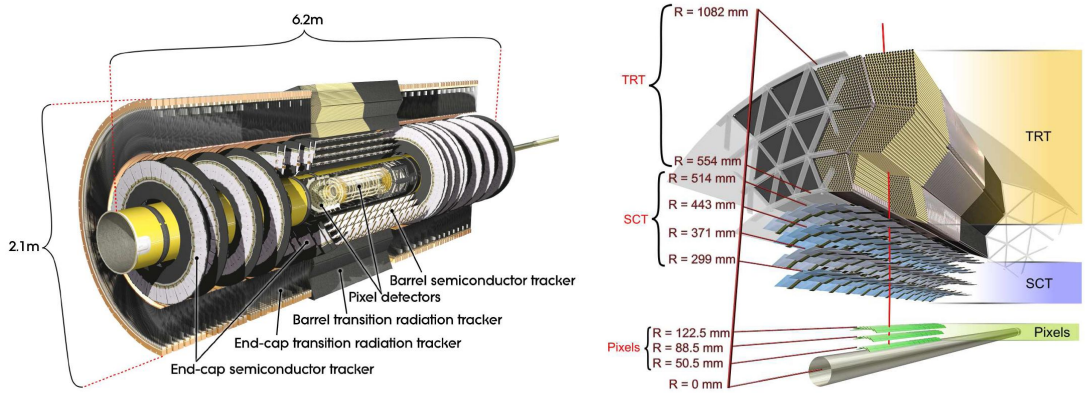

(a) (b)

Figure 2.5: (a) Schematic view of the ATLAS inner detector [93]. (b) Illustration of the sensors and structural elements traversed by a charged track in the barrel inner detector [93].

2.2.3.1 Pixel Detector

The pixel detector is situated the closest to the interaction point. It consists of three cylindrical layers in the barrel region and three concentric discs in each end-caps region, which are further divided into modules. Each module is composed of a 250 μm thick silicon sensor segmented into pixels with a nominal size of 400 μm along the z-axis and 50 μm in the $R-\phi$ plane[1]. A charged particle crosses typically all three pixel layers providing at least three measurement points, each with an intrinsic resolution of 10 μm in the $R-\phi$ plane and 115 μm in the z and R direction in the barrel and end-cap region, respectively. With approximately 80 million readout channels, the pixel detector is a high-precision and low-noise tracking device.

The innermost layer is located at $R = 50.5$ mm. It is often referred to as the B-layer as it is fundamental for the reconstruction of secondary vertices originating from b-quark decays. Given that this layer is most sensitive to radiation

[1]Here R denotes the radial distance from the beam pipe. The $R-\phi$ plane is thus the bending plane of the magnetic field.

damage, it degrades in terms of efficiency over time. During the first LHC shutdown between Run1 and Run2, an additional fourth layer called the *insertable B-layer* (IBL) was installed to compensate for these module failures and luminosity induced saturation effects [104,105]. It is the closest tracking detector situated at an average radius of 33 mm with a granularity of $50\,\mu\text{m} \times 250\,\mu\text{m}$ in $R-\phi\times z$. The IBL improves the tracking and vertexing performance of the current pixel detector.

2.2.3.2 Semiconductor Tracker

The semiconductor tracker (SCT) is the precision tracking detector composed of four cylindrical layers in the barrel region and nine end-cap discs on each side. Its concept and function is similar to that of the pixel detector but the lower particle density allows for silicon sensors to be segmented into long narrow strips. Each layer consists of two sets of strips with a relative rotation of 40 mrad, enabling a two-dimensional hit reconstruction and reducing noise. The SCT is designed to provide eight strip measurements per track, corresponding to four space-points, in the intermediate radial range. The spatial resolution in the barrel (end-caps) is 17 μm in the $R-\phi$ plane and 580 μm in the z (R) direction. The number of readout channels is approximately 6.3 million.

2.2.3.3 Transition Radiation Tracker

The transition radiation tracker (TRT) is the outermost layer of the inner detector. It consists of 73 layers of polyimide straw tubes in the barrel and 160 layers in each end-cap. These drift straw tubes with a diameter of 4 mm are filled with a Xe-based gas mixture. The TRT provides the position measurement only in the $R-\phi$ plane for $|\eta| < 2.0$, with an intrinsic accuracy of 130 μm per straw. This lower resolution is compensated by a large number of measurements per track, typically 36. In addition to the track measurement, the detector allows for particle identification through the detection of transition radiation photons emitted by charged particles passing a boundary of two dielectric materials. The intensity of the transition radiation is proportional to the Lorentz boost ($\gamma = E/m$) of particles and electrons are typically the only particles which can be identified within a given energy range. The TRT thus enables stand-alone electron identification.

The total number of TRT readout channels is approximately 351 000.

2.2.4 Calorimeter System

The calorimeter system is composed of a number of electromagnetic and hadronic detectors with the full ϕ symmetry and the coverage of $|\eta| < 4.9$, as shown in Figure 2.6. It is designed to provide an accurate energy measurement of electrons, photons and jets by fully absorbing electromagnetic cascades and hadronic showers[1], respectively. The segmentation of the calorimeter system provides additional information about the direction and shape of showers. This allows for precise position measurement, particle identification and good reconstruction of missing transverse energy which is important for many physics signatures, in particular for SUSY searches.

The ATLAS calorimeters are sampling calorimeters with alternating samples of absorber, inducing showering of incident particles, and active medium, detecting secondary particles. They employ different technologies across the large η range. The first layer of the system uses liquid argon scintillators as the active medium and consists of one electromagnetic calorimeter ($|\eta| < 1.475$) in the barrel region, one electromagnetic ($1.375 < |\eta| < 3.2$) and one hadronic ($1.5 < |\eta| < 3.2$) calorimeters in each end-cap region, and two forward calorimeters covering the regions closest to the beam ($3.1 < |\eta| < 4.9$). These detectors are housed inside three cryostats (one barrel and two end-caps) and kept at a temperature of approximately 80 K using liquid nitrogen. The outer layer makes use of plastic scintillating tiles as the active material and is formed by the hadronic tile calorimeters, with one central barrel ($|\eta| < 1.0$) and two extended barrels ($0.8 < |\eta| < 1.7$) on each side.

2.2.4.1 Electromagnetic Calorimeter

The electromagnetic (EM) calorimeter is a finely segmented sampling calorimeter with high granularity, which uses liquid argon (LAr) as the active material and

[1]The calorimeters are non-compensating, meaning that they have a different response to electromagnetic and hadronic showers. This degrades the resolution but can be corrected for by applying energy scale corrections, as discussed later.

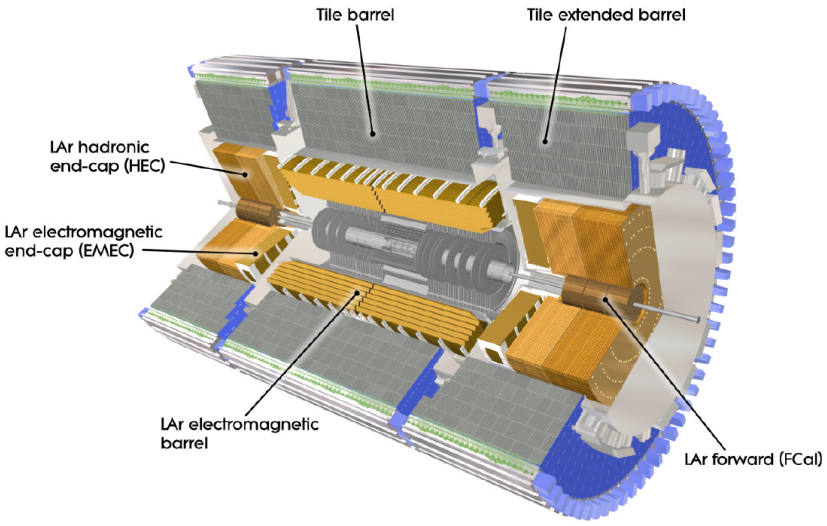

Figure 2.6: Schematic view of the ATLAS calorimeter system [93].

lead plates as the absorber. LAr was chosen for its linear and stable behaviour, high ionization yield and good resistance to radiation. The lead plates as well as kapton electrodes have a characteristic accordion-shaped structure which provides complete ϕ symmetry without azimuthal cracks. The EM calorimeter is divided into a barrel ($|\eta| < 1.475$) and two end-caps ($1.375 < |\eta| < 3.2$), referred to as EMB and EMEC. It is further segmented into three longitudinal layers, providing information about the shower development. The second layer collects the largest fraction of the EM shower energy and has a granularity of $\Delta\eta \times \Delta\phi = 0.025 \times 0.025$. A presampler, built from an active LAr layer, is mounted in front of the EM calorimeter in the region of $|\eta| < 1.8$ to correct for the energy lost in the inner detector and the solenoid coil. The calorimeter detects and identifies electrons and photons, and measures their energy with an excellent resolution of about $\sigma_E/E = 10\%/\sqrt{E\,[\text{GeV}]} \oplus 0.7\%$ [93]. The total thickness of the detector is > 22 radiation lengths[1] (X_0) in the barrel and > 24 X_0 in the end-caps to ensure that the whole EM shower is contained within the calorimetry.

[1]The radiation length represents the mean path length after which a high-energy electron loses all but $1/e$ of its energy due to bremsstrahlung.

2.2.4.2 Hadronic Calorimeter

The ATLAS hadronic calorimeter consists of two independent sampling calorimeters which use different detector technologies: the tile calorimeter in the barrel and the LAr technique in the hadronic end-cap. The former, referred to as TileCal, is placed directly outside the EM calorimeter envelope. It employs steel tiles as absorber and plastic scintillators as active material. The 5640 mm long central barrel covers the range of $|\eta| < 1.0$ and two 2910 mm long extended barrels cover the $0.8 < |\eta| < 1.7$ region. All barrel parts are segmented azimuthally into 64 modules and longitudinally into three layers. The tiles are read out at two sides using wavelength shifting fibres into separate photomultiplier tubes. The readout channels are grouped into cells forming a three-dimensional readout cell geometry. The resulting typical cell dimensions are $\Delta\eta \times \Delta\phi = 0.1 \times 0.1$ in the first two radial layers and $\Delta\eta \times \Delta\phi = 0.2 \times 0.1$ in the third one. As hadronic showers tend to be more diffuse than EM showers, this coarser granularity (with respect to the EM calorimeter) does not limit the jet reconstruction performance. The total TileCal thickness at the outer edge is 9.7 nuclear interaction lengths[1] (λ) at $\eta = 0$, guaranteeing full containment of hadronic showers. The hadronic end-cap calorimeter (HEC) provides the coverage of $1.5 < |\eta| < 3.2$. It is located directly behind the EMEC, sharing the same cryostat. This sampling calorimeter uses copper as passive material and LAr as active material since higher radiation resistance is needed at larger pseudorapidities. The design energy resolution of the barrel and end-cap hadronic calorimeters is $\sigma_E/E = 50\%/\sqrt{E\,[\text{GeV}]} \oplus 3\%$ [93].

2.2.4.3 Forward Calorimeter

The forward calorimeter (FCal), integrated into the end-cap cryostats, extends the coverage of the ATLAS calorimeter system to the far forward region $3.1 < |\eta| < 4.9$. It is a combined electromagnetic and hadronic calorimeter, consisting of three modules in each end-cap. The first module uses copper as passive material and is optimised for electromagnetic interactions. The remaining two modules are made of tungsten absorbers and are designed to measure predominantly hadronic

[1] The interaction length represents the mean free path length travelled by a hadron in the given material before undergoing an inelastic hadronic interaction.

energy deposition. LAr is used as active medium in all modules. The FCal design energy resolution is $\sigma_E/E = 100\%/\sqrt{E\,[\text{GeV}]} \oplus 10\%$ [93].

2.2.5 Muon Spectrometer

The muon spectrometer is the outermost and largest part of the ATLAS detector. It is designed to measure the deflection of muon tracks in the large superconducting air-core toroid magnets over the pseudorapidity range of $|\eta| < 2.7$ as well as to trigger on them in the $|\eta| < 2.4$ region. It combines precision chambers with trigger chamber technologies and consists of four subsystems: monitored drift tubes (MDTs), cathode strip chambers (CSCs), resistive plate chambers (RPCs) and thin gap chambers (TGCs).

The chambers are organized in three concentric cylindrical layers in the barrel region and in three large wheels perpendicular to the beam axis in the transition and end-cap regions. A layout of the muon system is given in Figure 2.7. The detectors designed for a precision measurement of the track coordinates in the principal bending direction are MDTs and CSCs. They are used in the central region ($|\eta| < 2.7$) and in the forward region of the inner layer ($2.0 < |\eta| < 2.7$), respectively. The chambers providing fast triggering information are RPCs and TGCs, which are used in the barrel and the end-caps, respectively. They also complement the precision chambers with additional information about the track position in the ϕ coordinate. The muon spectrometer allows for precise momentum measurement of high energetic muons, which is important mainly for new physics searches. Its design performance goal is a stand-alone transverse momentum resolution of $\sigma_{p_\text{T}}/p_\text{T} = 10\%$[1] for a 1 TeV track [93]. The bending of such trajectory translates into a sagitta along the beam axis of about 500 μm which has to be measured with an accuracy better than 50 μm.

[1]Only the muon spectrometer is used for the track reconstruction as its performance is independent of the inner detector system for high p_T-muons.

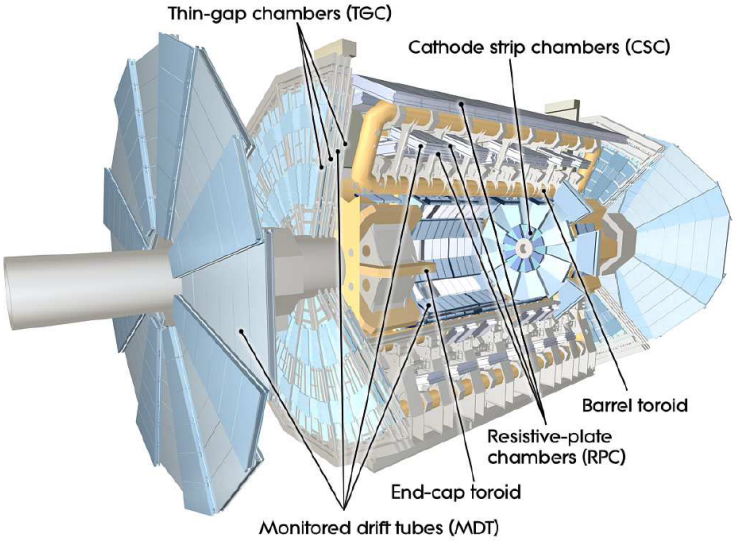

Figure 2.7: Schematic view of the ATLAS muon system [93].

2.2.6 Trigger and Data Acquisition System

The LHC is designed to collide bunches of protons every 25 ns. However, only a very small fraction of events can be recorded by the ATLAS experiment due to the technical limitations in the detector readout system and in the computational and storage resources. An online selection of potentially interesting events is performed by a multi-level triggering system [93], optimized for the nominal LHC running conditions. Its performance in 2012 has far exceeded the initial requirements [106].

The data rate reduction from the initial bunch crossing rate of 40 MHz (20 MHz in 2012) to about 200 Hz (400 Hz in 2012) is performed in three steps. Firstly, the level-1 (L1) trigger exploits the trigger chambers of the muon spectrometer and the full calorimeter system with reduced granularity information to make an initial selection. It searches for objects with high transverse momentum, e.g. muons, electrons, photons, jets and τ-leptons decaying into hadrons, as well as for large $E_{\mathrm{T}}^{\mathrm{miss}}$. The L1 trigger operates with custom-made electronics at the hardware level. Its accept rate is approximately 75 kHz (65 kHz in 2012) within the decision time less than 2.5 μs. In addition, it defines so-called regions of

interest (RoIs) in each event whose coordinates in η and ϕ are then passed on to the level-2 (L2) trigger. The L2 trigger uses software algorithms to process the full granularity information in the RoIs from all subdetectors. It reduces the event rate below 3.5 kHz (5.5 kHz in 2012) in about 10 ms. Finally, the full event is sent to the event filter (EF), the third trigger level, which uses a more complex software-based selections similar to the offline reconstruction algorithms. It is executed on commercially available computers and networking hardware. The output event rate is reduced to 200 Hz (400 kHz in 2012) within a processing time of 4 s. The selected events, with an average raw data size of about of 1.5 MB/event, are finally written to mass-storage devices available for further offline analysis. The second and third level triggers are commonly referred to as the high level trigger (HLT). Some trigger items might be *prescaled*. This means that their acceptance rate is artificially reduce by a factor P and only a random fraction of selected events is kept.

The trigger system with a three-layer structure has been optimized for Run2. The L2 and EF triggers are now merged together to allow better resource sharing and overall simplification on both the hardware and software sides [107].

The data acquisition (DAQ) system is responsible for collecting data from detector digitization systems, storing them pending the trigger decision and recording selected events on permanent storage for offline analysis in a suitable format.

2.2.7 Software and Computing

The events delivered by the ATLAS trigger and DAQ system are processed by the ATLAS offline software and then provided to physicists within the ATLAS collaboration. Moreover, the observed data has to be compared with the predictions of physics models in order to produce meaningful physics results. Therefore, the study of the detector response for a wide range of physics processes and scenarios needs to be carried out. The data processing as well as the detailed simulation require large-scale storage and computational power.

2.2.7.1 Software Environment

The simulation software chain can be divided into three steps [108]: *event generation* and prompt decays (e.g. Z or W decays), *detector simulation* and *digitization* of the energy deposited in the sensitive detector regions into voltages and currents. The output of this stage is intended to be in a format identical to the output of the ATLAS DAQ system. Therefore, both the simulated and real data can be processed by the same ATLAS trigger and reconstruction packages, and then compared. In addition to the hard scattering process which triggers the detector readout, multiple pp interactions per bunch crossing (pile-up) are accounted for by overlaying simulated *minimum-bias events*. The simulation program uses the GEANT4[1] toolkit [109], and is integrated into the ATLAS software framework called ATHENA[2] [110].

During Run1, both experimental and simulated data were promptly processed using ATHENA into first an *ESD* (Event Summary Data) and then an *AOD* (Analysis Object Data) format. The AODs were designed to be used as the primary format for analysis by the ATLAS collaboration. However, event data were further skimmed, slimmed and thinned[3] to produce reduced data formats, called *DPD* (Derived Physics Data) [111], commonly used as input to particular performance studies and physics analyses. The most popular format was the *D3PD* (ROOT ntuple [112]). Even though this model provided optimal flexibility for individual physics groups, the production of these derived formats became a significant workload. Moreover, the same events were available in several copies and formats resulting in the total disc space usage similar to that needed for the AODs. During the shutdown (2013-2014), the ATLAS collaboration introduced a new event data model for analysis, called the *xAOD* [113], to reduce the storage and CPU requirements. This format is directly readable in ATHENA as well as in ROOT.

[1] GEANT4 is a toolkit for simulating the passage of particles through matter.

[2] ATHENA is the ATLAS software framework designed for a wide range of physics data-processing applications, e.g. simulation, reconstruction and event analysis.

[3] Skimming is defined as the selection of interesting events, while slimming and thinning select specific data object relevant to a particular analysis.

2.2.7.2 Computing Model

The extensive computational requirements of the ATLAS collaboration for large-scale simulation, reconstruction, data processing and analysis have led to the development of a global distributed computing system known as the worldwide LHC computing grid (WLCG), which allows efficient data access and makes use of all available computing resources [114]. The WLCG infrastructure is used by the four main LHC experiments and, as of today, is spread among more than 170 computing centres (*sites*) in 42 countries connected by fast network links. The ATLAS distributed computing (ADC) enables the monitoring and the daily operations of the ATLAS grid resources and optimizes their usage within the LHC environment (CPU, storage, network, maintenance manpower). The ADC system has a multi-tiered architecture which consists of four classes of "regional facilities", namely Tier-0, Tier-1, Tier-2 and Tier-3, each providing a specific set of services. While the Tier-0 is based at CERN, the Tier-1/2/3 centres are located around the world.

During Run1, the ATLAS computing infrastructure followed the MONARC model (Models Of Networked Analysis at Regional Centres) [114] which is based on the hierarchical association of several Tier-2 computing centres to one Tier-1 site, usually located in the same geographical region. These so-called *clouds*, which are statically defined, set the boundaries for data transfers. In this model, the *Tier-0* facility records the raw data acquired with the ATLAS detector, performs the prompt reconstruction, provides the tape archival repository for the primary copy and distributes a second copy to Tier-1 sites. In addition to storing the copy of the raw data on tape and the reconstruction outputs on disc, *Tier-1* centres are also responsible for reprocessing of all of the raw data with improved calibrations and algorithms, performing skims of large primary datasets (enriched in particular physics signals) and providing archival storage on disc of simulated samples produced at Tier-2 sites belonging to the same cloud. *Tier-2* centres are the primary resources for simulation and data analysis. Finally, *Tier-3* centres provide additional computing resources, usually only to individual research institutes. As they are not fully integrated to the grid, they are not used for the official storage of datasets.

With the technological progress, the network infrastructure has improved and the difference in the functionalities between the Tier-1 and Tier-2 centres has been reduced. Therefore, the strict hierarchical model has been gradually replaced by a new flat model where all sites belong to a single cloud called WORLD. Computing resources are sub-partitioned for each task (simulation, data (re)processing, etc) into one nucleus and multiple satellites based on dynamic knowledge of their availability, network connectivity and configuration. *Nuclei* are all Tier-1 centres and reliable Tier-2 centres, where tasks are assigned and outputs aggregated. *Satellites* are the computing sites that execute tasks and transfer outputs to their nucleus [115, 116].

In order to pursue its ambitious physics research program, the LHC will require more computing resources in the upcoming few years than the WLCG infrastructure can provide nowadays. In particular, the requirements for large-scale simulations will increase significantly. To meet these challenges, the ADC is engaged in an effort to expand the current computing model beyond conventional grid sites including high-performance computing (HPCs) clusters, commercial and private clouds, and other opportunistic resources[1]. Given that each opportunistic facility is unique, the ATLAS systems and workflows must adapt to their specific conditions such as that tasks may be terminated without warning and that the ATLAS software needs to be installed locally on a shared filesystem if CVMFS [117] cannot be configured. The HPC machines are used for a wide range of computationally intensive tasks in various fields providing high-speed interconnects between worker nodes. A significant fraction of ATLAS computing power is now provided by HPCs (9.65%) [118]. For example, Titan [119] is a supercomputer built by Cray at Oak Ridge National Laboratory. It was the first large-scale system to use a hybrid architecture that utilizes worker nodes with both conventional 16-core AMD Opteron CPUs and NVIDIA Tesla K20 GPU accelerators. It has been recently integrated in the ATLAS production system [120] and validated with a variety of simulation workloads.

Finally, before starting a large-scale production of events on the computing

[1]The opportunistic resources are available for the ATLAS experiment whenever they are not fully engaged in the execution of their main tasks.

grid, it is important to validate a new software release as well as each new site or platform to ensure that the installed software is functioning as expected. For these purposes, a set of several physics "validation samples" is produced on the grid such that all aspects of the event reconstruction can be tested. The *physics validation* is carried out by comparing the results from each release to those of previous validated releases and checking the physics content of the generated samples. On the other hand, the so-called *technical validation* is performed by comparing statistically larger samples of the same physics process simulated at different sites and analysing their compatibility and reproducibility. This validation provides an important check of the simulation infrastructure at the computing sites which can spot for example differences of the runtime libraries. The validation of sites was done during the initial phase of the grid [121]. Given that the ATLAS computing model is under a continuous process of improvement and expansion, the technical validation is still necessary, especially for a new ROOT version, a new compiler as well as new platforms with specific grid settings, e.g HPC sites.

The author has developed tools to monitor the availability of the ATLAS computing resources (ASAP) used in Nucleus definition, improved workflows for technical validation and helped to expand the list of validated resources suitable for user analysis as well as Monte Carlo production. The work on the technical validation is documented in Appendix D.

2.3 Object Reconstruction

The electronic signals recorded by the ATLAS detector are translated into "physical objects" through various reconstruction algorithms which aim to identify particles and calibration procedures which provide accurate energy and position measurements. This section gives a brief overview of the reconstruction of physics objects which are relevant for the analyses presented in this thesis.

2.3.1 Electrons

Electrons in the central region of the detector ($|\eta| < 2.47$) are reconstructed from energy deposits in the electromagnetic (EM) calorimeter. Firstly, the EM calorimeter system is divided into a grid of towers of size $\Delta\eta \times \Delta\phi = 0.025 \times 0.025$,

corresponding to the granularity of the middle layer. Then, a sliding-window algorithm [122] is used to identify clusters. The algorithm searches for a local maximum of energy within a window of 3×5 towers across all layers. A seed-cluster is formed if the window transverse energy (defined as the total transverse energy of the towers contained in the window) exceeds 2.5 GeV. Afterwards, well-reconstructed inner detector (ID) tracks are extrapolated to the middle layer of the electromagnetic calorimeter and matched to the seed-cluster[1]. Finally, each of these clusters are treated as electron candidates and rebuilt with a larger window of 3×7 and 5×5 towers in the barrel and in the end-cap regions, respectively.

The clusters associated with electron candidates must satisfy a set of identification criteria in order to efficiently discriminate isolated signal electrons from background processes, such as hadronic jets mimicking the signature of an electron, electrons from heavy-flavour hadron decays or photon conversions. They are based on variables describing the transverse and longitudinal shower profiles, the track reconstruction quality, as well as the track-to-cluster matching. Three different sets of sequential selection cuts are defined with an increasing background rejection rate: *loose*, *medium* and *tight*[2] [123]. In the analyses presented in this thesis, the *medium* selection is applied for pre-selected electrons while the *tight* selection is required for signal electrons (see Sections 3.3.1 and 5.4.1).

The electron identification and reconstruction efficiency is measured in data with a tag-and-probe method using $Z \to ee$, $Z \to ee\gamma$ and $J/\psi \to ee$ events and compared to the Monte Carlo (MC) prediction. The discrepancy between data and MC simulation is corrected for using event-level weights. The efficiency increases with the electron transverse energy and decreases with the tightness of the selections, as shown in Figure 2.8. The combined efficiency for electrons with E_{T} around 25 GeV is about 92%, 78% and 68% for the loose, medium and tight cuts, respectively.

The electron four-momentum is reconstructed from the energy of the calorimeter cluster while the direction is taken from the the associated ID track. The

[1] The object is classified as a photon if no good matching candidate is found.

[2] A set of cut-based selections used for the 2012 data [123] are often referred to as the *++ menu*. The original cuts [124] have been revisited during Run1 to account for higher luminosity conditions.

detector energy response, corrected for shower leakage outside the cluster region and beyond the EM calorimeter, is then calibrated by applying the EM scale from the test-beam studies, MC-based corrections and in-situ corrections measured in $Z \to ee$ data events [123, 125]. Afterwards, the energy of the electron candidates in the MC simulation is smeared to match the resolution in data.

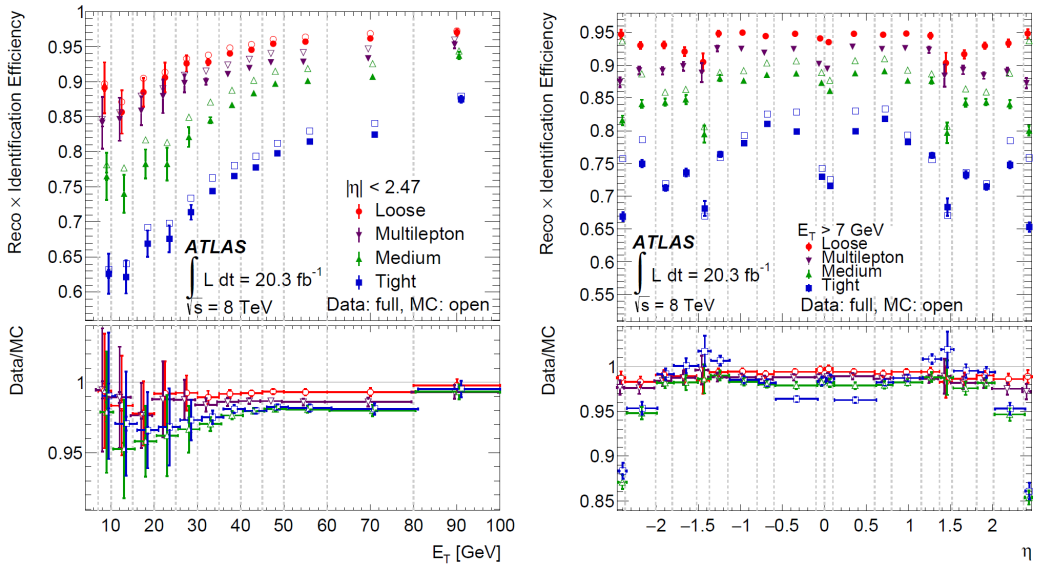

Figure 2.8: Electron combined reconstruction and identification efficiency as a function of E_{T} (left) and η (right) measured in $Z \to ee$ data events for the 2012 benchmark cut-based selections, compared to MC simulation [123]. The *multilepton* selection is a specific benchmark optimised for the reconstruction of low energy electrons from $H \to ZZ^* \to 4\ell$ decays.

2.3.2 Muons

Muons leave the ATLAS detector with only minimal energy losses and thus their signature is clean and well distinguishable from other charged particles in the SM. They can be reconstructed using the two ATLAS tracking systems, namely the ID ($|\eta| < 2.5$) and the muon spectrometer (MS) ($|\eta| < 2.7$), with several reconstruction criteria and algorithms [126]. Four different types of muons are available. *Combined* (CB) muons require independently reconstructed tracks in the ID and MS, which are then statistically combined. These candidates have the highest muon purity. *Segment-tagged* (ST) muons require a track in the ID and at least one associated track segment in the MS. They are particularly efficient to

recover muons with low momentum or muons falling in the regions with reduced MS acceptance. *Stand-alone* (SA) muons are reconstructed only in the MS, taking into account the expected energy loss in the calorimeter system. The tracks are extrapolated back to the interaction point to determine the impact parameters. These candidates extend the acceptance to the region which is not covered by the ID ($2.5 < |\eta| < 2.7$). Finally, *calorimeter-tagged* (CaloTag) muons are a combination of an ID track and energy deposits in the calorimeter compatible with minimum ionizing particles. These candidates have the lowest purity but recover acceptance in a region of $|\eta| < 0.1$ which is uncovered by the MS. The search for $WWW \to \ell\nu\,\ell\nu\,\ell\nu$ events uses CB muons (Section 3.3.2) while the search for supersymmetry makes use of CB as well as ST muons (Section 5.4.1). Both types are reconstructed using the "first chain" (or `STACO`) algorithm which statistically combines parameters of ID and MS tracks using the covariance matrices of both measurements [126].

The efficiency of the muon reconstruction is measured in data with a tag-and-probe method using $Z \to \mu\mu$ and $J/\psi \to \mu\mu$[1] events and compared to the expectation from MC simulation. The muon reconstruction efficiency in the simulation is then corrected using the corresponding scale factors. As shown in Figure 2.9, the efficiency of the combination of all the muon reconstruction types is found to be above 99% over most of the covered phase space of $|\eta| < 2.7$ [126].

The muon momentum scale and resolution are studied using large calibration samples of $Z \to \mu\mu$, $\Upsilon \to \mu\mu$ and $J/\psi \to \mu\mu$ decays [126]. Correction factors are extracted to introduce additional smearing in the MC simulation. They are then applied in the physics analyses in order to improve the data-MC agreement and to minimize the uncertainties.

2.3.3 Jets

Jets, introduced as collimated sprays of hadrons in the previous chapter, are defined at the reconstruction level using a number of algorithms. Each of these jet reconstruction algorithm definitions has to satisfy several criteria in order to

[1] The efficiencies derived from $Z \to \mu\mu$ decays are complemented at low p_{T} with results extracted from $J/\psi \to \mu\mu$ decays.

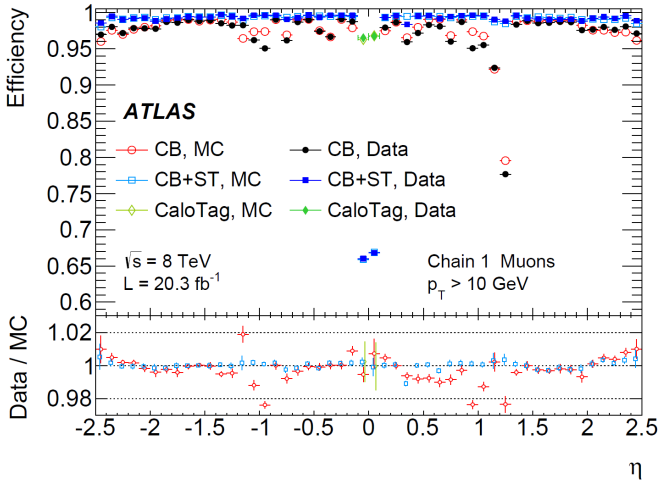

Figure 2.9: Muon reconstruction efficiency as a function of η measured in $Z \to \mu\mu$ events for different muon reconstruction types, compared to MC simulation [126].

be compatible with the cross-section calculations performed at the parton level. For example, they have to be collinear and infrared safe, which means that the resulting jets should not be sensitive to the collinear and soft splittings occurring in a parton shower. For the analyses presented here, jets are reconstructed from topological calorimeter clusters [122] using the `anti-k`$_t$ algorithm [127] with a distance parameter of $\Delta R = 0.4$. It is a sequential recombination algorithm which recombines the jet constituents according to the following distance measure:

$$d_{ij} = \min\{1/p_{\mathrm{T}i}^2, 1/p_{\mathrm{T}j}^2\} \cdot \Delta R_{ij}^2/R^2 \tag{2.4}$$

where $p_{\mathrm{T}i}$ is the transverse momentum of the constituent i, ΔR_{ij} is the geometrical distance between objects i and j and R is a parameter of the algorithm defining the characteristic radius of the resulting jet.

Given the non-compensating nature of the ATLAS calorimeter, the measured jet energy needs to be corrected. This is performed using a calibration method known as local cluster weighting (LCW) [128] which firstly classifies clusters as electromagnetic or hadronic, according to the cluster topology, and then applies correction factors to each calorimeter cell. The weights are derived from detailed MC simulations of neutral and charged pions and depend on the calorimeter

layer, cluster energy and cell energy density. The reconstructed jets are further calibrated by applying a jet energy scale (JES) determined from a combination of methods based on simulation and in-situ measurements [129]. It corrects for the energy offset introduced by pile-up interactions, adjusts the jet direction to point to the primary vertex, calibrates the jet energy and η back to particle level and takes into account residual effects not included in the initial calibration based on simulation.

The identification of jets arising from b-quark fragmentation (b-*tagging*) is performed by measuring of the impact parameters of the tracks from the b-hadron decay products (`IP3D`), identifying the secondary vertex due to relatively long lifetime of hadrons containing a b-quark (`SV1`) or exploiting the topology of b- and c-hadron decays (`JetFitter`) [130, 131]. The algorithm which shows the best performance uses a neural network to combine the outputs from the above mentioned algorithms into a single discriminating variable. It is called `MV1` and is used in both analyses presented in this thesis.

2.3.4 Missing Transverse Energy

Neutrinos or hypothetical neutral weakly interacting particles do not leave a signal in the detector and their presence can be inferred indirectly from the momentum imbalance in the plane perpendicular to the beam direction. Even though the initial momenta of the partons involved in the hard scattering interaction are unknown, their transverse projection can be treated as zero to a good approximation. This allows the missing transverse momentum vector $\vec{p}_{\mathrm{T}}^{\,\mathrm{miss}}$, with magnitude $E_{\mathrm{T}}^{\mathrm{miss}}$, to be obtained from the negative vector sum of the transverse momenta of all detected particles in the event.

The $E_{\mathrm{T}}^{\mathrm{miss}}$ reconstruction [132,133] uses energy deposits in the electromagnetic and hadronic calorimeters as well as muon tracks in the ID and MS. The two components are referred to as the calorimeter and muon term. The calorimeter contribution is calculated from energy deposits associated with reconstructed and identified high-p_{T} physics objects which are calibrated accordingly. Ambiguities between objects are resolved by applying a specific order of priority: electrons, photons, hadronically decaying τ-leptons, jets and muons. Additional low-energy

deposits in the calorimeter cells as well as the topological clusters and tracks not associated with any of the previously defined object classes are taken into account in the *soft term*[1]. The contribution from muons is included in the muon term. If the combined measurement of the muon momentum is used, the energy lost in the calorimeters is not added to the calorimeter term to avoid double energy counting. If only the MS measurement of the muon momentum is considered, the energy loss is covered by a muon calorimeter term.

[1]The $E_{\mathrm{T}}^{\mathrm{miss}}$ reconstruction for early Run2 data in the ATLAS detector is calculated from calibrated and corrected physics objects using a track-based soft term [134, 135].

CHAPTER 3

SEARCH FOR $W^{\pm}W^{\pm}W^{\mp} \to \ell^{\pm}\nu\,\ell^{\pm}\nu\,\ell^{\mp}\nu$ PRODUCTION

3.1 Introduction

The electroweak sector of the Standard Model theory is based on the symmetry group $SU(2)_L \otimes U(1)_Y$ and describes the weak and electromagnetic interactions via the exchange of the corresponding gauge vector fields. The non-Abelian character of this field theory leads to the triple (VVV) and quartic ($VVVV$) self-coupling vertices of the gauge bosons ($V = W, Z, \gamma$). Their direct measurement provides an important test of the electroweak symmetry breaking mechanism. Any deviation from the predictions would indicate new physics at higher energy scales than those probed at the LHC. Furthermore, the triple (TGC) and quartic (QGC) gauge coupling vertices contribute to diboson and triboson production processes. Given that they are the major background to several Higgs production modes as well as to many new phenomena scenarios, the measurement of their cross-sections is of particular interest.

In the SM theory, charged QGC vertices ($WWWW$, $WWZZ$, $WWZ\gamma$ and $WW\gamma\gamma$) are allowed while neutral QGC vertices ($ZZZZ$, $ZZ\gamma\gamma$, $Z\gamma\gamma\gamma$ and $\gamma\gamma\gamma\gamma$) are forbidden. Due to their small predicted production cross-sections, neither of these processes have been observed experimentally to date. However, many searches have been performed by the LEP experiments for the $WWZ\gamma$, $WW\gamma\gamma$

and $ZZ\gamma\gamma$ QGCs [136–141], by the D0 experiment at Tevatron for $WW\gamma\gamma$ QGC [142] and the LHC experiments for the $WWZ\gamma$, $WW\gamma\gamma$ and $WWWW$ QGCs [143–147]. With the large amount of proton-proton collision data provided by the LHC at $\sqrt{s} = 8$ TeV, the ATLAS collaboration announced the first evidence for a process involving a QGC vertex in 2014 [147]. The contribution of the $WWWW$ QGC was studied using the same-sign W boson pair production in association with two jets ($W^{\pm}W^{\pm}jj$). The analysis [148] introduced in this thesis presents the first search for the $WWWW$ vertex via triboson production ($W^{\pm}W^{\pm}W^{\mp}$).

Within the SM, the WWW production cross-section is known at the next-to-leading order precision in QCD and electroweak corrections [149–151]. This precise theoretical prediction allows for a more straightforward interpretation of the experimental data but its low value makes the measurement very difficult. The branching fractions of all possible decay modes are summarized in Figure 3.1. The search presented in this chapter is performed in the final state where all W bosons decay to electron and neutrino or muon and neutrino. Even though the branching ratio of this fully leptonic channel is the smallest among the other decay modes ($\sim 1\%$), it provides a clean signature in the hadronic environment of the LHC.

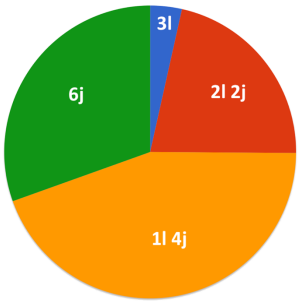

Figure 3.1: The SM predictions of the branching ratios for different WWW decay modes: fully leptonic decay mode $WWW \to \ell\nu\ell\nu\ell\nu$ (3.4%), semi-leptonic decay mode $WWW \to \ell\nu\ell\nu jj$ (21.3%), decay mode with one leptonic W boson decay $WWW \to \ell\nu jjjj$ (44.4%) and fully hadronic decay mode $WWW \to jjjjjj$ (30.9%). Here ℓ represents the lepton of any flavour (e, μ, τ) and j denotes the jet which materializes from the hadronization of quark.

3.2 Data and Simulated Event Samples

An overview of the data and simulated event samples used in this analysis is given in the following sections. Section 3.2.1 describes the analysed data sample while Section 3.2.2 gives more details on the simulation of the SM background processes. The simulation and cross-section calculation of the triboson production is described in Section 3.2.3.

3.2.1 Data

The data sample used in this analysis was recorded by the ATLAS detector at the LHC in 2012. During this period, the LHC was operated at a center-of-mass energy of 8 TeV. The total integrated luminosity of proton-proton collision data after applying basic data quality requirements is 20.3 ± 0.4 fb^{-1} [152]. These criteria ensure that all relevant detector subsystems were in stable operation during the run. The number of pp interactions per bunch crossing varies between approximately 10 and 30 with an average of 20.7 for this data set.

Events are selected using the un-prescaled single-lepton triggers with the lowest transverse momentum threshold of 24 GeV together with an isolation requirement. In order to increase the acceptance for high-p_{T} leptons, the triggers without any isolation requirement but with higher momentum threshold of 60 GeV for electrons and 36 GeV for muons are also used.

3.2.2 Background Processes

The contribution of each background process to the $WWW \to \ell\nu\ell\nu\ell\nu$ production is estimated either using Monte Carlo simulations or directly from data. Only the processes with at least three prompt leptons (WZ, ZZ, $t\bar{t}V$, VVV) or with two prompt leptons and one isolated photon ($Z\gamma$) are estimated using MC samples. However, additional background events (Z/W+jets, $t\bar{t}$, single top, $W\gamma$) are simulated for the purpose of design and validation of data-driven methods, described in Sections 3.5.2 and 3.5.3.

The background processes are generated using the following MC event generators: MadGraph [153], Powheg [154–156], Sherpa [157], AlpGen [158],

MC@NLO [159] and ACERMC [160]. All events calculated at the matrix element level, except those generated by SHERPA, are then interfaced to PYTHIA [90,161] or HERWIG [162] and JIMMY [163] for the simulation of parton showering, hadronisation and the underlying event modelling. SHERPA is a general-purpose tool which generates the matrix elements and simulates the parton showering, hadronisation and underlying events.

The samples of ZWW^* and ZZZ^* triboson events are produced using MADGRAPH and hadronised with PYTHIA6. The $Z\gamma$ samples are produced with SHERPA and the $W\gamma$ events are generated using ALPGEN interfaced to HERWIG+JIMMY. The dominant production of WZ, ZZ and WW events is simulated using POWHEG interfaced to PYTHIA8. The WW and ZZ diboson events can also be produced through the loop-induced $gg \to ZZ/WW$ processes. These contributions are estimated using the GG2ZZ/GG2WW generators [164,165] with HERWIG+JIMMY. The top-quark pair production in association with a vector boson is modelled using MADGRAPH with PYTHIA6. The MC@NLO event generator, whose next-to-leading order (NLO) matrix elements are matched to HERWIG+JIMMY parton showers, is used to simulate $t\bar{t}$ processes. Single top production in the s- and Wt-channels is generated in the same way as the $t\bar{t}$ samples, while ACERMC interfaced to PYTHIA6 is used for the t-channel. The production of Z and W bosons in association with jets is generated using SHERPA and ALPGEN with HERWIG+JIMMY, respectively. The W+jets events containing heavy-flavour quarks are simulated separately using leading-order (LO) matrix elements with massive b and c quarks. These are used to study the composition of fake leptons in the data-driven estimate, described in Section 3.5.3. Double parton scattering processes are also taken into account and generated using PYTHIA8. To avoid the double counting between V+jets and $V\gamma$ samples ($V = W, Z$), the contribution from the final-state photon radiation in V+jets production is removed.

Two different parton distribution function (PDF) sets are used together with the generators to describe the momentum distribution of the partons within the proton. For the SHERPA, POWHEG and MC@NLO samples, PDFs are taken from CT10 [166], while the CTEQ6L1 [167] PDF set is used with MADGRAPH, PYTHIA8, ALPGEN and ACERMC.

The MC generator parameters are tuned to reproduce experimental data and to provide an optimal description of hadronisation, fragmentation, initial- and final-state QCD radiation, and multiple parton interaction effects. The tuned parameter set AUET2B [168] is used with PYTHIA6 and HERWIG, and the set AU2 [169] is used with PYTHIA8.

The events from hard-scattering processes are then passed through detector simulation based on GEANT4[1] [109]. The effect of multiple pp collisions in the same or neighbouring bunch crossings (pile-up) is modelled by overlaying minimum-bias events, generated with PYTHIA8, onto the original hard-scattering event. Given that the average number of interactions per bunch crossing $\langle\mu\rangle$ varies according to the conditions of data-taking, the MC samples are reweighted by a factor of $1/1.09 \cdot \langle\mu\rangle$ to match the recorded data.

Finally, all background samples are normalized to the theoretical cross-sections from the most precise calculations available at the time the analysis was performed.

3.2.3 WWW Signal Processes

At the LO, four different types of processes contribute to charged triple vector boson production at the LHC. Specifically, the three W bosons can come: (1) from the fermion line; (2) from the intermediate Z/γ^* boson; (3) from the WH process where the Higgs boson decays into two W bosons; and (4) from a $WWWW$ QGC vertex. The Feynman diagrams for each of these processes are shown in Figure 3.2. The dominant contribution (about 64%) arises from the associated Higgs boson production. The NLO corrections in the strong QCD coupling constant α_s have been calculated [149, 150] and incorporated into two Monte Carlo programs: VBFNLO [171] and MADGRAPH [153] with MC@NLO [159]. The NLO electroweak corrections have also recently been calculated [151] but are not included in the present analysis.

The VBFNLO program simulates the processes $pp \to W^{\pm}W^{\pm}W^{\mp} + X$ with subsequent decay of the vector bosons in fully leptonic final state. All spin cor-

[1]Only low mass Drell-Yan samples employs a fast detector simulation ATLFAST-II [170], using a parametric response of the electromagnetic and hadronic calorimeters.

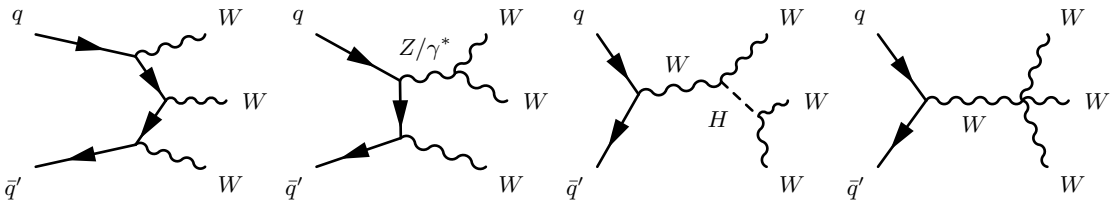

Figure 3.2: Feynman diagrams for the production of triboson $W^{\pm}W^{\pm}W^{\mp}$ final states: (1) Fermion-mediated, (2) Z/γ^*-mediated WWZ or $WW\gamma$ TGC vertex, (3) Higgs-mediated, (4) $WWWW$ QGC vertex.

relations of decay products, the Higgs boson exchange and off-shell contributions are taken into account. Even though the cross-sections can be computed at NLO QCD accuracy with the CT10 PDF set, the partonic events can be generated only at LO precision with the CTEQ6L1 PDF set. An appropriate k-factor is hence introduced and applied to all signal events after being processed through the Pythia8 [161] parton shower and the Geant4 [109] simulation. The MadGraph generator simulates the non-resonant ($pp \to W^{\pm}W^{\pm}W^{\mp}+X$ with on-shell W bosons) and resonant ($pp \to W^{\pm}H + X$ with $H \to WW^{(*)}$) processes separately at NLO QCD accuracy. The CTEQ6L1 PDF set is used and thus the samples are reweighted to CT10 NLO PDFs to match the QCD order. The generated events contain inclusive W boson decays and are showered though Pythia8. These samples are used as default for the total and fiducial cross-section calculation. This choice is especially convenient in view of the combination with the semi-leptonic channel $WWW \to \ell\nu\ell\nu jj$ [172] which is discussed in Chapter 4. Given that the MadGraph simulated signal events are not processed through the full reconstruction chain of the ATLAS detector, the VBFNLO samples are re-weighted to the MadGraph cross-section using the k-factor derived in the fiducial phase space (defined in Section 3.4.3). The calculated inclusive cross-sections are summarized in Table 3.1.

3.2.4 aQGC Signal Processes

The samples of aQGC processes described in Section 1.4, are generated using VBFNLO at NLO in QCD and passed through the full ATLAS detector simulation. Their production cross-sections are very sensitive to the values of $f_{S,0}/\Lambda^4$ and $f_{S,1}/\Lambda^4$. By definition, the effective Lagrangian approach is valid only up to

Sample		$\boldsymbol{\sigma^{\mathrm{SM}}}$ **[fb]**
VBFNLO	$W^+W^+W^- \to \ell\nu\ell\nu\ell\nu$	4.95 ± 0.007
	$W^-W^+W^- \to \ell\nu\ell\nu\ell\nu$	2.65 ± 0.004
	Sum	7.60 ± 0.008
MadGraph	$W^+W^-W^+ \to$ Anything	59.47 ± 0.11
	$W^-W^+W^- \to$ Anything	28.069 ± 0.076
	$W^+H \to W^+W^+W^-(*) \to$ Anything	99.106 ± 0.019
	$W^-H \to W^-W^+W^-(*) \to$ Anything	54.804 ± 0.010
	Sum	241.47 ± 0.13

Table 3.1: Inclusive cross-sections from VBFNLO and MadGraph at NLO with CT10 NLO PDFs. The difference in branching fractions between the two generators results in the different sum of the cross-sections. Only statistical uncertainties are shown.

a cut-off scale Λ, beyond which the tree-level unitarity may be violated. This can be fixed by applying the form-factor introduced in Equation 1.74. There is no theoretical algorithm to predict for which n and Λ_F values the cross-section would violate unitarity. After discussion with the VBFNLO authors, the exponent is set to unity whilst different values of Λ_F are considered. Finally, dedicated MC samples are produced for a grid of points in the ($f_{S,0}/\Lambda^4$, $f_{S,1}/\Lambda^4$) parameter plane with $\Lambda_F = 0.5$, 1, 2 and 3 TeV, as well as $\Lambda_F = \infty$ which corresponds to the non-unitarized case.

The parameters $f_{S,0}/\Lambda^4$ and $f_{S,1}/\Lambda^4$ can be expressed in terms of an alternative set of couplings, α_4 and α_5, using the following vertex-specific relations [173]:

$$\alpha_4 = \frac{f_{S,0}}{\Lambda^4}\frac{v^4}{8} \tag{3.1}$$

$$\alpha_4 + 2\alpha_5 = \frac{f_{S,1}}{\Lambda^4}\frac{v^4}{8} \tag{3.2}$$

where v is the Higgs vacuum expectation value. A general conversion is not possible since α_4 and α_5[1] correspond to different anomalous coupling operators [175, 176] than the ones described in Section 1.4 and a different symmetry group is assumed.

[1]These aQGC parameters are used by the Whizard [174] MC generator.

3.3 Object Definition

The reconstruction algorithms have been described in details in Section 2.3. All requirements applied to the physics objects used in this analysis and summarizes in the following. For the purpose of this analysis, leptons are defined as *pre-selected* (or *baseline*) and *signal*. The pre-selection of electron and muon candidates is used to estimate the contribution from non-isolated leptons, discussed in Section 3.5.3. The pre-selected leptons are then identified as signal leptons if they pass, in addition, more stringent identification criteria. Only a tighter set of lepton requirements is applied for the final selections.

3.3.1 Electrons

Pre-selected electrons must satisfy $p_{\mathrm{T}} > 10$ GeV and the *medium* quality criteria, described in [123, 177], which include requirements on the shower shape in the electromagnetic calorimeter, the track quality and the presence of hits in the pixel and SCT detectors. The charged-hadron background is rejected by identifying transition radiation in the TRT. Additional requirements are imposed on the impact parameters in order to reduce the background electrons from photon conversions. The transverse d_0 and longitudinal z_0 impact parameters are defined as the minimum distance between the reconstructed track and the primary vertex in the transverse and longitudinal planes[1], respectively.

Signal electrons fulfil the *tight* quality criteria [177] and $p_{\mathrm{T}} > 20$ GeV. This stringent selection requires at least one hit in the innermost pixel layer ('b-layer'), TRT hits compatible with an electron candidate and information about reconstructed photon conversion vertices. In addition, isolation requirements based on tracking and calorimeter information are applied. The calorimeter isolation is defined as the scalar sum of the transverse energy of topological clusters, corrected for pile-up effects, within a cone of radius $\Delta R = \sqrt{\Delta\eta^2 + \Delta\phi^2} = 0.2$ around the electron cluster. The ID isolation is calculated as the summed scalar p_{T} of additional tracks with $p_{\mathrm{T}} > 1$ GeV inside a cone of radius $\Delta R = 0.2$ originating from

[1]The uncertainty on the d_0 measurement is represented by σ_{d_0}. The polar angle of the reconstructed track is denoted as θ.

the same vertex. These isolation parameters, called $p_{\mathrm{T}}^{\mathrm{Cone0.2}}$ and $E_{\mathrm{T}}^{\mathrm{Cone\,0.2}}$, are required to be smaller than 4% and 10% of the electron's p_{T} and E_{T}, respectively. The selection requirements for pre-selected and signal electrons are summarized in Table 3.2.

Pre-selected electrons	
Algorithm	`AuthorElectron`
Acceptance	$p_{\mathrm{T}} > 10\,\mathrm{GeV}$, $\lvert\eta\rvert < 2.47$
Quality	Medium
Transverse impact parameter	$\lvert d_0/\sigma_{d_0}\rvert < 3$
Longitudinal impact parameter	$\lvert z_0 \sin\theta\rvert < 0.5$ mm
e-e isolation	$\Delta R(e,e) > 0.1$
e-μ isolation	$\Delta R(e,\mu) > 0.1$
Signal electrons	
Quality	Tight
Acceptance	$p_{\mathrm{T}} > 20\,\mathrm{GeV}$
Track isolation	$p_{\mathrm{T}}^{\mathrm{Cone\,0.2}}/p_{\mathrm{T}} < 0.04$
Calorimeter isolation	$E_{\mathrm{T}}^{\mathrm{Cone\,0.2}}/E_{\mathrm{T}} < 0.1$

Table 3.2: Summary of the electron selection criteria. The signal requirements are applied on top of the pre-selection criteria.

3.3.2 Muons

The muon candidates are required to satisfy $|\eta| < 2.5$ and $p_{\mathrm{T}} > 10$ GeV. Only candidates with the highest muon purity, so-called *combined* (CB) muons, are used in this analysis. Their tracks are reconstructed independently in the ID and MS and then statistically combined. The muon momentum is calculated as a weighted average of the p_{T} measured in the ID and MS. Given the p_{T} resolution dependence[1], the weight is determined as a function of muon p_{T}. Requirements on the impact parameters d_0 and z_0 ensure that muons originate from the primary

[1]The inner detector provides better resolution for low-p_{T} muons while the muon spectrometer for high-p_{T} muon.

vertex. The ID tracks associated to the muon candidates have to fulfil a number of quality requirements [126]. In order to reduce the mis-identification rate, the *tight* identification is considered [178].

Signal muons are required to have $p_{\mathrm{T}} > 20$ GeV and to be isolated in both the inner tracker and in the calorimeter within a cone $\Delta R = 0.2$. The calorimetric energy deposited in the cone, excluding the muon energy deposit, must be less than 0.1 times the E_{T} of the muon and the summed scalar p_{T} of additional tracks must be less than 0.04 times the muon p_{T}. All requirements applied on pre-selected and signal muons are summarized in Table 3.3.

Pre-selected muons	
Algorithm	`STACO` (CB muons)
Acceptance	$p_{\mathrm{T}} > 10\,\mathrm{GeV}$, $\lvert\eta\rvert < 2.5$
Quality	Tight
Inner detector track quality	MCP ID hits selection
Transverse impact parameter	$\lvert d_0/\sigma_{d_0}\rvert < 3$
Longitudinal impact parameter	$\lvert z_0 \sin\theta\rvert < 0.5$ mm
μ-μ isolation	$\Delta R(\mu,\mu) > 0.1$
Signal muons	
Acceptance	$p_{\mathrm{T}} > 20\,\mathrm{GeV}$
Track isolation	$p_{\mathrm{T}}^{\mathrm{Cone}\,0.2}/p_{\mathrm{T}} < 0.04$
Calorimeter isolation	$E_{\mathrm{T}}^{\mathrm{Cone}\,0.2}/E_{\mathrm{T}} < 0.1$

Table 3.3: Summary of the muon selection criteria. The signal requirements are applied on top of the pre-selection criteria.

3.3.3 Jets

Jets are reconstructed from topological clusters in the calorimeter using the `anti-`k_t algorithm with a cone size parameter of 0.4, as described in Section 2.3.3. They are required to fulfil $p_{\mathrm{T}} > 25$ GeV and $|\eta| < 4.5$. In order to reduce the number of jets originating from pile-up vertices, the jet vertex fraction (JVF)

defined as the summed scalar p_{T} of tracks associated with both the jet (with $p_{\mathrm{T}} < 50$ GeV and $|\eta| < 2.4$) and the primary vertex must be greater than 50% of the summed scalar p_{T} of all the tracks within a cone. Jets originating from b-quarks within $|\eta| < 2.5$ are identified using the `MV1` algorithm with an efficiency of 85%. The jet and b-jet selections are summarized in Table 3.4.

Jets	
Algorithm	`anti-`k_t with $\Delta R = 0.4$ (LCW+JES)
Acceptance	$p_{\mathrm{T}} > 25\,\mathrm{GeV}$, $\|\eta\| < 4.5$
JVF requirement	$\|\mathrm{JVF}\| > 0.5$ if $p_{\mathrm{T}} < 50\,\mathrm{GeV}$ and $\|\eta\| < 2.4$
j-e isolation	$\Delta R(j, e) > 0.2$
j-μ isolation	$\Delta R(j, \mu) > 0.2$
***b*-jets**	
Acceptance	$p_{\mathrm{T}} > 25\,\mathrm{GeV}$, $\|\eta\| < 2.5$
b-tagging	`MV1` algorithm 85%

Table 3.4: Summary of the jet selection criteria. The b-jet requirement is applied on top of the jet selection criteria.

3.3.4 Missing Transverse Energy

The missing transverse energy $E_{\mathrm{T}}^{\mathrm{miss}}$ is reconstructed from the energy deposited in the calorimeters and the muon momentum measured in the ID and MS [132,133], as described in Section 2.3.4. Since pile-up interactions significantly degrade the $E_{\mathrm{T}}^{\mathrm{miss}}$ reconstruction performance [179], the soft term contribution is further scaled with the soft term vertex fraction (STVF)[1].

3.3.5 Overlap Removal

As the reconstruction algorithms are independent of each other, several physics objects can be reconstructed from the same detectors inputs. Therefore, they

[1]The STVF is defined as the fraction of momenta of tracks matched to the soft term which are associated with the hard scattering vertex.

may overlap with each other inside the ATLAS detector. To remove this duplication, the following criteria are applied to jets and pre-selected leptons. Firstly, two electron duplicates lying within a distance $\Delta R < 0.1$ are typically reconstructed from two ID tracks but share the same EM cluster or vice versa. These occurrences are removed by keeping only the electron with higher p_{T}. To avoid duplicate muons, a muon candidate with a separation $\Delta R < 0.1$ from another one is discarded if its momentum is lower and kept otherwise. Given that muons can radiate photons which may then convert into electron-positron pairs, any electron found within $\Delta R < 0.1$ of a reconstructed muon is removed. Furthermore, if a jet and an electron are separated by $\Delta R < 0.2$, the jet is rejected. This is motivated by the fact that the electron reconstruction relies on the calorimeter energy deposits, which can be mis-reconstructed as a jet, as well as on a well defined ID track. Therefore, if an electron overlaps with a reconstructed jet, it is likely to be the signature of a high-p_{T} electron. Finally, muons with a distance $\Delta R < 0.2$ to the closest jet may originate from a heavy-flavour decay. These events are kept but only muons are considered.

3.4 Event Selection

As mentioned in Section 3.2.1, only data satisfying beam, detector and data quality criteria are considered. Collision events of interest to this analysis are selected using isolated or non-isolated single-lepton triggers. Afterwards, the reconstructed physics objects, detailed in Section 3.3, are defined. Simulated events are required to pass the same triggers and event reconstruction algorithms as the data. Differences are corrected by reweighting the MC events by factors derived from data control samples. They account for the lepton identification and reconstruction efficiencies, trigger efficiencies, momentum scale and resolution, and for the efficiency and mis-tag rate of the b-tagging.

Basic *pre-selection* requirements, applied to select well-reconstructed events with the signature of the $W^{\pm}W^{\pm}W^{\mp} \to \ell^{\pm}\nu\,\ell^{\pm}\nu\,\ell^{\mp}\nu$ production, are described in Section 3.4.1. Section 3.4.2 presents the selection criteria used to define the regions of the phase space with enhanced sensitivity to the signal (*signal regions*). The *fiducial phase spaces* determined at particle level are defined in Section 3.4.3.

3.4.1 Event Pre-selection

To remove non-collision background, each pre-selected event is required to have a primary vertex reconstructed from at least three tracks with $p_{\mathrm{T}} > 0.4$ GeV. For events with multiple reconstructed primary vertices along the beam axis due to the pile-up, the vertex with the largest $\sum p_{\mathrm{T}}^2$ of associated tracks is taken as the primary collision vertex. Additional cleaning requirements are applied to reject data events affected by noise bursts in the LAr calorimeter, events with corrupted Tile calorimeter data and events with incomplete detector information due to a restart of the system during the data-taking [180]. Moreover, jet candidates may be reconstructed from energy deposits arising from instrumental effects such as beam-induced particles and detector noise. Since these jets distort the measurement of the missing transverse energy, a recommended strategy is to drop the event if a high-p_{T} jet is identified as *bad* [181]. The technical details are given in Appendix A.

To select events with three leptonically decaying W bosons, they are required to contain exactly three signal leptons (electrons or muons) with $p_{\mathrm{T}} > 20$ GeV. At least one of these selected leptons is then required to be geometrically matched to an object that fired the trigger and to have p_{T} at least 1 GeV higher than the online trigger threshold[1].

3.4.2 Signal Regions

The $W^{\pm}W^{\pm}W^{\mp}$ signal can decay in eight different final states with equal production probability, specifically $e^{\pm}e^{\pm}e^{\mp}$, $e^{\pm}e^{\pm}\mu^{\mp}$, $e^{\pm}\mu^{\pm}e^{\mp}$, $\mu^{\pm}e^{\pm}e^{\mp}$, $\mu^{\pm}\mu^{\pm}e^{\mp}$, $\mu^{\pm}e^{\pm}\mu^{\mp}$, $e^{\pm}\mu^{\pm}\mu^{\mp}$ and $\mu^{\pm}\mu^{\pm}\mu^{\mp}$. Three signal regions are defined based on the number of same-flavour opposite-sign (SFOS) lepton pairs in the event: 0SFOS ($e^{\pm}e^{\pm}\mu^{\mp}$ and $\mu^{\pm}\mu^{\pm}e^{\mp}$), 1SFOS ($e^{\pm}\mu^{\pm}e^{\mp}$, $\mu^{\pm}e^{\pm}e^{\mp}$, $\mu^{\pm}e^{\pm}\mu^{\mp}$ and $e^{\pm}\mu^{\pm}\mu^{\mp}$) and 2SFOS ($e^{\pm}e^{\pm}e^{\mp}$ and $\mu^{\pm}\mu^{\pm}\mu^{\mp}$). When neglecting the charge mis-identification and the differences in lepton efficiencies, one can expect twice as many events in the 1SFOS signal region than in the other two regions. This classification is

[1] Single-lepton triggers listed in Section 3.2.1, which are used to record the events, have so-called *online* transverse energy thresholds. The *offline* lepton p_{T} thresholds, which are applied in the analysis, need to be chosen such that a high trigger efficiency is achieved.

motivated mainly by the electroweak WZ and ZZ processes which may result in events with a topology similar to the signal. If all three leptons from WZ decay are reconstructed and the fourth lepton in the ZZ decay fails the selection criteria, these processes contribute equally to the 1SFOS and 2SFOS signal regions, forming the dominant background. On the other hand, their contribution in the 0SFOS region is only due to the charge mis-measurement and leptonic τ decays, and hence small. Its background is almost entirely reducible and dominated by events where a jet overlaps with or is mis-identified as a lepton, called the *fake lepton* background.

In each signal region, a unique set of selection requirements is obtained from an optimization procedure that simultaneously maximizes the predicted signal yield and the precision on the expected SM cross-section measurement [148]. The optimization considers many different kinematic quantities and their combinations. For each permutation, the expected signal and background yields together with their systematic uncertainties, are determined and then used in the statistical framework described in Section 3.8.3. The uncertainty on the measurement is extracted from the profile likelihood contour. This value is then compared to the expected signal yield to ensure that a good sensitivity is not just an artefact due to the near absence of both signal and background. The final signal region selections are summarized in Table 4.1 and discussed below.

First of all, the WWW production with subsequent fully-leptonic decay leads to multi-lepton final states with little hadronic activity. In events where the triboson system is balanced by a hadronic recoil, one or more jets may be produced and thus need to be considered as a part of the signal signature. The jet multiplicity requirement of $N_{\text{jet}} \leq 1$ is found to be favourable for this measurement and is therefore applied in all signal regions. The top background is efficiently reduced by vetoing events with b-tagged jets. As described in Section 3.3.3, the operating point with the highest available b-tagging efficiency of 85% is found to be optimal for this analysis.

The backgrounds with Z bosons are characterized by a peak in the invariant mass distribution of two SFOS leptons around the Z-mass ($m_Z = 91.1876$ GeV [13]). Given that the same distribution for the WWW process is relatively flat,

	0SFOS	**1SFOS**	**2SFOS**
Pre-selection	Exactly 3 leptons with $p_T > 20$ GeV		
b-jet veto	$N_{b\text{-jet}} = 0$ (85 % b-tagging efficiency)		
SF mass	$m_{\text{SF}} > 20\,\text{GeV}$	–	–
Z veto	$\|m_{ee} - m_Z\| > 15\,\text{GeV}$	$m_Z - m_{\text{SFOS}} > 35\,\text{GeV}$ or $m_{\text{SFOS}} - m_Z > 25\,\text{GeV}$	$\|m_{\text{SFOS}} - m_Z\| > 20\,\text{GeV}$
$E_{\text{T}}^{\text{miss}}$	–	$E_{\text{T}}^{\text{miss}} > 45\,\text{GeV}$	$E_{\text{T}}^{\text{miss}} > 55\,\text{GeV}$
$3\ell - E_{\text{T}}^{\text{miss}}$ angle	$\|\phi(3\ell) - \phi(E_{\text{T}}^{\text{miss}})\| > 2.5$		
Inclusive jet veto	$N_{\text{jet}} \leq 1$		

Table 3.5: Optimized signal selection criteria, based on the number of same-flavour opposite-sign (SFOS) lepton pairs.

a Z-boson veto is applied in all signal regions without substantially affecting the signal efficiency. The mass windows are chosen by the optimization procedure for each signal region separately. In the 1SFOS and 2SFOS regions, the SFOS dilepton invariant mass is required to satisfy $m_{\text{SFOS}} \notin [m_Z - 35, m_Z + 20]$ and $m_{\text{SFOS}} \notin [m_Z - 20, m_Z + 20]$[1], respectively. An asymmetric window is chosen to remove the $Z\gamma$ contribution in the low-shoulder of the Z-peak. Even though there is no SFOS pair in the 0SFOS signal region by definition, a peak in the same-sign dielectron mass distribution shows up because of charge mis-identification. Therefore, a Z-boson veto is implemented here as well, with a mass window of $m_{ee} \notin [m_Z - 15, m_Z + 15]$. Moreover, the invariant mass of the same-flavour lepton pairs is required to be greater than 20 GeV in the 0SFOS region to avoid heavy-flavour meson resonances.

The signal signature is, besides the presence of three charged leptons, relatively large $E_{\text{T}}^{\text{miss}}$ arising from the neutrinos from the leptonic W boson decays. The $E_{\text{T}}^{\text{miss}}$ threshold is found to be correlated with Z-mass window due to the ability to remove the $Z\gamma$ background. Thus, the tighter Z-boson veto in the

[1] In the 2SFOS region, both sets of SFOS pairs are considered.

1SFOS region allows for a looser $E_{\mathrm{T}}^{\mathrm{miss}}$ requirement ($E_{\mathrm{T}}^{\mathrm{miss}} > 45$ GeV) and vice versa for the 2SFOS region where a threshold of $E_{\mathrm{T}}^{\mathrm{miss}} > 55$ GeV is applied. There is no $E_{\mathrm{T}}^{\mathrm{miss}}$ cut on the 0SFOS region. In addition, the signal $E_{\mathrm{T}}^{\mathrm{miss}}$ may be interpreted as the vector sum of the transverse momentum of three neutrinos. Since the tri-lepton system and $E_{\mathrm{T}}^{\mathrm{miss}}$ are expected to be back-to-back due to azimuthal symmetry, the following requirement is used in all signal regions: $|\phi(3l) - \phi(E_{\mathrm{T}}^{\mathrm{miss}})| > 2.5$.

3.4.3 Fiducial Regions

The cross-section measurement is performed in a restricted part of the phase space with respect to the phase space used for inclusive cross-section calculations (Table 3.1). This region, referred to as fiducial region, is defined at the generator level and is designed to match the experimental selections (defined at the reconstruction level in Table 4.1) as close by as possible.

	0SFOS	**1SFOS**	**2SFOS**
τ veto		$N_\tau = 0$	
Lepton selection		Exactly 3 leptons with $p_T > 20\,\mathrm{GeV}$	
Lepton OR		$\Delta R(\ell\ell) > 0.1$	
SF mass	$m_{\mathrm{SF}} > 20\,\mathrm{GeV}$	–	–
Z veto	$\lvert m_{ee} - m_Z\rvert > 15\,\mathrm{GeV}$	$m_Z - m_{\mathrm{SFOS}} > 35\,\mathrm{GeV}$ or $m_{\mathrm{SFOS}} - m_Z > 25\,\mathrm{GeV}$	$\lvert m_{\mathrm{SFOS}} - m_Z\rvert > 20\,\mathrm{GeV}$
$E_{\mathrm{T}}^{\mathrm{miss}}$	–	$E_{\mathrm{T}}^{\mathrm{miss}} > 45\,\mathrm{GeV}$	$E_{\mathrm{T}}^{\mathrm{miss}} > 55\,\mathrm{GeV}$
$3\ell - E_{\mathrm{T}}^{\mathrm{miss}}$ angle		$\lvert\phi(3\ell) - \phi(E_{\mathrm{T}}^{\mathrm{miss}})\rvert > 2.5$	
Inclusive jet veto		$N_{\mathrm{jet}} \leq 1$	

Table 3.6: Definition of fiducial regions based on the optimized signal selection criteria.

The fiducial selections, outlined in Table 3.6, are implemented in Rivet [182]. Only to electrons and muons originating from vector-boson decays are considered. These prompt leptons are then recombined with the final-state photons

from QED radiation within a cone of $\Delta R = 0.1$ to form so-called *dressed leptons*. Generator-level jets are reconstructed using the `anti-`k_t algorithm with the distance parameter $\Delta R = 0.4$ from all final-state particles after parton showering and hadronisation except prompt leptons, prompt photons and neutrinos. The generator-level neutrinos are used to calculate the missing transverse energy. Events with $W \to \tau\nu \to \ell\nu\nu\nu$ decays are not included in the fiducial cross-section definition. However, they are still counted as signal in the reweighted VBFNLO samples used in the final reconstruction level selection and contribute up to 20% of the total predicted signal yield. This approach allows for a simple fiducial definition which should be easily reproducible by theorists.

The VBFNLO and MadGraph cross-sections derived in the common fiducial-phase space are summarized in Table 3.7. The fiducial cross-sections are observed to agree within 2% between the two generators. As already mentioned, the VBFNLO samples are re-weighted to the MadGraph cross-section using a k-factor of 1.018.

Sample		$\sigma^{\text{fid SM}}$ **[fb]**
VBFNLO	$W^+W^+W^- \to \ell\nu\ell\nu\ell\nu$	0.2050 ± 0.0070
	$W^-W^+W^- \to \ell\nu\ell\nu\ell\nu$	0.0987 ± 0.0037
	Sum	0.3037 ± 0.0072
MadGraph	$W^+W^-W^+ \to$ Anything	0.0900 ± 0.0048
	$W^-W^+W^- \to$ Anything	0.0476 ± 0.0043
	$W^+H \to W^+W^+W^-(*) \to$ Anything	0.1114 ± 0.0029
	$W^-H \to W^-W^+W^-(*) \to$ Anything	0.0603 ± 0.0015
	Sum	0.3092 ± 0.0072
Generator k-factor (MadGraph / VBFNLO)		1.018 ± 0.024

Table 3.7: Fiducial cross-sections from VBFNLO and MadGraph at the NLO with CT10 NLO PDF. A k-factor is derived by comparing the two generators in the fiducial region of the phase space. Only statistical uncertainties are shown.

3.5 Background Estimation

The background to the WWW signal comes from events where all lepton candidates arise from electroweak gauge boson decays and events with at least one mis-identified lepton. Given that the signal regions are defined based on their flavour and charge, also the processes where the sign of one lepton is mis-measured contribute and require special treatment. The background events are divided into three classes: SM background (Section 3.5.1), charge-flip background (Section 3.5.2) and fake lepton background (Section 3.5.3). Their predictions are thoroughly tested with data in a set of dedicated validation regions (Section 3.5.4).

3.5.1 Standard Model Background

The SM processes with three prompt leptons from gauge bosons constitute an irreducible background for $WWW \to \ell\nu\ell\nu\ell\nu$ production. Their contribution is estimated purely from the MC simulations discussed in Section 3.2.2. The normalization factors for these predictions are summarized, with the corresponding errors, in Table 3.8. Representative Feynman diagrams for the dominant WZ process along with the $t\bar{t}W$ and ZZZ processes are shown in Figure 3.3.

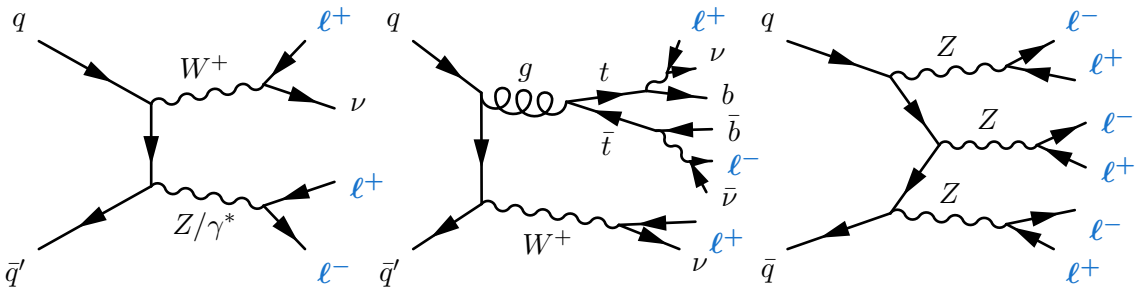

Figure 3.3: Examples of Feynman diagrams for the SM background processes with at least three prompt leptons: WZ (left), $t\bar{t}W$ (middle) and ZZZ (right) falling within 1SFOS, 0SFOS and 2SFOS category, respectively. Prompt isolated lepton candidates are shown in blue.

WZ process

The WZ production and the subsequent leptonic decays of the vector bosons are modelled at NLO in QCD using the POWHEG generator. The measurements

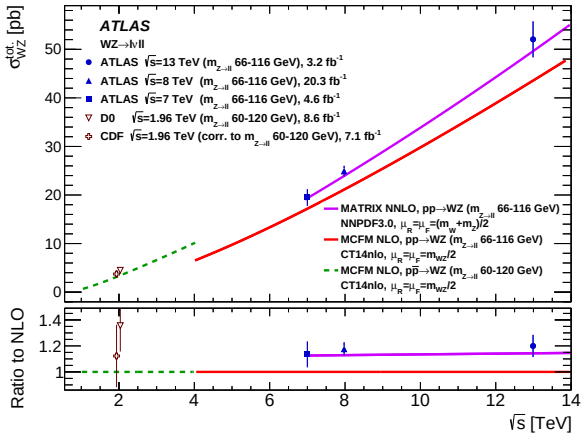

Figure 3.4: Comparison of WZ cross-section measurements at various centre-of-mass energies with the SM expectations, taken from [188]. Measurements in pp collisions are compared to the theoretical predictions at $\mathcal{O}(\alpha_s)$, obtained with MCFM using the CT14nlo PDF set, and at $\mathcal{O}(\alpha_s^2)$, obtained using MATRIX with NNPDF3.0 PDF set.

performed at 7 and 8 TeV by the ATLAS [183, 184] and CMS [185] collaborations found that the observed cross-section is systematically higher than the prediction. A very recent calculation at next-to-next-to-leading order (NNLO) in QCD showed that the NNLO corrections increase the NLO results [186]. The effect ranges from 8% at 7 TeV to 11% at 13 TeV and significantly improves the agreement with the ATLAS data, as can be seen in Figure 3.4. Given that these predictions have not been available at the time of the analysis, the WZ cross-section is normalized using a correction factor derived from a WZ-enriched region in data using a two-dimensional sideband method [148, 187]. The normalization factor of 1.08 ± 0.10 is then applied to the NLO POWHEG MC samples.

ZZ process

Another background producing multiple prompt leptons includes $ZZ^* \to \ell^{\pm}\ell^{\mp}\ell^{\pm}\ell^{\mp}$ events where one lepton is not reconstructed. The $q\bar{q} \to ZZ^*$ processes are generated with POWHEG at NLO and the loop-induced $gg \to ZZ^*$ processes with GG2ZZ at LO. The impact of the NNLO corrections in QCD with respect to the inclusive NLO cross-section is found to be about 11% at the center-of-mass of 8

TeV [189]. Given that the loop-induced gluon fusion contributes about 60% to the total NNLO effect, the POWHEG expectation is scaled by a factor of 1.05. An uncertainty of 15% is assigned to the ZZ background to account for the NNLO QCD corrections as well as for the NLO electroweak corrections [190, 191]. The recent ATLAS measurement at 13 TeV shows good agreement with $\mathcal{O}(\alpha_s^2)$ SM predictions [192].

$Z\gamma$ process

Events with a leptonically decaying Z boson and an on-shell photon contribute to the selection when the photon is mis-identified as an electron. They are modelled using the SHERPA generator which provides precise predictions for the kinematic variable shapes as well as for the normalization, as shown in the 7 TeV [187] and 8 TeV [193] ATLAS data.

Other background processes

Other background events originate from $t\bar{t}V$, ZWW, ZZZ processes and are estimated using MADGRAPH simulations. The $t\bar{t}W$ and $t\bar{t}Z$ LO samples are normalised to NLO predictions and a global normalization uncertainty of 30% is assigned, following the calculations in [194, 195] and the results in Section 5.6.1.1. An equivalent uncertainty of 30% is applied on the normalization of triboson processes. The contributions from double parton scattering (DPS) processes are found to be negligible.

Background	Normalization factor	Uncertainty
WZ	1.08	10%
ZZ	1.05	15%
$t\bar{t}W$	1.18	30%
$t\bar{t}Z$	1.34	30%
ZWW, ZZZ	1.0	30%

Table 3.8: Summary of the normalizations and their uncertainties for the prompt lepton background estimates used in the analysis.

3.5.2 Charge-flip Background

Background from charge mis-measurement, here referred to as "charge-flip" background, originates from processes where the charge of at least one prompt lepton is mis-identified. It contributes mostly to the 0SFOS signal region through WZ and ZZ processes. The dominant mechanism is the radiation of a hard photon from an electron followed by an asymmetric conversion where only the positron track is reconstructed. A representative of these so-called trident events ($e^{\pm} \to e^{\pm}\gamma \to e^{\pm}e^{\pm}e^{\mp}$) is shown in Figure 3.5.

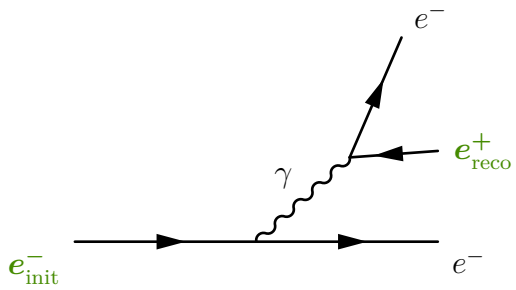

Figure 3.5: Process leading to electron charge mis-reconstruction. The initial electron may be reconstructed as a positron via Bremsstrahlung (shown in green).

The probability of mis-identifying the charge depends strongly on the material in the inner detector, which varies with η. It increases significantly at larger $|\eta|$ values and slightly with the p_{T} of electron. The charge-flip efficiency for muons is found to be negligible due to the rare muon Bremsstrahlung.

The charge-flip probability is extracted from data events with two signal electrons. Their invariant mass is required to satisfy $m_{ee} \in [m_Z - 10, m_Z + 10]$ GeV where m_Z is the mass of Z boson equal to 91.1876 GeV [13]. The selected events are then split into two categories, one with same-sign electron pairs (SS) and the other with opposite-sign electron pairs (OS). The measurement is performed using a likelihood-based method in p_{T} and η bins, listed in Table 3.9.

$\|\eta\|$ bin index	$\|\eta\|$	p_{T} bin index	p_{T}/GeV
1	$[0.0, 0.8]$	1	$[15, 30]$
2	$[0.8, 1.15]$	2	$[30, 40]$
3	$[1.15, 1.6]$	3	$[40, 50]$
4	$[1.6, 1.8]$	4	$[50, 60]$
5	$[1.8, 2.0]$	5	$[60, 80]$
6	$[2.0, 2.2]$	6	$[80, 120]$
7	$[2.2, 2.3]$	7	> 120
8	$[2.3, 2.4]$	–	–
9	$[2.4, 2.5]$	–	–

Table 3.9: The $|\eta|$ and p_{T} bins used for the measurement of charge-flip efficiencies.

Assuming that the charge-flip probabilities are independent across the different bins, the expected number of events with same-sign leptons in bins i and j $\langle N_{\mathrm{SS}}^{ij} \rangle$ can be expressed in terms of the total number of events N^{ij} as:

$$\begin{aligned} \langle N_{\mathrm{SS}}^{ij} \rangle &= N^{ij} \left(\xi_1^i (1 - \xi_2^j) + (1 - \xi_1^i) \, \xi_2^j \right) \\ &\approx N^{ij} \left(\xi_1^i + \xi_2^j \right) \end{aligned} \tag{3.3}$$

where ξ_1^i / ξ_2^i is the probability that a charge of leading/subleading lepton is mismeasured. It is equal to zero for the muons. The approximation is valid if the efficiencies are small, which is usually the case. Following the Poisson statistics assumption in each bin, one has:

$$\mathcal{P}(N_{\mathrm{SS}}^{ij} | \langle N_{\mathrm{SS}}^{ij} \rangle) = \frac{\langle N_{\mathrm{SS}}^{ij} \rangle^{N_{\mathrm{SS}}^{ij}}}{N_{\mathrm{SS}}^{ij} \, !} e^{-\langle N_{\mathrm{SS}}^{ij} \rangle} \tag{3.4}$$

where N_{SS}^{ij} is the observed number of same-sign events in a given (i, j) bin. The likelihood function is then constructed as a following product of all event permutations from m bins:

$$L(\xi^1, \ldots, \xi^m) = \prod_{i=1}^{m} \prod_{j=1}^{m} \mathcal{P}(N_{\mathrm{SS}}^{ij} \, | \langle N_{\mathrm{SS}}^{ij} \rangle) \tag{3.5}$$

It is convenient to consider rather the negative logarithm of the likelihood:

$$\begin{aligned} -\ln L(\xi^{1},\ldots,\xi^{m}) &= -\sum_{i=1}^{m}\sum_{j=1}^{m} \ln \mathcal{P}(N_{\mathrm{SS}}^{ij}\,|\langle N_{\mathrm{SS}}^{ij}\rangle) \\ &= -\sum_{i=1}^{m}\sum_{j=1}^{m} \left(N_{\mathrm{SS}}^{ij}\ln\langle N_{\mathrm{SS}}^{ij}\rangle - \langle N_{\mathrm{SS}}^{ij}\rangle\right) + \text{const} \\ &= -\sum_{i=1}^{m}\sum_{j=1}^{m} \left(N_{\mathrm{SS}}^{ij}\ln(N^{ij}(\xi_1^i+\xi_2^j)) - N^{ij}(\xi_1^i+\xi_2^j)\right) + \text{const} \end{aligned} \tag{3.6}$$

All charge-flip efficiencies $\xi^{1},\ldots,\xi^{m}$ can be simultaneously extracted by minimizing this function for a given set of measurements of N_{SS}^{ij} and N^{ij}. The constant terms are neglected as they do not affect the minimum.

Besides statistical uncertainties, two systematic errors are considered. Firstly, the charge-flip efficiencies are obtained using the MC $Z \to ee$ events. Since the MC simulations store details of the generated particles, the charge of the 'true' electron can be compared to its charge after the reconstruction. This allows to compute the efficiencies as a function of p_{T} and $|\eta|$. They are then compared to the efficiencies derived from the same MC sample using the likelihood method. The difference is taken as a systematic uncertainty. Secondly, the background contribution from non-resonant processes is subtracted using template fits. The signal template is determined from the $Z \to ee$ MC sample and the background template is extracted from data with looser selections. The dielectron invariant mass spectrum is fitted with the two templates, the background contribution is determined and subtracted from data in each bin. The efficiencies are then recomputed by maximizing the likelihood function 3.6. A systematic error is assigned to cover the difference between this new set of efficiencies and their central values.

The charge-flip probabilities with their uncertainties are summarized in Figure 3.6. The total systematic error is a quadratic sum of the uncertainty obtained by comparing the two methods (data-driven and MC-based) and the uncertainty from the background subtraction.

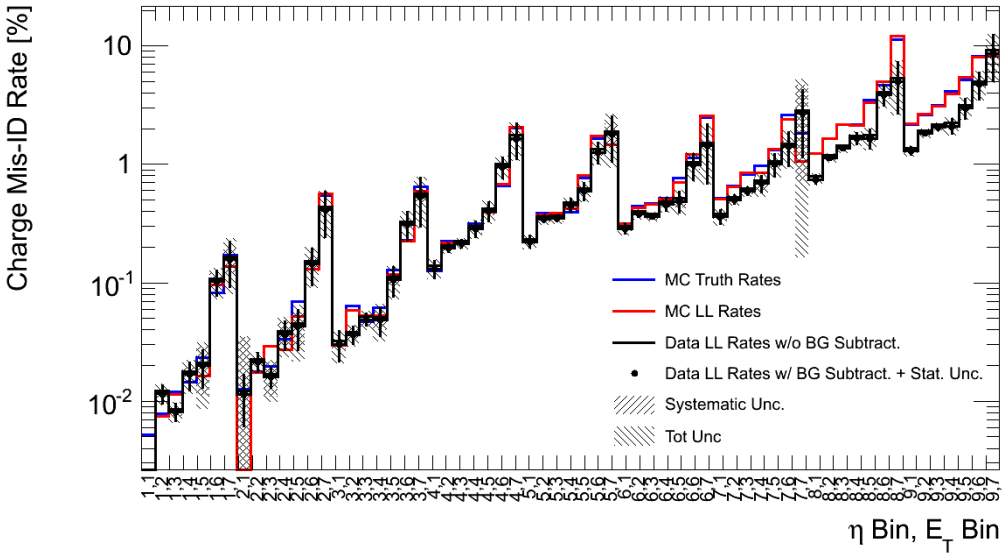

Figure 3.6: Electron charge-flip efficiencies obtained from data using the likelihood method (black points), with systematic and statistical uncertainties. The nominal values are compared to those measured in MC $Z \to ee$ samples using the likelihood method (red line) and the truth method (blue line). The x axis label is the $|\eta|$ and p_{T} bin index, as defined in Table 3.9.

Given that the charge-flip background in the 1SFOS and 2SFOS signal regions is negligible, its contribution is estimated only in the 0SFOS region. The event yield of this background is obtained by applying a weight to those MC simulated WZ and ZZ events with at least one electron-positron pair in the final state. The weight is approximately the sum of probabilities, one for each electron in the event, that a charge mis-identification occurs and migrates event into the 0SFOS category:

$$w(\xi^{i}, \ldots) \approx \sum_{k \in \mathrm{el.}} \xi_{k}^{i}\, \Theta_{k} \tag{3.7}$$

where ξ_{k}^{i} is the charge-flip efficiency for k^{th} electron in i^{th} bin and Θ_{k} represents the step function defined for an individual event. It is equal to one if flipping charge of k^{th} electron classifies event as 0SFOS and to zero otherwise. The final

charge-flip estimate can be then written as a sum of weights event by event:

$$\langle N^{\text{flip}}_{\text{0SFOS}} \rangle = \sum_{\alpha \in \text{MC}} \sum_{k \in \text{el.}} \xi^{i}_{k}\, \Theta_{k} \tag{3.8}$$

where the first sum runs over the appropriate MC events[1] and the second sum is taken over the electrons in a given event.

Consider an example where the event comes from the decay $WZ \to e^{+}\nu\, e^{+}e^{-}$. Assuming that all three charged leptons pass the reconstruction as well as the signal requirements, they can be labelled as $e^{+}_{1}e^{+}_{2}e^{-}_{3}$. This event falls into the 0SFOS category only if the charge of the electron is mis-measured and thus $\Theta_1 = 0$, $\Theta_2 = 0$, $\Theta_3 = 1$. The weight is then equal to the charge-flip efficiency for the electron based on its reconstructed η and p_{T} values i.e. $w(\xi^{\,i}) = \xi^{i}_{3}$. As another example, consider an event with the decay $ZZ \to \mu^{+}\mu^{-}\, e^{+}e^{-}$, assuming that one muon is not reconstructed in order to satisfy the three lepton selection. Three remaining leptons are labelled as $\mu^{-}_{1}e^{+}_{2}e^{-}_{3}$. The charge-flip of either electron or positron results in the event being classified as 0SFOS and thus $\Theta_1 = 0$, $\Theta_2 = 1$, $\Theta_3 = 1$. Therefore, the event weight is the sum of two efficiencies i.e. $w(\xi^{\,i}, \xi^{\,j}) = \xi^{i}_{2} + \xi^{j}_{3}$.

The charge-flip background estimation is validated on WZ and ZZ events by comparing the predictions taken directly from MC simulation to the predictions reweighted in the 0SFOS signal region. Figure 3.7 shows the η and p_{T} distributions for WZ (top) and ZZ (bottom) samples. Relatively good shape agreement is observed. An offset in the normalization is partially covered by the systematic uncertainties assigned to the procedure. The difference in efficiencies measured in data and MC samples at high η and p_{T} (see Figure 3.6) can reflect this discrepancy and motivate the use of a semi data-driven method.

[1] The following diboson decay channels are considered: $WZ \to e^{\pm}\nu\, e^{+}e^{-}$, $WZ \to \mu^{\pm}\nu\, e^{+}e^{-}$, $WZ \to \tau^{\pm}\nu\, e^{+}e^{-}$, $ZZ \to e^{+}e^{-}\, e^{+}e^{-}$ and $ZZ \to \mu^{+}\mu^{-}\, e^{+}e^{-}$. Some other channels, such as $WZ \to e^{\pm}\nu\,\tau^{+}\tau^{-}$, can appear in the 0SFOS region without any charge mis-measurement.

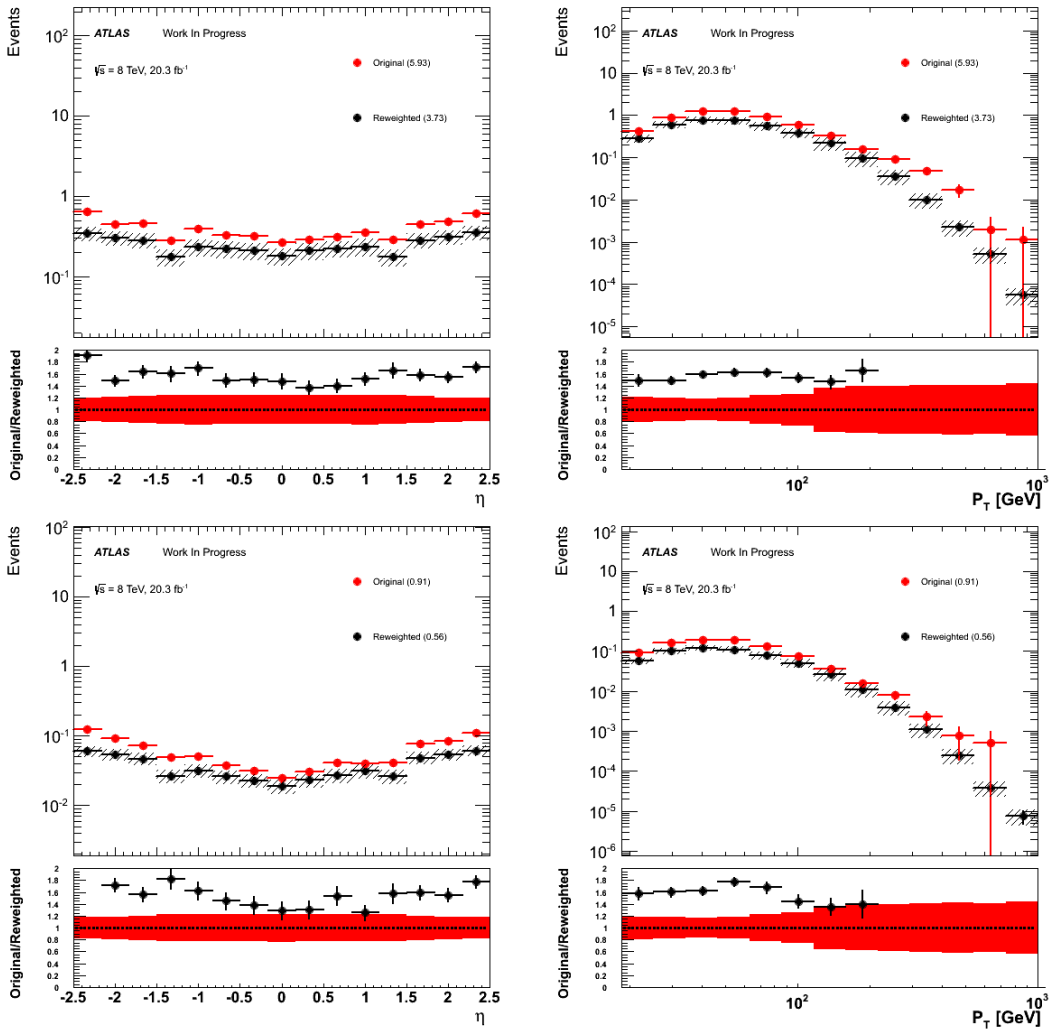

Figure 3.7: Validation of the charge-flip background comparing $WZ \to \ell^{\pm}\nu\, e^{\pm}e^{\mp}$ (top) and $ZZ \to \ell^{\pm}\ell^{\mp}\, e^{\pm}e^{\mp}$ (bottom) MC samples reweighted with the efficiencies measured in $Z \to e^{\pm}e^{\mp}$ MC events to the original MC predictions. Distributions of lepton p_{T} and η are shown. The red band represents the systematic uncertainty from the charge-flip estimate only.

3.5.3 Fake Lepton Background

The fake lepton background consists of events with at least one non-prompt lepton. While the leptons denoted as *prompt* come mainly from W or Z leptonic decays, the so called *non-prompt* leptons arise from semi-leptonic decays of heavy-flavour quarks, from mis-identified hadrons and from electrons from photon conversions. The contribution from the latter originates almost exclusively from the $Z\gamma$ process which is accurately modelled using Monte Carlo simulation. Therefore, only non-prompt leptons originating from jets are referred as *fake* leptons in this analysis. Figure 3.8 depicts representative Feynman diagrams for fake lepton production. This background is estimated using the generalised matrix method [196, 197] which is a fully data-driven technique.

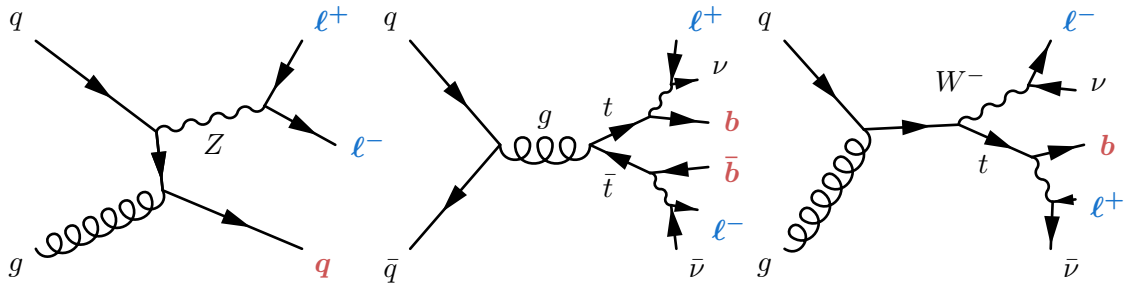

Figure 3.8: Examples of Feynman diagrams for the fake lepton background processes: Z+jets (left), $t\bar{t}$(middle) and single top (right). Prompt isolated lepton candidates are shown in blue, while the potential mis-reconstructed leptons are depicted in red.

3.5.3.1 Generalised Matrix Method

A fully data-driven method is used to estimate the fake lepton background, because the MC might not faithfully reproduce its behaviour. Furthermore, to obtain a sufficiently large statistics in the region of phase space specific for this analysis might be demanding. The matrix method classifies all leptons with $p_{\mathrm{T}} > 20$ GeV according to their identification and/or isolation quality criteria, introducing a fake-enriched class of *loose* leptons. These pass all pre-selection requirements and fail any of the signal selection criteria as defined in Tables 3.2

and 3.3. The *tight* leptons satisfy the signal definition and thus the two sets are disjoint. If the probabilities for prompt and fake pre-selected leptons to fulfil the tighter quality requirements are known, the number of events with at least one fake lepton can be predicted. The efficiencies depend on the lepton kinematics and the event characteristics. This analysis employs a generalised matrix method where an arbitrary number of pre-selected leptons can be present in the event. For illustration, events with one and two leptons are considered here. The extension to n leptons follows afterwards.

In a data sample consisting of **events with a single lepton**, the equation relating the number of events with prompt N_P and fake N_F lepton to the expected number of events with lepton reconstructed as tight $\langle N_T \rangle$ or loose $\langle N_L \rangle$ can be written as following:

$$\begin{pmatrix} \langle N_T \rangle \\ \langle N_L \rangle \end{pmatrix} = \begin{pmatrix} \varepsilon & \zeta \\ \bar{\varepsilon} & \bar{\zeta} \end{pmatrix} \begin{pmatrix} N_P \\ N_F \end{pmatrix} \tag{3.9}$$

where ε and ζ are the prompt and fake efficiencies, representing the probabilities for prompt and fake lepton to pass the signal lepton criteria, respectively. For convenience, the efficiencies of falling into a loose category are denoted as $\bar{\varepsilon} \equiv 1-\varepsilon$ and $\bar{\zeta} \equiv 1-\zeta$. Given the measurement of N_T and N_L, the expected prompt $\langle N_P \rangle$ and fake $\langle N_F \rangle$ contributions can be calculated from the inverted relation:

$$\begin{pmatrix} \langle N_P \rangle \\ \langle N_F \rangle \end{pmatrix} = \frac{1}{\varepsilon - \zeta} \begin{pmatrix} \bar{\zeta} & -\zeta \\ -\bar{\varepsilon} & \varepsilon \end{pmatrix} \begin{pmatrix} N_T \\ N_L \end{pmatrix} \tag{3.10}$$

The procedure to obtain an estimate for the number of events with a fake lepton passing the tight requirements $\langle N'_T \rangle$ is:

$$\begin{pmatrix} \langle N'_T \rangle \\ \langle N'_L \rangle \end{pmatrix} = \begin{pmatrix} \varepsilon & \zeta \\ \bar{\varepsilon} & \bar{\zeta} \end{pmatrix} \begin{pmatrix} 0 \\ \langle N_F \rangle \end{pmatrix} = \begin{pmatrix} \varepsilon & \zeta \\ \bar{\varepsilon} & \bar{\zeta} \end{pmatrix} \begin{pmatrix} 0 & 0 \\ 0 & 1 \end{pmatrix} \begin{pmatrix} \langle N_P \rangle \\ \langle N_F \rangle \end{pmatrix} \tag{3.11}$$

$$= \begin{pmatrix} \varepsilon & \zeta \\ \bar{\varepsilon} & \bar{\zeta} \end{pmatrix} \begin{pmatrix} 0 & 0 \\ 0 & 1 \end{pmatrix} \frac{1}{\varepsilon - \zeta} \begin{pmatrix} \bar{\zeta} & -\zeta \\ -\bar{\varepsilon} & \varepsilon \end{pmatrix} \begin{pmatrix} N_T \\ N_L \end{pmatrix} \tag{3.12}$$

For compactness, it is useful to rewrite Equation 3.9 introducing the following notation, where summation is implied over repeated indices:

$$p = \begin{pmatrix} N_P \\ N_F \end{pmatrix}, \quad \langle t \rangle = \begin{pmatrix} \langle N_T \rangle \\ \langle N_L \rangle \end{pmatrix}, \quad \phi = \begin{pmatrix} \varepsilon & \zeta \\ \bar{\varepsilon} & \bar{\zeta} \end{pmatrix} \quad \Rightarrow \quad \langle t_\beta \rangle = \phi_\beta{}^\alpha p_\alpha \tag{3.13}$$

Here α takes values corresponding to P or F, and similarly β for T or L. The expected number of tight leptons that are fake is then:

$$\langle t'_\nu \rangle = \phi_\nu{}^\mu \; \omega_\mu{}^\beta \; \phi^{-1}{}_\beta{}^\alpha t_\alpha \tag{3.14}$$

where $\alpha, \nu \in \{T, L\}$, $\beta, \mu \in \{P, F\}$. The selection of the fake component is represented by ω:

$$\omega = \begin{pmatrix} 0 & 0 \\ 0 & 1 \end{pmatrix} \tag{3.15}$$

In case of the **events with a pair of leptons**, a relation similar to Equation 3.9 can be written:

$$\begin{pmatrix} \langle N_{TT} \rangle \\ \langle N_{TL} \rangle \\ \langle N_{LT} \rangle \\ \langle N_{LL} \rangle \end{pmatrix} = \begin{pmatrix} \varepsilon_1\varepsilon_2 & \varepsilon_1\zeta_2 & \zeta_1\varepsilon_2 & \zeta_1\zeta_2 \\ \varepsilon_1\bar{\varepsilon}_2 & \varepsilon_1\bar{\zeta}_2 & \zeta_1\bar{\varepsilon}_2 & \zeta_1\bar{\zeta}_2 \\ \bar{\varepsilon}_1\varepsilon_2 & \bar{\varepsilon}_1\zeta_2 & \bar{\zeta}_1\varepsilon_2 & \bar{\zeta}_1\zeta_2 \\ \bar{\varepsilon}_1\bar{\varepsilon}_2 & \bar{\varepsilon}_1\bar{\zeta}_2 & \bar{\zeta}_1\bar{\varepsilon}_2 & \bar{\zeta}_1\bar{\zeta}_2 \end{pmatrix} \begin{pmatrix} N_{PP} \\ N_{PF} \\ N_{FP} \\ N_{FF} \end{pmatrix} \tag{3.16}$$

where N_{TT} represents the number of observed events with two tight leptons, N_{LL} with two loose leptons and N_{TL}/N_{LT} with one loose and one tight lepton. The leptons are ordered by p_{T} in the indexes. Further, ε_1 and ε_2 (ζ_1 and ζ_2) are the prompt (fake) efficiencies for the leading and subleading leptons, respectively. As already mentioned, these are functions of the lepton kinematic properties and thus are in general different. Since the method treats each lepton in the event independently, a 4×4 matrix can be rewritten as a Kronecker product of two 2×2 matrices:

$$\begin{pmatrix} \varepsilon_1\varepsilon_2 & \varepsilon_1\zeta_2 & \zeta_1\varepsilon_2 & \zeta_1\zeta_2 \\ \varepsilon_1\bar{\varepsilon}_2 & \varepsilon_1\bar{\zeta}_2 & \zeta_1\bar{\varepsilon}_2 & \zeta_1\bar{\zeta}_2 \\ \bar{\varepsilon}_1\varepsilon_2 & \bar{\varepsilon}_1\zeta_2 & \bar{\zeta}_1\varepsilon_2 & \bar{\zeta}_1\zeta_2 \\ \bar{\varepsilon}_1\bar{\varepsilon}_2 & \bar{\varepsilon}_1\bar{\zeta}_2 & \bar{\zeta}_1\bar{\varepsilon}_2 & \bar{\zeta}_1\bar{\zeta}_2 \end{pmatrix} = \begin{pmatrix} \varepsilon_1 & \zeta_1 \\ \bar{\varepsilon}_1 & \bar{\zeta}_1 \end{pmatrix} \otimes \begin{pmatrix} \varepsilon_2 & \zeta_2 \\ \bar{\varepsilon}_2 & \bar{\zeta}_2 \end{pmatrix} \tag{3.17}$$

As in the previous case, Equation 3.16 can be expressed more compactly as:

$$\phi_1 = \begin{pmatrix} \varepsilon_1 & \zeta_1 \\ \bar{\varepsilon}_1 & \bar{\zeta}_1 \end{pmatrix}, \quad \phi_2 = \begin{pmatrix} \varepsilon_2 & \zeta_2 \\ \bar{\varepsilon}_2 & \bar{\zeta}_2 \end{pmatrix} \quad \Rightarrow \quad \langle t_{\beta_1\beta_2} \rangle = \phi_{1\,\beta_1}^{\ \ \alpha_1} \phi_{2\,\beta_2}^{\ \ \alpha_2}\, p_{\alpha_1\alpha_2} \tag{3.18}$$

Given that all components in $t_{\alpha_1\alpha_2}$ are measured, the fake lepton background is estimated using the following formula:

$$\langle t'_{\nu_1\nu_2} \rangle = \phi_{\nu_1}^{\ \ \mu_1} \phi_{\nu_2}^{\ \ \mu_2}\, \omega_{\mu_1\mu_2}^{\ \ \ \beta_1\beta_2}\, \phi^{-1}{}_{\beta_1}^{\ \ \alpha_1} \phi^{-1}{}_{\beta_2}^{\ \ \alpha_2}\, t_{\alpha_1\alpha_2} \tag{3.19}$$

where $\alpha_1, \alpha_2, \nu_1, \nu_2 \in \{T, L\}$ and $\beta_1, \beta_2, \mu_1, \mu_2 \in \{P, F\}$. The contribution only from the fake components is selected by a ω matrix in the form:

$$\omega = \begin{pmatrix} 0 & 0 & 0 & 0 \\ 0 & 1 & 0 & 0 \\ 0 & 0 & 1 & 0 \\ 0 & 0 & 0 & 1 \end{pmatrix} \tag{3.20}$$

With the presented compact formalism, it is straightforward to generalise the matrix method to any number of pre-selected leptons. In particular, the expression for the **events with n leptons** is the following:

$$\langle t'_{\nu_1\cdots\nu_n} \rangle = \phi_{\nu_1}^{\ \ \mu_1} \cdots \phi_{\nu_n}^{\ \ \mu_n}\, \omega_{\mu_1\cdots\mu_n}^{\ \ \ \beta_1\cdots\beta_n}\, \phi^{-1}{}_{\beta_1}^{\ \ \alpha_1} \cdots \phi^{-1}{}_{\beta_n}^{\ \ \alpha_n} t_{\alpha_1\cdots\alpha_n} \tag{3.21}$$

Each ϕ contains the prompt and fake efficiencies appropriate for the given lepton index. The selector ω picks out the sets of indices β_i corresponding to the components one wish to count as fake background. In general, it looks like:

$$\omega_{\mu_1\cdots\mu_n}^{\ \ \ \beta_1\cdots\beta_n} = \delta_{\mu_1}^{\ \ \beta_1} \cdots \delta_{\mu_n}^{\ \ \beta_n}\, f(\beta_1, \ldots, \beta_n) \tag{3.22}$$

where δ_i^j is the Kronecker delta and f is a function of the indices taking values 1 (for a fake combination) and 0 (for a real combination).

The result of Equation 3.21 is typically calculated as a weight w for each event where only one component in $t_{\alpha_1 \cdots \alpha_n}$ is equal to one while the rest is zero, given the measurement. All pre-selected leptons, where each lepton is either loose or tight, enter the matrix method and the weight is assigned to every possible output configuration. The event is then processed separately for each weight.

The generalised matrix method has several benefits when compared to the standard matrix method. In a three lepton final state, the matrix would be 8×8 to account for all possible lepton configurations, and some approximations are often made to reduce its dimensionality to 7×7. The method used in this analysis avoids any simplification of this kind. Moreover, one has to invert only three 2×2 matrices instead of one 7×7 matrix, which makes the computation more straightforward and stable. Finally, the events with *at least* three pre-selected leptons are considered in the fake estimation procedure.

For example, two different events may enter the method, one with three pre-selected leptons $e^+e^-\mu^+$ with configuration TLL and another with four pre-selected leptons $e^+e^-e^+\mu^+$ with configuration $TTLL$. The output would be then:

Input	**Output**			
$e^+e^-\mu^+$, TLL	$\cdots$	$\cdots$		
	TTL	w_{TTL}	$e_T^+e_T^-\mu_L^+$	Fails selections
	TLT	w_{TLT}	$e_T^+e_L^-\mu_T^+$	Fails selections
	LTT	w_{LTT}	$e_L^+e_T^-\mu_T^+$	Fails selections
	TTT	w_{TTT}	$e_T^+e_T^-\mu_T^+$	Exactly 3ℓ with 1SFOS
$e^+e^-e^+\mu^+$, $TTLL$	$\cdots$	$\cdots$		
	$TLTL$	w_{TLTL}	$e_T^+e_L^-e_T^+\mu_L^+$	Fails selections
	$TTTL$	w_{TTTL}	$e_T^+e_T^-e_T^+\mu_L^+$	Exactly 3ℓ with 2SFOS
	$TTLT$	w_{TTLT}	$e_T^+e_T^-e_L^+\mu_T^+$	Exactly 3ℓ with 1SFOS
	$TLTT$	w_{TLTT}	$e_T^+e_L^-e_T^+\mu_T^+$	Exactly 3ℓ with 0SFOS
	$LTTT$	w_{LTTT}	$e_L^+e_T^-e_T^+\mu_T^+$	Exactly 3ℓ with 1SFOS
	$TTTT$	w_{TTTT}	$e_T^+e_T^-e_T^+\mu_T^+$	Fails selections

If one presumes that additional requirements are satisfied, only one of all possible combinations passes the selection cuts in the first event while four combinations are selected in the second event. Each of these "subevents" falls into a specific channel according to the number of same-flavour opposite-sign (SFOS) pairs.

To propagate uncertainties on the prompt and fake efficiencies to the final estimate of the fake lepton background, the derivatives of $t'_{\nu_1 \cdots \nu_n}$ with respect to ε_i and ζ_i for each lepton i need to be calculated. This can be done exactly and efficiently at runtime. Correlations between the prompt efficiencies measured in different p_{T} bins are neglected as the uncertainty on the measurement is small. Correlations between the fake efficiencies binned in p_{T} are preserved by propagating the systematic variation for each bin separately.

3.5.3.2 Prompt Lepton Efficiency

The efficiencies for prompt pre-selected leptons to pass the tight requirements are measured in data samples enriched in prompt leptons. The measurement is performed with the tag-and-probe method applied to the leptons from $Z \to e^{\pm}e^{\mp}$ and $Z \to \mu^{\pm}\mu^{\mp}$ decays. The tag is required to pass all signal lepton selections and to be trigger matched, while the requirement imposed to the probe is to satisfy the pre-selection criteria and to be inside the invariant mass window $m_{\ell\ell} \in [80, 100]$ GeV. In order to avoid any systematic bias in the choice of the tag, each lepton is alternatively considered as a possible tag and the other as a probe. The invariant mass distributions of two same-flavour opposite-sign leptons, illustrated in Figure 3.10, demonstrate that most of the pre-selected leptons are also prompt in these control regions.

Figure 3.11 shows the probe lepton p_{T} distributions which are used to derive the prompt lepton efficiencies ε. These are binned in p_{T} and calculated separately for electrons and muons as the following ratio:

$$\varepsilon = \frac{N_T^{\mathrm{Data}}}{N^{\mathrm{Data}}} \tag{3.23}$$

where N^{Data} is the total number of data events in a control region and N_T^{Data} denotes its fraction with the probe lepton passing also the tight requirements.

Two sources of systematic uncertainties are taken into account. First, the measurement is performed in Drell-Yan data without any specific treatment of the other backgrounds. Instead, the prompt efficiency is calculated in both data and MC samples and their difference is taken as a systematic uncertainty on the nominal estimate from data. This approach is rather conservative since it includes also the difference between the efficiencies from data and simulation. However, the uncertainty on the fake lepton estimate is dominated by the uncertainty on the fake efficiencies. Secondly, the measurement may be affected by the choice of a 20 GeV Z boson mass window. Therefore, it has been varied by 5 GeV. The final effect has been proved to be negligible. The final prompt rates measured in Drell-Yan events and MC events are shown in Figure 3.9 and are summarized in Table 3.10 for electrons and in Table 3.11 for muons.

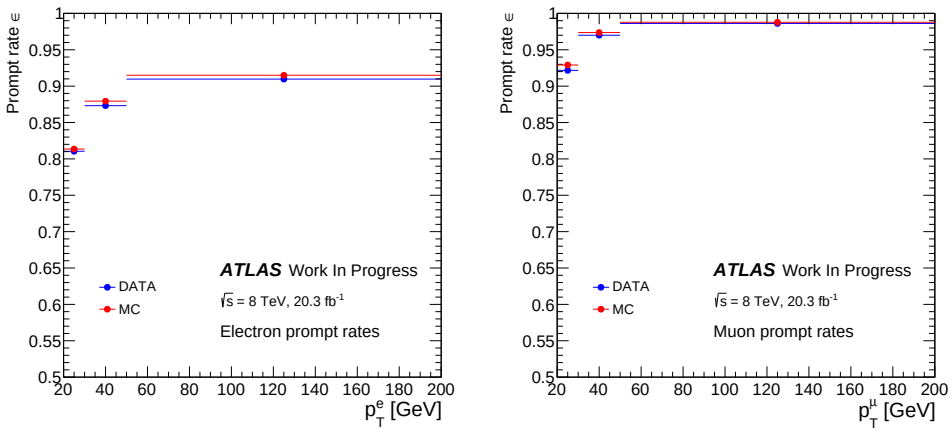

Figure 3.9: Real lepton efficiency as a function of p_{T} measured in data (blue) and MC (red) for electrons (left) and muons (right).

p_T/GeV		[20, 30]	[30, 50]	> 50
Data	ε	0.811	0.873	0.910
	σ_{stat}	0.001	0.001	0.001
MC	ε	0.813	0.879	0.915
	σ_{stat}	0.001	0.001	0.001
σ_{syst}		0.003	0.006	0.005

Table 3.10: Prompt efficiencies for electrons including statistical and systematic uncertainties. The systematic uncertainty is calculated as the difference between the efficiencies measured in data and MC samples. The efficiency from data is used as the nominal central value.

p_T/GeV		[20, 30]	[30, 50]	> 50
Data	ε	0.922	0.970	0.986
	σ_{stat}	0.001	0.001	0.001
MC	ε	0.929	0.974	0.988
	σ_{stat}	0.001	0.001	0.001
σ_{syst}		0.007	0.004	0.002

Table 3.11: Prompt efficiencies for muons including statistical and systematic uncertainties. The systematic uncertainty is calculated as the difference between the efficiencies measured in data and MC samples. The efficiency from data is used as the nominal central value.

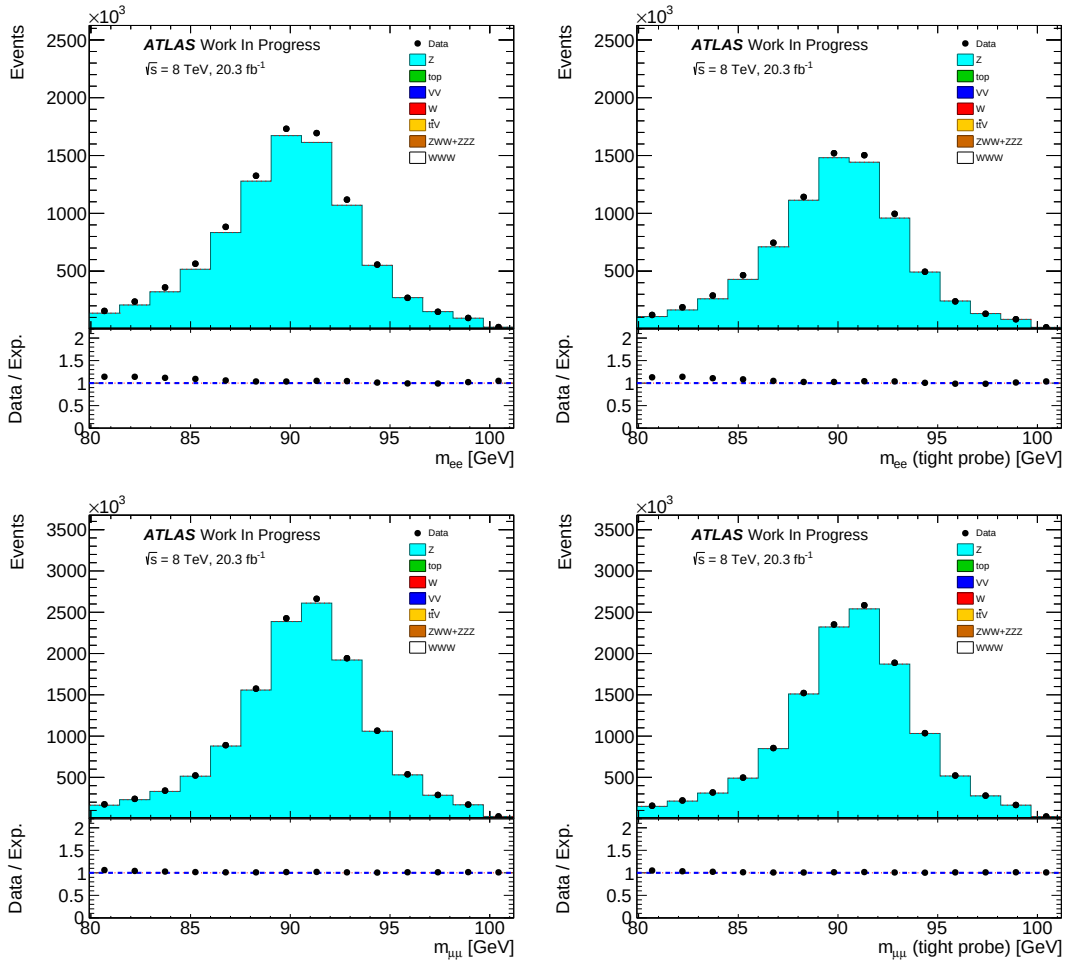

Figure 3.10: Invariant mass distribution of two same-flavour opposite-sign electrons (top) and muons (bottom) with at least one tag lepton. The control regions are shown without any additional requirement on the probe leptons (left) and with the probe leptons that pass the signal requirements (right).

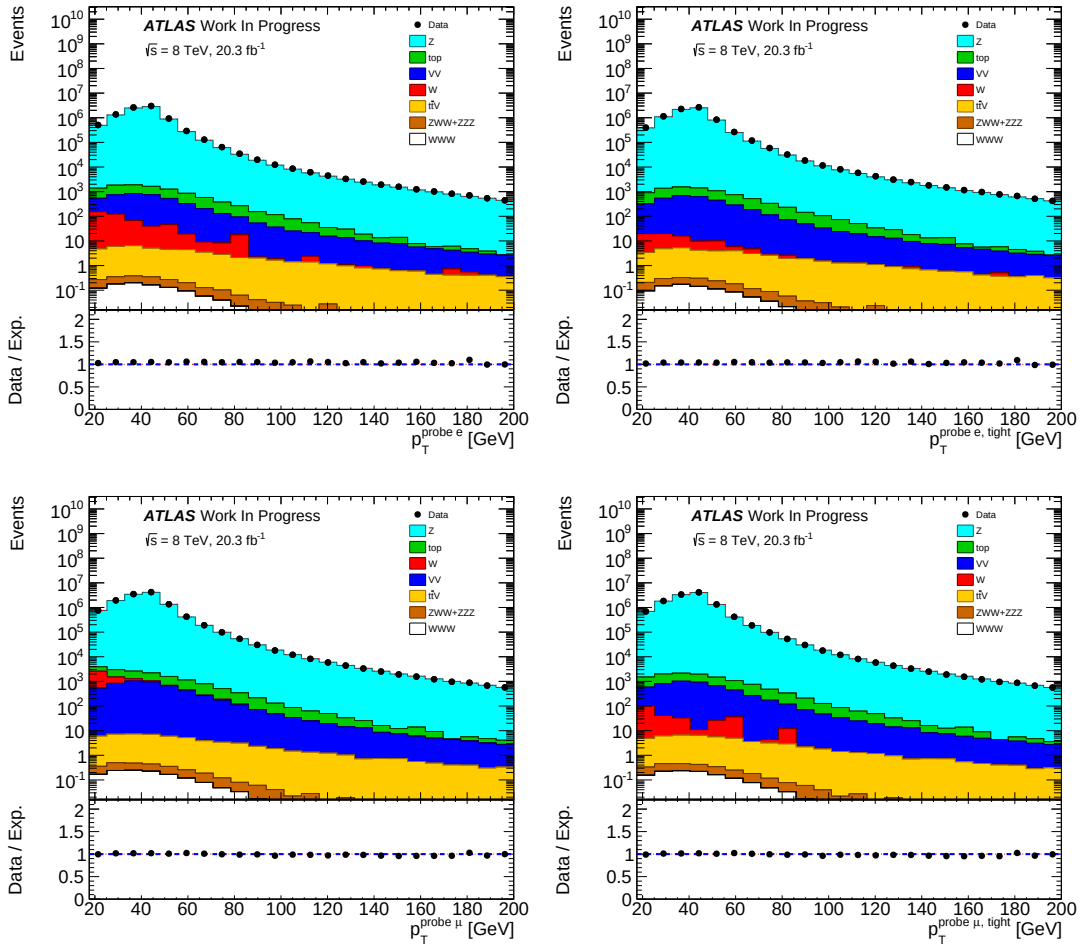

Figure 3.11: Probe lepton p_{T} distributions in the control regions used to derive electron (top) and muon (bottom) prompt efficiencies. Probe leptons pass the baseline lepton pre-selections (left) and the signal lepton selections (right).

3.5.3.3 Fake Lepton Efficiency

The fake efficiency represents the probability that a fake lepton passes the tight requirements. The measurement is performed in fake-enriched dilepton samples containing one signal lepton with $p_{\mathrm{T}} > 40$ GeV and one fake lepton candidate with $p_{\mathrm{T}} > 20$ GeV that satisfies the pre-selection criteria. Events with an additional pre-selected lepton with $p_{\mathrm{T}} > 10$ GeV and $E_{\mathrm{T}}^{\mathrm{miss}} < 10$ GeV are vetoed to reject diboson and QCD events. The contamination from processes with two prompt leptons in the final state, such as $t\bar{t}$, WW and Z, is reduced by selecting only events with same-sign leptons. The control regions are split based on the lepton flavour of the fake candidate as the efficiencies depend on its origin. Both regions use an isolated high-p_{T} muon as a prompt tag. This choice is motivated by the dominant contribution of the Z boson background in the $e^{\pm}e^{\pm}$ region due to electron charge mis-identification. Therefore, the electron efficiencies are determined in the $\mu^{\pm}e^{\pm}$ region and the muon efficiencies in the $\mu^{\pm}\mu^{\pm}$ region. Since the fake efficiencies are sensitive to the heavy-flavour content of the event, both control regions are further divided according to the presence of a b-tagged jet. The regions with at least one b-tagged jet ($N_{b\text{-jet}} > 0$) are used for the nominal value of the efficiencies since they contain more heavy-flavour contributions and thus better approximate the signal regions, as described later in Section 3.5.3.4.

The distributions of probe electron and probe muon transverse momentum are shown in Figures 3.12 and 3.13, respectively. The disagreement between data and MC predictions, especially in the low p_{T} region, is expected because of additional sources of fake leptons not modelled in the MC samples used in the analysis. It can be seen that there is a contamination due to prompt leptons, mostly from diboson production, which needs to be subtracted from the total number of observed data events. Since the fake leptons originating merely from jets are estimated using the data-driven method, the contribution from processes with photon-converted leptons in the final state, mainly from $W\gamma$, have to be corrected using MC. The efficiency, binned in p_{T}, is then determined as:

$$\zeta = \frac{N_T^{\mathrm{Data}} - N_T^{\mathrm{Prompt}} - N_T^{\mathrm{PC}}}{N^{\mathrm{Data}} - N^{\mathrm{Prompt}} - N^{\mathrm{PC}}} \tag{3.24}$$

where N^{Data} represents the number of events measured in data. The events from the MC samples with prompt and photon-converted leptons are denoted as N^{Prompt} and N^{PC}, respectively. The classification of leptons is performed at the truth level using the `MCTruthClassifier` tool [198]. The subscript T indicates events with a tight probe. Figures 3.14 and 3.15 illustrate the fraction of events which is subtracted from the control regions when calculating the efficiencies.

Three systematic effects contribute, together with the statistical uncertainty, to the overall uncertainty. Firstly, the subtraction of the events with two prompt leptons using the MC prediction introduces an uncertainty from the cross-sections of diboson and $t\bar{t}V$ processes. This effect is evaluated by varying their normalization by 20% and is fully correlated among different p_{T} bins. Secondly, given that the control and signal regions have different kinematic selections, a corresponding uncertainty is applied. The kinematic dependence is estimated by modifying the requirements in the dilepton control regions used for the fake efficiency measurement. In particular, the thresholds on $E_{\text{T}}^{\text{miss}}$ and tag lepton p_{T} are varied one by one in 5 GeV steps scanning a range of $\pm$10 GeV and $\pm$20 GeV around the nominal values, respectively. This is referred to as the uncorrelated uncertainty. The uncorrelated and correlated sources of uncertainty are then determined separately for electrons and muons on an event-by-event basis and combined by adding in quadrature. The third systematic contribution comes from the choice of the control region based on the number of b-tagged jets, as described earlier. The difference between the nominal efficiencies derived from the region with at least one b-tagged jet and the efficiencies from the region where no requirement is placed on the b-jet content, is chosen as a systematic error. This is motivated by the different fake lepton composition in the control and signal regions, as discussed in more detail in Section 3.5.3.4. The efficiencies depend on the fake lepton origin and thus their extrapolation may systematically affect the final estimate. The assigned uncertainty adequately covers this difference.

The fake efficiencies, along with the statistical and systematic uncertainties, are summarized in Figure 3.16 as well as in Tables 3.12 and 3.13. The final p_{T} binning is chosen to be coarse enough to have good statistics while also preserving the shape information as a function of p_{T}.

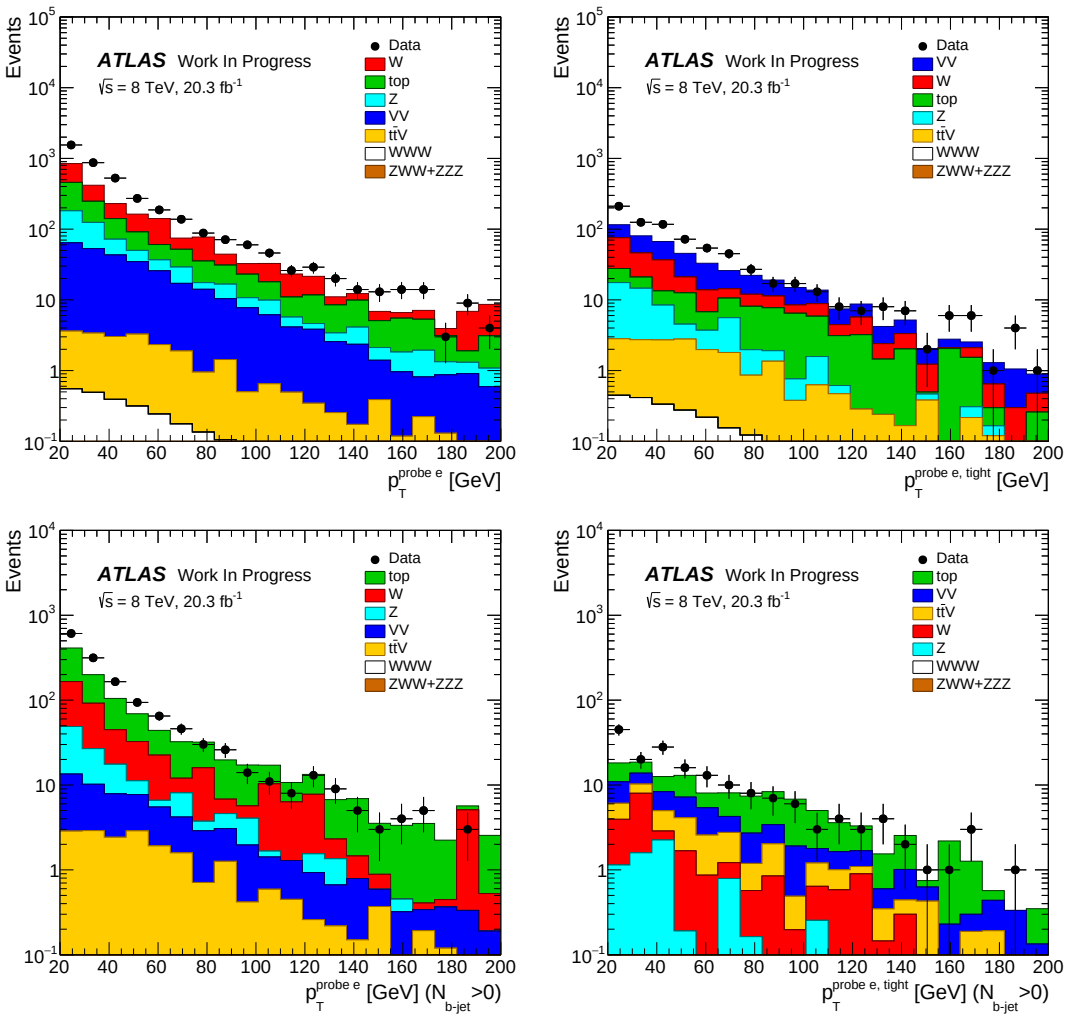

Figure 3.12: Transverse momentum distributions of tight probe electron (right) and all probe electrons (left) passing the pre-selection criteria in the $\mu^{\pm}e^{\pm}$ control region without any additional requirement on the b-jets in the event (top) and with at least one b-jet (bottom). The difference between the data and MC prediction does not affect the data-driven fake estimate.

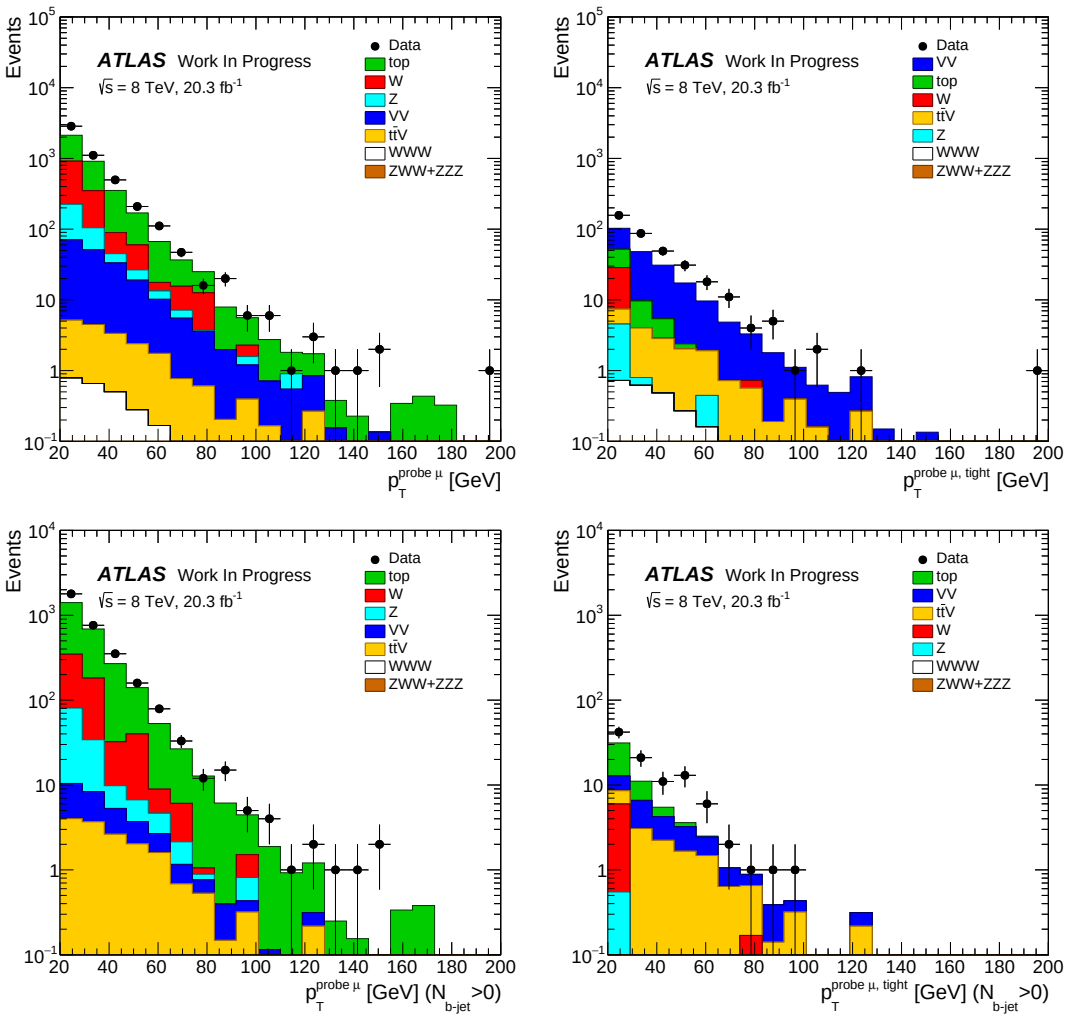

Figure 3.13: Transverse momentum distributions of tight probe muon (right) and all probe muons (left) passing the pre-selection criteria in the $\mu^{\pm}\mu^{\pm}$ control region without any additional requirement on the b-jets in the event (top) and with at least one b-jet (bottom). The difference between the data and MC prediction does not affect the data-driven fake estimate.

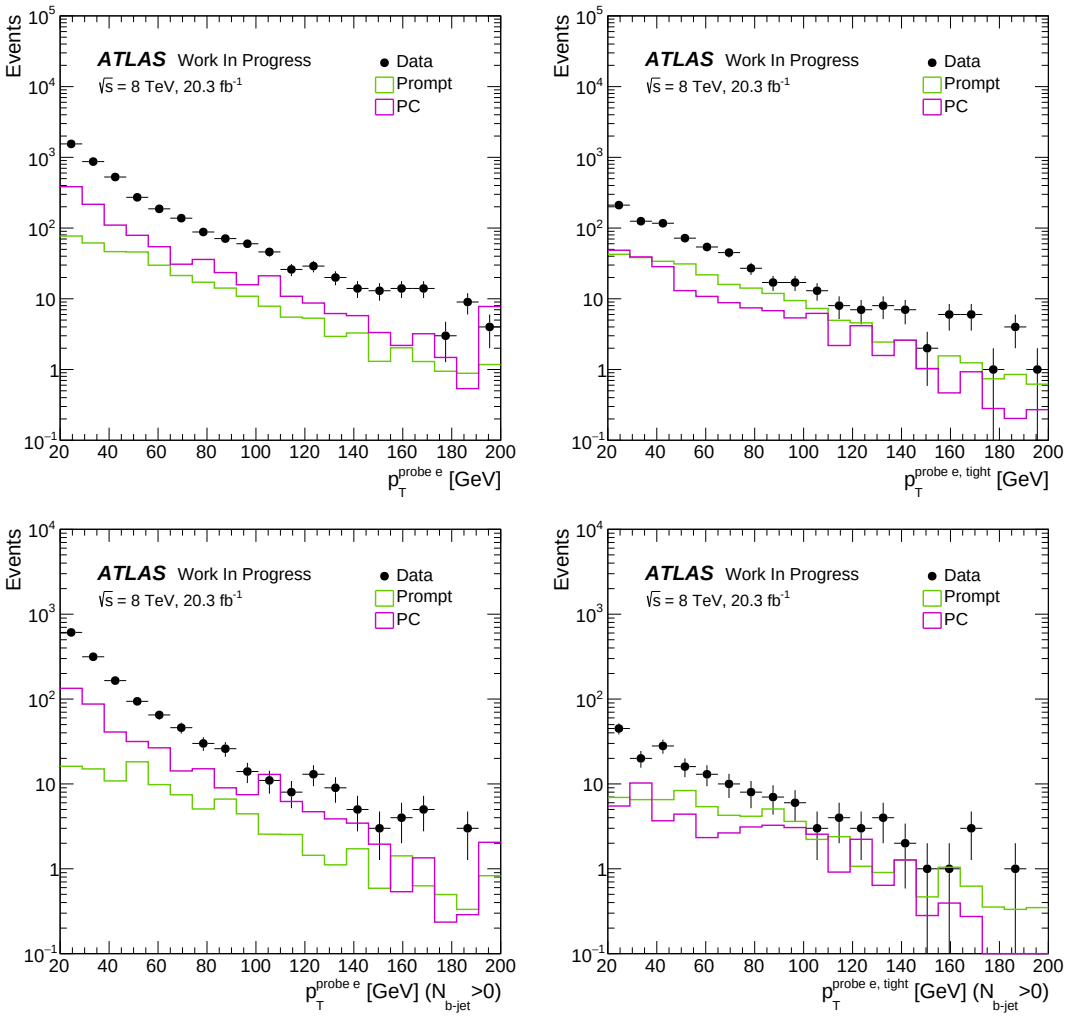

Figure 3.14: Transverse momentum distributions of tight probe electron (right) and all probe electrons (left) passing the pre-selection criteria in the $\mu^{\pm}e^{\pm}$ control region without any additional requirement on the b-jets in the event (top) and with at least one b-jet (bottom). The data yield (black points) corresponds to N^{Data} (left) and N_T^{Data} (right) in Equation 5.6. The prompt (green) and photon conversion (violet) contributions determined from the MC samples are shown separately without being stacked. The prompt lepton contribution corresponds to N^{Prompt} (left) and N_T^{Prompt} (right) and the photon conversion contribution to N^{PC} (left) and N_T^{PC} (right) in Equation 5.6.

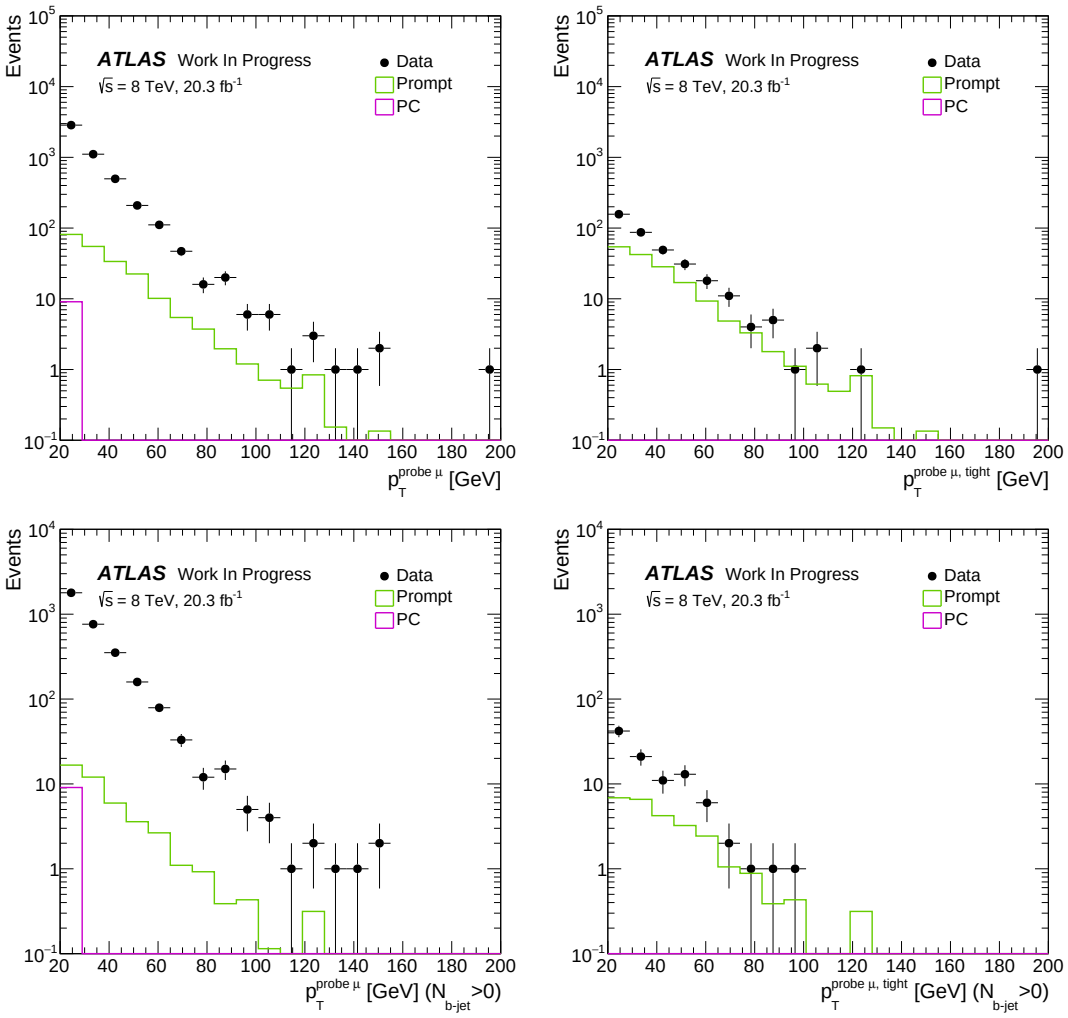

Figure 3.15: Transverse momentum distributions of tight probe muon (right) and all probe muons (left) passing the pre-selection criteria in the $\mu^{\pm}\mu^{\pm}$ control region without any additional requirement on the b-jets in the event (top) and with at least one b-jet (bottom). The data yield (black points) corresponds to N^{Data} (left) and N_T^{Data} (right) in Equation 5.6. The prompt (green) and photon conversion (violet) contributions determined from the MC samples are shown separately without being stacked. The prompt lepton contribution corresponds to N^{Prompt} (left) and N_T^{Prompt} (right) and the photon conversion contribution to N^{PC} (left) and N_T^{PC} (right) in Equation 5.6. The latter is negligible.

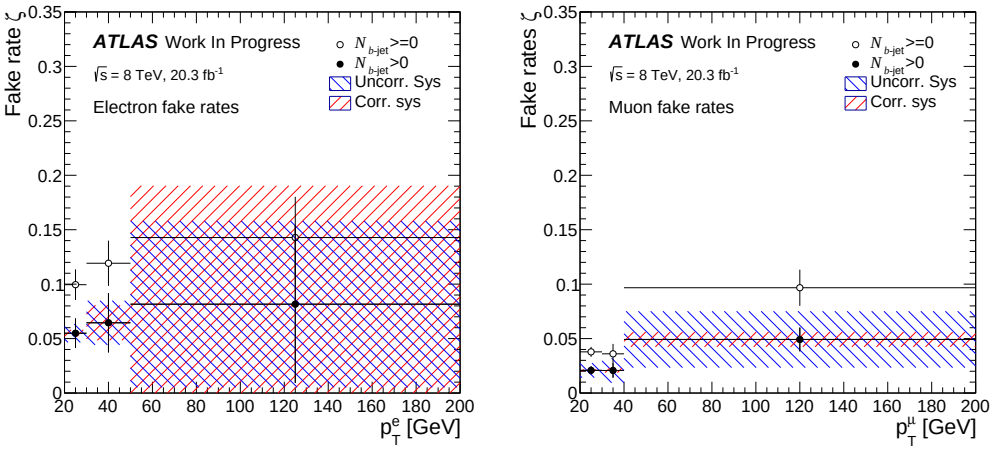

Figure 3.16: Electron (left) and muon (right) fake efficiencies as a function of p_{T} extracted from two control regions: with at least one b-jet and without any additional requirement on b-jets in the event.

$\boldsymbol{p_{\mathrm{T}}}$**/GeV**		**[20, 30]**	**[30, 50]**	**> 50**
$N_{b\text{-jet}} > 0$	ζ	0.055	0.065	0.082
	σ_{stat}	0.014	0.027	0.072
	$\sigma_{\mathrm{syst}}^{\mathrm{uncorr}}$	0.008	0.020	0.076
	$\sigma_{\mathrm{syst}}^{\mathrm{corr}}$	0.003	0.016	0.109
$N_{b\text{-jet}} \geq 0$	ζ	0.100	0.119	0.143
	σ_{stat}	0.014	0.021	0.037
	$\sigma_{\mathrm{syst}}^{\mathrm{uncorr}}$	0.027	0.032	0.043
	$\sigma_{\mathrm{syst}}^{\mathrm{corr}}$	0.010	0.023	0.067
$\sigma_{\mathrm{syst}}^{b\text{-jet selection}}$		0.045	0.055	0.061

Table 3.12: Fake efficiencies for electrons measured in two control regions: with at least one b-jet in a event and with no additional requirement on the presence of b-tagged jets. Statistical, correlated and uncorrelated systematic uncertainties are shown. The systematic uncertainty due to the b-jet selection is calculated as the difference between the efficiencies in the two regions. The efficiency from the control region with at least one b-jet is used as the nominal central value.

p_T/GeV		[20, 30]	[30, 50]	> 50
$N_{b\text{-jet}} > 0$	ζ	0.021	0.021	0.049
	σ_{stat}	0.004	0.007	0.011
	$\sigma_{\text{syst}}^{\text{uncorr}}$	0.007	0.011	0.026
	$\sigma_{\text{syst}}^{\text{corr}}$	0.001	0.002	0.007
$N_{b\text{-jet}} \geq 0$	ζ	0.038	0.036	0.097
	σ_{stat}	0.005	0.009	0.017
	$\sigma_{\text{syst}}^{\text{uncorr}}$	0.014	0.010	0.025
	$\sigma_{\text{syst}}^{\text{corr}}$	0.004	0.009	0.024
$\sigma_{\text{syst}}^{b\text{-jet selection}}$		0.017	0.015	0.048

Table 3.13: Fake efficiencies for muons measured in two control regions: with at least one b-jet in a event and with no additional requirement on the presence of b-tagged jets. Statistical, correlated and uncorrelated systematic uncertainties are shown. The systematic uncertainty due to the b-jet selection is calculated as the difference between the efficiencies in the two regions. The efficiency from the control region with at least one b-jet is used as the nominal central value.

3.5.3.4 Fake Lepton Composition

The generalised matrix method relies on the assumption that the fake efficiencies derived in the dilepton control regions can be extrapolated to the three lepton signal regions. The efficiencies depend primarily on the sources of the fake leptons which may be light-flavour jets, heavy-flavour jets or photon conversions. The validity of this assumption can be checked by comparing the composition of fake leptons in these regions using MC simulations. Since the contribution from photon converted leptons is estimated from MC samples, only the ratio of the fake leptons from heavy and light-flavour jets is of interest in this study.

The origin of fake electrons in the $\mu^{\pm}e^{\pm}$ control regions, in the pre-selection region and in the regions close to the signal regions is shown in Table 3.14. The composition is mostly dominated by the electrons from heavy-flavour jets (50% to 80%). Table 3.15 summarizes the source of fake muon candidates in the $\mu^{\pm}\mu^{\pm}$ control regions, the pre-selection region and the regions close to the signal regions. The majority of fake muons comes also from heavy-flavour jets (80% to 95%). The

differences in the composition between the inclusive b-jet ($N_{b-\text{jet}} \geq 0$) and the b-jet tagged ($N_{b-\text{jet}} > 0$) dilepton control regions are observed to be of a similar size to the differences in the composition between the regions close to the signal regions for both the electron and muon. Therefore, the systematic uncertainty estimated by comparing the two efficiencies covers any remaining differences in the composition. Moreover, the nominal efficiencies are taken from the region with at least one b-jet as its fraction of leptons coming from heavy-flavour jets better corresponds to the composition in the 0SFOS region which is dominated by the fake background.

Figure 3.17 and 3.18 show the stacked MC estimates from prompt and photon converted leptons as well as the leptons from heavy-flavour and light-flavour jets. It can be seen that while the probe electrons are dominated by photon conversions, the probe muons consist mainly of heavy-flavour jets. Since the the MC samples do not contain all the sources of fake leptons, a large uncertainty is effectively assigned to the composition estimates in this study. These additional processes are dominated by the QCD background, where the contribution from the photon conversions is assumed to be small. Therefore, the computation of fake efficiencies using Equation 5.6 is not affected.

Region	**HF**	**LF**
CR $N_{b\text{-jet}} > 0$	$75 \pm 5\%$	$25 \pm 3\%$
CR $N_{b\text{-jet}} \geq 0$	$57 \pm 4\%$	$43 \pm 6\%$
Pre-selection	$53.7 \pm 9.4\%$	$46.3 \pm 10.0\%$
0SFOS	$80.2 \pm 19.9\%$	$19.8 \pm 11.8\%$
1SFOS	$52.4 \pm 12.5\%$	$47.6 \pm 11.9\%$
2SFOS	$47.7 \pm 16.1\%$	$52.3 \pm 23.3\%$

Table 3.14: Composition of fake electrons taken from MC events in the $\mu^{\pm}e^{\pm}$ control regions used to extract electron fake efficiencies, in the pre-selection region as well as in the regions close to the signal regions. The composition is split as either Heavy-Flavour (HF) or Light-Flavour (LF).

Region	**HF**	**LF**
CR $N_{b\text{-jet}} > 0$	$95 \pm 3\%$	$4 \pm 1\%$
CR $N_{b\text{-jet}} \geq 0$	$89 \pm 4\%$	$11 \pm 1\%$
Pre-selection	$78.9 \pm 10.0\%$	$21.1 \pm 4.6\%$
0SFOS	$96.7 \pm 21.0\%$	$3.3 \pm 3.7\%$
1SFOS	$77.4 \pm 14.1\%$	$22.6 \pm 7.2\%$
2SFOS	$77.3 \pm 15.9\%$	$22.8 \pm 7.1\%$

Table 3.15: Composition of fake muons taken from MC events in the $\mu^{\pm}\mu^{\pm}$ control regions used to extract muon fake efficiencies, in the pre-selection region as well as in the regions close to the signal regions. The composition is split as either Heavy-Flavour (HF) or Light-Flavour (LF).

3.5.3.5 Closure Test

The ability of the generalised matrix method to estimate the fake lepton background is verified using a so called closure test. The fake efficiencies are computed from MC samples whose contribution is the most important after the event pre-selection requirements: Z+jets and $t\bar{t}$. To increase the statistics in the tested samples, the lepton p_{T} threshold is lowered to 10 GeV. Since the dilepton control regions are obviously not appropriate for this purpose, control regions with two signal muons/electrons and one pre-selected electron/muon are defined. In addition, the transverse momentum of tight leptons is required to be larger than 15 GeV and $E_{\mathrm{T}}^{\mathrm{miss}} > 10$ GeV. Figure 3.19 shows the fake efficiencies obtained from the MC yields in these control regions. The agreement between the pre-selected MC events and the MC events reweighted using the generalised matrix method is illustrated in Figure 3.20. It can be seen that the shape agreement as well as the overall normalization are very good in both the third lepton p_{T} and $E_{\mathrm{T}}^{\mathrm{miss}}$ distributions. This demonstrates that the matrix method is performing well.

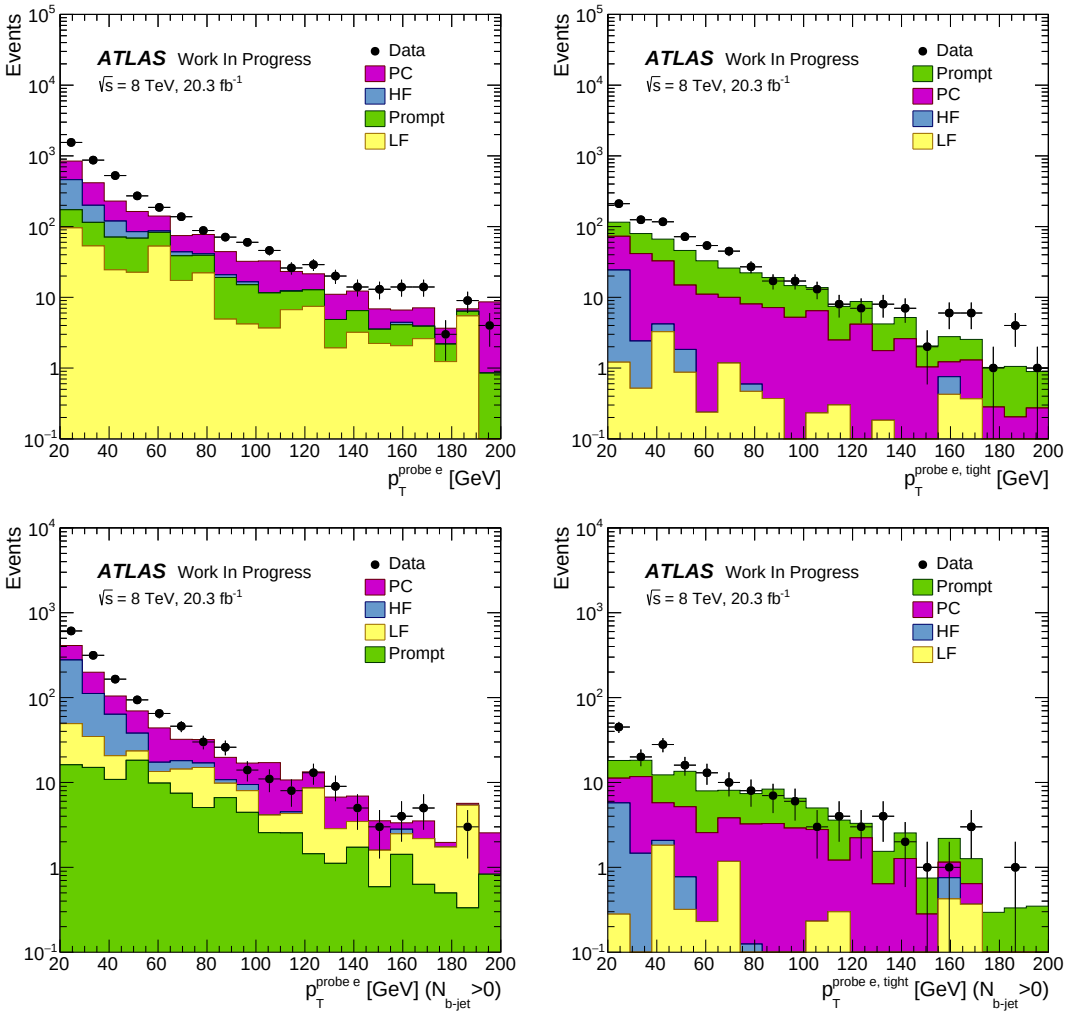

Figure 3.17: Transverse momentum distributions of tight probe electron (right) and all probe electrons (left) passing the pre-selection criteria in the $\mu^{\pm}e^{\pm}$ control region without any additional requirement on the b-jets in the event (top) and with at least one b-jet (bottom). The contributions with the probe electron coming from Z or W decay (green), photon conversion (violet), heavy-flavour jet (blue) and light-flavour jet (yellow) are shown stacked on top of each other and determined from MC samples.

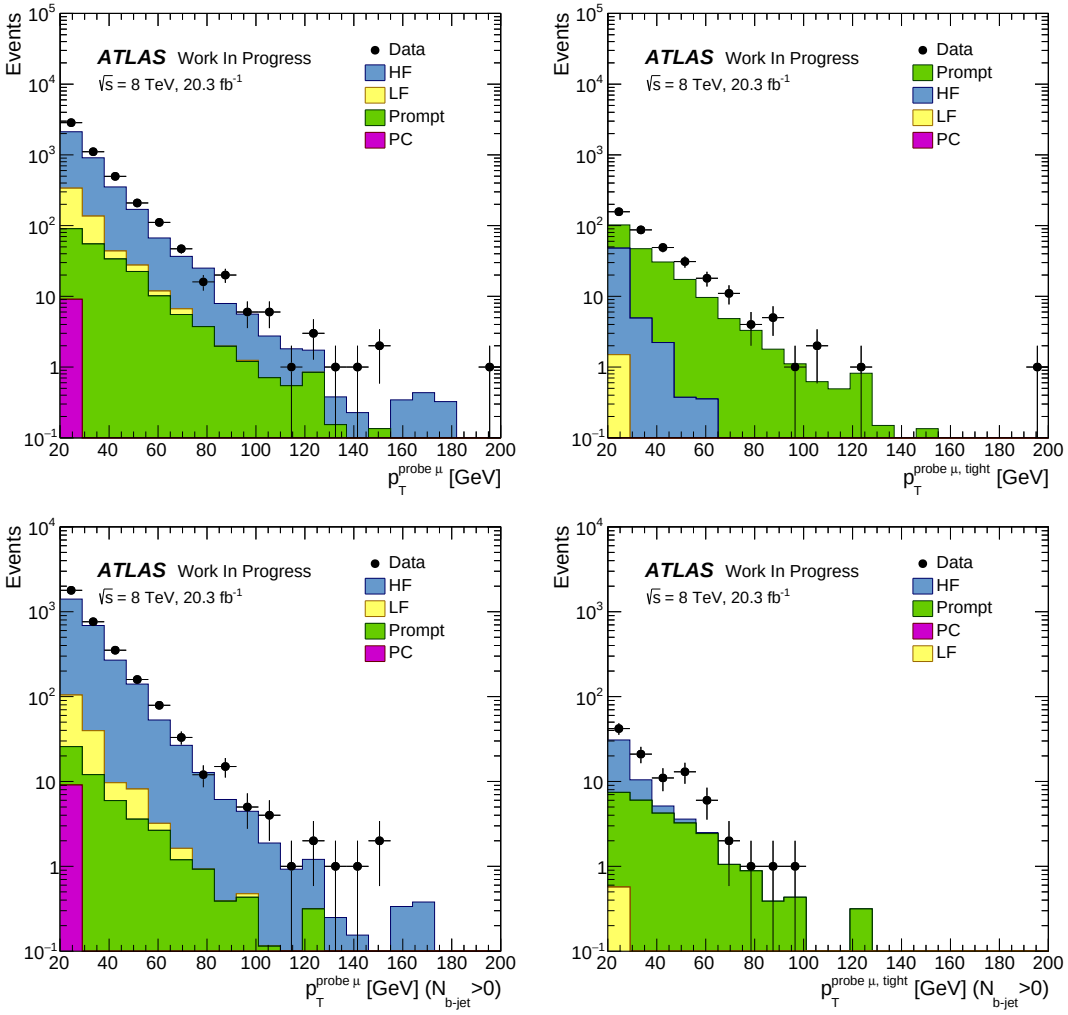

Figure 3.18: Transverse momentum distributions of tight probe muon (right) and all probe muons (left) passing the pre-selection criteria in the $\mu^{\pm}\mu^{\pm}$ control region without any additional requirement on the b-jets in the event (top) and with at least one b-jet (bottom). The contributions with the probe muon coming from Z or W decay (green), photon conversion (violet), heavy-flavour jet (blue) and light-flavour jet (yellow) are shown stacked on top of each other and determined from MC samples.

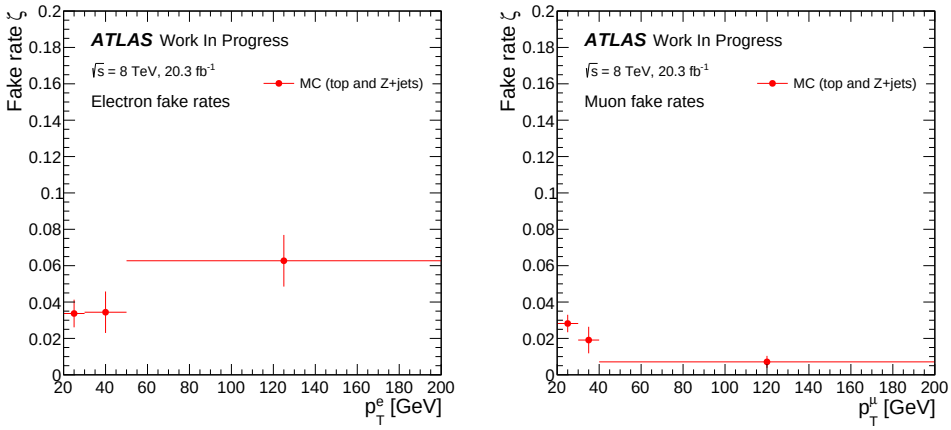

Figure 3.19: Fake efficiencies for electrons (left) and muons (right) obtained from MC samples in the control regions with three leptons. The errors are statistical only. These efficiencies are used to perform a MC closure check of the generalised matrix method.

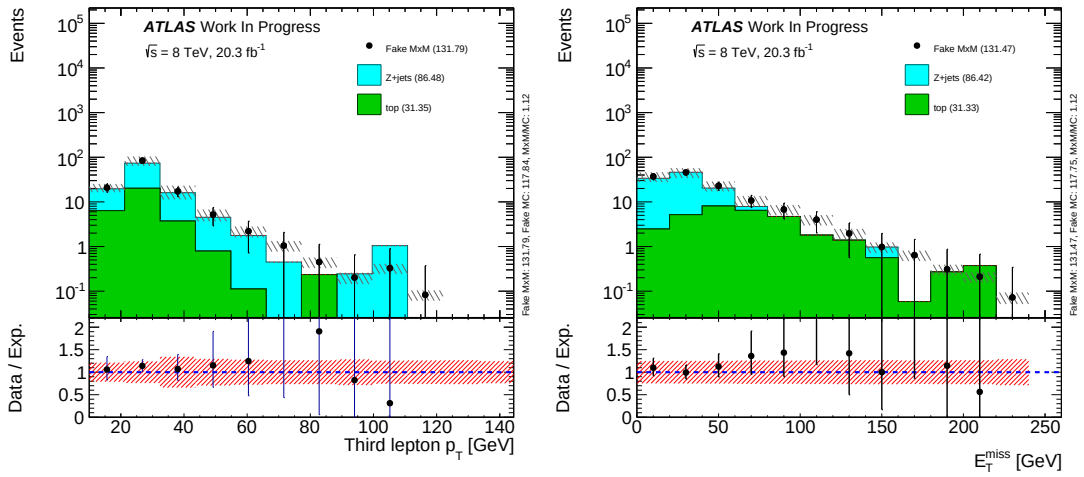

Figure 3.20: Distributions of the third lepton p_{T} (left) and $E_{\mathrm{T}}^{\mathrm{miss}}$ (right) in the event pre-selection region. The Z+jets and $t\bar{t}$ events are compared to the events from these samples reweigthed using the generalised matrix method and the efficiencies shown in Figure 3.19. The hashed band represents the systematic uncertainties purely from the fake estimate. Good agreement is observed.

3.5.4 Validation of Background Estimates

Three validation regions are designed in this analysis to verify the background modelling. Each region is defined to be enriched in events from the targeted background process whilst being kinematically close to the signal regions. Moreover, a negligible contribution from the signal events is required. The final predictions are compared to the data in Table 3.16.

Validation Region	**Signal**	**Background**	**Observed**
Pre-selection	$9.78 \pm 0.04 \pm 0.45$	$2388 \pm 7 \pm 298$	2472
$Z\gamma$	$0.32 \pm 0.01 \pm 0.02$	$119 \pm 3 \pm 20$	119
Fake lepton	$0.15 \pm 0.01 \pm 0.02$	$15 \pm 1 \pm 10$	18

Table 3.16: Expected signal and background yields in the validation regions compared to the number of events observed in data. Statistical and systematic uncertainties are shown.

The first validation region tests the modelling of the WZ background at the pre-selection level, defined in Section 3.4.1. Even though it includes the three signal regions, the signal contamination is less than 1%. Various kinematic distributions with a WZ purity of about 70% are shown in Figure 3.21. The description of the $Z\gamma$ process is tested in a region with a purity around 70%. The presence of only $\mu^+\mu^- e^\pm$ events where the three-lepton invariant mass is within 15 GeV of the Z-mass is required. The $m_{\ell\ell\ell}$ distribution as well as the distribution of the electron η are shown at the top of Figure 3.22. Good agreement between the data and the background expectations suggests that the photon conversion mechanism is well modelled. The performance of the fake lepton background estimate is also validated. Pre-selected events are required to contain no SFOS lepton pair in order to reduce the WZ background and at least one b-jet in order to be orthogonal to the 0SFOS signal region. The purity reaches up to 80% but the region is limited by the available statistics. The distributions of the jet multiplicity and $E_{\mathrm{T}}^{\mathrm{miss}}$ are shown at the bottom of Figure 3.22. The normalization as well as the shape of the observed and predicted distributions are in good agreement.

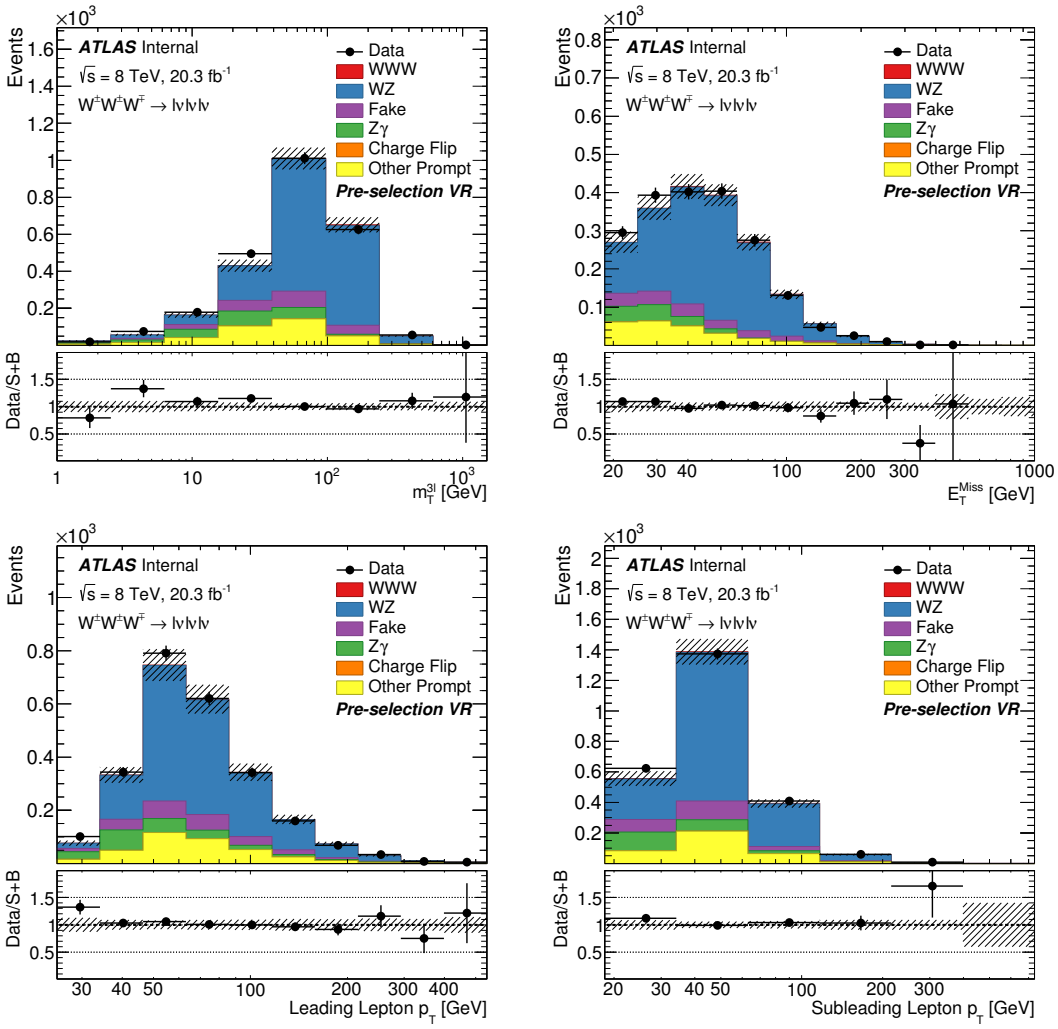

Figure 3.21: The observed data is compared to the signal plus background model in the pre-selection validation region as a function of $m_{\mathrm{T}}^{3\ell}$ (top left), $E_{\mathrm{T}}^{\mathrm{miss}}$ (top right), the leading lepton p_{T} (bottom left) and the subleading lepton p_{T} (bottom left). The error bars on the black points represent the statistical uncertainty on the data. The hashed area represents the total systematic uncertainties on the signal plus background model. The last bin includes the overflow.

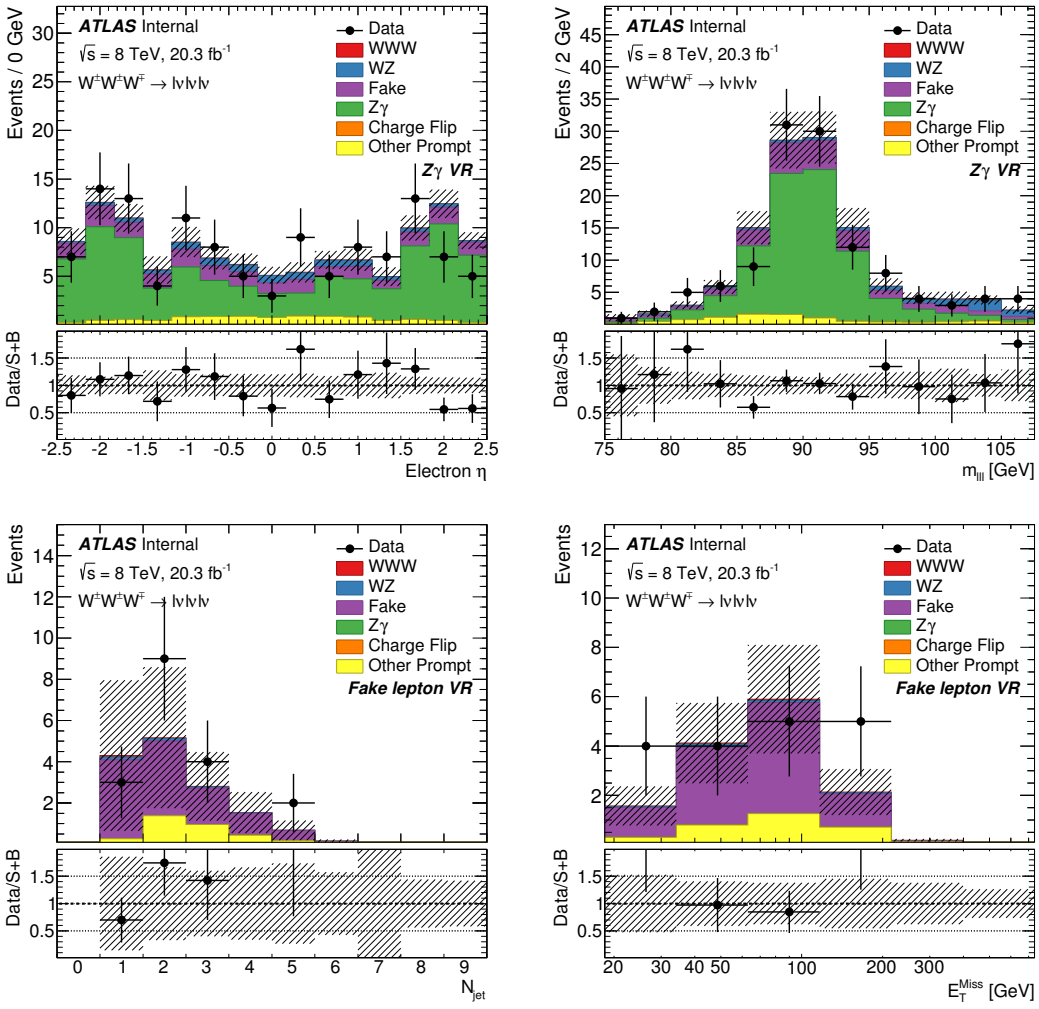

Figure 3.22: The observed data is compared to the signal plus background model in the $Z\gamma$ validation region as a function of the electron η (top left) and the three lepton invariant mass $m_{\ell\ell\ell}$ (top right), and in the fake lepton validation region as a function of the jet multiplicity N_{jet} (bottom left) and $E_{\text{T}}^{\text{miss}}$ (bottom right). The error bars on the black points represent the statistical uncertainty on the data. The hashed area represents the total systematic uncertainties on the signal plus background model. The last bin includes the overflow.

3.6 Systematic Uncertainties

Various systematic uncertainties, either from theoretical or experimental sources, affect the number of expected signal and background events. The *theoretical* uncertainties are related to the normalization of the signal and background MC cross-sections, while the *experimental* uncertainties arise from the modelling of the detector response, the luminosity measurement and the data-driven methods.

Correlations of the systematic uncertainties are maintained across different channels and between signal and backgrounds within a given channel. They are implemented as nuisance parameters in the profile likelihood fit described in Section 3.8.

A summary of the systematic uncertainties in the total background and signal predictions in each channel is shown in Tables 3.17 and 3.18, respectively. A more detailed breakdown can be found in Appendix B.

3.6.1 Theoretical Uncertainties

The systematic uncertainties assigned to the most important SM background cross-sections are described in Section 3.5.1 and summarized in Table 3.8. Given that the WZ process is the dominant irreducible background in all three signal regions, its relative uncertainty to the total background prediction is the largest, contributing about 2.6% in the 0SFOS channel and 8 - 9% in the other regions. The remaining theoretical uncertainties are mostly negligible in the 1SFOS and 2SFOS regions. In the 0SFOS region, where the WZ contribution is suppressed by charge mis-identification, the normalization uncertainty on the VVV background contributes about 1.4%.

The uncertainties on the SM signal cross-section arise from the choice of the PDF set and the renormalization and factorization scales. The former is determined by comparing three different NLO PDF sets: CT10, MSTW2008 [82] and NNPDF3.0 [84]. The latter is determined by varying each of them independently up or down by a factor of two. Since these are purely theoretical uncertainties, they do not enter the final cross-section extraction directly but serve only for comparison.

3.6.2 Experimental Uncertainties

The systematic uncertainties with the most significant impact on this measurement are of experimental nature. They arise from the identification and reconstruction procedures, imperfect knowledge of the energy scale and resolution of reconstructed objects, the trigger efficiencies, the effects of pile-up, the b-tagging algorithm as well as the luminosity measurement. While these uncertainties affect only the MC simulation-based estimates, other systematic uncertainties take into account limitations in the data-driven background modelling methods. The effect of each systematic uncertainty is estimated by varying the corresponding parameter and taking the relative difference between the nominal number of events and the number of events predicted with the systematic variation.

Lepton Reconstruction

Simulated event samples are corrected for differences with respect to the data in the trigger, reconstruction and identification efficiencies for electrons and muons. Moreover, the electron energy and the muon momentum are smeared in simulated events to account for differences in resolution between data and simulation. These efficiency and correction scale factors have been derived using the tag-and-probe techniques detailed in References [123, 125, 126, 177] and the associated uncertainties are propagated to the measurement on an event-by-event basis. They are specific to each lepton flavour and therefore different for each channel due to the lepton flavour combinatorics discussed in Section 3.4.2. As shown in Tables 3.17 and 3.18, the impact on the final prediction is relatively small.

Jet Reconstruction

The jet energy scale uncertainty is derived from simulation and in-situ measurements [129, 199]. There are several contributions accounting for response uncertainties due to the jet flavour composition, η intercalibration, pile-up corrections and other effects. The uncertainty on the jet energy resolution is determined from a comparison of the resolutions obtained in data and in simulated dijet events [200]. The resulting uncertainties for the jet energy scale and resolution range from 1% to 4% on the signal and background predictions. The efficiency to tag jets containing b-hadrons is corrected in MC events by applying b-tagging

scale factors extracted from $t\bar{t}$ and dijet measurements [201,202]. These scale factors are also applied for jets originating from light quarks that are mis-identified as b-jets [203]. The associated systematic uncertainties affect the analysis due to the b-jet veto requirement in the signal regions. Their contribution is below 1%.

Missing Transverse Energy

The systematic uncertainties associated with the momenta and energies of reconstructed objects are propagated to the $E_{\mathrm{T}}^{\mathrm{miss}}$ calculation. Additional uncertainties arise from low-p_{T} jets and energy deposits not associated with any reconstructed objects [132]. The size of this uncertainty is below 3% for signal and background in all channels.

Source of Uncertainty	**0SFOS %**	**1SFOS %**	**2SFOS %**
Lepton ID, $E_{\mathrm{T}}/p_{\mathrm{T}}$ scale & resolution	0.72	2.56	1.77
$E_{\mathrm{T}}^{\mathrm{miss}}$ scale & resolution	0.81	1.37	2.66
b-jet tagging	0.12	0.31	0.37
Jet E_{T} scale & resolution	1.08	2.61	4.20
Fake lepton background	58.6	12.6	4.35
Charge-flip background	0.45	–	–
Luminosity	0.68	1.66	1.81
Pile-up estimate	0.52	0.20	1.40
Trigger efficiency	0.05	0.09	0.21
WZ, ZZ, $t\bar{t}V$, VVV theory unc.	3.07	8.08	8.86
Statistics	11.0	2.67	2.2
Total uncertainty	59.7	16.8	11.64

Table 3.17: Summary of the systematic uncertainties on the background estimates, shown in percent of the nominal prediction. The individual uncertainties are correlated and therefore do not necessarily add up in quadrature to the total systematic uncertainty.

Pile-up

All the MC samples used in this analysis are reweighted to correctly reproduce the distribution of the vertex multiplicity in data. The accuracy of the average correction factor, introduced in Section 3.2.2, is estimated by varying the pile-up reweighting procedure. The resulting effect is found to be around 1%.

Luminosity

The uncertainty on the integrated luminosity affects the overall normalization of both the signal and background processes estimated using the MC simulation. It is derived to be ±1.9%, following the methodology detailed in [152]. Since some background contributions are estimated using data-driven methods, the luminosity uncertainty on the total background prediction is 0.68% in the 0SFOS channel, 1.66% in the 1SFOS channel and 1.81% in the 2SFOS channel.

Data-driven Background Modelling

The systematic uncertainties assigned to the data-driven modelling of the charge mis-identification and fake lepton backgrounds are described in Sections 3.5.2 and 3.5.3, respectively. The former affects only the prediction in the 0SFOS region and is found to be 0.5%. The latter contributes about 60% on the final background estimate in the 0SFOS channel and therefore represents the most significant uncertainty in this analysis. Due to smaller fake lepton contributions in the 1SFOS and 2SFOS channels, the associated uncertainties are 12% and 5%.

Source of Uncertainty	**0SFOS %**	**1SFOS %**	**2SFOS %**
Lepton ID, $E_{\mathrm{T}}/p_{\mathrm{T}}$ scale & resolution	1.65	1.76	1.35
$E_{\mathrm{T}}^{\mathrm{miss}}$ scale & resolution	1.75	0.85	0.33
b-jet tagging	0.27	0.30	0.30
Jet E_{T} scale & resolution	2.27	2.24	2.14
Fake lepton background	–	–	–
Charge-flip background	–	–	–
Luminosity	1.90	1.90	1.90
Pile-up estimate	0.92	1.30	1.50
Trigger efficiency	0.09	0.09	0.20
Signal theory unc.	5.55	5.55	5.55
Statistics	1.14	1.12	1.70
Total uncertainty	6.90	6.80	6.80

Table 3.18: Summary of the systematic uncertainties on the signal estimates, shown in percent of the nominal prediction. The individual uncertainties are correlated and therefore do not necessarily add up in quadrature to the total systematic uncertainty.

3.7 Results

3.7.1 Event Yields

The optimized signal selection criteria, outlined in Table 4.1, are applied to the data as well as the signal-plus-background model. The expected signal yields are calculated using the fiducial cross-sections from MadGraph, listed in Table 3.7. For each signal region, the signal and background predictions together with their uncertainties are compared to the observed data. These results are presented in Table 3.19 and in Figure 3.23, where the transverse mass distribution of the trilepton system, $m_{\mathrm{T}}^{3\ell} = \sqrt{2p_{\mathrm{T}}^{3\ell}E_{\mathrm{T}}^{\mathrm{miss}}(1-\cos[\Delta\phi(3\ell, E_{\mathrm{T}}^{\mathrm{miss}})])}$, is shown.

	0SFOS	**1SFOS**	**2SFOS**
WZ	$0.59 \pm 0.00 \pm 0.07$	$11.89 \pm 0.14 \pm 1.30$	$9.05 \pm 0.13 \pm 0.98$
Other Prompt	$0.21 \pm 0.01 \pm 0.02$	$0.78 \pm 0.02 \pm 0.11$	$0.60 \pm 0.02 \pm 0.10$
Charge-flip	$0.04 \pm 0.00 \pm 0.01$	–	–
$Z\gamma$	–	$0.20 \pm 0.13 \pm 0.29$	$0.11 \pm 0.10 \pm 0.29$
Fake	$1.51 \pm 0.26 \pm 1.40$	$1.90 \pm 0.34 \pm 1.90$	$0.49 \pm 0.16 \pm 0.47$
Signal	$1.34 \pm 0.02 \pm 0.09$	$1.39 \pm 0.02 \pm 0.09$	$0.61 \pm 0.01 \pm 0.04$
Total Background	$2.35 \pm 0.26 \pm 1.40$	$14.77 \pm 0.39 \pm 2.34$	$10.25 \pm 0.23 \pm 1.20$
Signal + Background	$3.69 \pm 0.26 \pm 1.40$	$16.16 \pm 0.39 \pm 2.31$	$10.86 \pm 0.23 \pm 1.17$
Data	5	13	6
s/b ($s/\sqrt{b}$)	57% (0.87)	9% (0.36)	6% (0.19)

Table 3.19: Summary of the observed data and the expected signal and background yields with statistical and systematic uncertainties for each signal region. "Other Prompt" background includes ZZ, ZWW, ZZZ, $t\bar{t}V$ and DPS production. The systematic uncertainties are quoted as a quadrature sum of all the individual sources only for illustration purpose. They are treated separately in the actual measurement, as discussed in Section 3.8. The last row reports the expected sensitivity for each channel with s (b) denoting the signal (total background) yield. The $s/\sqrt{b}$ ratio represents an approximate formula for the discovery significance, introduced later in Section 3.8.4.

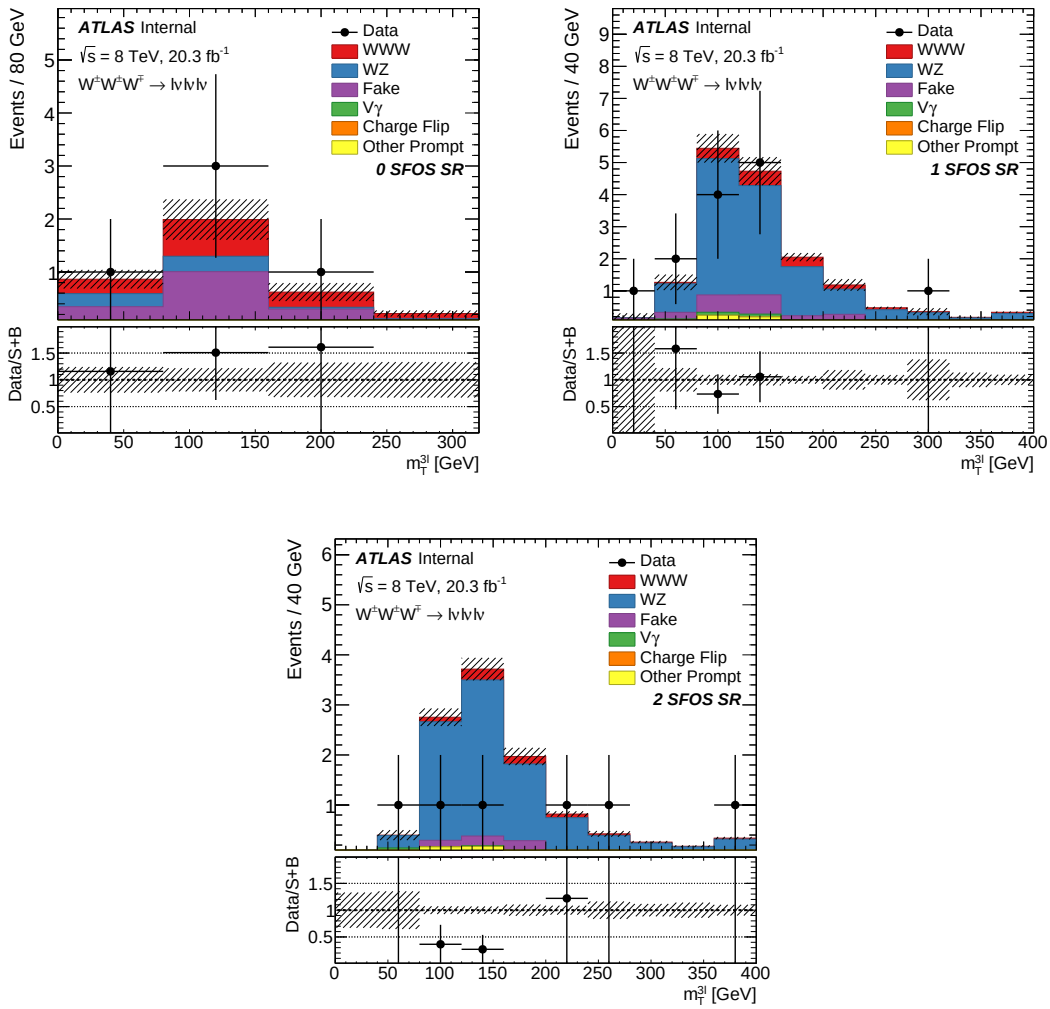

Figure 3.23: Comparison of data with the full background estimate for the distribution of the three lepton transverse mass ($m_{\mathrm{T}}{}^{3\ell}$) in each of the three signal regions: 0SFOS (top left), 1SFOS (top right) and 2SFOS (bottom). The "Other Prompt" background includes ZZ, ZWW, ZZZ, $t\bar{t}V$ and DPS production. The error bars on the black points represent the statistical uncertainty on the data. The statistical and systematic uncertainties on the background prediction are included in the hashed uncertainty band. The last bin of each histogram includes the overflow.

All three channels are statistically dominated. As expected from the s/b and $s/\sqrt{b}$ ratios provided in Table 3.19, the 0SFOS signal region is the most sensitive of the three channels. Events with at least one fake lepton contribute more than 50% to the total background expectation and hence form the major background in this region of the phase space. The sensitivity is also limited by the systematic uncertainty associated with the fake lepton background which reaches 60% of the total background yield. On the other hand, the 1SFOS and 2SFOS signal regions are dominated by the WZ background. While the fake background uncertainty dominates in the 1SFOS channel (13%), the largest systematic uncertainty in the 2SFOS region is the uncertainty on the normalization of the WZ background (10%). A deficit in the data corresponding to 1.3 standard deviations is observed with respect to the signal-plus-background model in the 2SFOS region. After a detailed study of the WZ background modelling, this deviation is found most likely to be a statistical fluctuation.

3.7.2 Correction Factors and Fiducial Cross-sections

In order to measure the fiducial cross-section of the SM WWW process, the number of expected signal events at the reconstruction level s_i^{reco}, listed in Table 3.19, needs to be factorised as a product of the corresponding fiducial cross-section $\sigma_i^{\text{fid SM}}$ and a *correction factor* C_i. The correction factor[1] accounts for differences between the predictions at particle and detector level and is calculated for each channel i as:

$$C_i = \frac{s_i^{\text{reco}}}{s_i^{\text{truth}}} \tag{3.25}$$

where s_i^{truth} is the number of generated signal events in the corresponding fiducial phase space. Both values, s_i^{reco} and s_i^{truth}, are derived from the VBFNLO generator using the selections in Tables 4.1 and 3.6, respectively. In addition, the number of expected fiducial events can be interpreted as a fiducial cross-section using the integrated luminosity $\mathcal{L}$:

[1] The correction factor is sometimes referred to as *detector efficiency*. However, it is not strictly speaking an "efficiency" because it considers also those reconstructed signal events where leptons are not matched to the truth level leptons.

$$s_i^{\text{truth}} = \mathcal{L} \cdot \sigma_i^{\text{fid SM}} \tag{3.26}$$

Here the values are taken from MadGraph since the MadGraph cross-sections are used in the final estimates. Finally, the SM fiducial cross-sections, given by:

$$\sigma_i^{\text{fid SM}} = \frac{s_i^{\text{reco}}}{\mathcal{L} \cdot C_i} \tag{3.27}$$

are summarized in Table 3.20 together with the correction factors.

Channel	$\boldsymbol{\sigma_i^{\text{fid SM}}}$ **[ab]**	$\boldsymbol{C_i}$
0SFOS	123.6 ± 4.7	0.534 ± 0.021
1SFOS	136.9 ± 4.7	0.500 ± 0.018
2SFOS	48.8 ± 2.9	0.615 ± 0.038
Sum	309.2 ± 7.2	–

Table 3.20: Fiducial cross-sections $\sigma_i^{\text{fid SM}}$ for NLO MadGraph samples with the CT10 NLO PDFs and correction factors C_i calculated separately for each signal region. The cross-section is shown also for the sum of all three signal regions. Only statistical uncertainties are quoted.

The sum of the fiducial cross-sections gives the combined fiducial cross-section which, along with PDF and scale uncertainties discussed in Section 3.2.3, is determined to be:

$$\sigma^{\text{fid SM}} = 309 \pm 7(\text{stat.})\, ^{+15}_{-9}(\text{PDF}) \pm 8(\text{scale})\ \text{ab} \tag{3.28}$$

The observed fiducial cross-section is extracted using a likelihood fit described in Section 3.8 based on the following equation:

$$\sigma_i^{\text{fid obs}} = \frac{N_i^{\text{obs}} - b_i}{\mathcal{L} \cdot C_i} \tag{3.29}$$

where N_i^{obs} and b_i are the number of observed events and the estimated number of background events.

3.8 Statistical Interpretation and Measurement

The signal and background expectations with the appropriate uncertainties are summarized, along with the measured data, in Table 3.19. To correctly interpret these results, a complete statistical model needs to be constructed. This section introduces its mathematical representation.

Since there is no discriminant variable in the measurement, it is statistically treated as a multichannel counting experiment. The expected event count in each channel $i \in (0\text{SFOS}, 1\text{SFOS}, 2\text{SFOS})$ is given by:

$$N_i^{\text{exp}}(\mu) = \mu s_i + b_i = \mu s_i + \sum_{j \in \text{Bkg}} b_{ij} \tag{3.30}$$

Here the parameter μ determines the strength of the signal process defined such that $\mu = 0$ corresponds to the background-only hypothesis and $\mu = 1$ is the nominal signal hypothesis. The expectation for the individual background components estimated using either MC simulation or data-driven methods is denoted as b_{ij} with $j \in (WZ$, Other Prompt, Charge-flip, $Z\gamma$ and Fake). The signal event yield[1] in each channel i is given by the integrated luminosity $\mathcal{L}$, the appropriate fiducial cross-section $\sigma_i^{\text{fid SM}}$ and correction factor C_i, as discussed in Section 3.7.2:

$$s_i = \mathcal{L} \cdot \sigma_i^{\text{fid SM}} \cdot C_i \tag{3.31}$$

The aim of the analysis is to determine which value of the signal strength parameter μ is the most compatible with the observed data (Section 3.8.3), to quantify the level of disagreement between data and the background-only hypothesis (Section 3.8.4) and to set the upper limit on μ at a confidence level (CL) of 95% (Section 3.8.5).

3.8.1 Likelihood Function

The statistical model used to estimate the signal strength parameter μ in this analysis is based on the profile likelihood technique. A likelihood function is constructed such that it contains all the information on the measurement. The

[1] In Section 3.7.2, the number of expected signal events is denoted as s_i^{reco}.

systematic and statistical uncertainties are included via so-called *nuisance parameters* $\boldsymbol{\theta}$. These are unknown parameters that need to be estimated from data along with the *parameter of interest* μ. Since the uncertainties affect the predictions of signal and background yields, the event expectation in each channel i becomes a function of the nuisance parameters:

$$N_i^{\text{exp}}(\mu, \boldsymbol{\theta}) = \mu s_i(\boldsymbol{\theta}) + b_i(\boldsymbol{\theta}) = \mu s_i(\boldsymbol{\theta}) + \sum_{j \in \text{Bkg}} b_{ij}(\boldsymbol{\theta}) \tag{3.32}$$

The probability for the expected number of events to produce the observed number of events in data follows a Poisson distribution:

$$\mathcal{P}(N_i^{\text{obs}} | N_i^{\text{exp}}(\mu, \boldsymbol{\theta})) = \frac{N_i^{\text{exp}}(\mu, \boldsymbol{\theta})^{N_i^{\text{obs}}}}{N_i^{\text{obs}}!} e^{-N_i^{\text{exp}}(\mu, \boldsymbol{\theta})} \tag{3.33}$$

Given the observed data, the likelihood is regarded as a function of the parameters μ and $\boldsymbol{\theta}$. It is constructed as the product of Poisson distributions $\mathcal{P}$, one for each signal region i, and of the probability density functions (*pdfs*) modelling the systematic C_{Sys} and statistical C_{Stat} uncertainties:

$$L(\mu, \boldsymbol{\theta}) = \prod_{i \in \text{SR}} \mathcal{P}(N_i^{\text{obs}} | N_i^{\text{exp}}(\mu, \boldsymbol{\theta})) \; C_{\text{Syst}} \; C_{\text{Stat}} \tag{3.34}$$

This clean factorised form is allowed because all sources of the uncertainties are taken to be either fully correlated or uncorrelated.

Systematics uncertainties $\boldsymbol{\alpha}$

A subset of nuisance parameters associated to the systematic uncertainties with external constraints is denoted by $\boldsymbol{\alpha}$. The prior knowledge on α_k is incorporated into the likelihood as a Gaussian *pdf* in a frequentist manner[1] $\mathcal{G}(\hat{\alpha}_k | \alpha_k, \hat{\sigma}_{\alpha_k})$, where $\hat{\alpha}_k$ is the nominal "measured" value and $\hat{\sigma}_{\alpha_k}$ is the estimated uncertainty. This term serves to constrain the true value of α_k. For convenience, the nuisance parameters α_k are normalized so that the distribution has zero mean and unit variance $\mathcal{G}(0 | \alpha_k, 1)$. The probability density function C_{Sys} is simply a product of

[1] In frequentist statistics, the probability is interpreted as the frequency of the outcome of a repeatable experiment whose replication results in different values. For example, $f(d|\mu)$ gives a probability of obtaining the data d given a hypothesis μ.

all the constraint terms:

$$C_{\text{Syst}} = \mathcal{G}(\mathcal{L}_0|\mathcal{L}, \sigma_{\mathcal{L}}) \prod_{k \in \text{Sys}} \mathcal{G}(0|\alpha_k, 1) \tag{3.35}$$

Here the first distribution describes an auxiliary measurement of the nominal integrated luminosity $\mathcal{L}_0 \pm \sigma_{\mathcal{L}}$ constraining the nuisance parameter $\mathcal{L}$ which is treated individually. It enters in the estimation of all MC-generated processes that are normalized to the integrated luminosity of the data sample.

The effect of each systematic uncertainty on the event expectation value is estimated in the analysis by $\pm 1\sigma$ variations of the corresponding parameter with respect to its nominal value, where 1σ means one standard deviation. These, usually three, discrete values need to be implemented in the likelihood as a continuous function of the nuisance parameter α_k. This is done by a so-called response function which represents a smooth parametrization. It is specific of each sample because the same source of uncertainty may have a different effect on the various signal and background processes. The interpolation approach can take either a linear or exponential form depending on the nature of the nuisance parameters.

A first set of α_k parametrizes the impact of *detector response effects*. In this class falls for example the Electron Energy Scale (EES) uncertainty which has been determined prior to this analysis with an independent calibration measurement performed by the Electron/Gamma performance group. These uncertainties affect the normalization as well as the shape and are fully correlated across the different channels and samples. The most straightforward interpolation strategy is chosen to parametrize these effects, the linear one:

$$b_{ij}(\boldsymbol{\alpha}) = b_{ij} \cdot \mathcal{B}_{ij}^{\text{lin}}(\boldsymbol{\alpha}) = b_{ij}(1 + \sum_{k \in \text{Sys}} \alpha_k \Delta_{ijk}) \tag{3.36}$$

where b_{ij} is the nominal yield of a background process j in channel i from (3.30) and $\mathcal{B}_{ij}^{\text{lin}}(\boldsymbol{\alpha})$ denotes the linear response function. Further, α_k represents the pulled nuisance variable[1] and Δ_{ijk} is the relative impact of the nuisance parameter

[1]The pulled nuisance parameter $\eta(\alpha_k)$ corresponding to α_k using renormalized subsidiary measurement $\mathcal{G}(0|\alpha_k, 1)$ is the following: $\eta(\alpha_k) = \frac{\alpha_k - \hat{\alpha}_k}{\hat{\sigma}_{\alpha_k}} = \alpha_k$.

α_k shifted by $\pm 1\sigma$ on the background event count; $\Delta_{ijk} = (b_{ij}^{+1\sigma} - b_{ij})/b_{ij}$ for $\alpha_k \geq 0$ and $\Delta_{ijk} = (b_{ij} - b_{ij}^{-1\sigma})/b_{ij}$ otherwise. A similar formula holds for the signal sample.

A second set of nuisance parameters α_k describes the *theoretical uncertainties*. A representative may be the NNLO scale uncertainty of 15% on the ZZ background prediction. They affect the global normalization of the samples and are fully correlated across the different regions but independent per process. In order to ensure a positive number of expected events (mainly for large values of the uncertainties), an exponential interpolation is used:

$$b_{ij}(\boldsymbol{\alpha}) = b_{ij} \cdot \mathcal{B}_{ij}^{\exp}(\boldsymbol{\alpha}) = b_{ij} \prod_{k \in \mathrm{Sys}} (1 + \Delta_{ijk})^{\alpha_k} \tag{3.37}$$

where $\mathcal{B}_{ij}^{\exp}(\boldsymbol{\alpha})$ is the exponential response function with $\Delta_{ijk} = (b_{ij}^{+1\sigma} - b_{ij})/b_{ij}$ for $\alpha_k \geq 0$ and $\Delta_{ijk} = (b_{ij}^{-1\sigma} - b_{ij})/b_{ij}$ otherwise. Moreover, if α_k is negative, the exponent is replaced by $-\alpha_k$.

Statistical uncertainties $\boldsymbol{\gamma}$

Since the full Monte Carlo simulation is very computationally expensive, some bins or even channels may end up being poorly populated. A possible treatment is to associate one nuisance parameter per bin for each statistically limited MC sample[1]. The statistical uncertainties are fully uncorrelated and can be implemented in the likelihood function using the same mechanism as for the systematic uncertainties. In this case, the subsidiary measurements are described by Poisson distributions:

$$C_{\mathrm{Stat}} = \prod_{i \in \mathrm{SR}} \Big(\mathcal{P}(s_i | \gamma_i s_i) \prod_{j \in \mathrm{Bkg}} \mathcal{P}(b_{ij} | \gamma_{ij} b_{ij}) \Big) \tag{3.38}$$

where the nuisance parameters γ_i and γ_{ij} reflect that the true rate of signal and background events may differ from the ones estimated using MC simulations in the channel i. Therefore, the event expectation in the likelihood function (3.34) depending on the full set of nuisance parameters $\boldsymbol{\theta} = (\boldsymbol{\alpha}, \boldsymbol{\gamma})$ has the following

[1] Since this is a counting experiment, there is only one bin per channel.

formula:

$$N_i^{\text{exp}}(\mu, \boldsymbol{\theta}) = \mu \cdot s_i(\boldsymbol{\alpha}) \cdot \gamma_i + \sum_{j \in \text{Bkg}} b_{ij}(\boldsymbol{\alpha}) \cdot \gamma_{ij} \tag{3.39}$$

To reduce the number of free parameters, an approach with only one nuisance parameter per channel associated with the sum of all MC estimates is used:

$$C_{\text{Stat}} = \prod_{i \in \text{SR}} \mathcal{P}(n_i | \gamma_i n_i) \tag{3.40}$$

where

$$n_i(\gamma_i) = n_i \cdot \gamma_i = (s_i + \sum_{j \in \text{Bkg}} b_{ij}) \cdot \gamma_i \tag{3.41}$$

The final form of the expected number of events parametrizing the effect of both, statistical and systematic, sources of uncertainty in each channel i is:

$$N_i^{\text{exp}}(\mu, \boldsymbol{\theta}) = (\mu \cdot s_i(\boldsymbol{\alpha}) + b_i(\boldsymbol{\alpha})) \cdot \gamma_i \tag{3.42}$$

Example

Assuming a simple counting experiment with only one channel, precisely known signal and one source of background estimated from MC simulation with limited statistics and affected by one systematic uncertainty on the EES, the likelihood function is the product of four probability density functions:

$$L(\mu, \alpha, \gamma) = \mathcal{G}(\mathcal{L}_0 | \mathcal{L}, \sigma_{\mathcal{L}}) \mathcal{P}(N^{obs} | \mu s + b\gamma(1 + \alpha\Delta)) \mathcal{P}(b | \gamma b) \mathcal{G}(0 | \alpha, 1) \tag{3.43}$$

where $(1 + \alpha\Delta)$ is the response function for the nuisance parameter α. For instance, if a unit shift in α results in 10% acceptance shift in the background, then $\Delta = 0.1$. In the case of multiple channels, a change in the parameter α coherently affects all measurements.

The likelihood function is constructed using the HistFactory tool [204] based on RooStats [205] and RooFit [206] frameworks. The tool builds the parametrized probability density functions from simple ROOT histograms. These contain the observed and expected number of events for the signal and all the

background processes as well as the event yield variations describing the impact of related systematic changes. Each histogram, one per channel, is organized via an XML configuration file. Its scheme classifies the uncertainties according to their sources and thereby ensures their specific treatment, as described above. A combination XML file allows for the specified channels to be statistically combined. The final *pdf* is stored in a `RooWorkspace` and saved to a ROOT file. It contains all the information necessary for the statistical analysis.

3.8.2 Profile Likelihood Ratio

Once the statistical model is built, all its free parameters are estimated by maximizing the likelihood function $L(\mu, \boldsymbol{\theta})$, given the observed data. The best fit values of the parameter of interest μ and the nuisance parameters $\boldsymbol{\theta}$ are denoted as the estimators $\hat{\mu}$[1] and $\hat{\boldsymbol{\theta}}$. A likelihood-based method used to estimate a *confidence interval* of the measurement as well as to perform an hypothesis test for a given parameter value μ is called the *profile likelihood* ratio and is defined as:

$$\lambda(\mu) = \frac{L(\mu, \hat{\hat{\boldsymbol{\theta}}}(\mu))}{L(\hat{\mu}, \hat{\boldsymbol{\theta}})} \tag{3.44}$$

It is the ratio of the *conditional* maximum likelihood to the *unconditional* maximum likelihood. The numerator alone depends on μ and $\hat{\hat{\boldsymbol{\theta}}}$ represents the values of nuisance parameters for the specified μ. Clearly $0 < \lambda(\mu) < 1$, where values close to 1 indicate good agreement between the data and the hypothesis μ. It is more convenient to consider the natural logarithm of the profile likelihood ratio $-2\ln\lambda(\mu)$ because the product in the likelihood function is then decomposed into a sum, while the maximum remains the same. This simplifies the fitting procedure performed by the MINUIT program [207].

Approximate distribution

In the large sample limit, the likelihood function converges asymptotically to a Gaussian distribution centred around the unconditional maximum likelihood

[1] This is defined as the value of the strength parameter maximizing the likelihood and hence can end up being negative. However, the Poisson mean value $\mu s_i + b_i$ remains positive.

estimator $\hat{\mu}$. The logarithm of the profile likelihood ratio has then a parabolic shape. The approximation due to Wald [208] has the following form[1]:

$$-2\ln\lambda(\mu) = \frac{(\mu-\hat{\mu})^2}{\sigma^2} + \mathcal{O}\left(\frac{1}{\sqrt{N}}\right) \tag{3.45}$$

where N denotes the size of the data sample and hence it is valid as far as the last term can be neglected. The estimator $\hat{\mu}$ itself is Gaussian distributed with a mean μ' and standard deviation σ. The latter can be obtained either from the covariance matrix of the estimators for all the parameters [209] or from an Asimov dataset using Equation 3.46 described below.

Asimov dataset

The Asimov dataset[2] is an artificial dataset where all the maximum likelihood estimators are set to their expected values: the parameter of interest is set to the mean of the $\hat{\mu}$ distribution ($\hat{\mu} = \mu'$) and the nuisance parameters are set to their nominal values ($\hat{\boldsymbol{\theta}} = \boldsymbol{\theta}$). It is used to evaluate the *Asimov profile likelihood ratio*:

$$-2\ln\lambda_{\mathrm{A}}(\mu) \approx \frac{(\mu-\mu')^2}{\sigma^2} \tag{3.46}$$

By using the Asimov dataset, one can easily characterize the sensitivity of a designed experiment through the expected confidence intervals of the measurement and the expected median significance of an hypothesis.

3.8.3 Cross-section Measurement

The measured value of the signal strength $\hat{\mu}$ is determined by minimizing the negative logarithm of the likelihood function simultaneously over all the parameters. For the combined channel the likelihood is given by the formulae 3.34, 3.35 and 3.40, while for an individual channel i the function is defined simply as:

$$L_i(\mu,\boldsymbol{\theta}) = \mathcal{P}(N_i^{\mathrm{obs}}|N_i^{\mathrm{exp}}(\mu,\boldsymbol{\theta}))\;\mathcal{P}(n_i|\gamma_i n_i)\;\mathcal{G}(\mathcal{L}_0|\mathcal{L},\sigma_{\mathcal{L}})\prod_{k\in\mathrm{Sys}}\mathcal{G}(0|\alpha_k,1) \tag{3.47}$$

[1] The formula is valid for a single parameter of interest, which is the case of this analysis.
[2] The name is inspired by the short story *Franchise* [210] written by Isaac Asimov.

The uncertainty on the measurement can be estimated from the contour of the negative logarithm of the profile likelihood ratio $-\ln\lambda(\mu)$ 3.44. In the asymptotic limit, it follows a parabolic function given by the Wald approximation 3.45. The one and two standard deviation confidence intervals on $\hat{\mu}$ are hence found to be[1]:

$$-\ln\lambda(\hat{\mu}+\sigma) \approx \frac{(\hat{\mu}+\sigma-\hat{\mu})^2}{2\sigma^2} = \frac{1}{2} \tag{3.48}$$

$$-\ln\lambda(\hat{\mu}+2\sigma) \approx \frac{(\hat{\mu}+2\sigma-\hat{\mu})^2}{2\sigma^2} = 2 \tag{3.49}$$

The same holds for the Asimov profile likelihood ratio (3.46) where the best-fit value $\hat{\mu}$ is replaced by the expected value μ' of the nominal signal model ($\mu' = 1$). This approach is valid even in the case of an asymmetric shape of the profile likelihood ratio due to its invariance property. The error calculation is performed numerically by the `MINOS` implementation of MINUIT.

The likelihood profile as a function of μ is shown in Figure 3.24. The observed contour is compared to the expected one obtained from the Asimov dataset. The former is distributed around the measured value $\hat{\mu}$, while the latter around the nominal value $\mu' = 1$. The impact of the statistical error can be estimated by profiling without the nuisance parameters $\boldsymbol{\alpha}$ parametrizing the systematic uncertainties. It can be seen that their absence only slightly narrows the profile. This implies that the total uncertainty on the measurement is predominantly due to the limited statistics. The systematic component is then determined by subtracting in quadrature the statistical component from the total uncertainty. As expected, the most sensitive channel is 0SFOS (Figure 3.24a) with a measured signal strength value close to 2. The other two channels have a mild downward data fluctuation with respect to the expectation (Figures 3.24b and 3.24c) and thereby $\hat{\mu}$ is negative. After the combination of all three channels (Figure 3.24d), the observed value is found to be close to the expected one:

$$\hat{\mu} = 1.02\ ^{+1.12}_{-1.08}(\text{stat.})\ ^{+1.03}_{-1.13}(\text{syst.}) \tag{3.50}$$

[1]The confidence level intervals of 68% (0.994σ) and 95% (1.959σ) correspond therefore to $-\ln\lambda = 0.49$ and $-\ln\lambda = 1.92$, respectively. If not stated otherwise, the 68% (95%) CL intervals are denoted by $\pm1\sigma$ ($\pm2\sigma$) in the following figures.

The best-fitted values $\hat{\mu}$ of the signal strength parameter for each individual channel and their combination are summarized in Figure 3.25.

The signal strength parameter measured in the channel i can be translated into the observed fiducial cross-section using the following formula:

$$\sigma_i^{\text{fid obs}} = \hat{\mu} \cdot \sigma_i^{\text{fid SM}} \tag{3.51}$$

where $\sigma_i^{\text{fid SM}}$ is the fiducial cross-section predicted by the SM, as calculated in Section 3.7.2. For instance, the expected value in the 0SFOS region, obtained from Asimov dataset, is:

$$\sigma_{\text{0SFOS}}^{\text{fid exp}} = 124\ ^{+210}_{-148}(\text{stat.})\ ^{+110}_{-135}(\text{syst.})\ \text{ab} \tag{3.52}$$

Given the measured data yield, the observed fiducial cross-section is higher:

$$\sigma_{\text{0SFOS}}^{\text{fid obs}} = 244\ ^{+241}_{-177}(\text{stat.})\ ^{+114}_{-134}(\text{syst.})\ \text{ab} \tag{3.53}$$

For the combination of all three channels, the relation between the observed and expected fiducial cross-section is given by:

$$\sigma^{\text{fid obs}} = \hat{\mu} \cdot \sum_{i \in \text{SR}} \sigma_i^{\text{fid SM}} \tag{3.54}$$

The expected value and uncertainties is found to be:

$$\sigma^{\text{fid exp}} = 309\ ^{+434}_{-338}(\text{stat.})\ ^{+314}_{-342}(\text{syst.})\ \text{ab} \tag{3.55}$$

while the observed one is:

$$\sigma^{\text{fid obs}} = 314\ ^{+348}_{-332}(\text{stat.})\ ^{+322}_{-346}(\text{syst.})\ \text{ab} \tag{3.56}$$

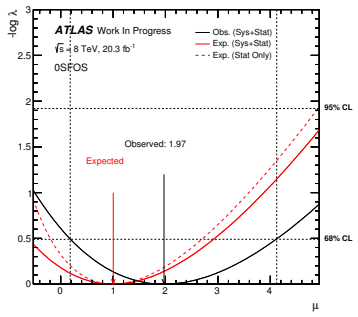

(a) 0SFOS

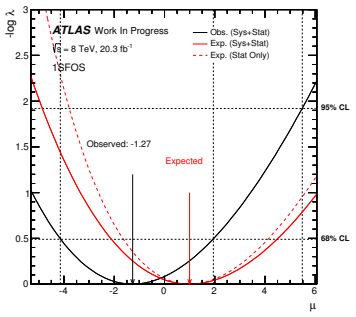

(b) 1SFOS

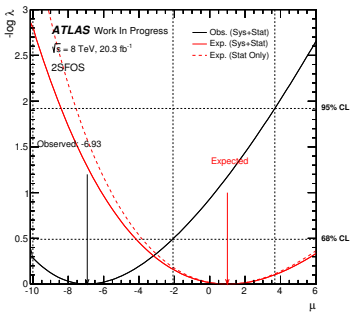

(c) 2SFOS

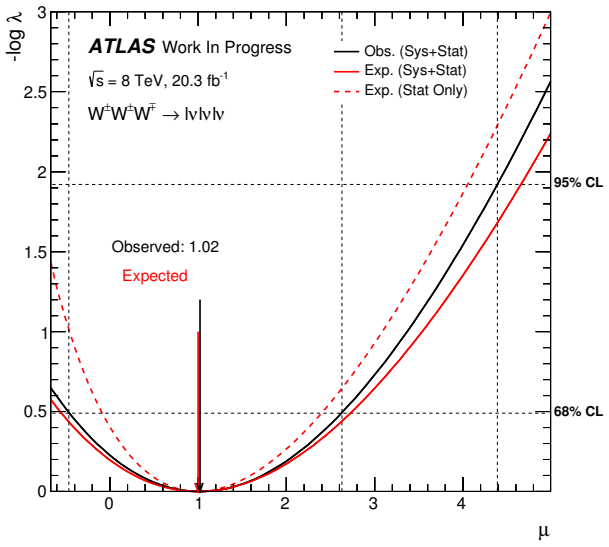

(d) combination

Figure 3.24: The likelihood profile as a function of μ for each channel separately as well as for their combination. The observed (black) contour is compared to the expected (solid red) one. The size of the statistical uncertainty is illustrated by the expected curve (dashed red) obtained by profiling only on the nuisance parameters $\boldsymbol{\gamma}$ that parametrize the statistical uncertainty. The horizontal dotted lines correspond to $-\ln\lambda = 0.49$ and $-\ln\lambda = 1.92$. Their intersections with the observed contour denote the 68% and 95% confidence level uncertainty on the measurement and are pointed up by the vertical dotted lines.

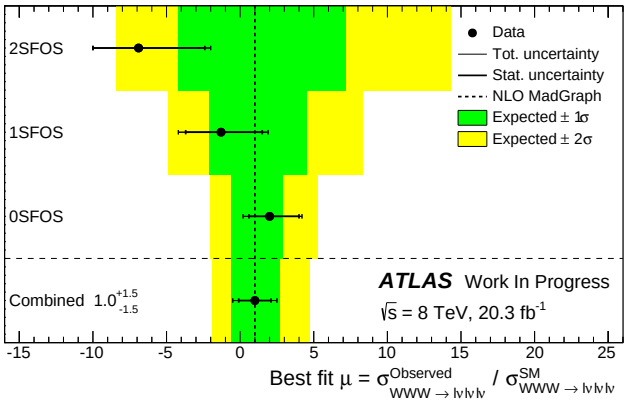

Figure 3.25: The measured values of the signal strength parameter for each of three channels and their combination. The statistical and total uncertainty on $\hat{\mu}$ are represented by the inner and total error bars, respectively. The green and yellow bands around the expected value show the corresponding $\pm 1\sigma$ and $\pm 2\sigma$ confidence intervals, respectively.

Incorporating all uncertainties affecting the measurement into the likelihood function via the nuisance parameters $\boldsymbol{\theta}$ allows for their correct propagation to the final uncertainty on the signal strength parameter $\hat{\mu}$. However, the result of the maximum likelihood fit needs to be firstly validated. In particular, the measurement should not be too sensitive to the nuisance parameters meaning that the fitted values $\hat{\boldsymbol{\theta}}$ should not strongly differ from the original values $\boldsymbol{\theta}_0$. So-called *pulls* are defined to quantify this deviation: $(\hat{\theta}_k - \theta_k)/\Delta\theta_k$. They are plotted for an unconstrained fit in Figure 3.26. Only the nuisance parameters parametrizing the systematic uncertainties with the expected uncertainty ± 1 are shown. Their 'in-situ' constraints are in general more appropriate for the phase space of the analysis but should be close to the prescribed values estimated by the subsidiary measurements. The underestimation or overestimation of the systematic uncertainty may result in considerably larger or smaller post-fit error of the corresponding nuisance parameter, respectively. It can be seen that all pulls, except the one coming from the WZ normalization, are distributed around zero with unit width. WZ is the dominant background in the 1SFOS and 2SFOS regions where a deficit of data events with respect to the expectation is observed. Therefore, the fit prefers a lower value than the nominal. Another important aspect that needs

to be understood is the correlation between the fit parameters. Figure 3.27 shows the *correlation matrix* obtained by the likelihood maximization. The largest correlation coefficient of the order of -52% is found to be between the signal strength μ and the nuisance parameter representing the fake background b-jet choice. This can be explained by the 0SFOS region which, besides being the most sensitive channel in the analysis, is dominated by the fake leptons. Moreover, the size of this uncertainty is significant.

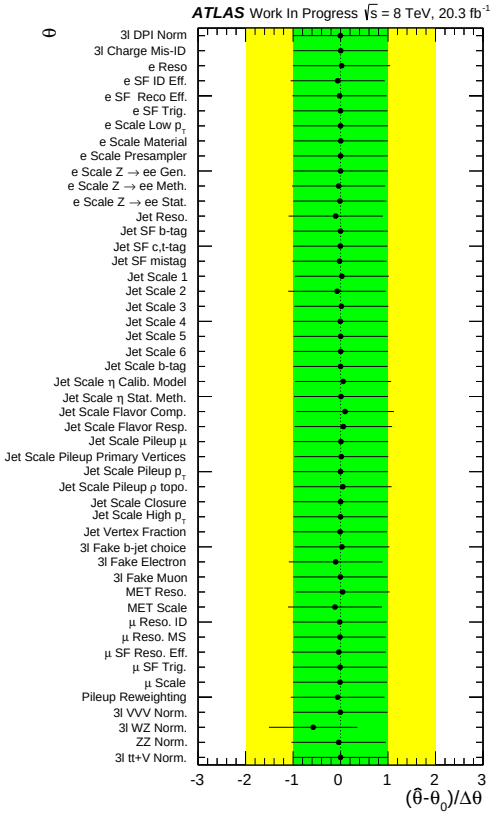

Figure 3.26: Pulls of the nuisance parameters representing all systematic uncertainties (uncertainties related to the detector effects as well as to the background normalization) after the likelihood fit to the data. The strength parameter μ is unconstrained i.e. considered as a floating parameter. The green and yellow bands represent the expected ± 1 and ± 2 uncertainties on the pre-fit estimates.

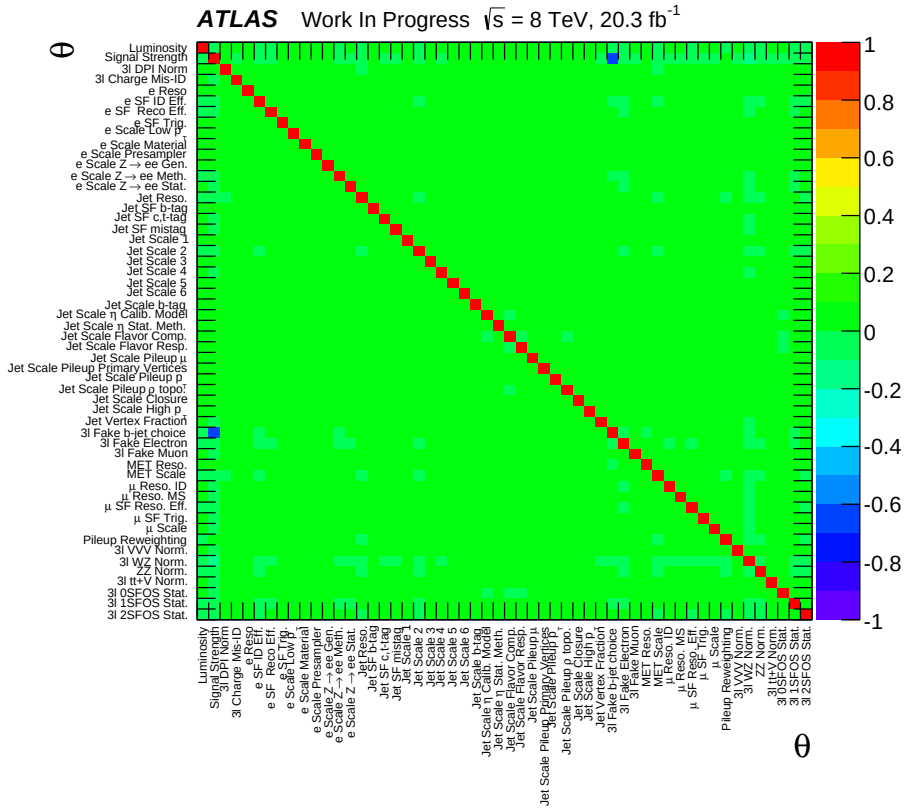

Figure 3.27: Matrix showing the correlation coefficients between the nuisance parameters and the signal strength parameter after the likelihood fit.

3.8.4 Test Statistic for Discovery Significance

Statistically, the discovery of a signal corresponds to rejecting the background-only hypothesis ($\mu = 0$). The appropriate test statistic q_0 is:

$$q_0 = \begin{cases} -2\ln\lambda(0) & \hat{\mu} \geq 0 \\ 0 & \hat{\mu} < 0 \end{cases} \tag{3.57}$$

where $\lambda(0)$ is the profile likelihood ratio defined in Equation 3.44 for $\mu = 0$. Higher values of q_0 imply greater disagreement between the data and the $\mu = 0$ hypothesis. In case of a deficit of data events with respect to the expected

background ($\hat{\mu} < 0$), the test statistic is set to 0 and hence is one-sided. This is appropriate since the presence of a signal leads to an increase and not a decrease in the number of events. The level of incompatibility of the data with the hypothesis is then quantified by the p-value:

$$p_0 = \int_{q_{0,\text{obs}}}^{\infty} f(q_0|0)\,\mathrm{d}q_0 \tag{3.58}$$

Here $q_{0,\text{obs}}$ is the experimental observation and $f(q_0|0)$ represents the *pdf* of the statistic q_0 under the assumption of background-only hypothesis. This sampling distribution follows the same convention as for the treatment of the nuisance parameters (discussed in Section 3.8.1): the frequentist one. The *pdf* is built by generating pseudo-experiments using toy MC approach. Wilks's theorem [211] states that, for a sufficiently large data sample, it can be approximated using an asymptotic approach by a half chi-square distribution χ^2 for one degree of freedom. The p-value can be interpreted in terms of Gaussian standard deviations as a discovery significance Z_0:

$$Z_0 = \Phi^{-1}(1 - p_0) \tag{3.59}$$

where Φ^{-1} is the inverse of the cumulative distribution (the quantile) of the Gaussian. Since the definition of q_0 is one-sided, $Z_0 = 0$ denoting a full agreement with the background-only hypothesis corresponds to $p_0 = 0.5$, while $Z_0 = 5$ defining a discovery of a signal corresponds to $p_0 = 2.87 \times 10^{-7}$. The expected discovery significance for rejecting the $\mu = 0$ hypothesis under the assumption of a signal model $\mu' = 1$ is obtained using the Asimov dataset [209]:

$$\text{med}[Z_0|\mu' = 1] = \sqrt{q_{0,\text{A}}} \tag{3.60}$$

The distribution $f(q_0|0)$ of the test statistic q_0 for the combination of all three channels is shown in Figure 3.28. It is determined using both methods, Monte Carlo toy experiments (50k) and a χ^2 distribution. It can be seen that the asymptotic formula represents a very good approximation. The observed value of p_0 is 0.24 corresponding to a significance of 0.70σ. The expected value is found

to be 0.25 corresponding to a significance of 0.66σ[1].

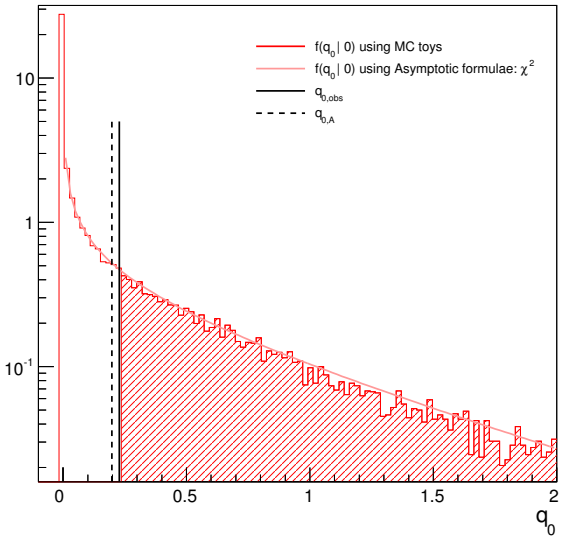

Figure 3.28: *pdf* of q_0 for the combined channel assuming the background-only hypothesis obtained from both, MC (red histogram) and asymptotic (pink line), methods. The black solid line represents the observed value $q_{0,\mathrm{obs}}$, while the black dashed line represents the expected value given by the Asimov dataset $q_{0,\mathrm{A}}$. The shaded area visualizes the p-value p_0.

3.8.5 Test Statistic for Upper Limits

Since the discovery significance Z_0 of the measurement is not high enough to confirm the observation or evidence[2] of the presence of a signal, an upper limit on the strength parameter μ is set using the one-sided test statistic q_μ:

$$q_\mu = \begin{cases} -2\ln\lambda(\mu) & \hat{\mu} \leq \mu \\ 0 & \hat{\mu} > \mu \end{cases} \tag{3.61}$$

[1]The significance is often approximated by a simplified formula $\mathrm{med}[Z_0|\mu'=1] \approx s/\sqrt{b}$ which is derived from Equation 3.60 assuming a simple counting experiment and replacing N^{obs} by the Asimov value $s+b$. It is valid only for $s \ll b$ and is used to estimate the expected sensitivity for each channel in Table 3.19. For the combined channel, one gets 0.64σ.

[2]Evidence corresponds to a significance Z_0 larger than 3σ.

where $\lambda(\mu)$ denotes the profile likelihood ratio (Equation 3.44). Higher values of q_μ correspond to increasing incompatibility between data and hypothesized value of μ. The upper limit is typically set by excluding the hypotheses of higher μ values than the measured one $\hat{\mu}$. Thus, q_μ is set to zero when the observed event yield increases above the event yield expected by the μ hypothesis[1]. Similarly to the discovery case, the level of disagreement is translated into the p-value:

$$p_\mu = \int_{q_{\mu,\text{obs}}}^{\infty} f(q_\mu|\mu)\,\mathrm{d}q_\mu \tag{3.62}$$

where $q_{\mu,\text{obs}}$ represents the observed value and $f(q_\mu|\mu)$ is the sampling distribution of q_μ assuming the hypothesis μ. The limiting issue herein may be the low experimental sensitivity. For the regions with a downward data fluctuation (e.g. the 1SFOS and 2SFOS signal regions with $\hat{\mu} < 0$), the $\mu = 0$ hypothesis is also tested and the resulting upper limit may end up being anomalously small. The p-value for the background-only hypothesis is hence introduced to control the sensitivity of a model:

$$1 - p_b = \int_{q_{\mu,\text{obs}}}^{\infty} f(q_\mu|0)\,\mathrm{d}q_\mu \tag{3.63}$$

where $f(q_\mu|0)$ is the *pdf* of q_μ assuming the background-only hypothesis $\mu = 0$. Both p-values, by convention defined as CL_{s+b} and CL_b, serve as the basis of an alternative test statistic called CL_s [212]. This method is conservative but suppresses the exclusion of hypothesized signal models with low sensitivity. It is defined as the following ratio:

$$CL_s(\mu) = \frac{p_\mu}{1 - p_b} = \frac{CL_{s+b}}{CL_b} \tag{3.64}$$

To quote the 95% confidence level upper limit on the strength parameter, further denoted as μ^{95}, many hypotheses μ need to be tested until CL_s reaches 5% i.e. $CL_s(\mu^{95}) = 0.05$. The 95% confidence level refers to the probability of having $\mu \leq \mu^{95}$. A signal model μ is regarded as excluded by the measurement if the appropriate CL_s value is below 5%. This threshold corresponds to a significance of

[1] Note the difference in definitions of q_0 (Equation 3.57) and q_μ (Equation 3.61) with $\mu = 0$.

1.64 standard deviations. The expected significance characterizing the sensitivity of the experiment can be estimated using the Asimov dataset:

$$\text{med}[Z_\mu|\mu' = 0] = \sqrt{q_{\mu,\text{A}}} \tag{3.65}$$

It is the median exclusion significance for rejecting the existence of a hypothesized signal process with a non-zero strength parameter μ assuming $\mu' = 0$.

The procedure described above requires performing two integrals (3.62 and 3.63) per hypothesis. To obtain the distributions $f(q_\mu|\mu)$ and $f(q_\mu|0)$ by using Monte Carlo sampling methods can be very computationally demanding. Therefore, the appropriate asymptotic formulae provide a useful simplification. Assuming the validity of the approximation 3.45, Wald's theorem [208] gives the general form of the probability density distribution. For $q_\mu > 0$, it is found to be:

$$f(q_\mu|\mu') = \frac{1}{2\sqrt{2\pi q_\mu}} \exp\Big[-\frac{(\sqrt{q_\mu} - \sqrt{\Lambda})^2}{2}\Big] \tag{3.66}$$

where Λ denotes the non-centrality parameter:

$$\Lambda = \frac{(\mu - \mu')^2}{\sigma^2} \tag{3.67}$$

The *pdf* $f(q_\mu|0)$ is equal to $f(q_\mu|\mu')$ assuming $\mu' = 0$ with $\Lambda = \mu^2/\sigma^2 = q_{\mu,\text{A}}$:

$$f(q_\mu|0) = \frac{1}{2\sqrt{2\pi q_\mu}} \exp\Big[-\frac{(\sqrt{q_\mu} - \sqrt{q_{\mu,\text{A}}})^2}{2}\Big] \tag{3.68}$$

For the special case $\mu' = \mu$, it is reduced to the Wilks's form, namely to a half chi-square distribution:

$$f(q_\mu|\mu) = \frac{1}{2\sqrt{2\pi q_\mu}} \exp\Big[-\frac{q_\mu}{2}\Big] \tag{3.69}$$

Before using the the asymptotic approach as the nominal one, it is important to verify that it gives compatible results with the MC approach for the sample size used by the analysis. The example of the q_μ statistics testing four different signal

hypotheses ($\mu = 1, 2, 3, 4$) is shown for the combined channel in Figure 3.29. The histograms $f(q_\mu|\mu)$ (red) and $f(q_\mu|0)$ (blue) generated by toy MC simulations (10k) are compared to the distributions from Equation 3.69 (pink) and Equation 3.68 (light blue). The agreement is very good. The vertical solid line represents the observed value $q_{\mu,\text{obs}}$ and the dashed line gives the median value of q_μ assuming $\mu' = 0$; $q_{\mu,\text{A}}$. The shaded red area visualizes the p-value CL_{s+b}, while the shaded blue area gives CL_b.

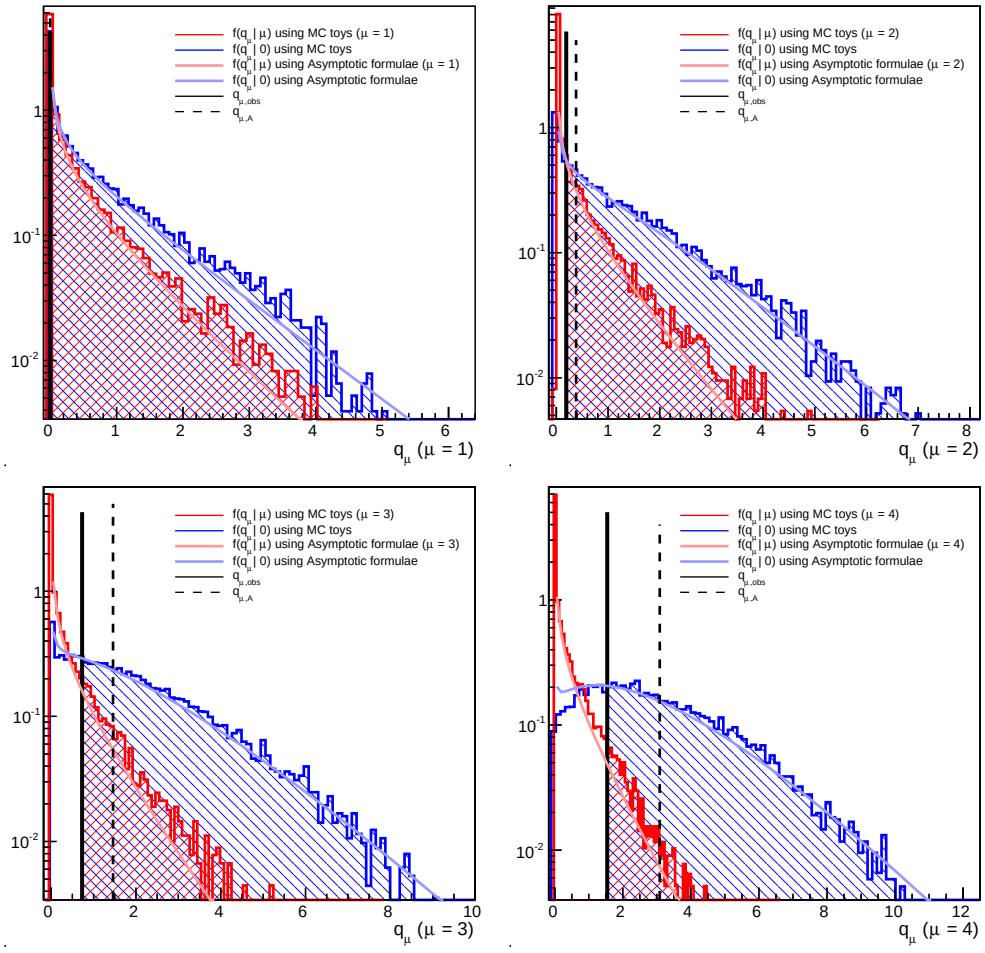

Figure 3.29: *pdf* of q_μ assuming the μ hypothesis ($\mu = 1, 2, 3, 4$). The *pdf* is determined using both methods, Monte Carlo toys and asymptotic formulae i.e. central and non-central χ^2 distribution.

The CL_s scan estimated using the asymptotic approximation has been performed over 20 different values of the strength parameter μ. The result for the combined channel is shown in Figure 3.30. The red points represent the observed CL_s values for a given μ. The measured values of CL_{s+b} and CL_b are denoted by blue and black points, respectively. The green and yellow bands present the $\pm 1\sigma$ and $\pm 2\sigma$ ranges of the background-only hypothesis $\mu' = 0$ with the median of the expected CL_s given by the dashed line. The 95% confidence level limit is indicated by the horizontal red line.

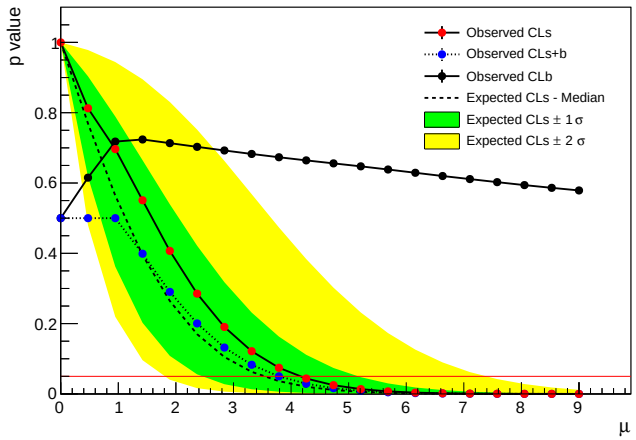

Figure 3.30: CL_s scan for the combined channel over the parameter of interest μ obtained using asymptotic formulae. The observed values of CL_s (red points), CL_{s+b} (blue points) and CL_b (black points) are shown. The expected CL_s values under the background-only hypothesis with $\pm 1\sigma$ and $\pm 2\sigma$ confidence intervals are indicated by the dashed line and the green/yellow bands.

Figure 3.31 shows the CL_s scan for each channel: (a) 0SFOS, (b) 1SFOS and (c) 2SFOS. Given the low event counts (especially in 0SFOS channel) pseudo-experiments have been used to determine the *pdfs*. The CL_s curve nicely demonstrates the good sensitivity of the 0SFOS channel. The observed line is deviated from the expected one toward the $+2\sigma$ band. On the contrary, the downward data fluctuation with respect to the background expectation in the 2SFOS channel accounts for the inclination toward the -2σ band. It can be also seen that the CL_{s+b} value alone would result in too low upper limit on μ.

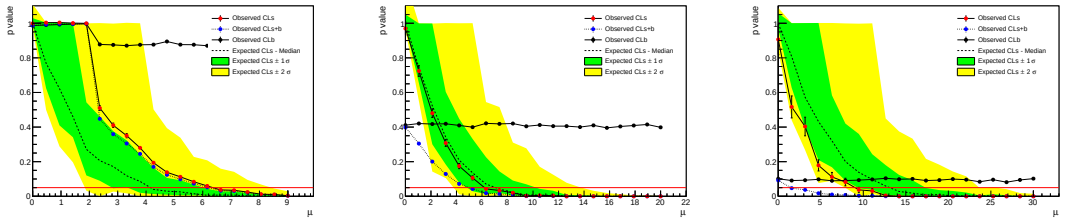

(a) 0SFOS (b) 1SFOS (c) 2SFOS

Figure 3.31: CL_s scan for the individual channels over the parameter of interest μ obtained using 2000 MC toys.

The upper limits μ^{95} on the strength parameter for each channel and their combination are summarized in Figure 3.32. A signal 4.2 times larger than the one predicted by SM is excluded at 95% confidence level using CL_s method. This value can be compared to the background-only expected limit of 3.5. If the SM WWW signal is also considered, the expected upper limit is 4.7.

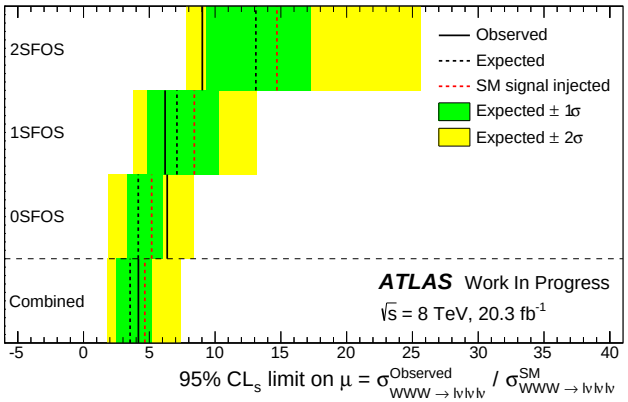

Figure 3.32: 95% confidence level upper limits on the measured fiducial cross-section relative to the one predicted by the SM. The observed limits are represented by the solid lines. The expected limits under the background-only hypothesis (black dashed lines) are surrounded by the $\pm 1\sigma$ and $\pm 2\sigma$ intervals (green and yellow bands respectively). The red dashed lines show the expected limits under the signal-plus-background hypothesis. The limits are calculated using the CL_s technique with MC pseudo-experiments for the individual channels and with the asymptotic approximation for their combination.

Finally, all results presented in this section are summarized in Table 3.21. The statistical interpretation is performed for the individual channels as well as for their combination. The best estimate of the signal strength parameter is determined by maximising the likelihood function and is quoted together with the uncertainty taken from the negative logarithm of the profile likelihood contour. The significance Z_0 quantifies the incompatibility between the data and the background-only hypothesis. The observed CL_s-based exclusion upper limits on μ at a 95% confidence level are compared to the background-only expectations. These are also interpreted as $\pm 1\sigma$ and $\pm 2\sigma$ confidence intervals.

Channel	**Best-fit μ**	**Z_0**	***UL***		***CL* interval**	
			Obs.	**Exp.**	**$\pm 1\sigma$**	**$\pm 2\sigma$**
0SFOS	$1.97\ ^{+2.15}_{-1.79}$	1.1σ	6.4	4.2	$[3.4, 6.0]$	$[1.9, 8.4]$
1SFOS	$-1.27\ ^{+3.21}_{-2.87}$	$< 0.1\sigma$	6.2	7.1	$[4.8, 10.3]$	$[3.8, 13.2]$
2SFOS	$-6.93\ ^{+4.85}_{-3.08}$	$< 0.1\sigma$	9.0	13.1	$[9.3, 16.2]$	$[7.8, 24.6]$
Combined	$1.02\ ^{+1.52}_{-1.56}$	0.7σ	4.2	3.5	$[2.5, 5.2]$	$[1.8, 7.4]$

Table 3.21: Summary of the measurement results from the individual channels and their combination. The best-fit value of the signal strength μ is provided with the total uncertainty. The observed significance Z_0 is obtained from the test statistic q_0 for the discovery. The 95% confidence level (CL) upper limit (UL) is given by the test statistic q_μ. It is compared to the median expected limit for the background-only hypothesis. The 68% and 95% confidence intervals around the expected value are denoted by $\pm 1\sigma$ and $\pm 2\sigma$, respectively.

3.9 aQGC Search

This analysis is sensitive to the anomalous quartic gauge coupling (aQGC) signal described in Section 1.4. The presence of aQGCs can modify the WWW production cross-section as well as the kinematic distributions. The fiducial cross-sections for the non-unitarized and unitarized aQGC signal samples, discussed in Section 3.2.4, are evaluated using the selection requirements from Table 3.6.

The reconstructed events are selected using the same criteria as in Table 4.1 only for the non-unitarized aQGC signal samples. The unitarized samples are not passed through the full reconstruction of the ATLAS detector. The corresponding correction factors are calculated according to Equation 3.25 as a function of $f_{S,1}/\Lambda^4$ and $f_{S,0}/\Lambda^4$ and averaged over the three signal regions. The difference between the averaged non-unitarized aQGC correction factors and the SM correction factor comes from a harder p_{T} spectrum of leptons and jets in aQGC events and is taken as a systematic uncertainty. It covers the differences between the non-unitarized and unitarized correction factors as well.

Since the results of the cross-section measurement show that data are in good agreement with the SM prediction, no aQGC signal has been found. Frequentist 95% confidence level upper limits on the aQGCs are hence extracted by forming a similar profile-likelihood-ratio as described in the previous section. The one-dimensional limits are shown in Table 3.22 while the two-dimensional limits are presented in Figure 4.2.

Λ_F [TeV]	CL interval [10^4 TeV^{-4}]			
	Observed		Expected	
	$f_{S,0}/\Lambda^4$	$f_{S,1}/\Lambda^4$	$f_{S,0}/\Lambda^4$	$f_{S,1}/\Lambda^4$
0.5	[-1.08, 1.23]	[-1.32, 1.61]	[-1.36, 1.54]	[-1.77, 2.10]
1	[-0.46, 0.56]	[-0.61, 0.77]	[-0.60, 0.73]	[-0.83, 1.01]
2	[-0.25, 0.35]	[-0.36, 0.47]	[-0.35, 0.45]	[-0.50, 0.63]
3	[-0.20, 0.30]	[-0.30, 0.40]	[-0.28, 0.38]	[-0.42, 0.53]
∞	[-0.14, 0.24]	[-0.23, 0.32]	[-0.22, 0.31]	[-0.34, 0.43]

Table 3.22: Expected and observed 95% confidence level (CL) intervals on $f_{S,0}/\Lambda^4$ ($f_{S,1}/\Lambda^4$) with different Λ_F values, assuming $f_{S,1}/\Lambda^4$ ($f_{S,0}/\Lambda^4$) is zero.

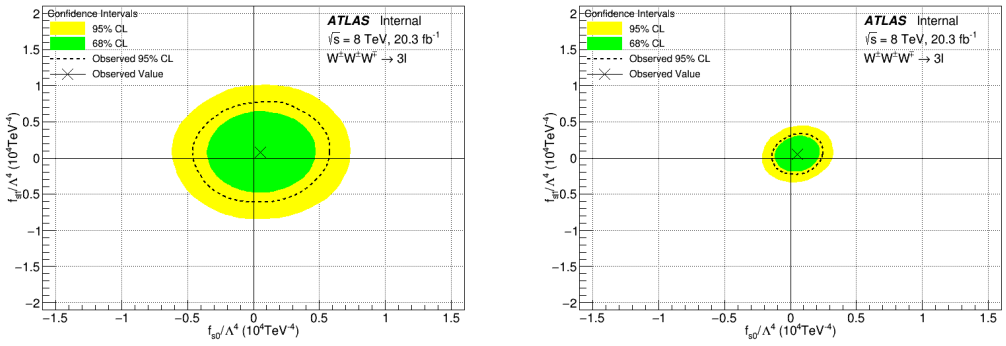

Figure 3.33: Expected 68% and 95% CL contour limits on $(f_{S,1}/\Lambda^4, f_{S,0}/\Lambda^4)$ compared to the observed 95% CL contour limit and observed best fit value for cases when $\Lambda_F = 1\,\text{TeV}$ (left) and $\Lambda_F = \infty$ (right).

3.10 Conclusion

A search for triboson $W^{\pm}W^{\pm}W^{\mp}$ production in the fully-leptonic channel is presented using 20.3 fb^{-1} of proton-proton collision data collected by the ATLAS experiment at $\sqrt{s} = 8$ TeV. Events with exactly three charged leptons (electrons or muons) are considered. The data are found to be in agreement with the standard model expectation in all signal regions. The measurement is performed in three fiducial phase spaces and in their combination. The combined fiducial cross-section is observed to be 314 $^{+348}_{-332}$(stat.) $^{+322}_{-346}$(syst.) ab, which is consistent with the predicted value of 309 ab. However, due to limited statistics and large systematic uncertainties, no evidence of the SM signal is found and upper limits at 95% confidence level are set. An observed (expected) limit of 4.2 (3.5) times the SM cross section is obtained. In addition, limits on the anomalous quartic gauge couplings $f_{S,1}/\Lambda^4$ and $f_{S,0}/\Lambda^4$ are derived.

CHAPTER 4

COMBINED SEARCH FOR $W^{\pm}W^{\pm}W^{\mp}$ PRODUCTION

4.1 Introduction

In order to increase the sensitivity to the triboson $W^{\pm}W^{\pm}W^{\mp}$ production, the fully-leptonic decay channel $W^{\pm}W^{\pm}W^{\mp} \to \ell^{\pm}\nu\,\ell^{\pm}\nu\,\ell^{\mp}\nu$ [148], described in Chapter 3, is statistically combined with the semi-leptonic channel $W^{\pm}W^{\pm}W^{\mp} \to \ell^{\pm}\nu\,\ell^{\pm}\nu\,jj$ [213]. The results of this combination [172] are interpreted in terms of the total Standard Model $W^{\pm}W^{\pm}W^{\mp}$ production cross-section and presented in this chapter.

4.2 Search for $W^{\pm}W^{\pm}W^{\mp} \to \ell^{\pm}\nu\,\ell^{\pm}\nu\,jj$ production

Candidate $\ell\nu\ell\nu jj$ events are required to have exactly two leptons (electrons or muons) with the same electric charge and at least two jets with an invariant mass consistent with a hadronically decaying W boson. The selection criteria are similar to those used in the same-sign WW vector boson fusion analysis [214] except for the requirements on the pseudorapidity separation between the two jets $|\eta_{jj}|$ and the dijet invariant mass m_{jj}. Three different final states are considered based on the lepton flavour: $e^{\pm}e^{\pm}$, $e^{\pm}\mu^{\pm}$ and $\mu^{\pm}\mu^{\pm}$. To reduce the contributions from diboson processes, events are rejected if they contain an additional lepton. The final kinematic selection criteria used to define the signal regions are listed in Table 4.1.

	$e^{\pm}e^{\pm}$	$e^{\pm}\mu^{\pm}$	$\mu^{\pm}\mu^{\pm}$
Lepton	Exactly 2 same-same leptons with $p_T > 30$ GeV		
Jets	At least 2 jets with $p_T > 30\,(20)$ GeV		
b-jet veto	$N_{b\text{-jet}} = 0$ (70 % b-tagging efficiency)		
$m_{\ell\ell}$	$m_{\ell\ell} > 40$ GeV		
$E_{\mathrm{T}}^{\mathrm{miss}}$	$E_{\mathrm{T}}^{\mathrm{miss}} > 55\,\mathrm{GeV}$		–
m_{jj}	65 GeV $< m_{jj} <$ 105 GeV		
$\Delta\eta_{jj}$	$\lvert\Delta\eta_{jj}\rvert < 1.5$		
Z veto	$m_{ee} < 70\,\mathrm{GeV}$ or $m_{ee} > 110\,\mathrm{GeV}$	–	–
Third lepton veto	No third lepton with $p_{\mathrm{T}} > 6$ GeV		

Table 4.1: Optimized signal selection criteria, based on the lepton flavour: $e^{\pm}e^{\pm}$, $e^{\pm}\mu^{\pm}$ and $\mu^{\pm}\mu^{\pm}$.

The background events are classified and estimated similarly as in the $\ell\nu\ell\nu\ell\nu$ analysis. The SM processes that produce two prompt same-sign leptons (WZ, ZZ, $t\bar{t}V$, ZWW and ZZZ) and where the photon is mis-reconstructed as a lepton ($W\gamma$+jets) are predicted purely from the MC simulation. The WZ production represents the dominant irreducible background in both decay channels. However, these events are generated with Sherpa in the $\ell\nu\ell\nu jj$ analysis because the Sherpa prediction provides better description of the measured jet multiplicity than Powheg, as shown in Figure 4.1. The charge-flip background is estimated using a data-driven method. The efficiencies, measured using $Z \to ee$ events as in Section 3.5.2, are applied on the data events with the same kinematic requirements but with opposite-sign leptons pairs. The fake lepton background is also estimated in data but uses a fake factor method instead of the generalised matrix method described in Section 3.5.3.

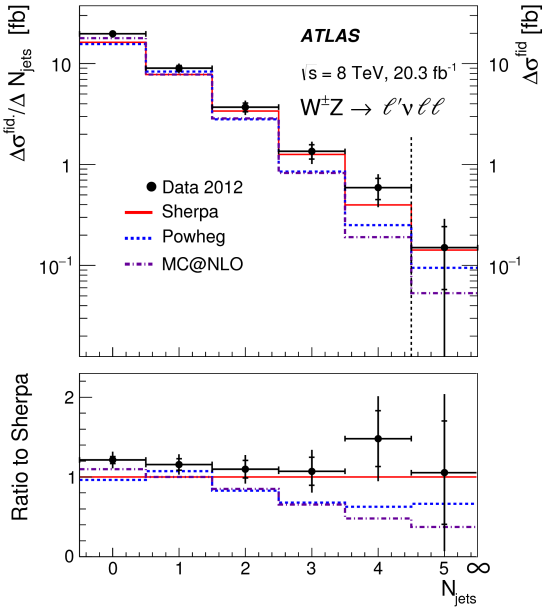

Figure 4.1: The measured WZ differential normalised cross-section in the fiducial phase space as a function of the exclusive jet multiplicity. The measurement is compared to the prediction from SHERPA (red line), POWHEG+PYTHIA8 (dashed blue line) and MC@NLO (dotted-dashed violet line) [184].

4.3 Results

The observed number of data events is compared in Table 4.2 to the signal and background predictions with systematic uncertainties for the three signal regions in the $\ell\nu\ell\nu jj$ channel. Most of the sensitivity comes from the $\mu^{\pm}\mu^{\pm}$ region, as outlined by the $s/\sqrt{b}$ ratio[1]. In the $e^{\pm}e^{\pm}$ channel, zero data events are observed while 4.51 are expected (4.04 background and 0.46 signal). The deviation from the background-only hypothesis corresponds to a significance of 1.99 standard deviations. The object-related systematic uncertainties are evaluated in the same way as in Section 3.6 and are therefore treated as fully correlated across both channels. The uncertainties related to the charge mis-identification and fake lepton backgrounds are derived and treated independently because of the different

[1]The $s/\sqrt{b}$ ratio is an approximation for the expected discovery significance defined in Equation 3.60.

estimation techniques used. The dominant sources of systematic uncertainty on both the background (15%) and signal (21%) estimations are due to jet energy modelling. A summary of the effect of the systematic uncertainties on the overall signal and background expectations is listed for both channels in Table 4.3.

	$e^{\pm}e^{\pm}$	$e^{\pm}\mu^{\pm}$	$\mu^{\pm}\mu^{\pm}$
WZ	$0.74 \pm 0.13 \pm 0.44$	$2.77 \pm 0.27 \pm 0.66$	$3.28 \pm 0.29 \pm 0.71$
Other Prompt	$0.46 \pm 0.05 \pm 0.16$	$1.33 \pm 0.10 \pm 0.38$	$1.33 \pm 0.15 \pm 0.38$
Charge-flip	$1.13 \pm 0.13 \pm 0.24$	$0.74 \pm 0.08 \pm 0.16$	–
$V\gamma$	$0.75 \pm 0.35 \pm 0.21$	$2.48 \pm 0.68 \pm 0.74$	–
Fake	$0.96 \pm 0.15 \pm 0.39$	$2.04 \pm 0.22 \pm 0.89$	$0.43 \pm 0.06 \pm 0.25$
Signal	$0.46 \pm 0.03 \pm 0.07$	$1.35 \pm 0.05 \pm 0.19$	$1.65 \pm 0.06 \pm 0.30$
Total Background	$4.04 \pm 0.42 \pm 0.69$	$9.36 \pm 0.77 \pm 1.39$	$5.04 \pm 0.34 \pm 0.82$
Signal + Background	$4.51 \pm 0.43 \pm 0.69$	$10.72 \pm 0.77 \pm 1.40$	$6.69 \pm 0.34 \pm 0.87$
Data	0	15	6
s/b ($s/\sqrt{b}$)	11% (0.23)	14% (0.44)	33% (0.74)

Table 4.2: Summary of the observed data and the expected signal and background yields with statistical and systematic uncertainties for all three signal regions in the $\ell\nu\ell\nu jj$ channel. The systematic uncertainties are quoted as a quadrature sum of all the individual sources only for illustration purpose. They are treated separately in the actual measurement, as discussed in Section 3.8. The last row reports the expected sensitivity for each channel with s (b) denoting the signal (total background) yield.

Figure 4.2 shows the $m_{\mathrm{T}}^{3\ell}$ distribution for the $\ell\nu\ell\nu\ell\nu$ channel and the $\sum p_{\mathrm{T}}$ distribution, defined as the scalar sum of all selected leptons and jets momenta $\sum p_{\mathrm{T}} = E_{\mathrm{T}}^{\mathrm{miss}} + p_{\mathrm{T}}^{\ell_1} + p_{\mathrm{T}}^{\ell_2} + p_{\mathrm{T}}^{j_1} + p_{\mathrm{T}}^{j_2}$, for the $\ell\nu\ell\nu jj$ channel, after summing over all three signal regions in each channel. A good agreement between data and the signal-plus-background model is observed for both distributions.

Source of Uncertainty	$\ell\nu\ell\nu\ell\nu$ %		$\ell\nu\ell\nu jj$ %	
	Signal	Bkg	Signal	Bkg
Lepton ID, $E_{\mathrm{T}}/p_{\mathrm{T}}$ scale & resolution	1.6	1.8	2.1	3.3
$E_{\mathrm{T}}^{\mathrm{miss}}$ scale & resolution	1.1	1.4	0.7	1.8
b-jet tagging	0.3	0.3	2.2	2.2
Jet E_{T} scale & resolution	2.3	2.8	21	15
Fake lepton background	0	13	0	8
Charge-flip background	0	0.04	0	2.2
Luminosity	1.9	1.6	1.9	1.4
Pile-up estimate	1.1	0.6	0.6	1.6
Trigger efficiency	0.1	0.1	0.1	0.01
WZ, ZZ, $t\bar{t}V$, VVV normalization	5.5	8	6.0	13
Statistics	1.2	3.2	2.7	5.1

Table 4.3: Summary of the systematic uncertainties on the total signal and background estimates. Numbers are shown in percent of the nominal prediction.

Given that the MadGraph $W^{\pm}W^{\pm}W^{\mp}$ samples used in the $\ell\nu\ell\nu\ell\nu$ channel are generated in a common phase space where each W boson can decay either leptonically or hadronically, the same signal samples are used in the $\ell\nu\ell\nu jj$ channel. The correction factors and fiducial cross-sections are calculated for each signal region using Equations 3.25 and 3.27, respectively. The combined fiducial cross-section with the PDF and scale uncertainties is expected to be:

$$\sigma_{\ell\nu\ell\nu jj}^{\text{fid SM}} = 286 \pm 6(\text{stat.})\,^{+14}_{-8}(\text{PDF}) \pm 10(\text{scale})\ \text{ab} \tag{4.1}$$

Even though different selection criteria are applied, this value is found to be close to that from the $\ell\nu\ell\nu\ell\nu$ channel, recalled here for convenience:

$$\sigma_{\ell\nu\ell\nu\ell\nu}^{\text{fid SM}} = 309 \pm 7(\text{stat.})\,^{+15}_{-9}(\text{PDF}) \pm 8(\text{scale})\ \text{ab} \tag{4.2}$$

As already mentioned, the two measurements are statistically combined and extrapolated to the total cross-section which is predicted to be:

$$\sigma_{WWW}^{\text{SM}} = 241.5 \pm 0.1(\text{stat.})\,^{+10.3}_{-6.1}(\text{PDF}) \pm 6.3(\text{scale})\ \text{fb} \tag{4.3}$$

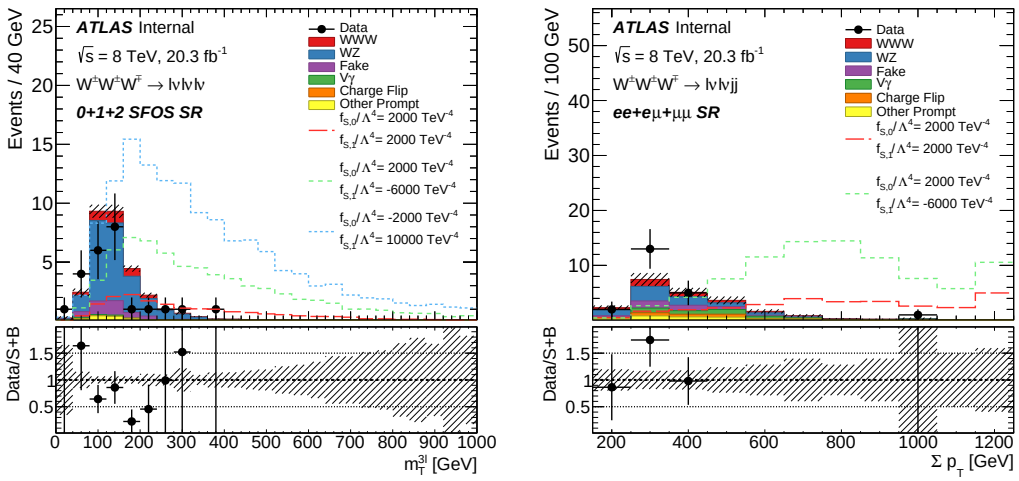

Figure 4.2: The $m_{\mathrm{T}}^{3\ell}$ distribution in the $\ell\nu\ell\nu\ell\nu$ channel (left) and the $\sum p_{\mathrm{T}}$ distribution in the $\ell\nu\ell\nu jj$ channel (right). All events from the three signal regions are summed in each channel. The error bars on the data points represent the statistical uncertainty on the data. The hashed area represents the total systematic uncertainties on the signal plus background model. The last bin includes the overflow. The non-unitarized ($\Lambda_F = \infty$) aQGC predictions with nonzero values of some of the anomalous coupling parameters are also represented by the dashed lines.

The extrapolation is performed by dividing a fiducial cross-section $\sigma_i^{\text{fid SM}}$ by a *signal acceptance* A_i, defined as the following ratio:

$$A_i = \frac{s_i^{\text{truth}}}{s^{\text{truth}}} \tag{4.4}$$

where s^{truth} represents all signal events generated using MadGraph and s_i^{truth} corresponds to their fraction falling within a fiducial phase space i. The acceptance values are listed for both channels, together with the correction factors, in Table 4.4. As they include also the W boson decay branching fractions, they end up being very small. Finally, the SM total cross-section can be written as:

$$\sigma_{WWW}^{\text{SM}} = \frac{\sigma_i^{\text{fid SM}}}{A_i} = \frac{s_i^{\text{reco}}}{\mathcal{L} \cdot C_i \cdot A_i} \tag{4.5}$$

where $\sigma_i^{\text{fid SM}}$ is taken from Equation 3.27.

Channel		C_i	A_i ($\times 10^{-3}$)
$\ell\nu\ell\nu\ell\nu$	0SFOS	0.534 ± 0.021	0.512 ± 0.019
	1SFOS	0.500 ± 0.018	0.567 ± 0.020
	2SFOS	0.615 ± 0.038	0.202 ± 0.012
$\ell\nu\ell\nu jj$	$e^{\pm}e^{\pm}$	0.456 ± 0.039	0.215 ± 0.011
	$e^{\pm}\mu^{\pm}$	0.595 ± 0.030	0.476 ± 0.016
	$\mu^{\pm}\mu^{\pm}$	0.713 ± 0.036	0.482 ± 0.016

Table 4.4: Correction factors C_i and acceptances A_i calculated separately for each signal region. Only statistical uncertainties are shown.

4.4 Statistical Interpretation and Measurement

The same statistical methodology as described in Section 3.8 is used to interpret the results from both the fully-leptonic (Table 3.19) and semi-leptonic (Table 4.2) channels. The signal strength parameter, μ, is defined as a scale factor multiplying the expected signal event yield in a signal region i, s_i, which can be expressed in terms of the production cross section, σ^{SM}_{WWW}:

$$s_i = \mathcal{L} \cdot \sigma_i^{\text{fid SM}} \cdot C_i = \mathcal{L} \cdot \sigma^{\text{SM}}_{WWW} \cdot C_i \cdot A_i \tag{4.6}$$

For the combination of all six signal regions, the likelihood is given by Equation 3.34 with $i \in (\text{0SFOS}, \text{1SFOS}, \text{2SFOS}, e^{\pm}e^{\pm}, e^{\pm}\mu^{\pm}, \mu^{\pm}\mu^{\pm})$. The measured value $\hat{\mu}$ is then translated into the observed total cross-section using a relation similar to that of Equation 3.54:

$$\sigma^{\text{obs}}_{WWW} = \frac{\hat{\mu}}{A} \cdot \sum_{i \in \text{SR}} \sigma_i^{\text{fid SM}} \tag{4.7}$$

where A is the overall acceptance which is found to be $A = (2.455 \pm 0.039) \times 10^{-3}$.

$$A = \sum_{i \in \text{SR}} A_i \tag{4.8}$$

The profile likelihood ratio is shown in Figure 4.3c. The expected value and uncertainties for the total cross-section is:

$$\sigma_{WWW}^{\text{exp}} = 241\ ^{+232}_{-199}(\text{stat.})\ ^{+152}_{-153}(\text{syst.})\ \text{fb} \tag{4.9}$$

while the observed is:

$$\sigma_{WWW}^{\text{obs}} = 227\ ^{+202}_{-198}(\text{stat.})\ ^{+154}_{-160}(\text{syst.})\ \text{fb} \tag{4.10}$$

The log-likelihood contours for the individual channels are shown in Figures 4.3a and 4.3b. The expected and observed fiducial cross-sections for the $\ell\nu\ell\nu\ell\nu$ channel are stated in Section 3.8.3 and for the $\ell\nu\ell\nu jj$ channel are:

$$\sigma_{\ell\nu\ell\nu jj}^{\text{fid exp}} = 286\ ^{+397}_{-332}(\text{stat.})\ ^{+211}_{-200}(\text{syst.})\ \text{ab} \tag{4.11}$$

$$\sigma_{\ell\nu\ell\nu jj}^{\text{fid obs}} = 242\ ^{+394}_{-325}(\text{stat.})\ ^{+193}_{-188}(\text{syst.})\ \text{ab} \tag{4.12}$$

Furthermore, the significance of a possible observation of the $W^{\pm}W^{\pm}W^{\mp}$ signal is estimated using the background-only hypothesis ($\mu = 0$) discussed in Section 3.8.4. The observed null p-value is found to be 0.96σ with an expected value of 1.05σ. Since the precision of the measurement is limited, one-sided 95% CL upper limits on the fiducial and total cross-sections are set using the CL_s method introduced in Section 3.8.5. The observed (expected) upper limit on the fiducial cross-section in the absence of a signal is determined to be 1.3 fb (1.1 fb) in the $\ell\nu\ell\nu\ell\nu$ channel and 1.1 fb (0.9 fb) in the $\ell\nu\ell\nu jj$ channel. When the two channels are combined, the observed upper limit on the total cross-section is 730 fb. The expected limits are 560 fb and 850 fb if the SM $W^{\pm}W^{\pm}W^{\mp}$ signal is absent and included, respectively.

Finally, all results are summarized in terms of the signal strength μ in Figure 4.4 and in Table 4.5 for the combined measurement as well as for the individual channels.

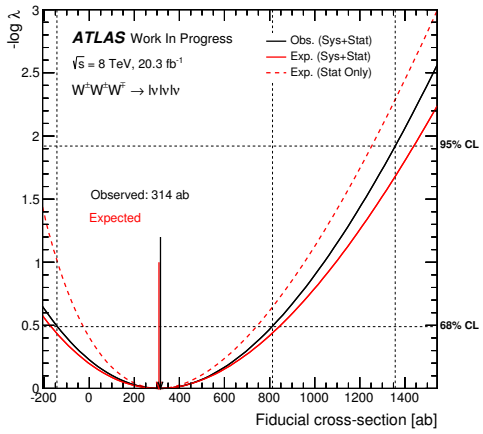

(a) $\ell\nu\ell\nu\ell\nu$

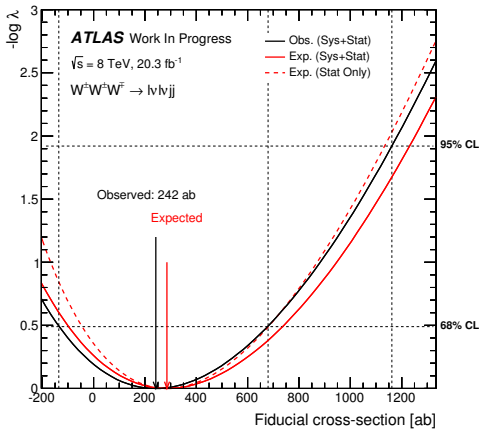

(b) $\ell\nu\ell\nu jj$

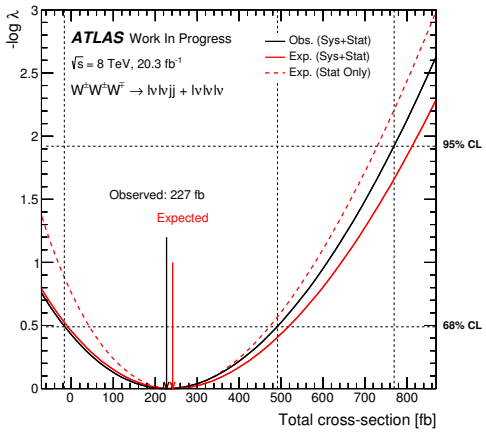

(c) combination

Figure 4.3: The likelihood profile as a function of the fiducial cross-section for fully-leptonic and semi-leptonic channels and as a function of the total cross-section for their combination. The observed (black) contour is compared to the expected (solid red) one. The size of the statistical uncertainty is visualized by the expected curve (dashed red) obtained by profiling only on the nuisance parameters $\boldsymbol{\gamma}$ parametrizing the statistical uncertainty. The horizontal dotted lines correspond to $-\ln\lambda = 0.49$ and $-\ln\lambda = 1.92$. Their intersections with the observed contour denote the 68% and 95% confidence level uncertainty on the measurement and are pointed up by the vertical dotted lines.

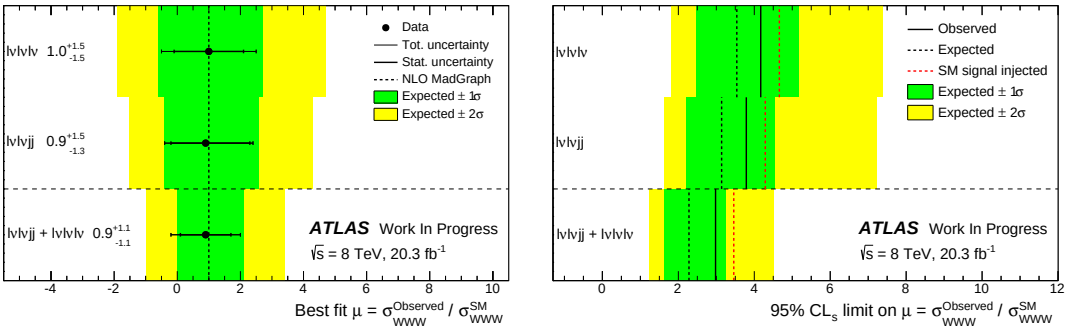

(a) Best fit μ values

(b) 95% CL_s upper limits

Figure 4.4: The expected and observed values of (a) best fit signal strength and (b) 95% CL_s upper limit on the signal strength, along with uncertainties for the $\ell\nu\ell\nu\ell\nu$ and $\ell\nu\ell\nu jj$ channels and their combination. The green and yellow bands around the expected value (black dashed lines) show the corresponding $\pm1\sigma$ and $\pm2\sigma$ confidence intervals. The statistical and total uncertainty on $\hat{\mu}$ are represented by the inner and total error bars, respectively. The red dashed lines show the expected upper limits under the signal-plus-background hypothesis.

Channel	**Best-fit μ**	**Z_0**	***UL***		***CL* interval**	
			Obs.	**Exp.**	**$\pm1\sigma$**	**$\pm2\sigma$**
$\ell\nu\ell\nu\ell\nu$	$1.02\ ^{+1.52}_{-1.56}$	0.7σ	4.2	3.5	$[2.5, 5.2]$	$[1.8, 7.4]$
$\ell\nu\ell\nu jj$	$0.85\ ^{+1.53}_{-1.32}$	0.6σ	3.8	3.1	$[2.2, 4.5]$	$[1.6, 7.2]$
Combined	$0.94\ ^{+1.05}_{-1.05}$	1.0σ	3.0	2.3	$[1.6, 3.2]$	$[1.2, 4.5]$

Table 4.5: Summary of the measurement results from the fully-leptonic and semi-leptonic channels. The best-fit value of the signal strength μ is provided with the total uncertainty. The observed significance Z_0 is obtained from the test statistic q_0 for the discovery. The 95% confidence level (CL) upper limit (UL) on μ is given by the test statistic q_μ. It is compared to the median expected limit for the background-only hypothesis. The 68% and 95% confidence intervals around the expected value are denoted by $\pm1\sigma$ and $\pm2\sigma$, respectively.

4.5 aQGC Search

The 95% confidence level intervals on the aQGC parameters $f_{S,0}$ and $f_{S,1}$ are computed using the same methodology as in Section 3.9. The combined one-dimensional limits, determined for each anomalous coupling with the other one set to zero, are listed in Table 4.6 while the two-dimensional limits, determined simultaneously for both couplings, are shown in Figure 4.5.

Non-unitarized limits can be compared to more stringent limits set by the CMS collaboration in a vector boson scattering channel [146]. Limits on aQGC parameters (α_4, α_5) have been derived by the ATLAS collaboration in [214] and [184]. Even though the limits obtained by this analysis can be converted into limits on α_4 and α_5 using Equations 3.1 and 3.2, a comparison is not possible because different unitarization scheme[1] has been used.

Λ_F [TeV]	CL interval [10^4 TeV^{-4}]			
	Observed		Expected	
	$f_{S,0}/\Lambda^4$	$f_{S,1}/\Lambda^4$	$f_{S,0}/\Lambda^4$	$f_{S,1}/\Lambda^4$
0.5	$[-0.74, 0.86]$	$[-0.99, 1.20]$	$[-0.79, 0.89]$	$[-1.06, 1.27]$
1	$[-0.34, 0.40]$	$[-0.48, 0.58]$	$[-0.36, 0.41]$	$[-0.52, 0.60]$
2	$[-0.20, 0.24]$	$[-0.29, 0.36]$	$[-0.22, 0.25]$	$[-0.33, 0.39]$
3	$[-0.16, 0.21]$	$[-0.25, 0.33]$	$[-0.19, 0.22]$	$[-0.29, 0.36]$
∞	$[-0.13, 0.18]$	$[-0.21, 0.27]$	$[-0.16, 0.19]$	$[-0.25, 0.30]$

Table 4.6: Expected and observed 95% confidence level (CL) intervals on $f_{S,0}/\Lambda^4$ ($f_{S,1}/\Lambda^4$) with different Λ_F values, assuming $f_{S,1}/\Lambda^4$ ($f_{S,0}/\Lambda^4$) is zero.

[1] The k-matrix unitarization scheme [175] is not applicable to triboson production.

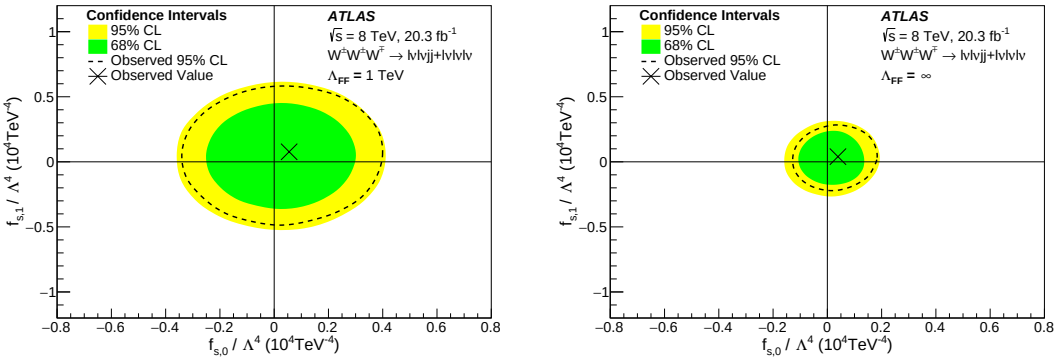

Figure 4.5: Expected 68% and 95% CL contour limits on $(f_{S,1}/\Lambda^4, f_{S,0}/\Lambda^4)$ compared to the observed 95% CL contour limit and observed best fit value for cases when $\Lambda_F = 1\,\text{TeV}$ (left) and $\Lambda_F = \infty$ (right).

CHAPTER 5

SEARCH FOR SUSY IN EVENTS WITH TWO SAME-SIGN OR THREE LEPTONS

5.1 Introduction

Direct searches for physics beyond the Standard Model are intensively pursued by the ATLAS collaboration. In particular, an extensive agenda is dedicated to the well-motivated supersymmetric extension of the SM (SUSY), described in Section 1.3. Given the variety of models leading to different final topologies, many specific analyses are designed.

The analysis [215] presented in this chapter searches for strongly produced supersymmetric particles in events with multiple jets and either two same-sign leptons or at least three leptons. Only electrons and muons are considered. This signature benefits from low SM backgrounds and therefore looser kinematic requirements can be used compared to other searches. Since gluinos are Majorana fermions which can be produced in pairs[1] and squarks can decay in cascades involving top quarks, charginos, neutralinos or sleptons, the topology studied in this analysis is predicted in many SUSY scenarios.

[1] Each gluino is expected to decay into a lepton of either charge with equal probability.

5.2 SUSY Signals

This analysis is sensitive to a large variety of new physics scenarios yielding signatures with two same-sign or three leptons. The results are interpreted in the context of eleven SUSY *simplified* models and four *phenomenological* models, which are described below.

5.2.1 Simplified Models

Simplified models are characterised by a limited number of Feynman diagrams describing the production and decay of SUSY particles, leading to the final states under study. All particles except those appearing in the decay chain of interest are decoupled by setting their masses to very high values. Moreover, only on-shell particles are considered and virtual particles are replaced by an effective vertex. Therefore, these models allow to reduce the dimensionality of the SUSY parameter space to two-to-four sparticle mass parameters providing the simplest spectra compatible with a SUSY-like topology. This strategy is based on the *on-shell effective field theory* [216] and offers a more efficient and transparent representation of experimental results. Moreover, complex models with multiple decay modes, such as the MSSM, can be studied by taking linear combinations of results from these single decay modes and assigning each of them the proper production cross-section and branching ratio [217, 218].

The simplified models studied in this analysis are illustrated in Figure 5.1. They can be divided into three classes: gluino-mediated top squark, gluino-mediated (or direct) squark and direct sbottom production. Their signal topologies, described below, are then used for the optimisation of the event selection.

Gluino-mediated top squarks

In the first category, gluinos are produced in pairs and decay to the top squark $\tilde{t}_1$ which is assumed to be the lightest squark, as motivated by naturalness arguments. The $\tilde{g} \to t\tilde{t}_1^{(*)}$ branching fraction is set to 100%. The decay mode of top squark is different for each of the four considered models: $\tilde{t}_1 \to t\tilde{\chi}_1^0$, $\tilde{t}_1 \to b\tilde{\chi}_1^{\pm}$, $\tilde{t}_1 \to c\tilde{\chi}_1^0$ or $\tilde{t}_1 \to bs$. Feynman diagrams for three of these models are shown in Figure 5.2.

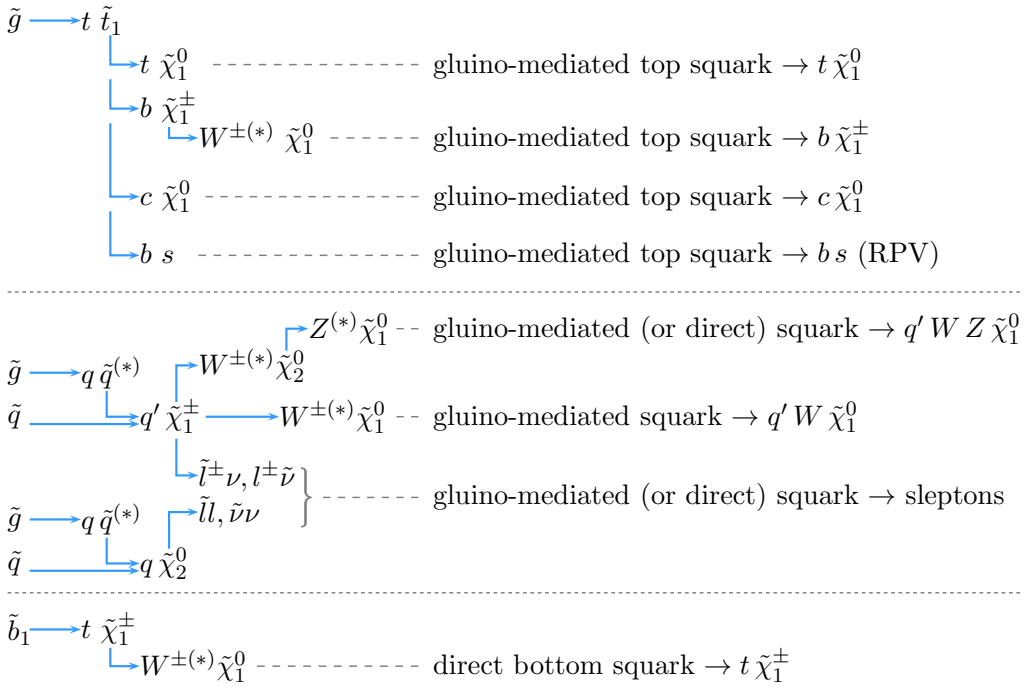

Figure 5.1: Overview of the decay modes present in the simplified SUSY models considered by this analysis. The initial SUSY particles ($\tilde{g}$, $\tilde{q}$ or $\tilde{b}_1$) are produced in pairs. The superscript * denotes the off-shell particle in the SM (e.g. W^* is off-shell W) while the antiparticle in the SUSY models (e.g. $\tilde{t}_1^*$ is top antisquark).

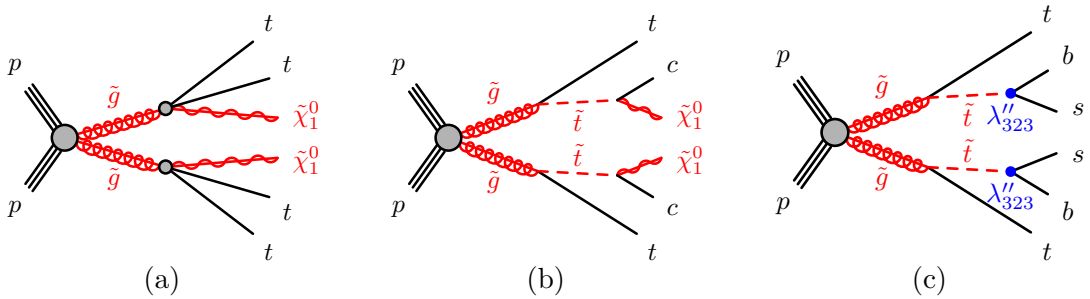

Figure 5.2: Examples of Feynman diagrams [219] illustrating the considered simplified models for gluino-mediated top squark production: (a) off-shell top squark decaying to $t\tilde{\chi}_1^0$, (b) on-shell top squark decaying to $c\tilde{\chi}_1^0$ and (c) on-shell top squark decaying to bs via the *UDD*-type RPV coupling.

In the *gluino-top squark ($t\tilde{\chi}_1^0$) off-shell* model, the mass of top squark is set to 2.5 TeV while all other squarks are decoupled. The gluino is assumed to be lighter than the squarks and therefore decays through an off-shell top quark to

a top quark pair and a stable neutralino, $\tilde{g} \to t\tilde{t}_1^* \to tt\tilde{\chi}_1^0$. The final state is $\tilde{g}\tilde{g} \to bbbb\,WWWW\,\tilde{\chi}_1^0\tilde{\chi}_1^0$ with the kinematic bound of $m_{\tilde{g}} > 2m_t + m_{\tilde{\chi}_1^0}$.

In the *gluino-top squark ($b\tilde{\chi}_1^\pm$) on-shell* model, the top squark is produced on-shell, $m_{\tilde{g}} > m_t + m_{\tilde{t}_1}$, and subsequently decays to $b\tilde{\chi}_1^\pm$. Since the masses of $\tilde{\chi}_1^\pm$ and $\tilde{\chi}_1^0$ are set to 118 GeV and 60 GeV, respectively, the chargino decays via a virtual W boson to a stable neutralino. The final state is therefore $\tilde{g}\tilde{g} \to bbbb\,WWW^*W^*\,\tilde{\chi}_1^0\tilde{\chi}_1^0$.

In the *gluino-top squark ($c\tilde{\chi}_1^0$) on-shell* model, there is a small mass splitting between the on-shell top squark and stable neutralino, $\Delta m(\tilde{t}_1, \tilde{\chi}_1^0) = 20$ GeV. The top squark decaying to a top quark is hence forbidden and the $c\tilde{\chi}_1^0$ channel is allowed exclusively. With the constraint that $m_{\tilde{g}} > m_t + m_c + m_{\tilde{\chi}_1^0}$, the final state is $\tilde{g}\tilde{g} \to bbcc\,WW\,\tilde{\chi}_1^0\tilde{\chi}_1^0$.

In the *gluino-top squark (bs) RPV* model, the on-shell top squark decays with an R-parity- and baryon-number-violating coupling $\lambda''_{323} = 1$ into bottom and strange quarks. Unlike the other models, this one gives rise to final state with rather small missing transverse energy, $\tilde{g}\tilde{g} \to bbbb\,ss\,WW$.

Gluino-mediated (or direct) 1st and 2nd generation squarks

In the second class of simplified models, the left-handed partners of the light-flavour quarks are degenerate in mass and are together referred to as squarks ($\tilde{q}$). They are produced either directly in pairs ($\tilde{q}\tilde{q}$) or via gluinos ($\tilde{g}\tilde{g} \to qq\tilde{q}\tilde{q}$), and the $\tilde{\chi}_1^0$ is assumed to be the LSP. Figure 5.3 shows the allowed decay chains for each considered model.

In the *squark production with one-step decay*, the squark decays to $qW\tilde{\chi}_1^0$ via a chargino whose mass is twice that of the LSP, $m_{\tilde{\chi}_1^\pm} = 2m_{\tilde{\chi}_1^0}$. The final states for direct (gluino-mediated) production are therefore $(qq)\,q'q'\,W^{(*)}W^{(*)}\,\tilde{\chi}_1^0\tilde{\chi}_1^0$. Since gluinos are Majorana particles, same-sign leptons can arise only from the $\tilde{g}\tilde{g}$ case.

In the *squark production with two-step decay via gauginos*, squarks decay in a cascade involving a chargino and a heavy neutralino, $\tilde{q} \to q'\tilde{\chi}_1^\pm \to q'W\tilde{\chi}_2^0 \to q'WZ\tilde{\chi}_1^0$. The intermediate particle masses are set to $m_{\tilde{\chi}_1^\pm} = (m_{\tilde{g}/\tilde{q}} + m_{\tilde{\chi}_1^0})/2$ and $m_{\tilde{\chi}_2^0} = (m_{\tilde{\chi}_1^\pm} + m_{\tilde{\chi}_1^0})/2$. The final state for direct (gluino-mediated) production is $(qq)\,q'q'\,W^{(*)}W^{(*)}Z^{(*)}Z^{(*)}\,\tilde{\chi}_1^0\tilde{\chi}_1^0$. The W and Z bosons are on-shell or off-shell

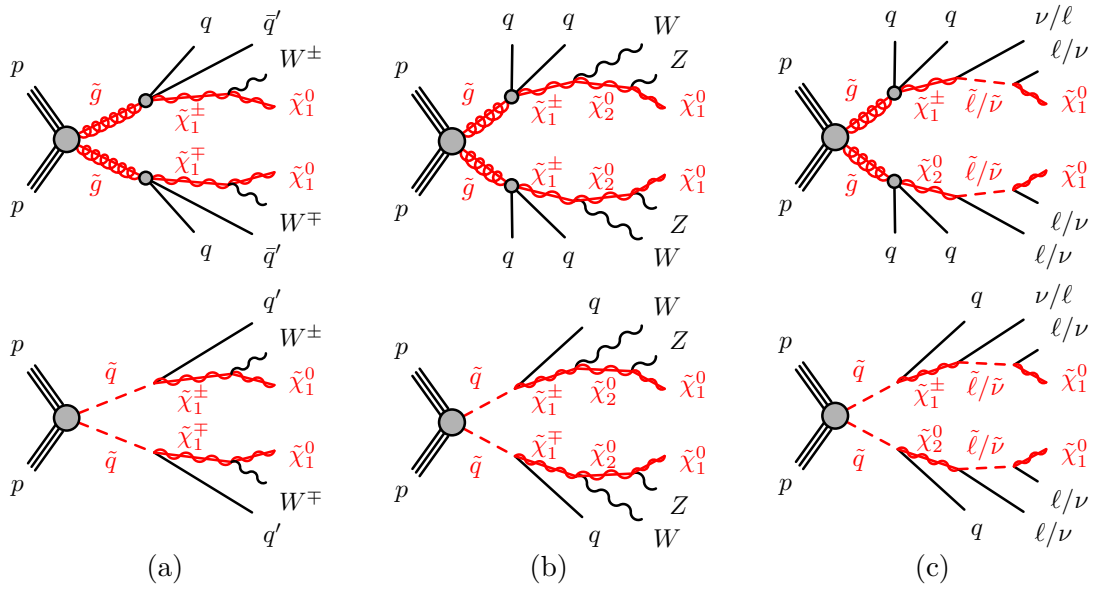

Figure 5.3: Feynman diagrams [219] illustrating the considered simplified models for gluino-mediated (first row) and direct (second row) squark production: (a) one-step decay, (b) two-step decay via gauginos and (c) two-step decay via sleptons.

according to the mass splitting $\Delta m(\tilde{g}/\tilde{q}, \tilde{\chi}_1^0)$.

In the *squark production with two-step decay via sleptons*, two decay channels for a squark are allowed with equal probabilities, $\tilde{q} \to q'\tilde{\chi}_1^\pm$ and $\tilde{q} \to q\tilde{\chi}_2^0$. Furthermore, the chargino and the second neutralino decay with equal branching fractions as $\tilde{\chi}_1^\pm \to \tilde{\ell}\nu/\ell\tilde{\nu}$ or $\tilde{\chi}_2^0 \to \ell\tilde{\ell}/\nu\tilde{\nu}$, respectively. Finally, sleptons and sneutrinos decay always to the LSP as follows: $\tilde{\ell} \to \ell\tilde{\chi}_1^0$ and $\tilde{\nu} \to \nu\tilde{\chi}_1^0$. The masses of the intermediate gauginos are assumed to be equal and set to $m_{\tilde{\chi}_1^\pm} = m_{\tilde{\chi}_2^0} = (m_{\tilde{g}/\tilde{q}} + m_{\tilde{\chi}_1^0})/2$. The masses of all three slepton generations are degenerated and assumed to be equal to those of sneutrinos, $m_{\tilde{\ell}} = m_{\tilde{\nu}} = (m_{\tilde{\chi}_2^0} + m_{\tilde{\chi}_1^0})/2$. The possible final states for a squark decay are therefore $\tilde{q} \to q'\ell\nu\tilde{\chi}_1^0$, $\tilde{q} \to q\ell\ell\tilde{\chi}_1^0$ and $\tilde{q} \to q\nu\nu\tilde{\chi}_1^0$.

Direct bottom squarks

In this scenario, the pair production of bottom squarks is followed by two subsequent decays with branching fractions of 100%: $\tilde{b}_1 \to t\tilde{\chi}_1^\pm$ and $\tilde{\chi}_1^\pm \to W^{(*)}\tilde{\chi}_1^0$.

Two models where the $\tilde{\chi}_1^0$ is the LSP are considered: one with $m_{\tilde{\chi}_1^0} = 60$ GeV and another with $m_{\tilde{\chi}_1^\pm} = 2m_{\tilde{\chi}_1^0}$. The corresponding Feynman diagram is shown in Figure 5.4.

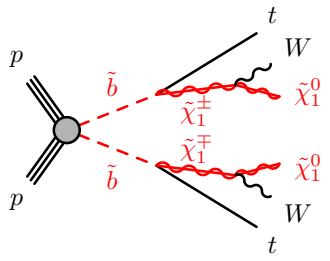

Figure 5.4: Feynman diagram [219] illustrating the considered simplified model for direct bottom squark production.

5.2.2 Phenomenological Models

In addition to the simplified scenarios, the results are interpreted in the context of four complex models where many different production and decay processes contribute: mSUGRA/CMSSM [220–225], bRPV [226], GMSB [227–232] and mUED [233].

mSUGRA

In the minimal supergravity (mSUGRA) framework, also known as constrained MSSM (CMSSM) [220–225], the SUSY breaking mechanism is mediated from the "hidden" to the "visible" sector by the gravitational interactions. It is characterised by mass unification at the grand unified theory (GUT) scale which reduces the number of MSSM parameters to five: the universal scalar and gaugino mass parameters m_0 and $m_{1/2}$, the universal trilinear coupling parameter A_0, the ratio of the vacuum expectation values of the two Higgs doublets $\tan(\beta)$ and the sign of the SUSY Higgs mass parameter μ. Three of these parameters are set to the following values: $\tan(\beta) = 30$, $A_0 = -2m_0$ and $\mu > 0$, which allow for a Higgs boson mass between 122 and 128 GeV [234].

bRPV

The bRPV [226] scenario is based on the mSUGRA/CMSSM model, but R-parity violation is allowed through the bilinear terms in the superpotential. The

neutralino LSP is thus unstable and decays promptly to $W^{(*)}\tau$, $W^{(*)}\mu$, $Z^{(*)}\nu_\tau$ or $h^{(*)}\nu_\tau$. The coupling parameters are determined by a fit to neutrino oscillation data [235] under the tree-level dominance scenario [236].

GMSB

The gauge-mediated SUSY breaking (GMSB) model postulates that the SUSY breaking is communicated to the MSSM via the SM gauge interactions [227–232]. It is described by six free parameters: the SUSY-breaking mass scale Λ, the mass of the messenger field(s) M_{mess}, the number of $SU(5)$ messenger fields N_5, the ratio of the vacuum expectation values of the two Higgs doublets $\tan(\beta)$, the sign of the SUSY Higgs mass parameter μ and the scale factor for the gravitino mass C_{grav}. Four parameters are fixed such that the production of squark and/or gluino pairs dominates at the present LHC energy: $M_{\text{mess}} = 250$ TeV, $N_5 = 3$, $\mu > 0$ and $C_{\text{grav}} = 1$, as previously used in [237–239]. The LSP is the gravitino with very small mass of $\mathcal{O}$(keV).

mUED

The minimal universal extra dimension (mUED) [233] scenario is a non-SUSY model with one additional universal spatial dimension. The Kaluza-Klein (KK) quark decays to the lightest KK particle (the KK photon) which is stable and escapes detection, resulting in a signature similar to that of the SUSY decay chains described previously. The radius of the compact dimension R and the cut-off scale Λ are the two parameters of the model.

5.3 Data and Simulated Event Samples

5.3.1 Data

This search uses 20.3 fb^{-1} of pp collision data collected with the ATLAS detector at $\sqrt{s} = 8$ TeV, selected using the same quality requirements as the analysis described in Section 3. The uncertainty on the integrated luminosity is 2.8% following the same methodology as in [240].

Events are selected using a combination of $E_{\mathrm{T}}^{\mathrm{miss}}$, non-isolated single-lepton and di-lepton triggers. The trigger threshold for high-$E_{\mathrm{T}}^{\mathrm{miss}}$ events is 80 GeV. The transverse momentum thresholds for single-lepton triggers are 60 GeV for electrons and 36 GeV for muons. Di-electron and electron-muon events are selected using lower p_{T} threshold triggers (12 GeV for electrons and 8 GeV for muons). The di-muon trigger features two different p_{T} thresholds of 18 GeV for the leading muon and 8 GeV for the subleading muon. Neither of the leptonic triggers is considered if an event is already selected using the $E_{\mathrm{T}}^{\mathrm{miss}}$ trigger.

5.3.2 Background Processes

SM processes with two prompt same-sign leptons or three leptons in the final state represent the irreducible backgrounds which are estimated using MC simulations. Samples for $t\bar{t}V$, $t\bar{t}WW$, tZ, $t\bar{t}t\bar{t}$, VVV ($V = W, Z$) are generated with MadGraph interfaced to Pythia6. Diboson production of ZZ is simulated using Powheg with Pythia8, while the WZ, $W^{\pm}W^{\pm}$ processes are modelled using Sherpa with matrix elements producing up to three final-state partons. This choice is motivated by the good description of jet multiplicity provided by the Sherpa prediction, as discussed in Section 4. The Pythia8 generator is used to simulate the $t\bar{t}H$ and VH samples. To calculate the MC modelling systematic uncertainties, alternative $t\bar{t}V$ and ZZ samples are generated with Alpgen interfaced to Herwig+Jimmy and Mc@nlo, respectively. The latter is matched either to Pythia6 or Herwig+Jimmy parton showers.

Other processes which can produce the same experimental signature as the SUSY signals through lepton mis-reconstruction, are estimated by data-driven methods. Nevertheless, the corresponding MC samples are generated for the purpose of dedicated studies and cross-checks. Samples of W/Z+jets and $W^{+}W^{-}$ are simulated with Sherpa. The $W\gamma$ process is generated with Alpgen interfaced to Herwig+Jimmy. Simulated $t\bar{t}$ events, used to provide corrections to the data-driven background estimates, are produced using Powheg with Pythia6. In order to increase the statistical power, additional $t\bar{t}$ samples generated with Powheg, Mc@nlo and Alpgen, all interfaced to Herwig+Jimmy, are also used. Single top production is simulated with Mc@nlo (s-channel and Wt pro-

cess) and AcerMC (t-channel).

The PDF sets, tunes for parton shower and hadronization modelling, and minimum-bias events are applied in the same way as described in Section 3.2.2. All MC background samples are processed through the full detector response simulation[1].

5.3.3 Signal Processes

The signal samples corresponding to the models considered by this analysis are generated with Herwig or MadGraph interfaced to Pythia6, using CTEQ6L1 parton distribution function (PDF) set. Cross-sections are calculated at next-to-leading order (NLO) including the resummation of soft gluon emission at next-to-leading-logarithmic (NLL) accuracy [241–245]. Cross-section uncertainties are obtained by comparing the predictions using different PDF sets and factorisation and renormalisation scales, as described in [246]. Except for the gluino-top squark models in the off-shell ($t\tilde{\chi}_1^0$) and on-shell ($b\tilde{\chi}_1^\pm$) channels, all signal samples are simulated using Atlfast-II.

5.4 Object Definition

This section briefly describes the selection criteria for all reconstructed objects used in this analysis. Most of the baseline requirements are defined by the ATLAS SUSY working group. More stringent definitions for leptons, referred to as signal leptons, are optimized for this particular SUSY search.

5.4.1 Leptons

Leptons are reconstructed using the same algorithms as in the previous analysis (Sections 3.3.1 and 3.3.2). However, the requirements on the track parameters d_0 and z_0 are in this case imposed on the signal leptons and a looser criteria $|d_0/\sigma_{d_0}| < 5$ is added to the baseline electron definition in order to reduce the charge-flip background. Both *combined* (CB) and *segment-tagged* (ST) muons

[1] Atlfast-II is used only for $t\bar{t}$ Powheg samples.

are used. The latter type extrapolates the inner detector tracks into the muon spectrometer (MS) and searches for matched hits in the MS segments. Here the *loose* muon quality is considered [178]. Signal leptons fulfil tighter selection criteria and $p_{\mathrm{T}} > 15$ GeV. This rather soft p_{T} requirement increases the sensitivity of the analysis in the compressed regions of the phase space. To further reduce the fake lepton background, the calorimeter and track isolations have been studied using different thresholds and cone radiuses ($\Delta R = 0.2$ or $\Delta R = 0.3$). It has been shown that tighter definitions for leptons with $p_{\mathrm{T}} < 60$ GeV increase the signal significance, defined in Equation 5.1. The final selection requirements for electrons and muons are summarised in Tables 5.1 and 5.2, respectively.

Pre-selected electrons	
Algorithm	`AuthorElectron`
Acceptance	$p_{\mathrm{T}} > 10\,\mathrm{GeV}$, $\lvert\eta\rvert < 2.47$
Quality	Medium
Transverse impact parameter	$\lvert d_0/\sigma_{d_0}\rvert < 5$
e-j isolation	$\Delta R(e, j) > 0.4$
e-μ isolation	$\Delta R(e, \mu) > 0.1$
Signal electrons	
Quality	Tight
Acceptance	$p_{\mathrm{T}} > 15\,\mathrm{GeV}$
Transverse impact parameter	$\lvert d_0/\sigma_{d_0}\rvert < 3$
Longitudinal impact parameter	$\lvert z_0 \sin\theta\rvert < 0.4$ mm
Track isolation	$p_{\mathrm{T}}^{\mathrm{Cone}\,0.2}/\min(p_{\mathrm{T}}, 60\ \mathrm{GeV}) < 0.06$
Calorimeter isolation	$E_{\mathrm{T}}^{\mathrm{Cone}\,0.2}/\min(E_{\mathrm{T}}, 60\ \mathrm{GeV}) < 0.06$

Table 5.1: Summary of the electron selection criteria. The signal requirements are applied on top of the pre-selection. For electrons with $p_{\mathrm{T}} > 60$ GeV, the relative track and calorimeter isolation is replaced by a fixed upper limit of 3.6 GeV ($0.06 \cdot 60$ GeV) on the $p_{\mathrm{T}}^{\mathrm{Cone}\,0.2}$ and $E_{\mathrm{T}}^{\mathrm{Cone}\,0.2}$ variables.

Pre-selected muons	
Algorithm	`STACO` (CB or ST)
Acceptance	$p_{\mathrm{T}} > 10\,\mathrm{GeV}$, $\lvert\eta\rvert < 2.5$
Quality	Loose
Inner detector track quality	MCP ID hits selection
μ-j isolation	$\Delta R(\mu, j) > 0.4$
Signal muons	
Acceptance	$p_{\mathrm{T}} > 15\,\mathrm{GeV}$
Transverse impact parameter	$\lvert d_0/\sigma_{d_0}\rvert < 3$
Longitudinal impact parameter	$\lvert z_0 \sin\theta\rvert < 0.4$ mm
Track isolation	$p_{\mathrm{T}}^{\mathrm{Cone}\,0.3}/\min(p_{\mathrm{T}}, 60\ \mathrm{GeV}) < 0.12$
Calorimeter isolation	$E_{\mathrm{T}}^{\mathrm{Cone}\,0.3}/\min(E_{\mathrm{T}}, 60\ \mathrm{GeV}) < 0.12$

Table 5.2: Summary of the muon selection criteria. The signal requirements are applied on top of the pre-selection. For muons with $p_{\mathrm{T}} > 60$ GeV, the relative track and calorimeter isolation is replaced by a fixed upper limit of 7.2 GeV ($0.12 \cdot 60$ GeV) on the $p_{\mathrm{T}}^{\mathrm{Cone}\,0.3}$ and $E_{\mathrm{T}}^{\mathrm{Cone}\,0.3}$ variables.

5.4.2 Jets

The jet reconstruction procedure and calibration scheme applied in this analysis are identical to those described in Section 3.3.3. Selected jets are required to have transverse momentum $p_{\mathrm{T}} > 20$ GeV and $|\eta| < 2.8$. Since it has been shown that the jet multiplicity in the events with two leptons and several jets is not sensitive to pile-up effects, no requirement on the jet vertex fraction is applied. The *MV1* algorithm with an efficiency of 70% is used to tag b-jets with $p_{\mathrm{T}} > 20$ GeV and $|\eta| < 2.5$. The p_{T} of signal jets is increased to 40 GeV. The selection requirements for jets and b-jets are summarized in Table 5.3.

5.4.3 Missing Transverse Energy

The definition of missing transverse energy described in Section 3.3.4 is used, except a few differences. Firstly, since this analysis does not include reconstructed

Pre-selected jets	
Algorithm	anti-k_t with $\Delta R = 0.4$ (LCW+JES)
Acceptance	$p_{\mathrm{T}} > 20\,\mathrm{GeV}$, $\lvert\eta\rvert < 2.8$
j-e isolation	$\Delta R(j, e) > 0.2$
***b*-jets**	
Acceptance	$p_{\mathrm{T}} > 20\,\mathrm{GeV}$, $\lvert\eta\rvert < 2.5$
b-tagging	MV1 algorithm 70%
Signal jets	
Acceptance	$p_{\mathrm{T}} > 40\,\mathrm{GeV}$, $\lvert\eta\rvert < 2.8$

Table 5.3: Summary of the jet selection criteria. The b-jet and signal requirements are applied on top of the jet selection.

τ-jets, a specific variant of $E_{\mathrm{T}}^{\mathrm{miss}}$ algorithm is applied. The contribution from hadronic τ-leptons is then included either in the jet term or in the soft term, according to the p_{T} of the associated jet. These are typically used to recover low-p_{T} muons without independent p_{T} measurement in the muon spectrometer. Secondly, no additional soft term vertex fraction (STVF) corrections suppressing the pile-up are implemented, in order to harmonise with other SUSY analyses and ease comparisons and combinations.

5.4.4 Overlap Removal

Given that the reconstruction algorithms are independent, the same particle may be reconstructed as two different objects within the ATLAS detector. These ambiguities are resolved by applying the following criteria in subsequent steps. Jets within a distance $\Delta R < 0.2$ of a pre-selected electron are removed. To reject leptons originating from (heavy-flavour) hadron decays, lepton candidates must be well separated from any remaining jet, i.e. $\Delta R > 0.4$[1]. If an electron is separated by less than $\Delta R = 0.1$ from a muon, the electron is discarded. Leptons and jets considered in the overlap removal procedure pass the pre-selection criteria.

[1]This overlap removal is not applied in the previously described SM analysis (Section 3) because targeted SUSY signatures contain, besides well isolated leptons, also jets.

5.5 Event Selection

Events are selected following the trigger and object selection criteria described in Sections 5.3.1 and 5.4. The main advantage of using a logical OR of $E_{\mathrm{T}}^{\mathrm{miss}}$ and single-lepton and di-lepton triggers is the increase in event selection efficiency. The thresholds applied offline to $E_{\mathrm{T}}^{\mathrm{miss}}$ and the leading and subleading lepton p_{T} are higher than those applied online, in order to ensure that trigger efficiencies are constant in the phase space of interest. Contributions from detector noise and non-collision backgrounds are removed using the same cleaning requirements as in Section 3.4.1. An additional veto on bad and cosmic muons rejects events with poorly reconstructed muons and muons with $|z_0| > 1$ mm and $|d_0| > 0.2$ mm. Moreover, the primary vertex of the event must have at least five associated tracks with $p_{\mathrm{T}} > 0.4$ GeV.

Candidate events are further required to contain at least two signal leptons with the p_{T} of the leading one higher than 20 GeV. To remove events with pairs of energetic leptons from heavy-flavour hadron decays, the invariant mass of a leading lepton pair is required to be above 12 GeV.

5.5.1 Signal Regions

Five non-overlapping signal regions are defined based on a combination of the signal regions from a previous version of this analysis [247] and a dedicated three lepton search [248]. Events are firstly divided into two exclusive samples according to the lepton multiplicity. In the sample with exactly two signal leptons, they have to be of the same electric charge and satisfy $p_{\mathrm{T}} > [20, 15]$ GeV. In the sample with at least three tight leptons, the three with the highest p_{T} must fulfil $p_{\mathrm{T}} > [20, 15, 15]$ GeV, respectively. Afterwards, the following kinematic variables are computed for each event: missing transverse energy ($E_{\mathrm{T}}^{\mathrm{miss}}$), jet and b-jet multiplicities (N_{jet} and $N_{b\text{-jet}}$), effective mass (m_{eff}) and transverse mass (m_{T}). The effective mass is calculated from all signal leptons and selected jets as $m_{\mathrm{eff}} = E_{\mathrm{T}}^{\mathrm{miss}} + \sum p_{\mathrm{T}}^{\ell} + \sum p_{\mathrm{T}}^{\mathrm{jet}}$ and the transverse mass is computed from the leading lepton (ℓ_1) as $m_{\mathrm{T}} = \sqrt{2 p_{\mathrm{T}}^{\ell_1} E_{\mathrm{T}}^{\mathrm{miss}} (1 - \cos[\Delta\phi(\ell_1, E_{\mathrm{T}}^{\mathrm{miss}})])}$.

The event selection criteria are optimized by maximising the expected discovery significance using simulated events from the simplified models in Figure 5.1. The following approximate formula, derived from Equation 3.60 assuming a simple counting experiment [209], is used:

$$\text{med}[Z_0|1] \approx \sqrt{2\left((s+b)\ln\left(1+\frac{s}{b}\right)-s\right)} = Z_0^{\text{opt}} \tag{5.1}$$

where s and b represent the expected number of signal and background events. To account for the systematic uncertainties on the background estimate, the background yield b is substituted by $b + \sigma_b$ where σ_b is fixed to 40%. This simplified approach has been validated and found to be reliable.

The final signal region selections are summarized in Table 5.4. As will be further discussed in Section 5.9, the analysis performs two fits: one for *discovery* and one for *exclusion*. Additional requirements on m_{eff} are used only in the discovery fit configuration. To ensure that all five signal regions are mutually exclusive, an SR3b veto is included. The invariant mass of all possible opposite-sign same-flavour lepton combinations is required to be outside the Z-mass window ($85 < m_{\ell\ell} < 98$ GeV) in SR3Llow to reduce the contribution from Z production. No Z veto is applied in SR3Lhigh as one signal model produces Z bosons in the decay chain. In addition, Z backgrounds are already suppressed by the higher $E_{\text{T}}^{\text{miss}}$ requirement.

Each signal region is motivated by a different SUSY model. The signal regions requiring at least one b-jet (SR3b and SR1b) are sensitive to gluino-mediated top squark scenarios. The SR1b definition is more appropriate for events containing two b-quarks, while the SR3b selections allow to target models with small mass differences between the predicted particles as well as RPV models. The b-jet veto in the SR0b signal region enhances the sensitivity to gluino-mediated and directly produced squarks of the first and second generations. The three-lepton signal regions address mainly scenarios with two-step decays. The cascades producing off-shell and on-shell vector bosons are targeted by the SR3Llow and SR3Lhigh regions, respectively.

	SR3b	**SR0b**	**SR1b**	**SR3Llow**	**SR3Lhigh**
Leptons	SS or 3L	SS	SS	3L	3L
$N_{b\text{-jets}}$	≥ 3	$= 0$	≥ 1	–	–
N_{jets}	≥ 5	≥ 3	≥ 3	≥ 4	≥ 4
$E_{\text{T}}^{\text{miss}}$/GeV	–	> 150	> 150	$\in [50, 150]$	> 150
m_{T} /GeV	–	> 100	> 100	–	–
Veto	–	–	SR3b	SR3b and Z	SR3b
m_{eff} /GeV	> 350	> 400	> 700	> 400	> 400

Table 5.4: Definition of the signal regions. Two same-sign or three leptons must fulfil $p_{\text{T}} > [20, 15]\,\text{GeV}$ or $p_{\text{T}} > [20, 15, 15]\,\text{GeV}$, respectively. Jets ($b$-jets) are selected with $p_{\text{T}} > 40\,\text{GeV}$ ($p_{\text{T}} > 20\,\text{GeV}$). The m_{eff} requirement is only applied when running the discovery fit.

5.6 Background Estimation

As already mentioned, this analysis can impose looser kinematic requirements than other SUSY searches because of the low SM background. The processes passing the lepton selection criteria can be classified into three categories, ordered by relevance: events with prompt multi-leptons, fake leptons and charge mis-measured leptons.

5.6.1 Standard Model Background

The processes with two same-sign or three prompt leptons in the final state represent the irreducible background. The expected contribution is estimated from the MC samples normalised to NLO calculations as described in Section 5.3. The signal regions with and without b-jets are dominated by $t\bar{t}V$ and diboson processes, respectively. Several generator uncertainties are assigned to these events to ensure that the MC modelling is accurate within the estimated systematics. Other background processes, such as triboson production, single top with a Z boson, $t\bar{t}H$ and $t\bar{t}t\bar{t}$, are also considered.

5.6.1.1 Associate $t\bar{t}V$ Production

The production of top quark pair in association with a leptonically decaying vector boson ($V = W, Z$) represents the main source of background in the signal regions including b-jets. Representative Feynman diagrams are shown in Figure 5.5. These processes have been observed only recently [249, 250] due to the low cross-sections. The analysis has thus to rely on the theoretical predictions to assess this background.

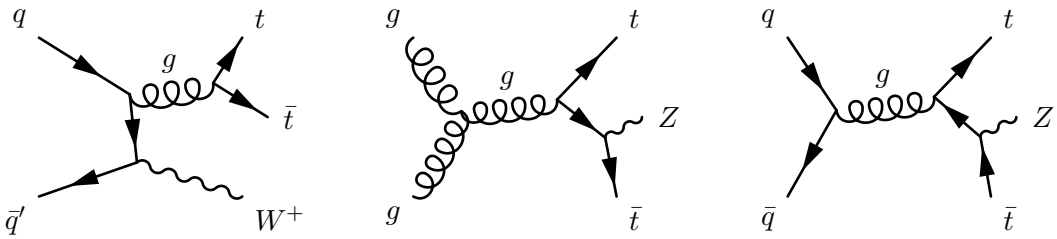

Figure 5.5: The dominant leading order Feynman diagrams for $t\bar{t}W$ and $t\bar{t}Z$ production in pp collisions. These have the same signature as the SUSY signals with b-jets, as mostly $t \to b + W$.

The NLO calculations have been performed in [194, 195]. The theoretical uncertainty assigned to the cross-section accounts for PDF and/or scale variations. The results are summarized in Table 5.5. The total uncertainty in [194] is a quadratic sum of scale and PDF+α_s uncertainties. Given that only [194] considers the effect of different PDF sets and that the scale dependence is of the same order for $t\bar{t}W$ and $t\bar{t}Z$ [195], the same theoretical uncertainty of 22% is quoted for both processes.

Although the cross section is known to NLO, MC samples are generated at LO. The events are simulated using MadGraph with matrix elements for up to two extra partons and showered with Pythia6. To avoid the double counting between matrix element and parton shower generated jets, the so-called MLM matching procedure is employed [88, 251]. The samples are normalised to the inclusive NLO cross-section using corresponding k-factors, assuming they are identical for different parton multiplicities. A shape uncertainty is expected therefore to be significant and needs to be properly assessed.

Process	μ_0	μ	σ_{NLO} [fb]	Uncertainties [%]		
				Scale	PDF+α_s	Total
$t\bar{t}W^+$	m_t	$[\mu_0/4, 4\mu_0]$	161	$(+12, -20)$	$(+7, -8)$	$(+14, -22)$
$t\bar{t}W^-$	m_t	$[\mu_0/4, 4\mu_0]$	71	$(+16, -21)$	$(+6, -8)$	$(+17, -22)$
$t\bar{t}W^+$	$m_t+m_W/2$	$[\mu_0/2, 2\mu_0]$	142.6	$(+10, -11)$	–	–
$t\bar{t}W^-$	$m_t+m_W/2$	$[\mu_0/2, 2\mu_0]$	60.5	$(+10, -12)$	–	–
$t\bar{t}Z$	$m_t+m_Z/2$	$[\mu_0/2, 2\mu_0]$	205.7	$(+9, -13)$	–	–

Table 5.5: Total NLO cross-sections at $\sqrt{s} = 8$ TeV with relative theoretical uncertainties from [194] (first two rows) and [195] (last three rows). The renormalization scale μ_R and factorization scale μ_F are set to be equal ($\mu = \mu_R = \mu_F$) and are varied up-and-down by a factor of two. The total uncertainties are quadratic sum of scale and PDF+α_s uncertainties.

The effect of the theoretical uncertainties in the factorisation and renormalisation scales, the parameters related to ISR and FSR, and the MLM matching scale `xqcut` are studied by varying these parameters up-and-down[1]. For each variation a new sample is produced at generator level. These are then used to estimate their impact on the kinematic distributions. Figure 5.6 illustrates the normalized distributions of m_{eff} and leading lepton p_{T} without applying any selection criteria. The former shows the large shape dependence due to ISR variations while the former does not depend strongly on neither of the variations.

The efficiency after each selection criteria for two simplified versions of the signal regions is plotted in Figure 5.7. Even though the baseline selection requires two same-sign or three leptons, here events with two leptons of any sign are selected in order to gain statistics. One region of the phase space is kinematically close to the SR0b and SR1b signal regions and the other one represents the SR3b with low requirement on $E_{\text{T}}^{\text{miss}}$. The biggest shift with respect to the nominal value can be seen at the jet selection stage for the samples with a varied amount of ISR in the event.

[1]The renormalisation and factorisation scales are varied up-and-down simultaneously, further denoted as "scale".

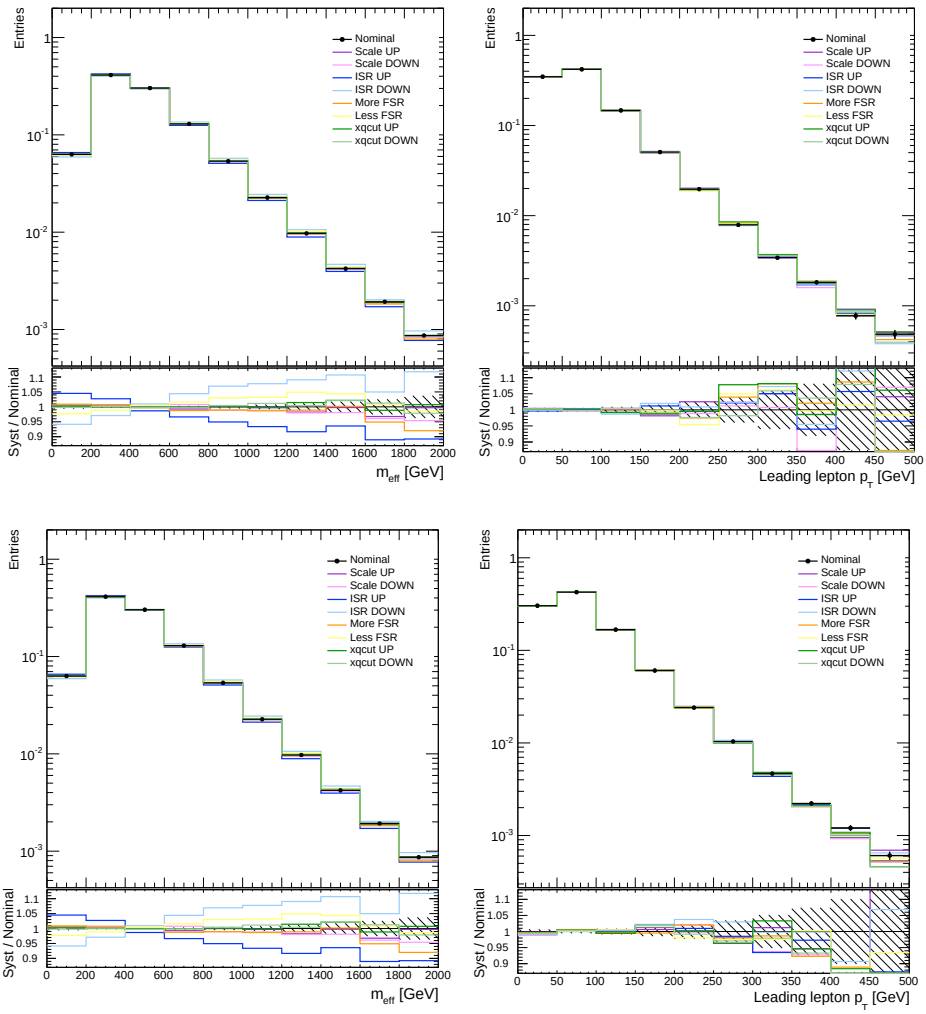

Figure 5.6: Normalized kinematic distributions of m_{eff} (left) and leading lepton p_{T} (right) for $t\bar{t}W$ (top) and $t\bar{t}Z$ (bottom) without applying any selection criteria. A sample with the nominal generator settings (black) is compared to the samples with one modified parameter value (up or down). The statistical uncertainty on the nominal sample is represented by the hashed band.

The relative deviation of each systematic variation with respect to the nominal value at each step of the selection is summarised in Table 5.6 . Since these generator uncertainties are expected to be mostly independent, they are symmetrised and combined in quadrature. The dominant uncertainty of 12% originates from the requirement on at least five jets in a simplified SR3b selection.

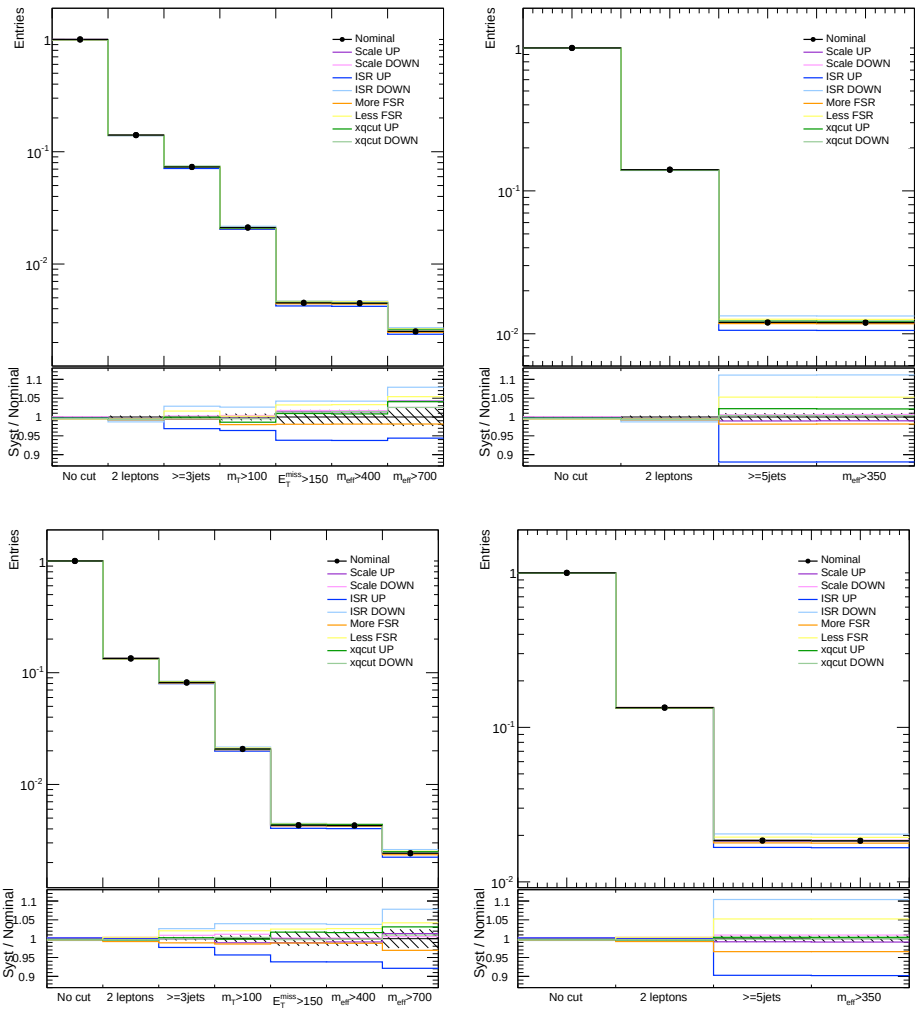

Figure 5.7: Cut efficiency for $t\bar{t}W$ (top) and $t\bar{t}Z$ (bottom) in the regions of the phase space close to SR0b and SR1b (left) and SR3b (right). A sample with the nominal generator settings (black) is compared to the samples with one modified parameter value (up or down). The statistical uncertainty on the nominal sample is represented by the hashed band.

Finally, a rather conservative uncertainty of 30% is assigned to $t\bar{t}V$ production to cover the normalization as well as the shape uncertainty.

	Variation	Baseline		SR3b		SR0b/SR1b			
		2ℓ	$3j$	$5j$	m_{eff}	m_{T}	$E_{\text{T}}^{\text{miss}}$	m_{eff}^{400}	m_{eff}^{700}
$t\bar{t}W$	scale	0.1	0.4	0.8	0.8	0.3	0.1	0.1	0.9
	ISR	0.3	3.0	11.5	11.6	3.1	5.2	5.2	6.7
	FSR	0.1	1.1	3.6	3.6	1.1	2.6	2.7	3.8
	`xqcut`	0.0	0.2	0.9	0.9	0.5	0.1	0.2	0.9
	Total	0.4	3.2	12.1	12.2	3.3	5.8	5.8	7.9
$t\bar{t}Z$	scale	0.2	0.4	0.9	0.9	1.1	0.6	0.5	0.4
	ISR	0.3	2.5	10.1	10.1	4.1	5.0	5.0	7.8
	FSR	0.6	1.6	4.3	4.3	1.7	1.8	1.9	3.6
	`xqcut`	0.0	0.1	0.2	0.2	0.2	1.1	1.0	1.1
	Total	0.7	3.0	11.0	11.0	4.6	5.5	5.4	8.6

Table 5.6: Summary of the relative systematic variations for $t\bar{t}W$ and $t\bar{t}Z$ at each step of two simplified signal regions, expressed in percent. The baseline selection consists of requiring two leptons and at least three jets. The selection criteria in the two simplified regions, denoted as SR3b and SR0b/SR1b, are applied on top of them. The scale variations are added in quadrature.

5.6.1.2 Diboson Production

The production of multiple vector bosons decaying leptonically constitutes the dominant background in the signal region vetoing b-jets. Representative Feynman diagrams for diboson production are shown in Figure 5.8. These processes pass the signal region requirements only if several additional partons are produced. As a result, they are not as precisely predicted theoretically as the inclusive production of diboson events.

The diboson processes with up to NLO QCD corrections[1] have been studied together with the theoretical uncertainties in [252, 253]. These predictions at the LHC operating energy of 8 TeV are given in Table 5.7. The cross-section uncertainties in [252] are estimated from their dependencies on factorisation and renormalization scales, PDF sets and α_s values. The scale variation alone is

[1]The first computations of next-to-next-to-leading order (NNLO) QCD corrections to the diboson processes [186, 189] were not available at the time of this analysis.

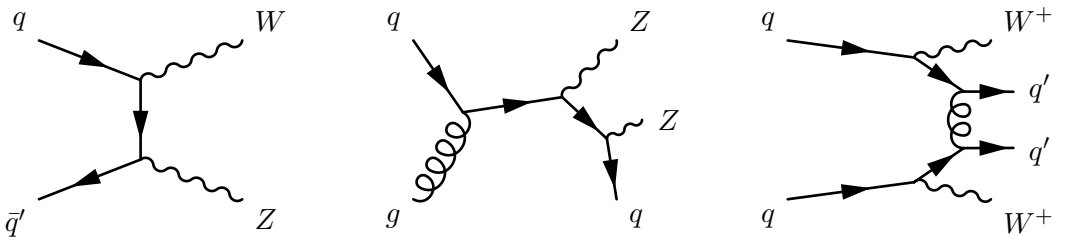

Figure 5.8: Examples of Feynman diagrams at leading and next-to-leading orders for WZ, ZZ and W^+W^+ production in pp collisions. Same signature as the SUSY signals without b-jets, as characterized by leptons and jets.

considered in [253]. A theoretical uncertainty of 7% is assigned for WZ and 5% for ZZ, as recommended in [252].

Process	μ_0	μ	σ_{NLO} [pb]	**Uncertainties** [%]		
				Scale	**PDF+α_s**	**Total**
W^+Z	$m_W+m_Z/2$	$[\mu_0/2, 2\mu_0]$	14.45	$(+5.5, -4.2)$	$(+4.3, -3.4)$	$(+7.0, -5.5)$
W^-Z	$m_W+m_Z/2$	$[\mu_0/2, 2\mu_0]$	8.38	$(+5.7, -4.3)$	$(+4.3, -4.0)$	$(+7.1, -5.9)$
ZZ	m_Z	$[\mu_0/2, 2\mu_0]$	7.27	$(+2.6, -2.1)$	$(+4.3, -3.5)$	$(+5.0, -4.1)$
W^+Z	$m_W+m_Z/2$	$[\mu_0/2, 2\mu_0]$	14.48	$(+5.2, -4.0)$	–	–
W^-Z	$m_W+m_Z/2$	$[\mu_0/2, 2\mu_0]$	8.40	$(+5.4, -4.1)$	–	–
ZZ	m_Z	$[\mu_0/2, 2\mu_0]$	7.92	$(+4.7, -3.0)$	–	–

Table 5.7: Total NLO cross sections at $\sqrt{s} = 8$ TeV with relative theoretical uncertainties from [252] (first three rows) and [253] (last three rows). The renormalization scale μ_R and factorization scale μ_F are set to be equal and are generally chosen to be the average mass of the vector bosons. They are varied independently up-and-down by a factor of two ($\mu = \mu_R$ or $\mu = \mu_F$) but with the constraint $0.5 \leq \mu_R/\mu_F \leq 2$ in [252]. In [253], the common scale is varied around the central value by a factor of two ($\mu = \mu_R = \mu_F$). The total uncertainties are quadratic sum of scale and PDF+α_s uncertainties.

The WZ process is modelled at NLO using Sherpa with matrix elements producing up to three final-state partons. The merging of matrix elements and parton showers is accomplished through the application of the CKKW merging

algorithm [87,251]. To estimate the impact of the theoretical uncertainties, three generator parameters are varied with respect to the nominal configuration: factorisation scale, renomalisation scale and CKKW matching scale. Six samples with these up-and-down variations are generated at the truth level and used to study how the shape of the predictions is affected. Given that these samples are produced with two additional partons instead of three, the requirement on the number of jets is relaxed by one with respect to the selections applied in the analysis. Additional MC modelling uncertainty arises from the limited number of hard jets that can be produced from the matrix element calculations in SHERPA samples.

The ZZ events used in the analysis are generated at NLO with POWHEG interfaced to PYTHIA8. The theoretical uncertainty estimate is assessed by comparing the samples with various values of the renormalisation and factorisation scale. Given that these are modelled with MC@NLO, another uncertainty is assigned to this background by symmetrising the largest difference between the predictions of various MC generators, such POWHEG+PYTHIA8, MC@NLO+PYTHIA6 and MC@NLO+HERWIG.

The impact of the above mentioned theoretical uncertainties on the shape of the distributions is studied in three regions of the phase space which reproduce the SR0b and SR1b, SR3b and SR3Llow signal regions but are less limited by statistics. Figures 5.9 and 5.10 show the normalized m_{eff} distribution with no selection applied together with the cut efficiencies for WZ and ZZ, respectively. The most significant variation is found to be associated to the factorisation scale. Tables 5.8 and 5.9 summarise the relative contributions of each uncertainty in the simplified signal regions. The difference between the WZ samples with two and three extra partons gives the largest uncertainty of 163% in SR3b, after the requirement on the jet multiplicity. Nevertheless, the contribution from diboson processes is negligible in this region. Moreover, the statistical uncertainty dominates in the ZZ results and prevents a quantitative statement on the size of the theoretical uncertainties in the regions of interest.

Finally, the total theoretical uncertainty assigned to the diboson processes varies from 35% to 163% according to the signal region.

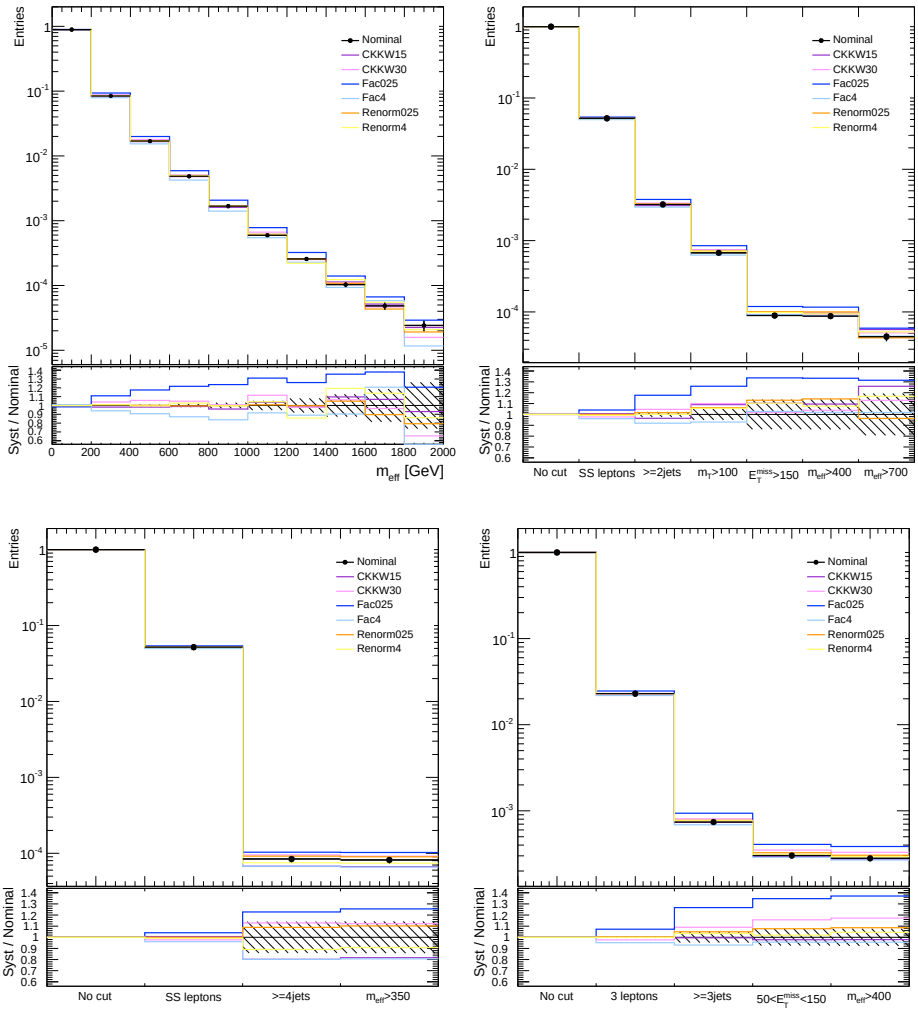

Figure 5.9: WZ systematic variations in the normalized m_{eff} distribution without applying any selection criteria (top left) and cut efficiencies in the regions for the phase space close to SR0b and SR1b (top right), SR3b (bottom left) and SR3Llow (bottom right). A sample with the nominal generator settings (black) is compared to the samples with one modified parameter value (up or down). The statistical uncertainty on the nominal sample is represented by the hashed band.

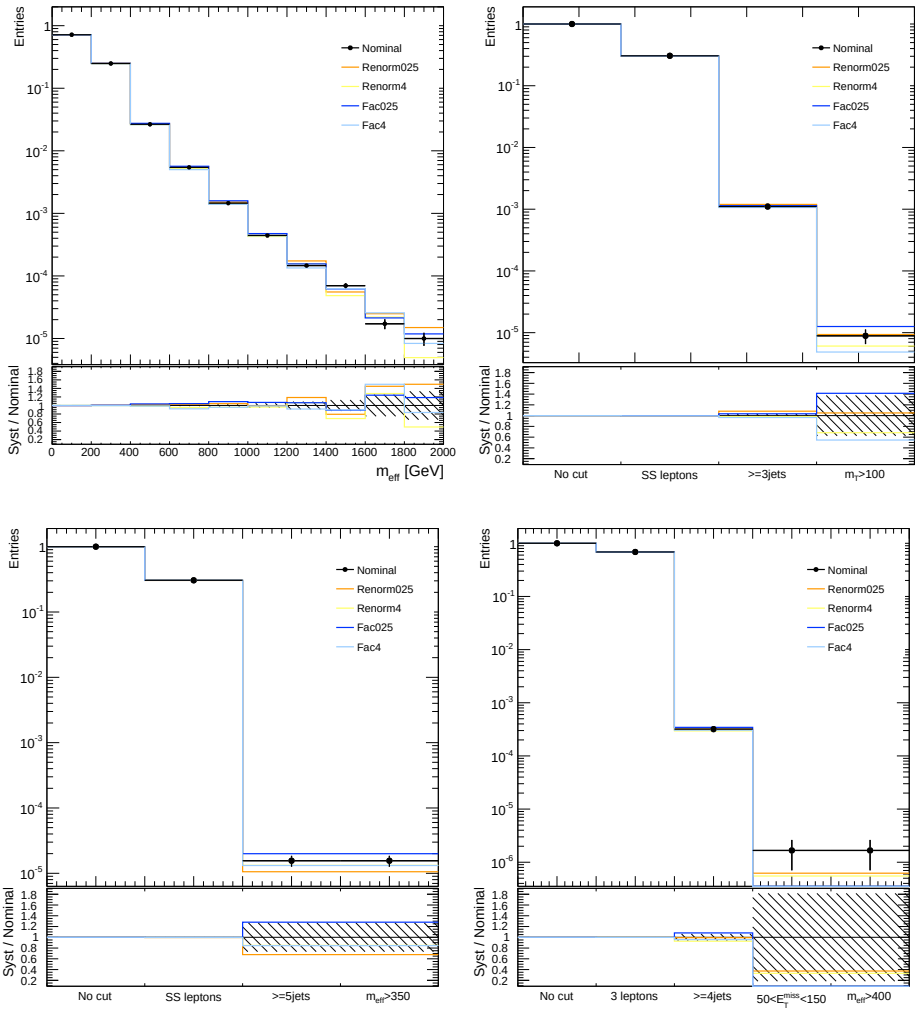

Figure 5.10: ZZ systematic variations in the normalized m_{eff} distribution without applying any selection criteria (top left) and cut efficiencies in the regions for the phase space close to SR0b and SR1b (top right), SR3b (bottom left) and SR3Llow (bottom right). A sample with the nominal generator settings (black) is compared to the samples with one modified parameter value (up or down). The statistical uncertainty on the nominal sample is represented by the hashed band.

	Variation	Baseline		SR3b		SR0b/SR1b		
		SS	$2/3j$	$4/5j$	m_{eff}	m_{T}	$E_{\text{T}}^{\text{miss}}$	m_{eff}^{400}
WZ	CKKW	1.5	4.1	16.3	15.3	0.5	4.2	2.9
	μ_F	4.0	12.9	21.3	22.5	16.5	15.4	15.7
	μ_R	0.4	0.8	9.9	9.7	0.3	1.4	3.3
	Total	4.3	13.6	28.6	28.9	16.5	16.0	16.3
	Extra partons	0.8	28.7	163.4	163.3	27.6	29.0	29.5
ZZ	μ_R	0.1	3.5	21.8	21.8	43.3	–	–
	μ_F	0.2	5.0	8.6	8.6	18.4	–	–
	Total	0.2	6.1	23.4	23.4	47.1	–	–
	MC generator	4.5	37.3	78.3	78.3	–	–	–

Table 5.8: Summary of the relative systematic variations for WZ and ZZ at each step of two simplified signal regions, expressed in percent. The baseline selection consists of requiring two same-sign leptons and at least two and three jets for WZ and ZZ, respectively. The selection criteria in the two simplified regions, denoted as SR3b and SR0b/SR1b, are applied on top of them. A – symbol indicates that the estimated value is not statistically significant. The scale variations are added in quadrature.

	Variation	SR3Llow			
		3ℓ	$3/4j$	$E_{\text{T}}^{\text{miss}}$	m_{eff}
WZ	CKKW	1.2	4.7	9.0	9.6
	μ_F	6.1	16.8	19.6	20.8
	μ_R	0.2	0.8	2.9	2.1
	Total	6.2	17.5	21.8	23.0
	Extra partons	4.4	56.3	50.4	49.6
ZZ	μ_R	0.0	6.2	–	–
	μ_F	0.0	3.3	–	–
	Total	0.1	7.0	–	–
	MC generator	6.4	81.8	–	–

Table 5.9: Summary of the relative systematic variations for WZ and ZZ at each step of the simplified signal region kinematically close to SR3Llow, expressed in percent. Further details are the same as in Table 5.8.

5.6.2 Charge-flip Background

Events with two opposite-sign leptons for which the charge of a lepton is mis-identified constitute an important background for the signal regions with two same-sign leptons. As discussed in Section 3.5.2, this is caused mostly by trident events where one electron undergoes a hard photon Bremsstrahlung in the inner detector. The presence of charge-flip events is characterized by a peak in same-sign dilepton pairs. Figure 5.11 shows that $e^{\pm}e^{\pm}$ invariant mass peaks around Z boson mass while no such structure is found in $\mu^{\pm}\mu^{\pm}$ invariant mass. Therefore, the probability of mis-identifying the charge of a muon is negligible in this analysis.

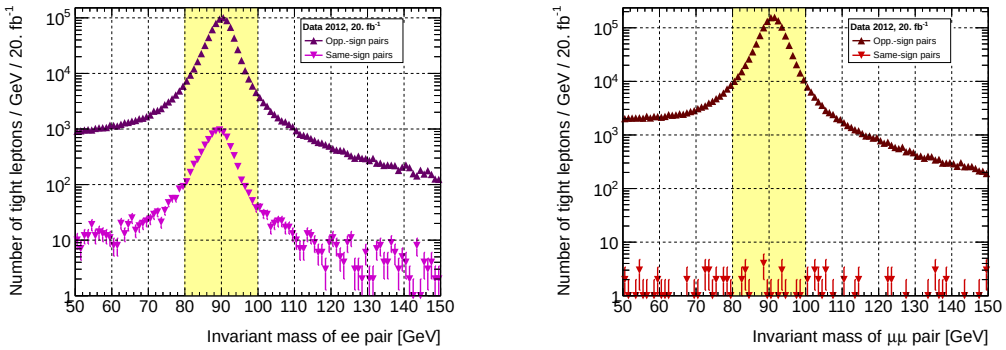

Figure 5.11: Invariant mass distribution of two opposite-sign and same-sign electrons (left) and muons (right) in a region with $|\eta| > 2.1$. Leptons with high η values are selected to enhance the probability of a charge mis-measurement. The Z peak in same-sign dielectron invariant mass corresponds to 1% of total events. Note the absence of Z peak in same-sign dimuon invariant mass.

The charge-flip probability is extracted in two Z boson data samples, one with same-sign electron pairs and the other with opposite-sign electron pairs, where the invariant mass of the two electrons is required to be $m_{ee} \in [75, 100]$ GeV. An asymmetric window around the Z boson mass is chosen because trident electrons lose more energy in the detector than electrons with correctly identified charge, for which the energy calibration is performed. The efficiencies, binned in η and p_{T} of the lepton, are then obtained via the maximization of a likelihood function that is constructed similarly as in Section 3.5.2. These are the nominal efficiencies as they are measured in events with two signal electrons. However,

the corrections to the fake lepton background (discussed in the following Section 5.6.3) requires estimating the charge-flip contribution also in events with two pre-selected leptons. Figure 5.12 illustrates two sets of charge-flip probabilities, one for (tight) electrons passing the signal requirements and the other for (loose) electrons failing these selections.

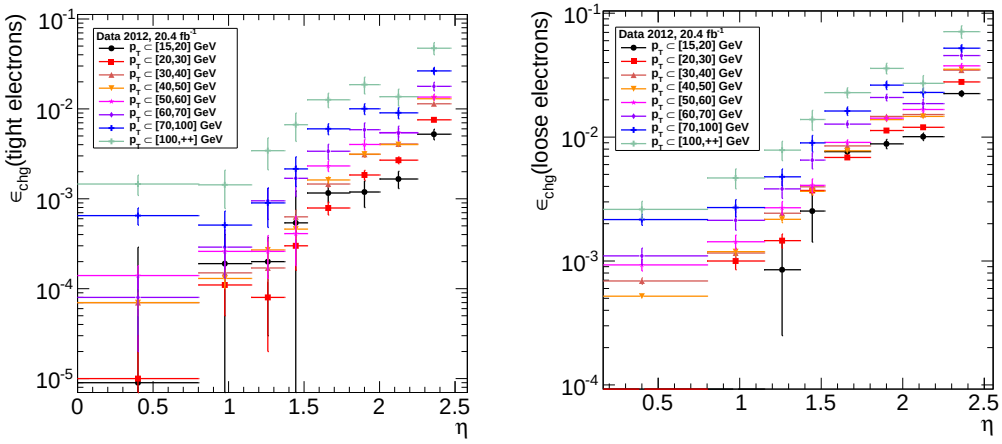

Figure 5.12: Charge-flip probabilities for tight (left) and loose (right) electrons measured in data as a function of p_{T} and η. Only the statistical uncertainties are shown.

The background contamination in the same-sign dielectron invariant mass distribution is estimated in 25 GeV sidebands above and below the Z peak. Its average is considered as the non-resonant contribution within the Z peak itself. The symmetrised absolute difference in the efficiencies obtained with and without this subtraction procedure is then taken as a systematic uncertainty. In order to validate the measured charge-flip rates, a closure test is performed. The observed difference in normalization between opposite-sign events weighted with a corresponding factor and the observed same-sign events is covered by another uncertainty assigned to the charge-flip estimate. The total uncertainty on the charge-flip probabilities includes the statistical uncertainty due to the limited statistics in $Z \to ee$ data samples and the systematic errors coming from the background subtraction and the closure test.

As already outlined, the expected charge-flip contribution in a signal region with same-sign dilepton events is estimated by applying the weight to the data

region with the same kinematic requirements but with opposite-sign lepton pairs. It is therefore a fully data-driven method. To define this weight, one has to firstly know the relation between the expected number of observed opposite-sign events $\langle N_{\mathrm{OS}}^{ij} \rangle$ and the total number of events N^{ij}:

$$\langle N_{\mathrm{OS}}^{ij} \rangle = N^{ij}((1-\xi_1^i)(1-\xi_2^j) + \xi_1^i \xi_2^j) \tag{5.2}$$

$$\approx N^{ij}(1-\xi_1^i)(1-\xi_2^j) \tag{5.3}$$

where ξ_1^i and ξ_2^j is the efficiency for leading and subleading lepton, respectively. The approximation neglects the scenario where the charge of both leptons is mis-identified. From Equations 3.3 and 5.3, one get:

$$\langle N_{\mathrm{SS}}^{ij} \rangle = w(\xi^i, \xi^j) \langle N_{\mathrm{OS}}^{ij} \rangle \quad \Rightarrow \quad w(\xi^i, \xi^j) = \frac{\xi_1^i + \xi_2^j}{(1-\xi_1^i)(1-\xi_2^j)} \tag{5.4}$$

Since every opposite-sign event is weighted by the factor $w(\xi^i, \xi^j)$, the charge-flip background estimation can be written as the sum of weights event by event:

$$\langle N_{\mathrm{SS}}^{\mathrm{flip}} \rangle = \sum_{\alpha \in \mathrm{OS}} w_\alpha \tag{5.5}$$

where $w_\alpha \equiv w(\xi^i, \xi^j)$ is the weight assigned to an event α in the data region with two signal electrons in bins i and j and of different charge.

5.6.3 Fake Lepton Background

As discussed in Section 3.5.3, the events requiring one or more isolated leptons may be faked by the events consisting of non-prompt leptons arising from heavy-flavour quark decays, mis-reconstructed jets or photon conversions in the inner detector material. It has been shown in one of the previous versions of this analysis [254] that they are dominated by non-isolated leptons originating from b-quark-initiated jets, mostly from $t\bar{t}$ processes.

Given that the signal events contain either two same-sign leptons or three leptons, the size of the matrix used to estimate the fake lepton background needs to be dynamically adjusted according to the number of pre-selected leptons in

the event. As a consequence, a generalised matrix method has been developed by the analysis team [196, 197].

For example, if an event with three pre-selected leptons, $e^+e^-\mu^+$, with configuration TLL, is measured, the matrix method produces the following output:

Input	**Output**			
$e^+e^-\mu^+, TLL$	$\cdots$	$\cdots$		
	TTL	w_{TTL}	$e_T^+e_T^-\mu_L^+$	Fails selections
	TLT	w_{TLT}	$e_T^+e_L^-\mu_T^+$	2 leptons SS
	LTT	w_{LTT}	$e_L^+e_T^-\mu_T^+$	Fails selections
	TTT	w_{TTT}	$e_T^+e_T^-\mu_T^+$	>2 leptons

Only two combinations pass the selection cuts (assuming trigger matching and other requirements are also satisfied). The weight w, whose general form is given by Equation 3.21, is a function of the probabilities for prompt and fake pre-selected leptons with $p_{\mathrm{T}} > 15$ GeV to satisfy the signal selections, as defined in Tables 5.1 and 5.2. These efficiencies depend on the lepton flavour and kinematic quantities, such as p_{T} and η. Their measurement is performed in the control regions that are required to be as kinematically close to the signal regions as possible.

5.6.3.1 Prompt Lepton Efficiency

Similarly as in the analysis presented in Chapter 3, the prompt lepton efficiencies are determined from a data sample enriched in prompt leptons from $Z \to \ell^{\pm}\ell^{\mp}$ decays, obtained with the tag-and-probe method. The difference consists mainly in the classification of the leptons as loose or tight (cf. Tables 3.2 and 3.2). The tag lepton is required to pass the tight selection criteria and the invariant mass of two same-flavour opposite-sign leptons must satisfy $m_{\ell\ell} \in [80, 100]$ GeV. Since both leptons are expected to be prompt, they are alternatively considered as a possible tag.

Figure 5.13 shows the invariant mass distributions in the $e^{\pm}e^{\mp}$ and $\mu^{\pm}\mu^{\mp}$ control regions. The data events where a probe lepton passes and fails the signal requirement are compared.

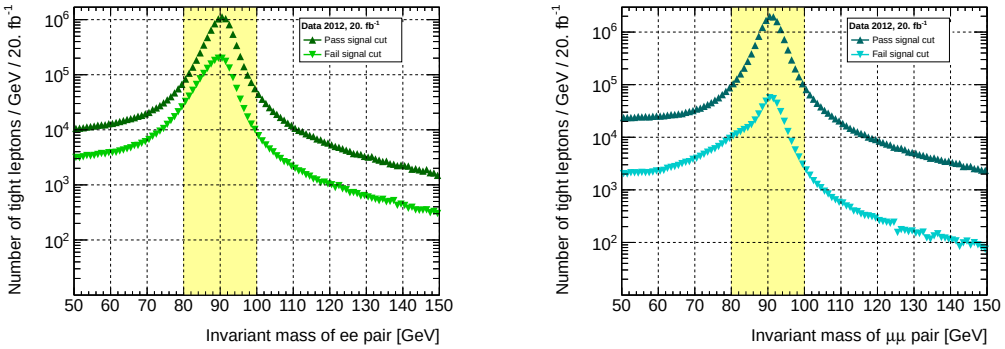

Figure 5.13: Invariant mass distribution of two opposite-sign electrons (left) and muons (right) with at least one tag lepton. The data are classified into two categories: probe lepton passes and fails the tight requirements. The shoulder in looser muon selection is caused by the energy loss after radiating FSR photons. These muons then fail the calorimeter isolation cut in the signal muon definition.

The prompt efficiencies are extracted as a function of p_{T} and η, illustrated in Figure 5.14. They are then compared to the efficiencies computed from MC simulation and the difference between the two is taken as a systematic uncertainty. In addition, the measurement is performed in Drell-Yan data events with limited hadronic activity while the efficiencies are applied to the signal regions with several jets. Their dependence on the jet multiplicity and m_{eff} has been studied in $t\bar{t}$ MC samples and a uniform systematic uncertainty of 3% has been introduced to take this extrapolation into account.

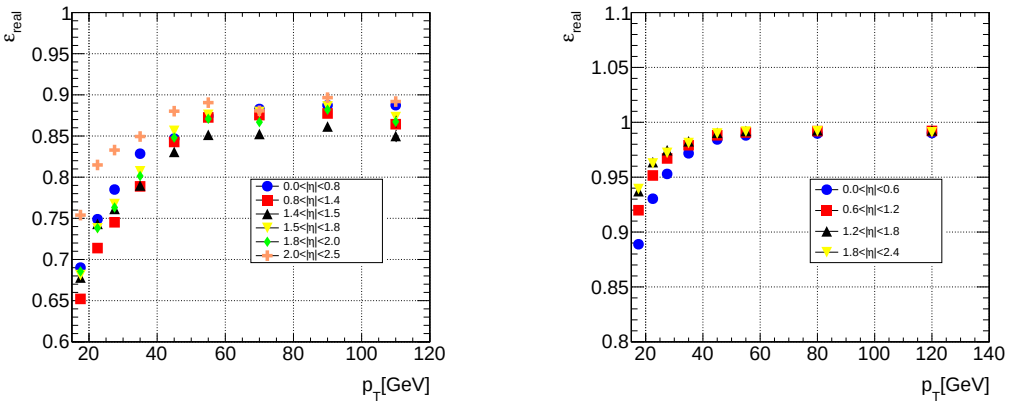

Figure 5.14: Prompt efficiencies for electrons (left) and muons (right) measured in data as a function of p_{T} and η.

5.6.3.2 Fake Lepton Efficiency

The probability for fake leptons to pass the signal selection criteria is measured in fake-enhanced samples containing one tight lepton with $p_{\mathrm{T}} > 40$ GeV (a 'tag') and one pre-selected lepton with $p_{\mathrm{T}} > 15$ GeV (a 'probe'). To reduce the contribution from the leptonic diboson decays, events with a third lepton passing the pre-selections with $p_{\mathrm{T}} > 10$ GeV are rejected. The control region used to extract the fake efficiencies for electrons requires a same-sign μe pair with muon as a prompt tag. As already mentioned, the prevalent source of fake leptons comes from b-quark decays. Given that the electron fake efficiency is sensitive to the heavy-flavour component in the event[1] and that the signal regions place different requirements on b-jet multiplicity, it is measured in two regions: with a b-jet veto and with at least one b-jet. The muon fake efficiency is extracted from the same-sign $\mu\mu$ control region with at least two jets with $p_{\mathrm{T}} > 25$ GeV. No strong dependence on whether or not these jets are also b-tagged is observed. The highest p_{T} muon is considered as a possible tag and the measurement is performed in p_{T} bins of the softer probe muon with $p_{\mathrm{T}} < 40$ GeV. Due to the high contamination from prompt leptons, in particular diboson events, the efficiency for high-p_{T} muons ($p_{\mathrm{T}} > 40$ GeV) cannot be reliably estimated from data events. Therefore, the value from the previous p_{T} bin is used and scaled according to a factor derived from the $t\bar{t}$ MC prediction. Finally, the size of the data sample is not sufficient to directly extract neither the electron nor the muon efficiency for the signal region with at least three b-jets. Extrapolation factors are thus derived from the $t\bar{t}$ MC sample and applied directly to the expected fake component.

After the control regions are defined and validated, the fake efficiencies are determined from the following ratio:

$$\zeta = \frac{n_T^{\mathrm{Data}} - n_T^{\mathrm{Prompt}}}{n^{\mathrm{Data}} - n^{\mathrm{Prompt}}} \tag{5.6}$$

where n^{Data} represents the number of data events and n^{Prompt} those events from the MC prediction which contain prompt leptons. The subscript T denotes events

[1] The efficiency for fake electrons arising from b-jet decays is smaller than when coming from light-flavour jets or conversions.

with a probe satisfying the tight requirements.

The electron fake efficiencies, binned in p_{T} and, for $p_{\mathrm{T}} < 35$ GeV, also in η, are shown together with their statistical and systematic uncertainties in Table 5.10 (b-jet scenario) and Table 5.11 (b-veto scenario). A finer binning in the low p_{T} region is possible due to the available statistics. Table 5.12 summarizes the fake efficiencies for muons as a function of p_{T}.

Three systematic uncertainties are associated with the fake efficiencies. Firstly, to cover the effect of the prompt lepton subtraction, conservative uncertainties of $\pm 30\%$ and $\pm 50\%$ on the production cross-section of the diboson and $t\bar{t}V$ MC samples are introduced, respectively. Secondly, a study is performed to exploit the differences in event kinematics between the control and signal regions. The requirements on jet multiplicity, m_{eff}, $E_{\mathrm{T}}^{\mathrm{miss}}$ and m_{T} are varied and the fully symmetrized maximum deviation is taken as a systematic uncertainty. Additional uncertainties resulting from the MC-based corrections are assigned and are dominated mostly by the MC statistics. Lastly, the validity of the assumption that the tag lepton is prompt is verified. It is found to be wrong only 2% (3%) of the time for electrons (muons) and this effect is thus negligible with respect to the other sources. All these uncertainties are then split into correlated and uncorrelated components.

p_{T}/GeV	$\lvert\eta\rvert$	ζ	σ_{stat}	σ_{syst}
$[15, 20]$	< 1.5	0.055	0.015	0.022
$[15, 20]$	$[1.5, 2.5]$	0.059	0.024	0.032
$[20, 25]$	< 1.5	0.101	0.028	0.049
$[20, 25]$	$[1.5, 2.5]$	0.083	0.045	0.036
$[25, 35]$	< 1.5	0.035	0.018	0.019
$[25, 35]$	$[1.5, 2.5]$	0.045	0.040	0.039
$[35, 45]$	–	0.080	0.037	0.035
$[45, 65]$	–	0.043	0.042	0.042
≥ 65	–	0.055	0.072	0.092

Table 5.10: Measured electron fake efficiencies ζ including statistical and systematic uncertainties, in the presence of at least one b-jet.

p_{T}/GeV	$\lvert\eta\rvert$	ζ	σ_{stat}	σ_{syst}
$[15, 20]$	< 1.5	0.035	0.006	0.006
$[15, 20]$	$[1.5, 2.5]$	0.055	0.008	0.017
$[20, 25]$	< 1.5	0.052	0.010	0.022
$[20, 25]$	$[1.5, 2.5]$	0.075	0.013	0.059
$[25, 35]$	< 1.5	0.032	0.009	0.020
$[25, 35]$	$[1.5, 2.5]$	0.070	0.013	0.039
$[35, 45]$	–	0.100	0.014	0.061
$[45, 65]$	–	0.107	0.019	0.070
≥ 65	–	0.131	0.028	0.085

Table 5.11: Measured electron fake efficiencies ζ including statistical and systematic uncertainties, requiring there be no b-jets in the events.

p_{T}/GeV	ζ	σ_{stat}	σ_{syst}
$[15, 20]$	0.107	0.019	0.042
$[20, 25]$	0.087	0.032	0.064
$[25, 40]$	0.128	0.051	0.148

Table 5.12: Measured muon fake efficiencies ζ including statistical and systematic uncertainties.

It is important to mention that there is an overlap between the fake lepton background described in this section and the charge-flip background outlined in Section 5.6.2. The generalised matrix method is applied to data which includes also the electrons with mis-reconstructed charge and thus the final fake lepton estimate needs to be corrected. A prediction for the fake component in the region with two same-sign signal leptons is evaluated by summing the weights from corresponding pre-selected data events:

$$\langle N_{\mathrm{SS}}^{\mathrm{fake}} \rangle = \sum_{\alpha \in \text{ pre-sel. SS}} w_{\alpha}^{\mathrm{fake}} \tag{5.7}$$

where $w_{\alpha}^{\mathrm{fake}}$ denotes the weight t'_{TT} (Equation 3.19) assigned to an event α. To

estimate the overlapping contribution, the matrix method is applied on the data-driven charge-flip estimate i.e. on the opposite-sign events reweighted by the appropriate charge-flip factor. After its subtraction, the corrected expression for fake estimate is:

$$\langle N_{\mathrm{SS}}^{\text{fake corr}} \rangle = \sum_{\alpha \in \text{pre-sel. SS}} w_{\alpha}^{\text{fake}} - \sum_{\beta \in \text{pre-sel. OS}} w_{\beta}^{\text{fake}} w_{\beta}^{\text{flip}} \tag{5.8}$$

where w_{β}^{fake} corresponds to the fake factor for an event β with two opposite-sign pre-selected leptons and w_{β}^{flip} is the charge-flip factor from Equation 5.4.

5.6.4 Validation of Background Estimates

Several regions kinematically close to the signal regions are defined to validate the data-driven background estimates. Since the data-driven methods are based on control regions with less stringent requirements on the (b-)jet multiplicities, total transverse energy and/or $E_{\mathrm{T}}^{\mathrm{miss}}$, it is particularly important to verify their extrapolation to the signal regions. Various kinematic distributions are studied for each lepton (ee, $e\mu$ and $\mu\mu$) and jet (with and without a b-jet) channel. Good agreement between the prediction and the measured data is observed. Selected distributions are shown in Figure 5.15.

In addition, three alternative methods have been developed to cross-check the data-driven background estimates, detailed in [215]. A tag-and-probe method and a simulation-based technique are employed for the electron charge-flip and fake lepton backgrounds, respectively. The generalised matrix method is applied to estimate the contribution from fake b-tags which are expected to completely dominate in the SR3b region. The predicted numbers of background events are consistent with those obtained from the nominal methods but with generally larger uncertainties.

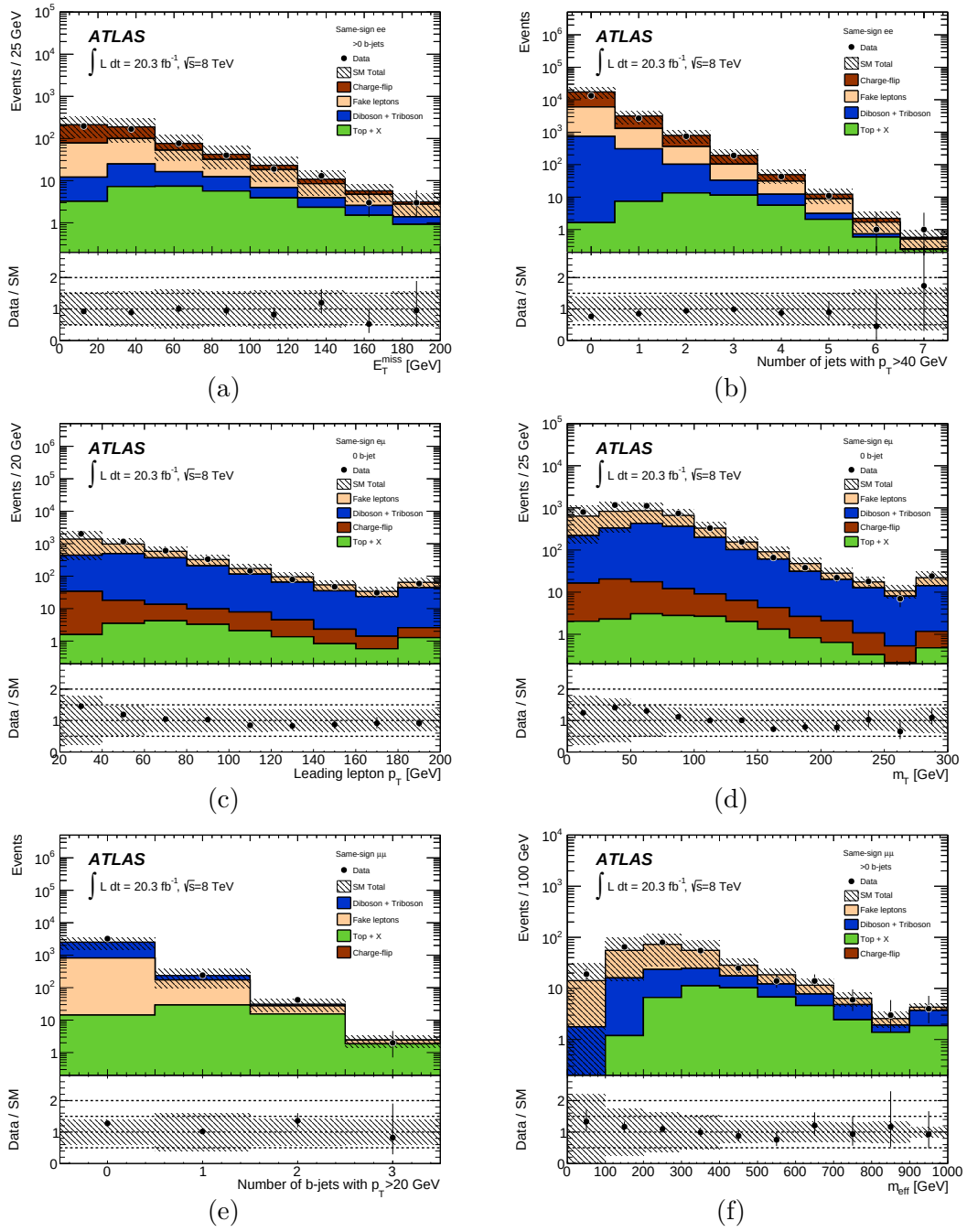

Figure 5.15: Distributions of kinematic variables in the same-sign background validation regions: (a) $E_{\mathrm{T}}^{\mathrm{miss}}$ with at least one b-jet, (b) number of jets for the ee channel, (c) leading lepton p_{T} with b-jet veto, (d) m_{T} with b-jet veto for the $e\mu$ channel, (e) number of b-jets and (f) m_{eff} with at least one b-jet for the $\mu\mu$ channel. The statistical and systematic uncertainties on the background prediction are included in the uncertainty band. The last bin includes overflows.

Finally, three dedicated validation regions are defined to test the MC modelling of the major irreducible backgrounds: $t\bar{t}W$, $t\bar{t}Z$ and WZ+jets. The event selections, presented in Table 5.13, are optimised to ensure that each region is enriched in a specific background process. This is a very important verification as the WZ+jets process forms the dominant background in the signal region with a b-jet veto and the $t\bar{t}V$ production dominates otherwise. The distributions in effective mass are shown in Figure 5.16. The good agreement between data and MC confirms the validity of our estimates.

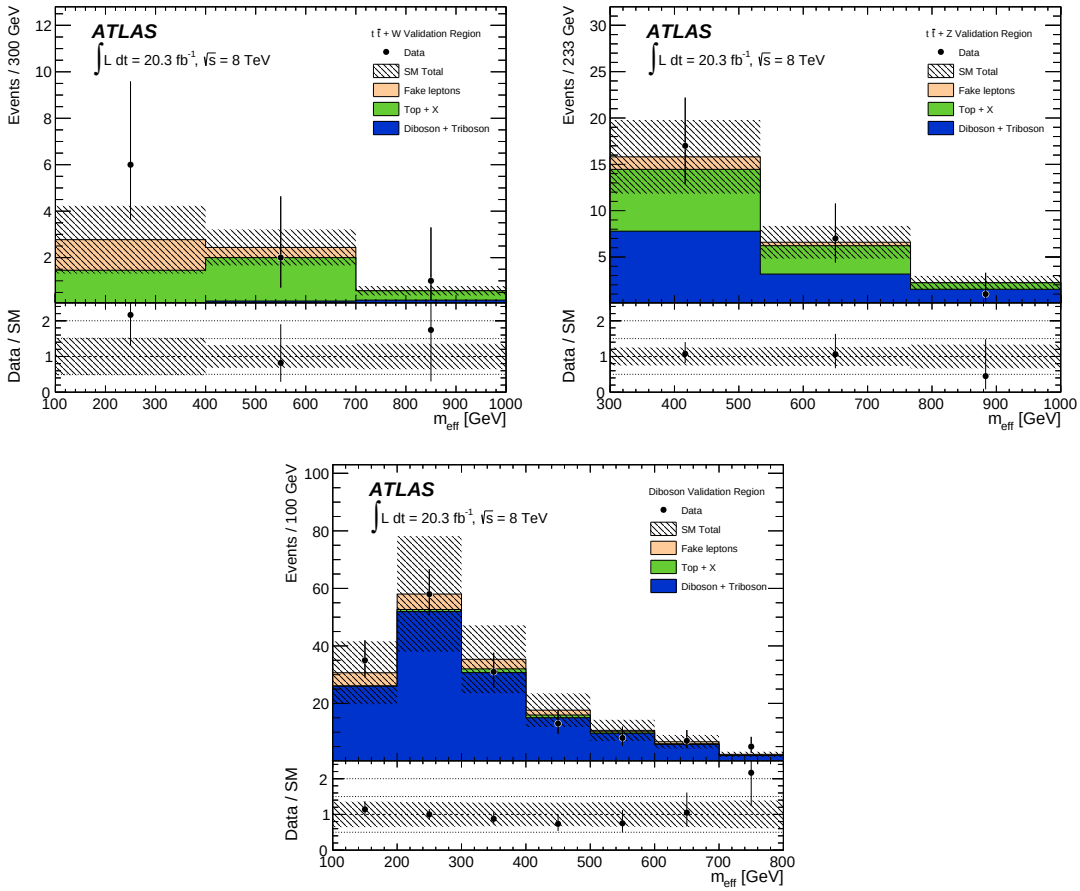

Figure 5.16: Comparison of data with the full background estimate for the effective mass (m_{eff}) distribution in each of the three validation regions: $t\bar{t}W$ (top left), $t\bar{t}Z$ (top right) and WZ+jets (bottom). The statistical and systematic uncertainties on the background prediction are included in the hashed uncertainty band. The last bin of each histogram includes the overflow.

	$t\bar{t}W$	$t\bar{t}Z$	WZ+jets
Leptons	SS $\mu\mu$	3L	SS $\mu\mu$
$N_{b\text{-jets}}$	$= 2$	1 or 2	$= 0$
N_{jets}	≥ 1 (30 GeV)	≥ 2 (40 GeV)	≥ 2 (20 GeV)
$E_{\text{T}}^{\text{miss}}$/GeV	$\in [20, 120]$	$\in [20, 120]$	$\in [20, 120]$
m_{T} /GeV	> 80	–	> 100
m_{eff} /GeV	–	> 300	–
$m_{\ell\ell}$ /GeV	–	$\in [84, 98]$	–

Table 5.13: Definition of the validation regions for rare SM backgrounds. The jet p_{T} requirement is indicated in parentheses. The p_{T} threshold of all selected leptons is 20 GeV.

5.7 Systematic Uncertainties

The background and signal predictions are subject to a number of systematic uncertainties related to object reconstruction and calibration, MC simulation and background estimation. Table 5.14 summarizes the breakdown of uncertainties on the expected background estimates, expressed in units of events.

The systematic uncertainties on the processes with two same-sign or three prompt leptons arise from the MC generator modelling and normalisation of the SM cross-sections, as detailed in Section 5.6.1. A summary of these theoretical uncertainties is presented in Table 5.15.

The detector-related systematic uncertainties considered in the fit are the same as those presented in Section 3.6.2. In this analysis, the uncertainty on the integrated luminosity is ±2.8%. It is derived from a preliminary calibration of the luminosity scale derived from beam-separation scans performed in November 2012 [240]. The uncertainties associated with the data-driven charge-flip and fake lepton backgrounds are discussed in Sections 5.6.2 and 5.6.3.

The largest systematic uncertainties come from the estimation of the fake-lepton probability and from the theoretical predictions for diboson and $t\bar{t}V$ processes. The former dominates in the SR3b and SR3Llow signal regions while the

latter in the SR0b, SR1b and SR3Lhigh channels.

Source of Uncertainty	**SR3b**	**SR0b**	**SR1b**	**SR3Llow**	**SR3Lhigh**
Fake lepton background	± 0.6	$^{+1.5}_{-1.2}$	$^{+1.2}_{-0.8}$	± 1.6	< 0.1
VV theory unc.	< 0.1	± 1.5	± 0.3	± 0.4	± 0.4
Jet and $E_{\mathrm{T}}^{\mathrm{miss}}$ scale & resolution	± 0.1	± 0.7	± 0.4	± 0.4	± 0.3
Monte Carlo statistics	± 0.1	± 0.5	± 0.2	± 0.4	± 0.4
b-jet tagging	± 0.2	± 0.5	± 0.1	< 0.1	± 0.1
$t\bar{t}V$, $t\bar{t}H$, tZ, $t\bar{t}t\bar{t}$ theory unc.	± 0.4	± 0.3	± 1.7	± 1.0	± 0.6
Trigger, luminosity and pile-up	< 0.1	± 0.1	± 0.1	± 0.1	± 0.1
Charge-flip background	± 0.1	± 0.1	± 0.1	–	–
Lepton identification	< 0.1	± 0.1	< 0.1	± 0.1	± 0.1
Total uncertainty	± 0.80	± 2.34	± 2.14	± 2.06	± 0.92

Table 5.14: Summary of the systematic uncertainties on the expected background estimates, shown in units of events. The individual uncertainties are correlated and therefore do not necessarily add up in quadrature to the total systematic uncertainty.

Background	**Uncertainty**	**SR0b/SR1b**	**SR3b**	**SR3Llow/high**
$t\bar{t}V$	Normalization	22%	22%	22%
	Shape	12%	12%	12%
WZ	Normalization	7%	7%	7%
	Shape	17%	29%	23%
	Parton multiplicity	30%	163%	56%
ZZ	Normalization	5%	5%	5%
	Shape	47%	23%	7%
	MC generator	37%	78%	82%

Table 5.15: Summary of theoretical systematic uncertainties on $t\bar{t}V$ and VV samples resulting from the cross-section normalization, its dependence on the factorisation and renormalisation scales, and the effects of ISR and FSR, as estimated in Sections 5.6.1.1 and 5.6.1.2.

5.8 Results

The event yields for observed data and estimated backgrounds in the signal regions, after the application of the additional requirements on m_{eff}, are detailed in Table 5.16. The expected numbers of signal events from the SUSY models of particular sensitivity to each signal region are included for illustration purposes. These models are further discussed in Section 5.9.2. The effective mass distributions are shown in Figure 5.17 for each signal region.

	SR3b	**SR0b**	**SR1b**	**SR3Llow**	**SR3Lhigh**
$t\bar{t}V$, $t\bar{t}H$, tZ, $t\bar{t}t\bar{t}$	1.3 ± 0.5	0.9 ± 0.4	2.5 ± 1.7	1.6 ± 1.0	1.3 ± 0.7
VV, VVV	< 0.1	4.2 ± 1.7	0.9 ± 0.4	1.2 ± 0.6	1.2 ± 0.6
Fake	0.7 ± 0.6	$1.2^{+1.5}_{-1.2}$	$0.8^{+1.2}_{-0.8}$	1.6 ± 1.6	< 0.1
Charge-flip	0.2 ± 0.1	0.2 ± 0.1	0.5 ± 0.1	–	–
Total Background	2.2 ± 0.8	6.5 ± 2.3	4.7 ± 2.1	4.3 ± 2.1	2.5 ± 0.9
Benchmark Signal	3.4 ± 0.7	24.3 ± 3.5	16.4 ± 3.0	10.6 ± 1.0	5.0 ± 0.8
Data	1	14	10	6	2
p_0	0.50	0.03	0.07	0.29	0.50
Z_0^{opt}	1.91	6.87	5.53	3.98	2.55

Table 5.16: Summary of the observed data events and the expected background predictions with their total uncertainties for the discovery signal regions SR3b, SR0b, SR1b, SR3Llow and SR3Lhigh. The expected signal events correspond to SUSY models of particular sensitivity in each signal region and are shown for illustration together with their experimental uncertainties. The p-value of the observed events for the background-only hypothesis is denoted by p_0. By definition (Equation 3.58), the p_0 value is truncated at 0.50 when the number of observed data events is smaller than the expected backgrounds. The last row shows the expected signal sensitivity as defined in Equation 5.1.

For all signal regions the background uncertainty is dominated by the statistical uncertainty on the background estimates. Signal regions which require one

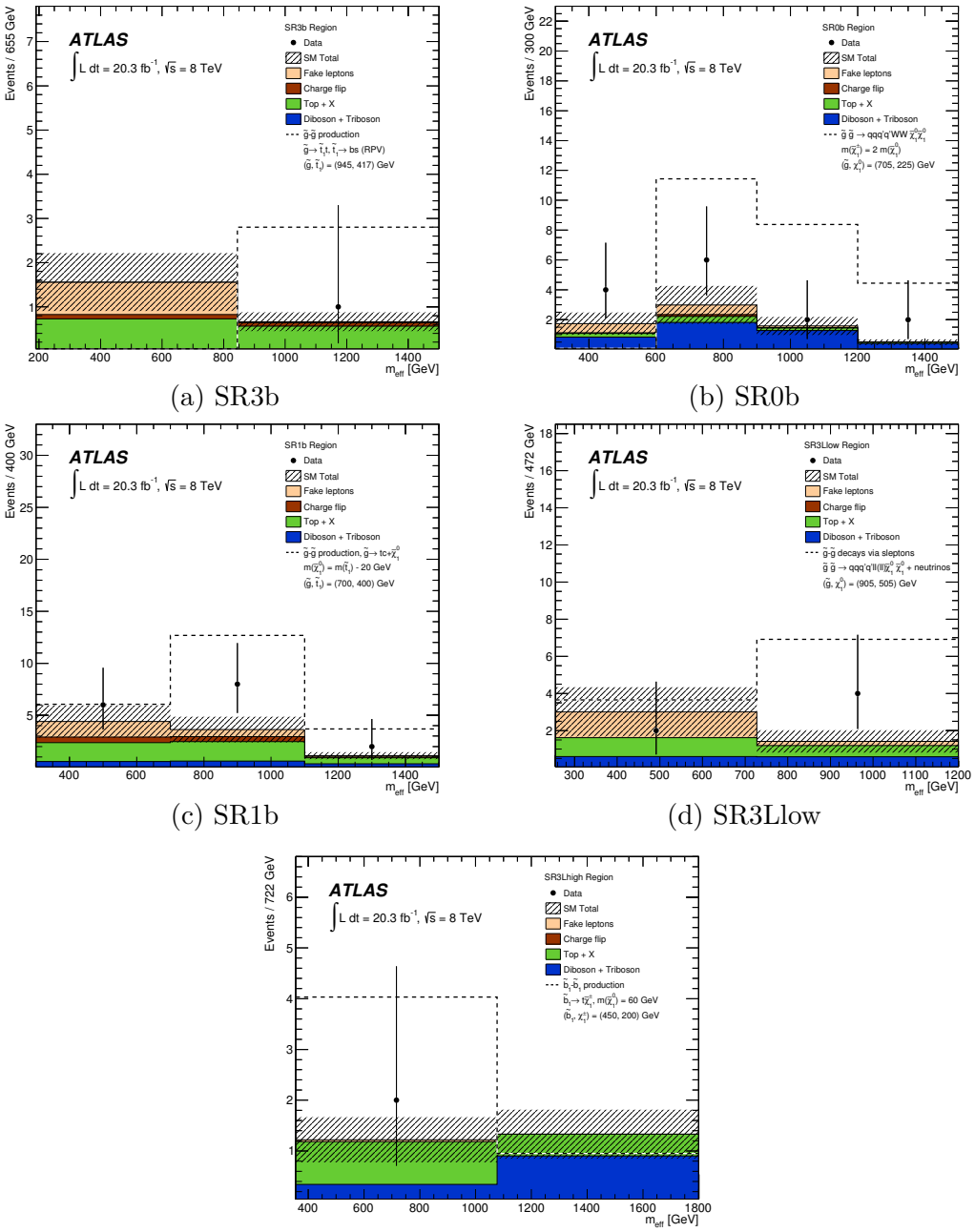

Figure 5.17: Effective mass (m_{eff}) distributions in the signal regions used as input for the exclusion fits. The hatched bands represent the statistical and systematic uncertainties on the overall background prediction. The error bars on the black points represent the statistical uncertainty on the data. The dashed lines denote the overlaid distributions of selected simplified model points, shown in Table 5.16. The last bin includes overflows.

or more b-jets (SR1b and SR3b) are dominated by $t\bar{t}V$ events. Diboson production in association with jets is the largest background in the region with a b-jet veto (SR0b). Both these SM processes contribute significantly in the 3L signal regions. The fake lepton background is particularly important in regions with no or low requirement on $E_{\mathrm{T}}^{\mathrm{miss}}$ (SR3b and SR3Llow). Finally, the contribution from the electron charge-flip background, which is applicable only in the signal regions with two same-sign leptons, is in general small. The level of compatibility of the data with the background prediction is quantified by calculating the p-value for each signal region, denoted as p_0 in Table 5.16. While the results from the SR3b, SR3Llow and SR3Lhigh channels are consistent with the SM prediction, small excesses are observed in the SR0b and SR1b regions. They correspond to 1.8 and 1.5 standard deviations, respectively. The significance of the excess in the combined region SR0b+SR1b becomes 2.1 standard deviations.

One particular data event with the highest m_{eff} of all signal regions is visualized using the `VP1` event display [255] in Appendix C.

5.9 Statistical Interpretation

As no significant deviation from the SM predictions is observed, the results can be interpreted as *upper limits* on possible beyond the SM (BSM) contributions to the signal regions and as *exclusion limits* in the context of the various phenomenological or simplified models discussed in Section 5.2. The HistFitter framework [256], which is based on a profile likelihood method [209] described in Section 3.8.2, is used to determine 95% confidence level limits following the CL_s prescription [212].

5.9.1 Model-independent Upper Limits

Setting model-independent upper limits allows to check whether any signal model of interest can be excluded by the measurement or not. They are calculated for each signal region individually using a *discovery fit*. This fit configuration is constructed as a single-bin counting experiment since no assumption about the shape of signal is made. The number of BSM events, S, in a signal region is a

free parameter of the fit. Otherwise, the fit proceeds in the same way as in the previous analysis described in Section 3.8. The corresponding likelihood for a signal region i can be written as:

$$L_i(\mu, \boldsymbol{\theta}) = \mathcal{P}(N_i^{\text{obs}}|N_i^{\text{exp}}(\mu, \boldsymbol{\theta}))\mathcal{P}(b_i|\gamma_i b_i)\mathcal{G}(\mathcal{L}_0|\mathcal{L}, \sigma_{\mathcal{L}}) \prod_{k\in\text{Sys}} \mathcal{G}(0|\alpha_k, 1) \tag{5.9}$$

The expected event count depend on a set of nuisance parameters $\boldsymbol{\theta}$ and the signal strength μ which can be interpreted as the number of BSM events S:

$$N_i^{\text{exp}}(\mu, \boldsymbol{\theta}) = \mu \cdot 1 + b_i(\boldsymbol{\theta}) = S + b_i(\boldsymbol{\theta}) \tag{5.10}$$

Following the formula 3.64, all values $S > S^{95}$, where S^{95} represents the 95% confidence level upper limit on S (i.e. $CL_s(S^{95}) = 0.05$), are excluded by the measurement. After normalising these by the integrated luminosity of the data sample, they can be translated into upper limits on the visible BSM cross-section σ_{vis} which is defined as the product of acceptance, detector efficiency and production cross-section. The limits are derived using 5000 pseudo-experiments and are summarized in Table 5.17.

	SR3b	**SR0b**	**SR1b**	**SR3Llow**	**SR3Lhigh**
$\langle\sigma_{\text{vis}}\rangle^{95}_{\text{obs}}$ [fb]	0.19	0.80	0.65	0.42	0.23
S^{95}_{obs}	3.9	16.3	13.3	8.6	4.6
S^{95}_{exp}	$4.4^{+1.7}_{-0.6}$	$8.9^{+3.6}_{-2.0}$	$8.0^{+3.3}_{-2.0}$	$7.2^{+2.9}_{-1.3}$	$5.0^{+1.6}_{-1.1}$

Table 5.17: The observed 95% CL upper limits on the visible cross section ($\langle\sigma_{\text{vis}}\rangle^{95}_{\text{obs}}$), and the observed and expected 95% CL upper limits on the number of BSM events (S^{95}_{obs} and S^{95}_{exp}).

5.9.2 Model-dependent Exclusions

The results of this measurement are also used to place exclusion limits on a wide variety of supersymmetric models. For each model, the limits are calculated using an *exclusion fit* which is performed in five statistically independent signal

regions simultaneously. Moreover, the final m_{eff} requirements are not applied and the signal regions are divided into bins of m_{eff}, shown in Table 5.18 and Figure 5.17, which is found to be a signal-sensitive variable in this analysis. Both the statistical combination of the signal regions and the additional shape information shall, in general, give better exclusion sensitivity.

	SR3b	**SR0b**	**SR1b**	**SR3Llow**	**SR3Lhigh**
Bin 1	$190-845$	$300-600$	$300-700$	$255-727.5$	$355-1077.5$
Bin 2	>845	$600-900$	$700-1100$	>727.5	>1077.5
Bin 3	–	$900-1200$	>1100	–	–
Bin 4	–	>1200	–	–	–

Table 5.18: The binning of each signal region in m_{eff} [GeV] used for the exclusion fit.

A grid of signal samples is produced for each model by varying some of its parameters, such as the masses of supersymmetric particles. The final likelihood is built for each of these grid points as the following product:

$$L(\mu,\boldsymbol{\theta}) = \prod_{i\in \text{SR}} \prod_{l\in \text{Bin}} \mathcal{P}(N_{il}^{\text{obs}}|N_{il}^{\text{exp}}(\mu,\boldsymbol{\theta}))\mathcal{P}(n_{il}|\gamma_{il}n_{il})\mathcal{G}(\mathcal{L}_0|\mathcal{L},\sigma_{\mathcal{L}}) \prod_{k\in \text{Sys}} \mathcal{G}(0|\alpha_k,1) \quad (5.11)$$

The CL_s value is then calculated assuming the presence of a signal as predicted by the theoretical model under study:

$$CL_s = \frac{p_1}{1-p_b} \quad (5.12)$$

where p_1 is the p-value defined in Equation 3.62 corresponding to the nominal hypothesis $\mu = 1$. The signal hypothesis is excluded with 95% confidence level if $CL_s < 0.05$. Since this procedure needs to be repeated for each parameter point of each signal model, exclusion limits are obtained using the asymptotic formulae [209]. Examples of the CL_s scans for five specific SUSY models, shown in Table 5.16 and Figure 5.17, are illustrated in Figure 5.18. These models will be further described below.

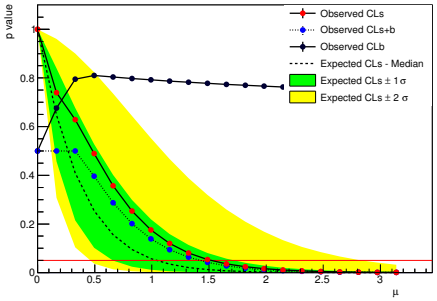

(a) $\tilde{t}_1 \to bs$ (RPV)
$(\tilde{g}, \tilde{t}_1) = (945, 417)$ GeV

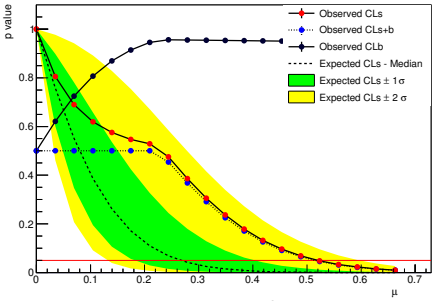

(b) $\tilde{g} \to q'W\tilde{\chi}_1^0$
$(\tilde{g}, \tilde{\chi}_1^0) = (705, 225)$ GeV

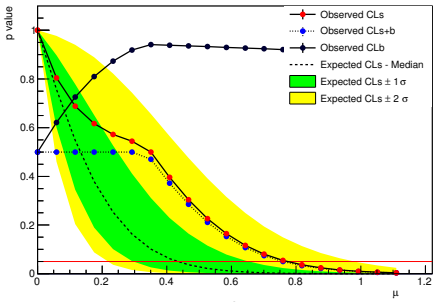

(c) $\tilde{t}_1 \to c\tilde{\chi}_1^0$
$(\tilde{g}, \tilde{t}_1) = (700, 400)$ GeV

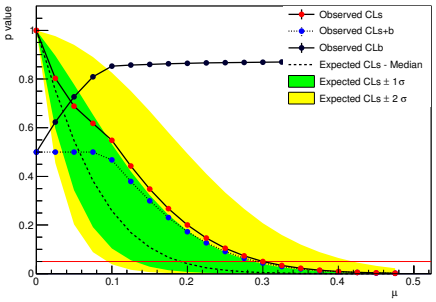

(d) $\tilde{g} \to$ sleptons
$(\tilde{g}, \tilde{\chi}_1^0) = (905, 505)$ GeV

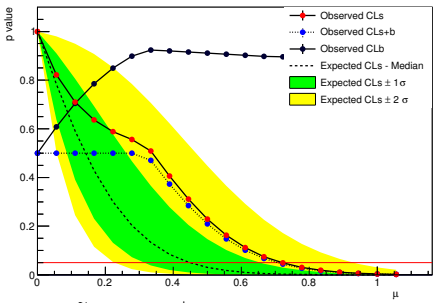

(e) $\tilde{b}_1 \to t\tilde{\chi}_1^{\pm}$, $m_{\tilde{\chi}_1^0} = 60$ GeV
$(\tilde{b}_1, \tilde{\chi}_1^{\pm}) = (450, 200)$ GeV

Figure 5.18: CL_s scan over the parameter of interest μ for selected SUSY benchmark scenarios (shown in Table 5.16 and Figure 5.17) obtained from the exclusion fit using asymptotic formulae. The observed values of CL_s (red points), CL_{s+b} (blue points) and CL_b (black points) are shown. The expected CL_s values under the SM background-only hypothesis with $\pm 1\sigma/\pm 2\sigma$ confidence intervals are indicated by the dashed line and the green/yellow bands. It can be seen that only (a) model is not excluded by the measurement.

In addition, 95% confidence level upper limits on the product of the production cross-section and branching fraction ($\sigma^{\text{SUSY}} \cdot \mathcal{B}$) are derived for each simplified model as a function of the sparticle masses. The numbers of signal events are translated into corresponding signal cross-sections using a similar formula as in Equation 4.6. The product of reconstruction efficiency and fiducial acceptance ($\epsilon_i \cdot A_i$) is calculated with Equations 3.25 and 4.4, respectively, for a signal region that dominates the sensitivity. These upper limits are available in the HepData database [257]. Therefore, they can be easily compared with theoretical expectations from a more general (SUSY or non-SUSY) model, predicting events with the same topology, to check whether the theory is compatible with data or not.

Finally, each signal model has typically a set of free parameters. Several physically motivated assumptions are made to reduce the parameter space and to allow for two-dimensional exclusions to be drawn. The observed and expected limits are displayed as solid red lines and dashed grey lines, respectively. Both curves are interpolated from a grid of CL_s values calculated for each signal sample that has been produced. A yellow band around the expected exclusion shows the $\pm 1\sigma$ uncertainty which includes all uncertainties (statistical and systematic) except the theoretical uncertainties on the signal cross-section. The dashed red lines around the observed limits represent the effect of changing the signal cross-section by one standard deviation. All limits quoted later in this section correspond to the $-1\sigma^{\text{SUSY}}_{\text{theory}}$ hypothesis. When available, results are compared with the observed limits obtained by previous ATLAS searches [237, 258–261].

5.9.2.1 Simplified Models

Gluino-mediated top squarks

The sensitivity of gluino-mediated top squark scenarios, favoured by naturalness arguments, is typically dominated by the SR3b signal region due to the high multiplicity of b-quarks in the final states. In the *gluino-top squark ($t\tilde{\chi}_1^0$) off-shell* model, the results are interpreted in the $(m_{\tilde{g}}, m_{\tilde{\chi}_1^0})$ mass plane as shown in Figure 5.19a. For any $\tilde{\chi}_1^0$ mass, gluino masses below 950 GeV are excluded at 95% CL. The exclusion limits in the $(m_{\tilde{g}}, m_{\tilde{t}_1})$ mass plane for the models including on-shell top squark are presented in Figures 5.19b, 5.19c and 5.19d. In

the context of the *gluino-top squark ($b\tilde{\chi}_1^{\pm}$) on-shell* model, gluino masses below 1 TeV are excluded at 95% CL for top squark masses above 200 GeV. The exclusion is less stringent in the *gluino-top squark ($c\tilde{\chi}_1^0$) on-shell* model, where softer jets are expected because of the small mass splitting between the top squark and the neutralino. The SR1b signal region has the dominant sensitivity as the final state is characterized by fewer b-quarks. For any $\tilde{t}_1$ and $\tilde{\chi}_1^0$ masses, gluino masses below 640 GeV are excluded at 95% CL. Finally, in the *gluino-top squark (bs) RPV* model, gluino masses below 850 GeV are excluded at 95% CL for any top squark mass.

Gluino-mediated (or direct) 1st and 2nd generation squarks

Results for five simplified models of gluino-mediated and direct production of first- and second-generation squarks are presented in the $(m_{\tilde{g}}, m_{\tilde{\chi}_1^0})$ and $(m_{\tilde{q}}, m_{\tilde{\chi}_1^0})$ mass planes, respectively. In the model with *one-step decay*, the sensitivity is dominated by the SR0b signal region. Gluino masses up to 860 GeV and neutralino masses up to 400 GeV are excluded at 95% CL, as shown in Figure 5.20a. No limits are set on squark masses since this search has no sensitivity to the direct squark pair-production decaying into the $q'q'WW\tilde{\chi}_1^0\tilde{\chi}_1^0$ final state, as discussed in Section 5.2.1. The scenarios *with two-step decay via gauginos* produce final states with several leptons from the W and Z bosons decays. The sensitivity is dominated by the three lepton signal regions: by SR3Lhigh at large $\Delta m(\tilde{g}/\tilde{q}, \tilde{\chi}_1^0)$ values and by SR3Llow in more compressed region. As illustrated in Figures 5.20b and 5.20c, gluino masses are excluded up to 1040 GeV for $\tilde{\chi}_1^0$ masses up to 520 GeV and squarks masses up to 670 GeV for $\tilde{\chi}_1^0$ masses up to 300 GeV. In the model with *two-step decay via sleptons*, the SR3Lhigh signal region has the best sensitivity. Gluino (squark) masses up to 1200 (780) GeV and $\tilde{\chi}_1^0$ masses up to 660 (460) GeV are excluded at 95% CL, as presented in Figures 5.20d and 5.20e. The limits are more stringent for long decay chains involving sleptons than for decays involving W and Z bosons because of the smaller leptonic branching fractions.

Direct bottom squarks

Exclusion limits for direct bottom squark production simplified models with

$m_{\tilde{\chi}_1^0} = 60$ GeV and $m_{\tilde{\chi}_1^\pm} = 2m_{\tilde{\chi}_1^0}$ are set in the $(m_{\tilde{b}_1}, m_{\tilde{\chi}_1^\pm})$ and $(m_{\tilde{b}_1}, m_{\tilde{\chi}_1^0})$ mass planes, respectively. The sensitivity is dominated by the three lepton signal regions as well as by the SR1b signal region. Bottom squark masses are excluded up to 440 GeV at 95% CL, as shown in Figures 5.21a and 5.21b.

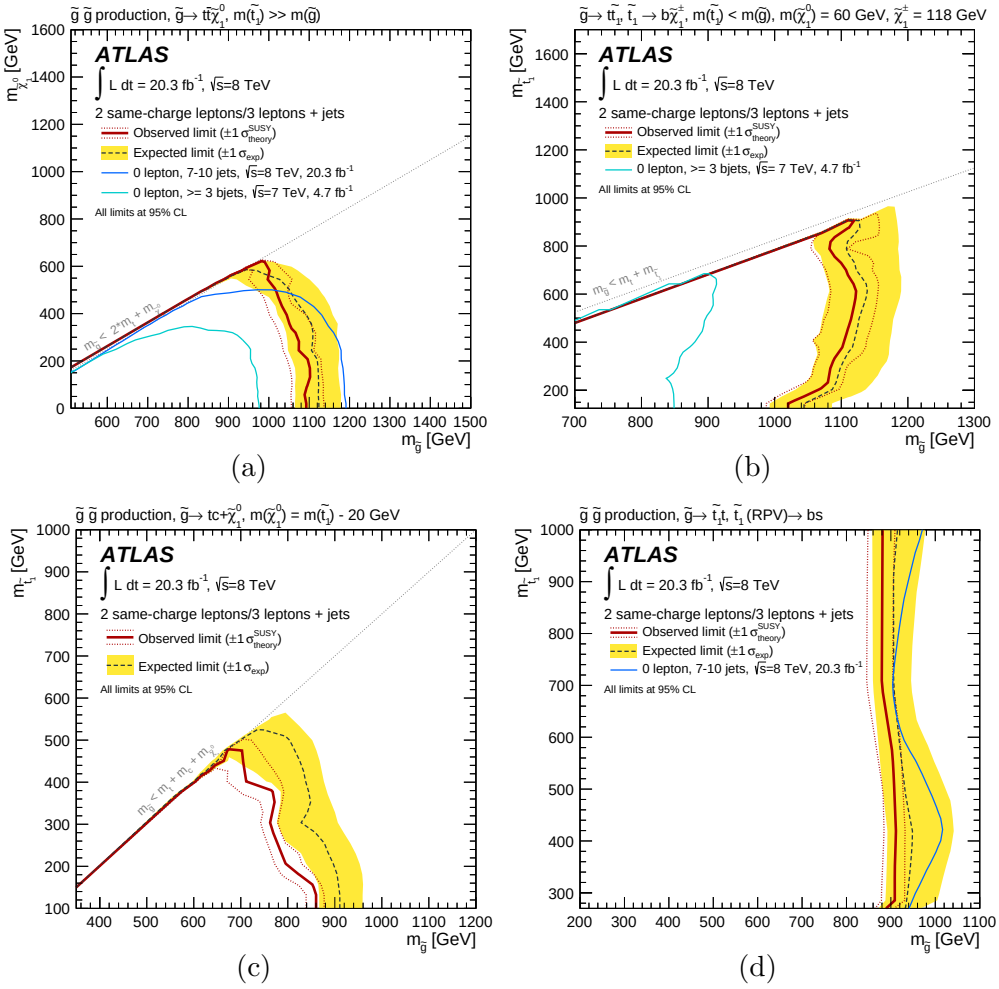

Figure 5.19: Exclusion limits on gluino-mediated top squark production for four different models: (a) gluino-top squark ($t\tilde{\chi}_1^0$) off-shell, (b) gluino-top squark ($b\tilde{\chi}_1^\pm$) on-shell, (c) gluino-top squark ($c\tilde{\chi}_1^0$) on-shell and (d) gluino-top squark (bs) RPV. A comparison with the previous ATLAS searches available at the time of publication is shown [260, 261].

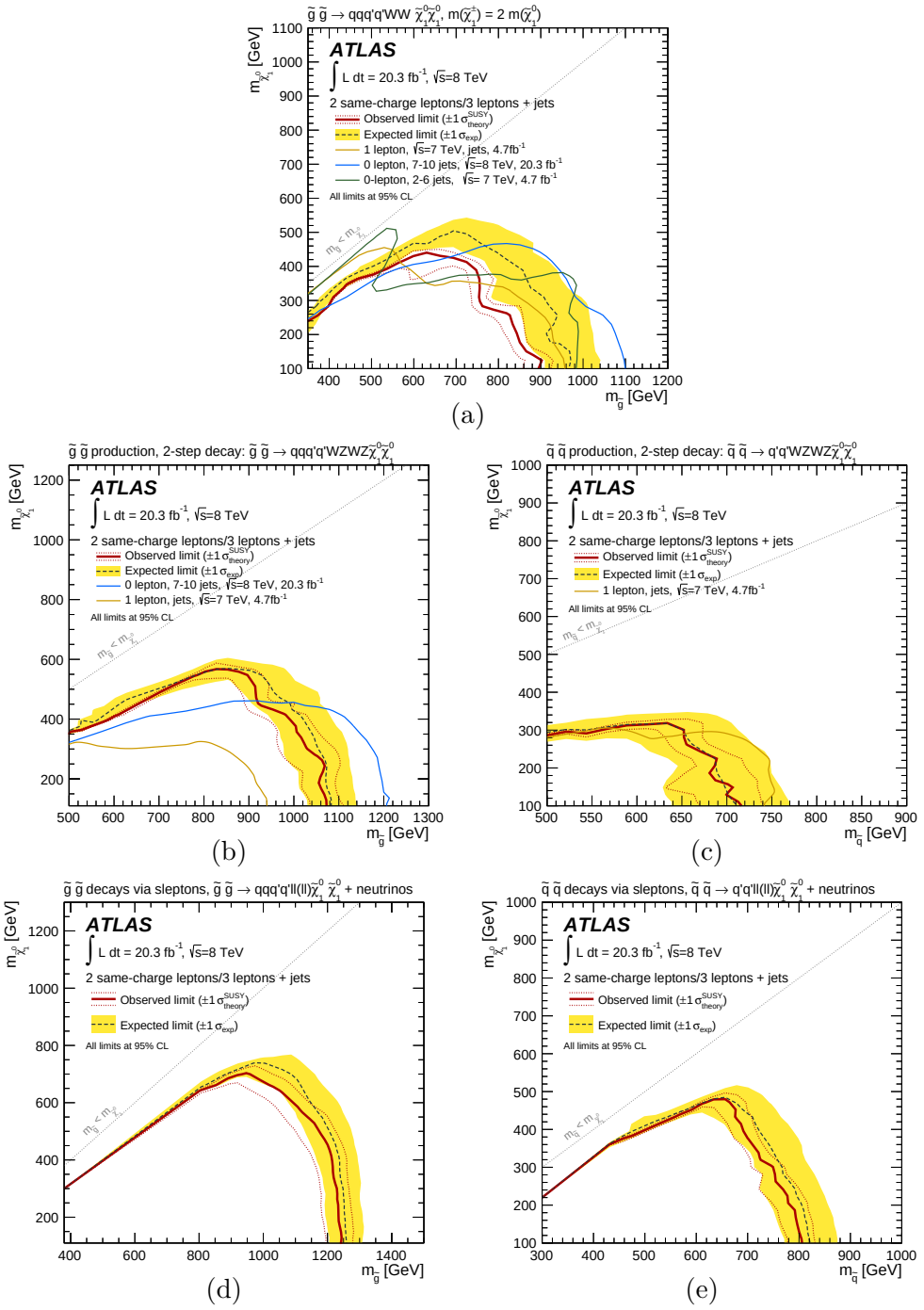

Figure 5.20: Exclusion limits on first- and second-generation squark production for five different models: (a) gluino-mediated with one-step decay, (b) gluino-mediated with two-step decay via gauginos, (c) direct with two-step decay via gauginos, (d) gluino-mediated with two-step decay via sleptons and (e) direct with two-step decay via sleptons. A comparison with the previous ATLAS searches available at the time of publication is shown [237, 258, 261].

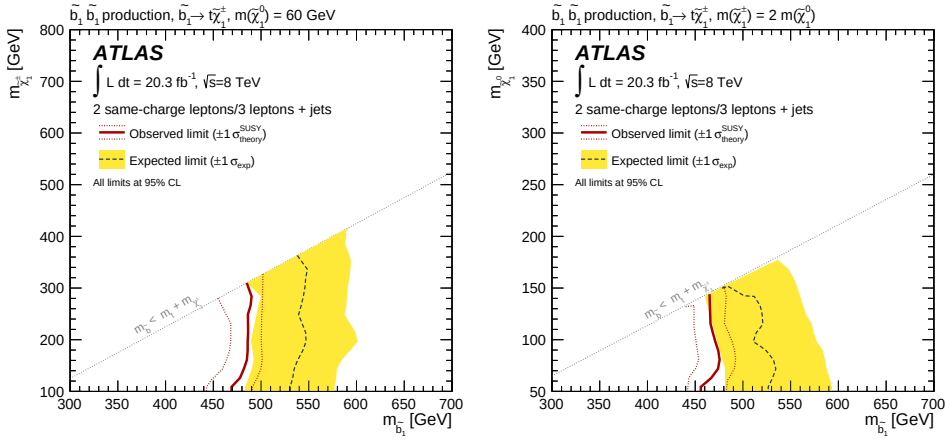

(a) (b)

Figure 5.21: Exclusion limits on direct bottom squark production for $\tilde{b}_1 \to t\tilde{\chi}_1^{\pm}$ for two different models: (a) $m_{\tilde{\chi}_1^0} = 60$ GeV and (b) $m_{\tilde{\chi}_1^{\pm}} = 2m_{\tilde{\chi}_1^0}$.

5.9.2.2 Phenomenological Models

Exclusion limits in the $(m_0, m_{1/2})$ plane of the mSUGRA/CMSSM model are shown in Figure 5.22a. For universal scalar masses m_0 up to 6 TeV, values of $m_{1/2}$ are excluded between 200 GeV and 490 GeV at 95% CL. In the context of the bRPV model, values of $m_{1/2}$ are excluded between 200 and 490 GeV for m_0 values below 2.1 TeV, as illustrated in Figure 5.22b. The lepton acceptance is highly reduced for $m_{1/2} < 200$ GeV due to the increased lifetime of the neutralino. Therefore, these models are not considered in the analysis. Results for the GMSB model are expressed as a function of Λ and $\tan(\beta)$ and presented in Figure 5.22c. Values of Λ below 75 TeV are excluded at 95% CL for $\tan(\beta)$ below 60. The region of large $\tan(\beta)$ and small Λ is unphysical since it leads to tachyonic states. Finally, exclusions limits for the mUED model are plotted in the plane of $(1/R, \Lambda R)$, as shown in Figure 5.22d. Values of $1/R$ below 850 GeV are excluded at 95% CL for $R > 18$.

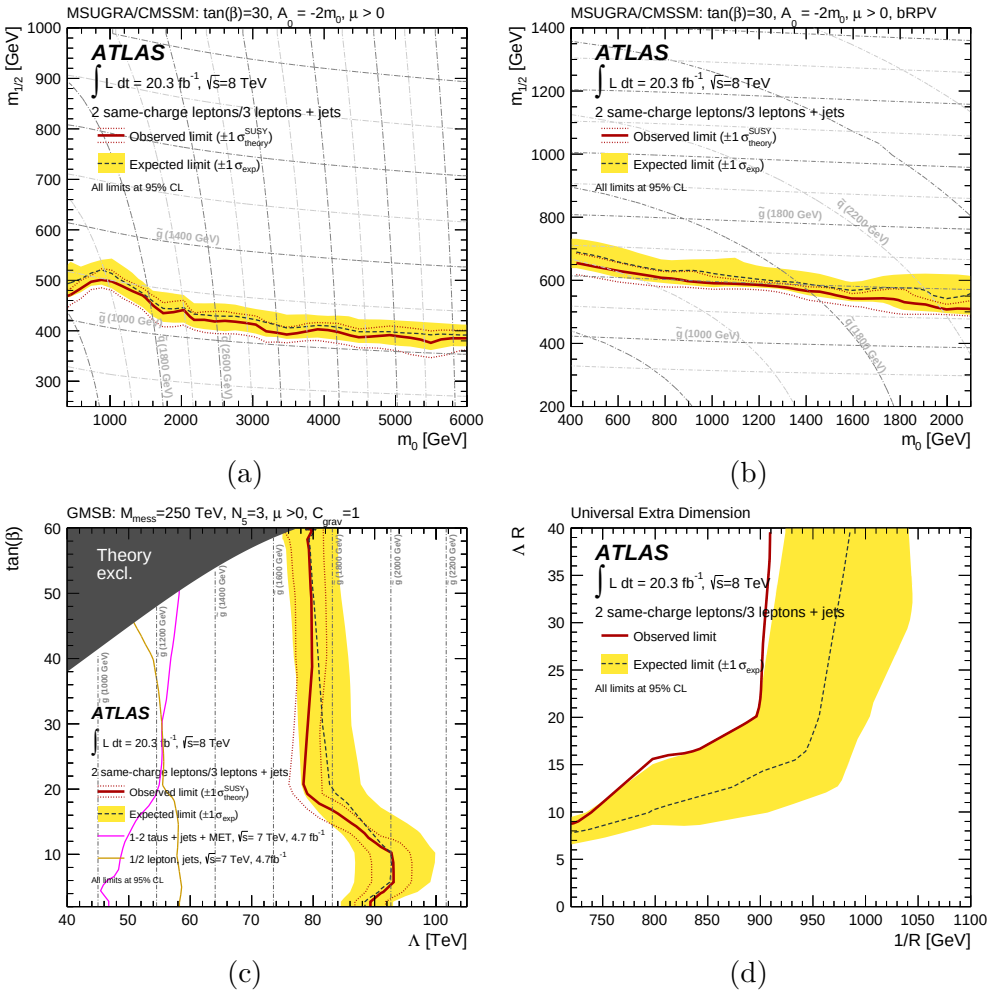

Figure 5.22: Exclusion limits for four phenomenological models: (a) mSUGRA/CMSSM, (b) bRPV, (c) GMSB and (d) mUED. A comparison with the previous ATLAS searches available at the time of publication is shown [237, 259, 261].

5.10 Conclusion

A search for supersymmetry in events with exactly two leptons of the same electric charge or at least three leptons (electrons or muons) is presented using the full 2012 dataset of LHC proton-proton collisions at $\sqrt{s} = 8$ TeV, corresponding to an integrated luminosity of 20.3 fb^{-1}. Five exclusive signal regions are defined according to the lepton and b-jet multiplicities. No significant excess above the Standard Model expectations is observed in any of the signal regions, and model-independent upper limits are set on the visible cross-section for new physics processes. In addition, a m_{eff}-shape fit is performed in the five signal regions simultaneously in order to place exclusion limits on 14 SUSY models and one mUED model. The achieved results put new or improved limits in a well motivated region of the SUSY parameter phase space, as well as on some non-SUSY models.

CONCLUSIONS AND PERSPECTIVES

Experimental data recorded with the ATLAS experiment corresponding to an integrated luminosity of 20.3 fb^{-1} proton-proton collisions at $\sqrt{s} = 8$ TeV were analysed in searches for the $W^{\pm}W^{\pm}W^{\mp}$ production as well as for supersymmetry in multi-jets events with two same-sign or three leptons.

A search for the production of three W bosons has been performed in the fully-leptonic decay channel, $W^{\pm}W^{\pm}W^{\mp} \to \ell^{\pm}\nu\,\ell^{\pm}\nu\,\ell^{\mp}\nu$. The sought signature features exactly three charged leptons (electrons or muons) and very little hadronic activity. The event selection has been optimized and three signal regions have been defined based on the number of same-flavour opposite-sign lepton pairs. The main aspects of the analysis have been addressed, in particular the data-driven technique used to estimate the background with at least one mis-reconstructed lepton. The search sensitivity is enhanced by combining these results with those from the semi-leptonic decay channel, $W^{\pm}W^{\pm}W^{\mp} \to \ell^{\pm}\nu\,\ell^{\pm}\nu\,jj$. A likelihood model is built and fitted to data which are found to be in good agreement with the Standard Model predictions. The observed total cross-section for the $W^{\pm}W^{\pm}W^{\mp}$ process is measured to be $227\ ^{+202}_{-198}$(stat.) $^{+154}_{-160}$(syst.) fb, which is consistent with the expected value of 241.5 fb. However, the precision of the measurement is limited due to large statistical and systematic uncertainties and a 95% confidence level upper limit on the $W^{\pm}W^{\pm}W^{\mp}$ production cross-section is set. The observed (expected) upper limit in the absence of the signal is 730 fb (560 fb). Further-

more, one- and two-dimensional limits are placed on the anomalous quartic gauge coupling parameters $f_{S,0}/\Lambda^4$ and $f_{S,1}/\Lambda^4$.

A search for supersymmetry in events with exactly two leptons of the same charge or at least three leptons (electrons or muons), multiple jets, b-jets and $E_{\mathrm{T}}^{\mathrm{miss}}$ has also been presented. Five statistically independent signal regions have been designed to cover various superymmetric scenarios. Dedicated studies have been performed to estimate and validate the background processes with similar signatures as the signal in the detector, especially the processes with prompt leptons arising mainly from W and Z boson decays. No deviation from the Standard Model expectation is observed. Exclusion limits are therefore placed on eleven supersymmetric simplified models and four phenomenological models using a binned shape fit in the m_{eff} distribution performed simultaneously in all signal regions. Moreover, model-independent upper limits on beyond the Standard Model contributions are derived separately for each signal region.

After a mostly successful first run, the LHC is currently performing proton-proton collisions at the unprecedented center-of-mass energy of 13 TeV. The full Run2 dataset will allow to measure rare electroweak processes which have not been observed so far, including the $W^{\pm}W^{\pm}W^{\mp}$ production. Besides testing the non-Abelian structure of the $SU(2)_L \otimes U(1)_Y$ gauge symmetry group in the electroweak sector, one can probe the Standard Model itself since the predicted gauge boson self-interactions are sensitive to contributions from new physics. Furthermore, these processes represent an important irreducible background to many searches for new particles. Precise electroweak measurements will be of increasing importance when addressing all corners of the supersymmetric phase space, such as scenarios with compressed mass spectra. Finally, the higher centre-of-mass energy of collisions as well as an upgraded detector with a new silicon layer close to the interaction point allows to search for new physics even in experimentally very challenging signatures.

APPENDIX A

EVENT QUALITY REQUIREMENTS

A list of good quality luminosity blocks approved for physics analysis is provided in a *Good Run List* (GRL). Furthermore, information about possible malfunctions in specific ATLAS detector components is stored in so-called *event quality flags* provided in the ntuples used as input for the analysis. Events affected by noise bursts in the LAr calorimeter and corrupted events in the Tile calorimeter are rejected by requiring `larError!=2` and `tileError!=2`, respectively. The so-called Timing, Trigger and Control (TTC) restart procedure has been deployed in order to recover the system during the data-taking. Events recorded immediately after the TTC restart need to be rejected by requiring `coreFlags&0x40000==0`, due to incomplete detector information in the corresponding luminosity block. The Tile calorimeter suffered from module trips which resulted in corrupted data events. Removal of these events is done using the officially provided `TileTripReader` tool [180]. In addition, periods B1 and B2 were affected by a hot cell which was not masked for the jet reconstruction algorithms. This is mitigated by removing events where a jet points close to the corresponding calorimeter module. Finally, *bad* jet candidates are rejected using the cleaning flag `isBadLooseMinus!=1` in order to avoid the $E_{\mathrm{T}}^{\mathrm{miss}}$ computation from mis-measured jets [181].

APPENDIX B

SYSTEMATIC UNCERTAINTIES IN FULLY-LEPTONIC WWW ANALYSIS

Additional information about the systematics in the $W^{\pm}W^{\pm}W^{\mp} \to \ell^{\pm}\nu\,\ell^{\pm}\nu\,\ell^{\mp}\nu$ analysis.

B.1 Theoretical Uncertainties

Source of Uncertainty		WZ	ZZ	VVV	$t\bar{t}V$	DPS	$Z\gamma$	Fake	**Bkg**	**Signal**
Signal	PDF	—	—	—	—	—	—	—	—	4.90
	μ_R and μ_F choice	—	—	—	—	—	—	—	—	2.60
Norm.	WZ	10.00	—	—	—	—	—	—	2.63	—
	ZZ	—	15.00	—	—	—	—	—	0.42	—
	VVV	—	—	30.00	—	—	—	—	1.44	—
	$t\bar{t}V$	—	—	—	30.00	—	—	—	0.50	—
	DPS	—	—	—	—	50.00	—	—	—	—

Table B.1: Breakdown of the theoretical systematic uncertainties in the 0SFOS signal region, expressed in percent of the nominal prediction. Systematics are only shown if they are applicable and their contribution is at least 0.02%.

Source of Uncertainty		WZ	ZZ	VVV	$t\bar{t}V$	DPS	$Z\gamma$	Fake	**Bkg**	**Signal**
Signal	PDF	—	—	—	—	—	—	—	—	4.90
	μ_R and μ_F choice	—	—	—	—	—	—	—	—	2.60
Norm.	WZ	10.00	—	—	—	—	—	—	8.05	—
	ZZ	—	15.00	—	—	—	—	—	0.59	—
	VVV	—	—	30.00	—	—	—	—	0.28	—
	$t\bar{t}V$	—	—	—	30.00	—	—	—	0.10	—
	DPS	—	—	—	—	50.00	—	—	—	—

Table B.2: Breakdown of the theoretical systematic uncertainties in the 1SFOS signal region, expressed in percent of the nominal prediction. Systematics are only shown if they are applicable and their contribution is at least 0.02%.

Source of Uncertainty		WZ	ZZ	VVV	$t\bar{t}V$	DPS	$Z\gamma$	Fake	**Bkg**	**Signal**
Signal	PDF	—	—	—	—	—	—	—	—	4.90
	μ_R and μ_F choice	—	—	—	—	—	—	—	—	2.60
Norm.	WZ	10.00	—	—	—	—	—	—	8.83	—
	ZZ	—	15.00	—	—	—	—	—	0.70	—
	VVV	—	—	30.00	—	—	—	—	0.23	—
	$t\bar{t}V$	—	—	—	30.00	—	—	—	0.07	—
	DPS	—	—	—	—	50.00	—	—	0.11	—

Table B.3: Breakdown of the theoretical systematic uncertainties in the 2SFOS signal region, expressed in percent of the nominal prediction. Systematics are only shown if they are applicable and their contribution is at least 0.02%.

B.2 Experimental Uncertainties

Source of Uncertainty		WZ	ZZ	VVV	$t\bar{t}V$	DPS	$Z\gamma$	Fake	**Bkg**	**Signal**
Electron	Efficiency	1.80	1.83	1.52	1.42	–	–	–	0.62	1.45
	Scale	0.96	1.63	1.75	2.00	–	–	–	0.29	0.51
	Resolution	0.18	0.88	1.83	1.23	–	–	–	0.10	0.23
Muon	Efficiency	0.52	0.53	0.54	0.55	–	–	–	0.19	0.54
	Scale	0.12	0.30	–	–	–	–	–	–	–
	Resolution	–	0.48	0.75	–	–	–	–	–	0.10
Jet	Flavour tagging	0.26	0.42	0.49	4.25	–	–	–	0.12	0.27
	Flavour composition	1.44	2.25	3.07	3.55	–	–	–	0.60	1.36
	Scale	1.58	2.60	5.66	11.96	–	–	–	0.80	1.45
	Resolution	0.57	0.84	1.55	6.20	–	–	–	0.35	1.06
	Pile-up	0.35	0.30	1.80	1.91	–	–	–	0.19	0.24
	Vertex fraction	0.08	0.06	–	2.27	–	–	–	0.06	0.12
$E_{\mathrm{T}}^{\mathrm{miss}}$	Scale	2.54	2.74	1.33	1.30	–	–	–	0.79	1.74
	Resolution	0.23	0.77	2.42	2.21	–	–	–	0.16	0.13
Trigger	Electron	0.09	0.10	–	–	–	–	–	–	0.06
	Muon	0.18	0.17	–	–	–	–	–	0.05	0.07
Fake	Electron	–	–	–	–	–	–	9.62	6.20	–
	Muon	–	–	–	–	–	–	5.06	3.26	–
	b-jet selection	–	–	–	–	–	–	90.19	58.14	–
Charge-flip		1.58	1.31	–	–	–	–	–	0.45	–
Pile-up		1.42	0.31	4.11	2.51	–	–	–	0.52	0.92
Luminosity		1.90	1.90	1.90	1.90	1.90	1.90	–	0.68	1.90

Table B.4: Breakdown of the experimental systematic uncertainties in the 0SFOS signal region, expressed in percent of the nominal prediction. Systematics are only shown if they are applicable and their contribution is at least 0.02%.

Source of Uncertainty		WZ	ZZ	VVV	$t\bar{t}V$	DPS	$Z\gamma$	Fake	**Bkg**	**Signal**
Electron	Efficiency	1.59	1.96	1.51	1.52	0.69	2.10	—	1.41	1.56
	Scale	1.03	1.26	1.01	—	—	75.62	—	1.72	0.59
	Resolution	0.21	0.84	1.29	1.01	—	43.66	—	0.66	0.07
Muon	Efficiency	0.54	0.50	0.52	0.55	0.32	0.87	—	0.47	0.53
	Scale	0.21	—	—	—	—	—	—	0.17	0.10
	Resolution	0.59	0.86	0.22	0.85	—	43.44	—	0.96	0.07
Jet	Flavour tagging	0.34	0.81	0.77	4.97	1.23	0.61	—	0.31	0.30
	Flavour composition	1.82	3.57	2.56	6.92	—	2.56	—	1.67	1.20
	Scale	2.15	4.02	3.52	6.78	—	—	—	1.91	1.32
	Resolution	0.32	2.34	0.43	6.44	0.24	2.63	—	0.41	1.31
	Pileup	0.41	1.62	2.10	4.81	—	—	—	0.41	0.34
	Vertex fraction	0.12	0.34	0.70	1.89	—	—	—	0.12	0.15
$E_{\mathrm{T}}^{\mathrm{miss}}$	Scale	0.33	5.90	1.57	1.65	—	44.87	—	0.98	0.71
	Resolution	0.32	0.25	1.38	2.13	—	51.75	—	0.96	0.47
Trigger	Electron	0.06	0.10	—	0.05	—	—	—	0.05	0.05
	Muon	0.08	0.13	—	—	—	0.26	—	0.07	0.07
Fake	Electron	—	—	—	—	—	—	36.50	4.69	—
	Muon	—	—	—	—	—	—	5.11	0.66	—
	b-jet selection	—	—	—	—	—	—	91.16	11.72	—
Charge-flip		—	—	—	—	—	—	—	—	—
Pile-up		0.35	4.30	1.80	2.52	28.56	38.30	—	0.20	1.30
Luminosity		1.90	1.90	1.90	1.90	1.90	1.90	–	1.66	1.90

Table B.5: Breakdown of the experimental systematic uncertainties in the 1SFOS signal region, expressed in percent of the nominal prediction. Systematics are only shown if they are applicable and their contribution is at least 0.02%.

Source of Uncertainty		WZ	ZZ	VVV	$t\bar{t}V$	DPS	$Z\gamma$	Fake	**Bkg**	**Signal**
Electron	Efficiency	1.01	0.64	1.28	0.81	1.65	3.00	—	0.97	0.99
	Scale	0.69	0.51	0.59	2.34	—	0.37	—	0.64	0.33
	Resolution	0.18	0.28	0.22	1.17	—	86.94	—	1.00	0.24
Muon	Efficiency	0.73	0.85	0.67	0.75	0.48	—	—	0.69	0.71
	Scale	0.25	0.26	—	—	—	—	—	0.23	0.13
	Resolution	0.58	0.61	1.03	—	—	—	—	0.51	0.41
Jet	Flavour tagging	0.36	0.72	0.96	4.87	0.49	2.02	—	0.37	0.30
	Flavour composition	1.44	2.35	2.44	5.91	—	122.95	—	2.66	1.26
	Scale	1.43	1.85	3.05	16.16	—	91.84	—	2.24	1.41
	Resolution	1.31	2.13	—	16.44	42.30	86.96	—	2.31	0.99
	Pileup	0.34	0.82	—	3.23	—	—	—	0.34	0.19
	Vertex fraction	0.28	0.44	—	3.47	—	—	—	0.28	0.07
$E_{\mathrm{T}}^{\mathrm{miss}}$	Scale	1.29	8.67	1.08	4.41	55.97	86.94	—	2.46	0.20
	Resolution	—	1.79	1.74	4.70	55.97	86.94	—	1.00	0.26
Trigger	Electron	—	—	—	—	—	—	—	—	—
	Muon	0.22	0.31	0.19	0.24	0.44	—	—	0.21	0.20
Fake	Electron	—	—	—	—	—	—	22.21	1.07	—
	Muon	—	—	—	—	—	—	6.80	0.33	—
	b-jet selection	—	—	—	—	—	—	87.19	4.20	—
Charge-flip		—	—	—	—	—	—	—	—	—
Pile-up		1.12	8.04	6.69	0.19	7.67	16.49	—	1.40	1.50
Luminosity		1.90	1.90	1.90	1.90	1.90	1.90	–	1.81	1.90

Table B.6: Breakdown of the experimental systematic uncertainties in the 2SFOS signal region, expressed in percent of the nominal prediction. Systematics are only shown if they are applicable and their contribution is at least 0.02%.

APPENDIX C

EVENT DISPLAY

Data event from the SR1b signal region with the highest m_{eff} of all the other regions ($m_{\text{eff}} = 1.67$ TeV) is visualized using the ATLAS `VP1` event display [255]. The event contains four signal jets and thus fails to pass the SR3b selections.

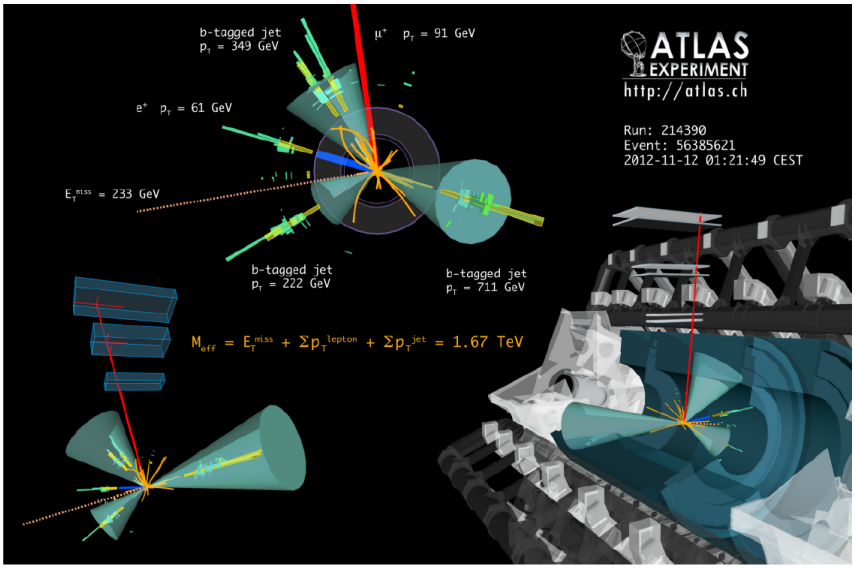

Figure C.1: Data event display from the SR1b region. The coloured cones represent the three leading jets ($p_{\text{T}} = 711$, 349 and 222 GeV) which are b-tagged, and the arrows indicate the muon, electron and missing transverse energy ($E_{\text{T}}^{\text{miss}} = 233$ GeV). The same event is shown with three different views.

APPENDIX D

TECHNICAL VALIDATION

New software releases are validated centrally by the *physics validation* team. A detailed histogram-by-histogram comparison is performed between two sets of validation samples; one produced using a new version of the software and the other one using previously validated release. The compatibility is evaluated by a χ^2 statistical test. A dedicated group of experts confirm whether or not the resulting distributions are correctly reproduced and whether the observed differences are expected given the changes in the software code. This procedure is complex and very time consuming (typically two weeks).

It is often desirable to perform a *technical validation* where the full compatibility between two samples, produced at different sites but with the same validated software release, is expected. In addition to the site validation (e.g. an HPC site), this would include the validation of an operating system and/or CPU architecture, of a production system workflow, of a new ROOT version etc. Therefore, a task force has been established by the OAB (Offline Activity Coordination Board) [262], of which the author has been a member, to design such automated setup.

As the starting point, the physics validation tool based on the data quality (DQ) monitoring framework [263] has been used to compare the histograms. It creates a web page with thousands of plots flagged as good/warning/alarm according to the χ^2/ndf values. This tool has been tuned to achieve a setup which

is more stable and optimized. Some histograms have been removed from the display because they were either sensitive to statistical fluctuations or not providing any additional information. Firstly, the results from two standard WLCG Tier-1 sites (BNL[1] and RAL[2]) have been compared for the reference. It has been found that they are not fully compatible due to the generation of random seeds in the simulation algorithm. The non-reproducible behaviour of the digitization and reconstruction parts (digi+reco) of the software chain is just residual. Therefore, it has been decided that only simulation runs on a site under validation, while the digi+reco runs on any standard WLCG grid site. Few examples of summary plots are shown in Figure D.1. Afterwards, the same comparison has been performed between another two sites (HPC2N[3] and SiGNET[4]) which are also integrated into the WLCG but have instead the AMD architecture. The results have shown similar scale of agreement. Finally, to study possible performance differences between Intel and AMD CPUs, BNL has been tested against SiGNET and RAL against HPC2N. The distributions of the χ^2/ndf values from all relevant histograms are shown in Figure D.2 for all these comparisons. It has been found that due to tiny differences in math libraries, such as rounding characteristics, a divergence occurs and the simulation results cannot be reproduced between different architectures [265]. Given these technical challenges, the work on an easy-to-use technical validation setup is still in progress and in close collaboration with the ATLAS software group.

During this work, the supercomputer Titan [119] has been successfully validated against HPC2N, as shown in Figure D.3. The residual discrepancies have been discussed with experts and confirmed to come solely from the statistical fluctuations.

[1] Brookhaven National Laboratory in the US.
[2] Rutherford Appleton Laboratory in the UK.
[3] High-Performance Computing Center North in Sweden [264].
[4] Slovenian Grid NETwork in Slovenia.

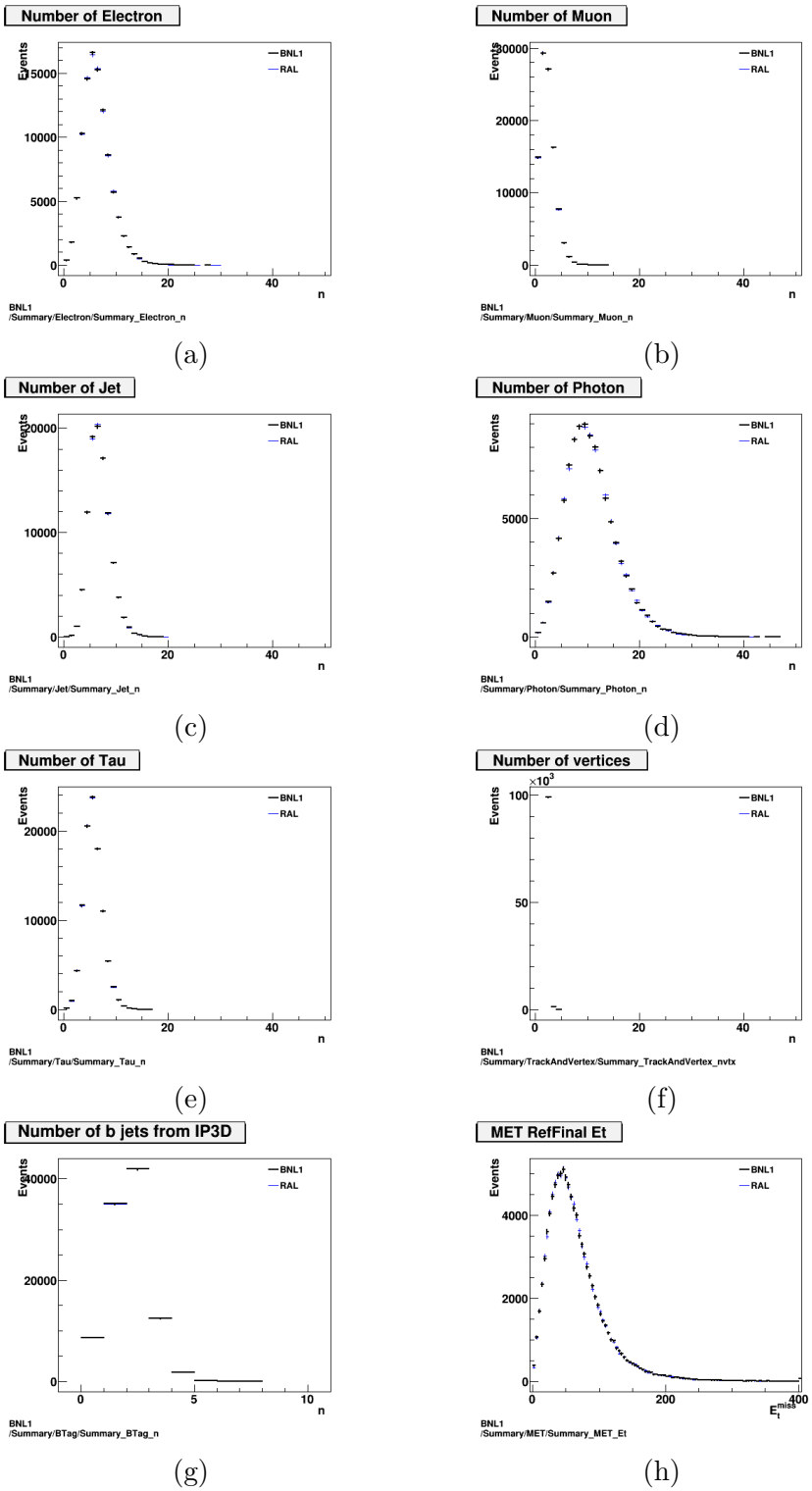

Figure D.1: Selected plots from the BNL vs RAL comparison, all with $\chi^2/\text{ndf} < 1$.

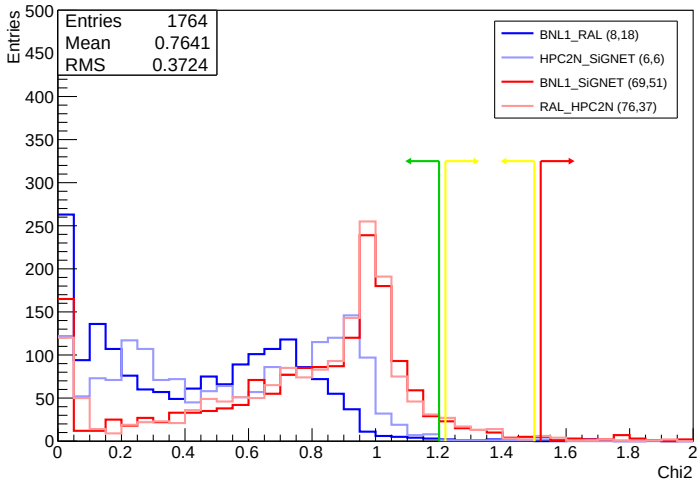

Figure D.2: χ^2/ndf distributions from the histogram-by-histogram comparisons between two sites with the same architecture (blue, light blue) and with different architectures (red, pink). The vertical lines denote two thresholds (1.2 and 1.5) defining the good/warning/alarm flag. The label of sites which have been tested as well as the number of plots with the warning and alarm flags are indicated in the legend.

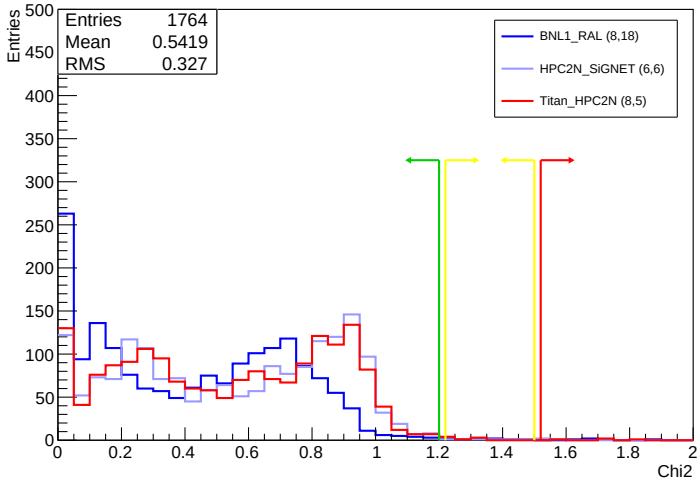

Figure D.3: Titan validation. The results from the simulation running on HPC2N can be reproduced by Titan to the same accuracy as by a WLCG site, SiGNET. See caption of Figure D.2 for more information.

BIBLIOGRAPHY

[1] D. J. Gross and F. Wilczek, *Ultraviolet Behavior of Nonabelian Gauge Theories*, *Phys. Rev. Lett.* **30** (1973) 1343–1346. 6, 10

[2] H. D. Politzer, *Reliable Perturbative Results for Strong Interactions?*, *Phys. Rev. Lett.* **30** (1973) 1346–1349. 6, 10

[3] H. Fritzsch, M. Gell-Mann and H. Leutwyler, *Advantages of the Color Octet Gluon Picture*, *Phys. Lett.* **B47** (1973) 365–368. 6, 10

[4] S. L. Glashow, *Partial Symmetries of Weak Interactions*, *Nucl. Phys.* **22** (1961) 579–588. 6, 12

[5] A. Salam, *Weak and Electromagnetic Interactions*, *Conf. Proc.* **C680519** (1968) 367–377. 6, 12

[6] S. Weinberg, *A Model of Leptons*, *Phys. Rev. Lett.* **19** (Nov, 1967) 1264–1266. 6, 12

[7] J. Goldstone, *Field theories with « superconductor » solutions*, *Il Nuovo Cimento (1955-1965)* **19** (1961) 154–164. 6

[8] F. Englert and R. Brout, *Broken symmetry and the mass of gauge vector mesons*, *Phys. Rev. Lett.* **13** (Aug, 1964) 321–323. 6, 17

[9] P. W. Higgs, *Broken symmetries and the masses of gauge bosons*, *Phys. Rev. Lett.* **13** (Oct, 1964) 508–509. 6, 17

[10] G. S. Guralnik, C. R. Hagen and T. W. B. Kibble, *Global conservation laws and massless particles*, *Phys. Rev. Lett.* **13** (Nov, 1964) 585–587. 6, 17

[11] Super-Kamiokande collaboration, Y. Fukuda et al., *Evidence for oscillation of atmospheric neutrinos*, *Phys. Rev. Lett.* **81** (1998) 1562–1567, [hep-ex/9807003]. 7, 26

[12] SNO collaboration, Q. R. Ahmad et al., *Direct evidence for neutrino flavor transformation from neutral current interactions in the Sudbury Neutrino Observatory*, *Phys. Rev. Lett.* **89** (2002) 011301, [nucl-ex/0204008]. 7, 26

[13] Particle Data Group collaboration, K. A. Olive et al., *Review of Particle Physics*, *Chin. Phys.* **C38** (2014) 090001. 7, 8, 29, 33, 82, 89

[14] M. Gell-Mann, *A Schematic Model of Baryons and Mesons*, *Phys. Lett.* **8** (1964) 214–215. 10

[15] G. Zweig, *An SU_3 model for strong interaction symmetry and its breaking; Version 1*, Tech. Rep. CERN-TH-401, CERN, Geneva, Jan, 1964. 10

[16] E. D. Bloom, D. H. Coward, H. DeStaebler, J. Drees, G. Miller, L. W. Mo et al., *High-energy inelastic $e-p$ scattering at 6° and 10°*, *Phys. Rev. Lett.* **23** (Oct, 1969) 930–934. 10

[17] M. Breidenbach, J. I. Friedman, H. W. Kendall, E. D. Bloom, D. H. Coward, H. C. DeStaebler et al., *Observed Behavior of Highly Inelastic electron-Proton Scattering*, *Phys. Rev. Lett.* **23** (1969) 935–939. 10

[18] O. W. Greenberg, *Spin and unitary-spin independence in a paraquark model of baryons and mesons*, *Phys. Rev. Lett.* **13** (Nov, 1964) 598–602. 10

[19] J. J. Aubert, U. Becker, P. J. Biggs, J. Burger, M. Chen, G. Everhart et al., *Experimental Observation of a Heavy Particle J*, *Phys. Rev. Lett.* **33** (Dec, 1974) 1404–1406. 10

[20] G. S. Abrams, D. Briggs, W. Chinowsky, C. E. Friedberg, G. Goldhaber, R. J. Hollebeek et al., *Discovery of a second narrow resonance in e^+e^- annihilation*, *Phys. Rev. Lett.* **33** (Dec, 1974) 1453–1455. 10

[21] S. W. Herb et al., *Observation of a Dimuon Resonance at 9.5-GeV in 400-GeV Proton-Nucleus Collisions*, *Phys. Rev. Lett.* **39** (1977) 252–255. 10

[22] D0 collaboration, S. Abachi et al., *Observation of the top quark*, *Phys. Rev. Lett.* **74** (1995) 2632–2637, [hep-ex/9503003]. 10

[23] CDF collaboration, F. Abe et al., *Observation of top quark production in $\overline{p}p$ collisions with the collider detector at fermilab*, *Phys. Rev. Lett.* **74** (Apr, 1995) 2626–2631. 10

[24] P. Soding, B. Wiik, G. Wolf and S. L. Wu, *The First evidence for three jet events in e^+e^- collisions at PETRA: First direct observation of the gluon*, in *High-energy physics. Proceedings, International Europhysics Conference, HEP '95, Brussels, Belgium, July 27-August 2, 1995*, pp. 3–14, 1996. 10

[25] E. Fermi, *An attempt of a theory of beta radiation. 1.*, *Z. Phys.* **88** (1934) 161–177. 12

[26] T. D. Lee and C. N. Yang, *Question of parity conservation in weak interactions*, *Phys. Rev.* **104** (Oct, 1956) 254–258. 12

[27] C. S. Wu, E. Ambler, R. W. Hayward, D. D. Hoppes and R. P. Hudson, *Experimental test of parity conservation in beta decay*, *Phys. Rev.* **105** (Feb, 1957) 1413–1415. 12

[28] E. C. G. Sudarshan and R. e. Marshak, *Chirality invariance and the universal Fermi interaction*, *Phys. Rev.* **109** (1958) 1860–1860. 12

[29] R. P. Feynman and M. Gell-Mann, *Theory of the fermi interaction*, *Phys. Rev.* **109** (Jan, 1958) 193–198. 12

[30] Gargamelle Neutrino collaboration, F. J. Hasert et al., *Observation of Neutrino Like Interactions Without Muon Or Electron in the Gargamelle Neutrino Experiment*, *Phys. Lett.* **B46** (1973) 138–140. 12

[31] UA1 collaboration, G. Arnison et al., *Experimental observation of isolated large transverse energy electrons with associated missing energy at* $\sqrt{s} = 540$ *GeV*, *Phys. Lett.* **B122** (1983) 103–116. 12

[32] UA1 collaboration, G. Arnison et al., *Experimental observation of lepton pairs of invariant mass around 95 GeV/*c^2 *at the CERN SPS collider*, *Phys. Lett.* **B126** (1983) 398–410. 12

[33] ATLAS collaboration, G. Aad et al., *Observation of a new particle in the search for the Standard Model Higgs boson with the ATLAS detector at the LHC*, *Phys. Lett.* **B716** (2012) 1–29, [1207.7214]. 17

[34] CMS collaboration, S. Chatrchyan et al., *Observation of a new boson at a mass of 125 GeV with the CMS experiment at the LHC*, *Phys. Lett.* **B716** (2012) 30–61, [1207.7235]. 17

[35] J. Horejsi, *Fundamentals of Electroweak Theory*. Karolinum Press, 2002. 17

[36] N. Cabibbo, *Unitary Symmetry and Leptonic Decays*, *Phys. Rev. Lett.* **10** (1963) 531–533. 21

[37] M. Kobayashi and T. Maskawa, *CP Violation in the Renormalizable Theory of Weak Interaction*, *Prog. Theor. Phys.* **49** (1973) 652–657. 21

[38] Z. Maki, M. Nakagawa and S. Sakata, *Remarks on the unified model of elementary particles*, *Prog. Theor. Phys.* **28** (1962) 870–880. 21

[39] G. 't Hooft and M. J. G. Veltman, *Regularization and Renormalization of Gauge Fields*, *Nucl. Phys.* **B44** (1972) 189–213. 23

[40] G. 't Hooft, *Dimensional regularization and the renormalization group*, *Nucl. Phys.* **B61** (1973) 455–468. 23

[41] K. G. Wilson and J. Kogut, *The renormalization group and the ϵ expansion*, *Physics Reports* **12** (1974) 75 – 199. 24

[42] Planck collaboration, P. A. R. Ade et al., *Planck 2013 results. XVI. Cosmological parameters*, *Astron. Astrophys.* **571** (2014) A16, [1303.5076]. 25

[43] F. R. Klinkhamer, *Neutrino mass and the Standard Model*, *Mod. Phys. Lett.* **A28** (2013) 1350010, [1112.2669]. 26

[44] M. Drewes, *The Phenomenology of Right Handed Neutrinos*, *Int. J. Mod. Phys.* **E22** (2013) 1330019, [1303.6912]. 26

[45] P. Minkowski, $\mu \to e\gamma$ *at a Rate of One Out of* 10^9 *Muon Decays?*, *Phys. Lett.* **B67** (1977) 421–428. 26

[46] M. Gell-Mann, P. Ramond and R. Slansky, *Complex Spinors and Unified Theories*, *Conf. Proc.* **C790927** (1979) 315–321, [1306.4669]. 26

[47] R. N. Mohapatra and G. Senjanovic, *Neutrino Mass and Spontaneous Parity Violation*, *Phys. Rev. Lett.* **44** (1980) 912. 26

[48] U. Amaldi, W. de Boer and H. Fürstenau, *Comparison of grand unified theories with electroweak and strong coupling constants measured at LEP*, *Phys. Lett. B* **260** (Mar, 1991) 447–455. 20 p. 26

[49] H. Miyazawa, *Baryon number changing currents*, *Progress of Theoretical Physics* **36** (1966) 1266–1276. 26

[50] P. Ramond, *Dual theory for free fermions*, *Phys. Rev. D* **3** (May, 1971) 2415–2418. 26

[51] Yu. A. Golfand and E. P. Likhtman, *Extension of the Algebra of Poincare Group Generators and Violation of p Invariance*, *JETP Lett.* **13** (1971) 323–326. 26

[52] A. Neveu and J. H. Schwarz, *Factorizable dual model of pions*, *Nucl. Phys.* **B31** (1971) 86–112. 26

[53] A. Neveu and J. H. Schwarz, *Quark model of dual pions*, *Phys. Rev. D* **4** (Aug, 1971) 1109–1111. 26

[54] J.-L. Gervais and B. Sakita, *Field Theory Interpretation of Supergauges in Dual Models*, *Nucl. Phys.* **B34** (1971) 632–639. 26

[55] D. V. Volkov and V. P. Akulov, *Is the Neutrino a Goldstone Particle?*, *Phys. Lett.* **B46** (1973) 109–110. 26

[56] J. Wess and B. Zumino, *A Lagrangian Model Invariant Under Supergauge Transformations*, *Phys. Lett.* **B49** (1974) 52. 26

[57] J. Wess and B. Zumino, *Supergauge Transformations in Four-Dimensions*, *Nucl. Phys.* **B70** (1974) 39–50. 26

[58] R. Haag, J. T. Lopuszanski and M. Sohnius, *All Possible Generators of Supersymmetries of the S-Matrix*, *Nucl. Phys.* **B88** (1975) 257. 26

[59] S. Coleman and J. Mandula, *All Possible Symmetries of the S-Matrix*, *Phys. Rev.* **159** (Jul, 1967) 1251–1256. 26

[60] Super-Kamiokande collaboration, H. Nishino et al., *Search for Nucleon Decay into Charged Anti-lepton plus Meson in Super-Kamiokande I and II*, *Phys. Rev.* **D85** (2012) 112001, [1203.4030]. 31

[61] C. Degrande, N. Greiner, W. Kilian, O. Mattelaer, H. Mebane, T. Stelzer et al., *Effective Field Theory: A Modern Approach to Anomalous Couplings*, *Annals Phys.* **335** (2013) 21–32, [1205.4231]. 32

[62] O. J. P. Eboli, M. C. Gonzalez-Garcia and J. K. Mizukoshi, *$pp \to jje^{\pm}\mu^{\pm}\nu\nu$ and $jje^{\pm}\mu^{\mp}\nu\nu$ at $\mathcal{O}(\alpha_{\rm em}^6)$ and $\mathcal{O}(\alpha_{\rm em}^4\alpha_s^2)$ for the study of the quartic electroweak gauge boson vertex at CERN LHC*, *Phys. Rev.* **D74** (2006) 073005, [hep-ph/0606118]. 33

[63] O. J. P. Eboli, M. C. Gonzalez-Garcia and S. M. Lietti, *Bosonic quartic couplings at CERN LHC*, *Phys. Rev.* **D69** (2004) 095005, [hep-ph/0310141]. 34

[64] M. Lamont, *Status of the LHC*, *J. Phys.: Conf. Ser.* **455** (2013) 012001. 35, 46

[65] S. D. Drell and T.-M. Yan, *Partons and their applications at high energies*, *Annals of Physics* **66** (1971) 578 – 623. 35

[66] J. C. Collins, D. E. Soper and G. Sterman, *Factorization for short distance hadron-hadron scattering*, *Nuclear Physics B* **261** (1985) 104 – 142. 35

[67] J. C. Collins, D. E. Soper and G. Sterman, *Soft gluons and factorization*, *Nuclear Physics B* **308** (1988) 833 – 856. 35

[68] G. T. Bodwin, *Factorization of the drell-yan cross section in perturbation theory*, *Phys. Rev. D* **31** (May, 1985) 2616–2642. 35

[69] J. M. Campbell, J. W. Huston and W. J. Stirling, *Hard Interactions of Quarks and Gluons: A Primer for LHC Physics*, *Rept. Prog. Phys.* **70** (2007) 89, [hep-ph/0611148]. 36

[70] R. P. Feynman, *Very high-energy collisions of hadrons*, *Phys. Rev. Lett.* **23** (Dec, 1969) 1415–1417. 36

[71] T. Kinoshita, *Mass singularities of Feynman amplitudes*, *J. Math. Phys.* **3** (1962) 650–677. 37

[72] T. D. Lee and M. Nauenberg, *Degenerate systems and mass singularities*, *Phys. Rev.* **133** (Mar, 1964) B1549–B1562. 37

[73] J. D. Bjorken, *Asymptotic sum rules at infinite momentum*, *Phys. Rev.* **179** (Mar, 1969) 1547–1553. 37

[74] M. Breidenbach, J. I. Friedman, H. W. Kendall, E. D. Bloom, D. H. Coward, H. DeStaebler et al., *Observed behavior of highly inelastic electron-proton scattering*, *Phys. Rev. Lett.* **23** (Oct, 1969) 935–939. 37

[75] E. D. Bloom, D. H. Coward, H. DeStaebler, J. Drees, G. Miller, L. W. Mo et al., *High-energy inelastic $e-p$ scattering at 6° and 10°*, *Phys. Rev. Lett.* **23** (Oct, 1969) 930–934. 37

[76] Y. L. Dokshitzer, *Calculation of the Structure Functions for Deep Inelastic Scattering and e+ e- Annihilation by Perturbation Theory in Quantum Chromodynamics.*, *Sov. Phys. JETP* **46** (1977) 641–653. 37

[77] V. N. Gribov and L. N. Lipatov, *Deep inelastic e p scattering in perturbation theory*, *Sov. J. Nucl. Phys.* **15** (1972) 438–450. 37

[78] G. Altarelli and G. Parisi, *Asymptotic Freedom in Parton Language*, *Nucl. Phys.* **B126** (1977) 298–318. 37

[79] S. Moch, J. A. M. Vermaseren and A. Vogt, *The Three loop splitting functions in QCD: The Nonsinglet case*, *Nucl. Phys.* **B688** (2004) 101–134, [hep-ph/0403192]. 38

[80] A. Vogt, S. Moch and J. A. M. Vermaseren, *The Three-loop splitting functions in QCD: The Singlet case*, *Nucl. Phys.* **B691** (2004) 129–181, [hep-ph/0404111]. 38

[81] H.-L. Lai, M. Guzzi, J. Huston, Z. Li, P. M. Nadolsky, J. Pumplin et al., *New parton distributions for collider physics*, *Phys. Rev.* **D82** (2010) 074024, [1007.2241]. 38

[82] A. D. Martin, W. J. Stirling, R. S. Thorne and G. Watt, *Parton distributions for the LHC*, *Eur. Phys. J.* **C63** (2009) 189–285, [0901.0002]. 38, 39, 121

[83] R. D. Ball et al., *Parton distributions with LHC data*, *Nucl. Phys.* **B867** (2013) 244–289, [1207.1303]. 38

[84] NNPDF collaboration, R. D. Ball et al., *Parton distributions for the LHC Run II*, *JHEP* **04** (2015) 040, [1410.8849]. 38, 121

[85] W.J. Stirling, "Private communication." 40

[86] R. Assmann, R. Bailey, O. Brüning, O. Dominguez Sanchez, G. de Rijk, J. M. Jimenez et al., *First Thoughts on a Higher-Energy LHC*, Tech. Rep. CERN-ATS-2010-177, CERN, Geneva, Aug, 2010. 40, 47

[87] S. Catani, F. Krauss, R. Kuhn and B. R. Webber, *QCD matrix elements + parton showers*, *JHEP* **11** (2001) 063, [hep-ph/0109231]. 41, 186

[88] M. L. Mangano, M. Moretti, F. Piccinini and M. Treccani, *Matching matrix elements and shower evolution for top-quark production in hadronic collisions*, *JHEP* **01** (2007) 013, [hep-ph/0611129]. 41, 180

[89] B. Andersson, G. Gustafson, G. Ingelman and T. Sjöstrand, *Parton fragmentation and string dynamics*, *Physics Reports* **97** (1983) 31 – 145. 42

[90] T. Sjostrand, S. Mrenna and P. Z. Skands, *PYTHIA 6.4 Physics and Manual*, *JHEP* **05** (2006) 026, [hep-ph/0603175]. 42, 72

[91] J.-C. Winter, F. Krauss and G. Soff, *A Modified cluster hadronization model*, *Eur. Phys. J.* **C36** (2004) 381–395, [hep-ph/0311085]. 42

[92] L. Evans and P. Bryant, *LHC Machine*, *JINST* **3** (2008) S08001. 43

[93] ATLAS collaboration, G. Aad et al., *The ATLAS Experiment at the CERN Large Hadron Collider*, *JINST* **3** (2008) S08003. 43, 45, 47, 48, 50, 51, 54, 55, 56, 57

[94] R. Bailey and P. Collier, *Standard Filling Schemes for Various LHC Operation Modes*, Tech. Rep. LHC-PROJECT-NOTE-323, CERN, Geneva, Sep, 2003. 44

[95] Wikipedia, "Map of the CERN accelerator complex." http://en.wikipedia.org/wiki/File:Cern-accelerator-complex.svg, 2016. 45

[96] CMS collaboration, S. Chatrchyan et al., *The CMS experiment at the CERN LHC*, *JINST* **3** (2008) S08004. 45

[97] LHCb collaboration, A. A. Alves, Jr. et al., *The LHCb Detector at the LHC*, *JINST* **3** (2008) S08005. 45

[98] ALICE collaboration, K. Aamodt et al., *The ALICE experiment at the CERN LHC*, *JINST* **3** (2008) S08002. 45

[99] TOTEM collaboration, G. Anelli et al., *The TOTEM experiment at the CERN Large Hadron Collider*, *JINST* **3** (2008) S08007. 45

[100] LHCf collaboration, O. Adriani et al., *The LHCf detector at the CERN Large Hadron Collider*, *JINST* **3** (2008) S08006. 45

[101] MoEDAL collaboration, J. Pinfold, R. Soluk, Y. Yao, S. Cecchini, G. Giacomelli, M. Giorgini et al., *Technical Design Report of the MoEDAL Experiment*, Tech. Rep. CERN-LHCC-2009-006. MoEDAL-TDR-001, Jun, 2009. 45

[102] ATLAS collaboration, "ATLAS Twiki: Luminosity Public Results." https://twiki.cern.ch/twiki/bin/view/AtlasPublic/LuminosityPublicResults, 2016. 47

[103] G. Apollinari, I. Béjar Alonso, O. Brüning, M. Lamont and L. Rossi, *High-Luminosity Large Hadron Collider (HL-LHC): Preliminary Design Report*. CERN, Geneva, 2015. 47

[104] M. Capeans, G. Darbo, K. Einsweiller, M. Elsing, T. Flick, M. Garcia-Sciveres et al., *ATLAS Insertable B-Layer Technical Design Report*, Tech. Rep. CERN-LHCC-2010-013. ATLAS-TDR-19, Sep, 2010. 52

[105] F. Djama, *Overview of the ATLAS insertable B-layer project*, *Journal of Instrumentation* **8** (2013) C01034. 52

[106] ATLAS collaboration, R. Hauser, *The ATLAS Data Acquisition and High Level Trigger Systems: Experience and Upgrade Plans*, *PoS* **ICHEP2012** (2013) 517. 57

[107] ATLAS collaboration, M. Aaboud et al., *Performance of the ATLAS Trigger System in 2015*, 1611.09661. 58

[108] ATLAS collaboration, G. Aad et al., *The ATLAS Simulation Infrastructure*, *Eur. Phys. J.* **C70** (2010) 823–874, [1005.4568]. 59

[109] GEANT4 collaboration, S. Agostinelli et al., *GEANT4: A Simulation toolkit*, *Nucl. Instrum. Meth.* **A506** (2003) 250–303. 59, 73, 74

[110] P. Calafiura, W. Lavrijsen, C. Leggett, M. Marino and D. Quarrie, *The athena control framework in production, new developments and lessons learned*, in *Computing in high energy physics and nuclear physics. Proceedings, Conference, CHEP'04, Interlaken, Switzerland, September 27-October 1, 2004*, pp. 456–458, 2005. 59

[111] P. J. Laycock, N. Ozturk, M. Beckingham, R. Henderson and L. Zhou, *Derived physics data production in atlas: Experience with run 1 and looking ahead*, *Journal of Physics: Conference Series* **513** (2014) 032052. 59

[112] R. Brun and F. Rademakers, *ROOT: An object oriented data analysis framework*, *Nucl. Instrum. Meth.* **A389** (1997) 81–86. 59

[113] A. Buckley, T. Eifert, M. Elsing, D. I. Gillberg, K. Koeneke, A. Krasznahorkay et al., *Implementation of the ATLAS Run 2 event data model*, Tech. Rep. ATL-SOFT-PROC-2015-003. 7, CERN, Geneva, May, 2015. 59

[114] ATLAS collaboration, G. Duckeck, D. Barberis, R. Hawkings, R. Jones, N. McCubbin, G. Poulard et al., *ATLAS computing: Technical design report*, . 60

[115] F. H. Barreiro Megino, K. De, A. Di Girolamo, T. Maeno and R. Walker, *ATLAS WORLD-cloud and networking in PanDA*, Tech. Rep. ATL-SOFT-PROC-2017-008, CERN, Geneva, Jan, 2017. 61

[116] F. H. Barreiro Megino, K. De, A. Klimentov, T. Maeno, P. Nilsson, D. Oleynik et al., *PanDA for ATLAS distributed computing in the next decade*, Tech. Rep. ATL-SOFT-PROC-2017-016, CERN, Geneva, Jan, 2017. 61

[117] P. Buncic, C. A. Sanchez, J. Blomer, L. Franco, A. Harutyunian, P. Mato et al., *CernVM – a virtual software appliance for LHC applications*, *Journal of Physics: Conference Series* **219** (2010) 042003. 61

[118] D. Cameron, A. Filipčič, W. Guan, V. Tsulaia, R. Walker and T. Wenaus, *Exploiting Opportunistic Resources for ATLAS with ARC CE and the Event Service*, Tech. Rep. ATL-SOFT-PROC-2017-013, CERN, Geneva, Jan, 2017. 61

[119] "Titan at OLCF web page." https://www.olcf.ornl.gov/titan/, 2017. 61, 230

[120] K. De, A. Klimentov, D. Oleynik, S. Panitkin, A. Petrosyan, J. Schovancova et al., *Integration of PanDA workload management system with Titan supercomputer at OLCF*, *Journal of Physics: Conference Series* **664** (2015) 092020. 61

[121] ATLAS DC1 Task force collaboration, R. Sturrock et al., *A step towards a computing grid for the LHC experiments: ATLAS data challenge 1*, *Submitted to: Nucl. Instrum. Methods* (2004) . 62

[122] W. Lampl, S. Laplace, D. Lelas, P. Loch, H. Ma, S. Menke et al., *Calorimeter Clustering Algorithms: Description and Performance*, Tech. Rep. ATL-LARG-PUB-2008-002. ATL-COM-LARG-2008-003, CERN, Geneva, Apr, 2008. 63, 66

[123] ATLAS collaboration, *Electron efficiency measurements with the ATLAS detector using the 2012 LHC proton-proton collision data*, Tech. Rep. ATLAS-CONF-2014-032, CERN, Geneva, Jun, 2014. 63, 64, 76, 122

[124] ATLAS collaboration, G. Aad et al., *Electron performance measurements with the ATLAS detector using the 2010 LHC proton-proton collision data*, *Eur. Phys. J.* **C72** (2012) 1909, [1110.3174]. 63

[125] ATLAS collaboration, G. Aad et al., *Electron and photon energy calibration with the ATLAS detector using LHC Run 1 data*, *Eur. Phys. J.* **C74** (2014) 3071, [1407.5063]. 64, 122

[126] ATLAS collaboration, G. Aad et al., *Measurement of the muon reconstruction performance of the ATLAS detector using 2011 and 2012 LHC proton–proton collision data*, *Eur. Phys. J.* **C74** (2014) 3130, [1407.3935]. 64, 65, 66, 78, 122

[127] M. Cacciari, G. P. Salam and G. Soyez, *The Anti-k(t) jet clustering algorithm*, *JHEP* **04** (2008) 063, [0802.1189]. 66

[128] T. Barillari, E. Bergeaas Kuutmann, T. Carli, J. Erdmann, P. Giovannini, K. J. Grahn et al., *Local Hadronic Calibration*, Tech. Rep. ATL-LARG-PUB-2009-001-2. ATL-COM-LARG-2008-006. ATL-LARG-PUB-2009-001, CERN, Geneva, Jun, 2008. 66

[129] ATLAS collaboration, G. Aad et al., *Jet energy measurement with the ATLAS detector in proton-proton collisions at* $\sqrt{s} = 7$ *TeV*, *Eur. Phys. J.* **C73** (2013) 2304, [1112.6426]. 67, 122

[130] ATLAS collaboration, G. Aad et al., *Performance of b-Jet Identification in the ATLAS Experiment*, *JINST* **11** (2016) P04008, [1512.01094]. 67

[131] ATLAS collaboration, *Calibration of the performance of b-tagging for c and light-flavour jets in the 2012 ATLAS data*, Tech. Rep. ATLAS-CONF-2014-046, CERN, Geneva, Jul, 2014. 67

[132] ATLAS collaboration, G. Aad et al., *Performance of Missing Transverse Momentum Reconstruction in Proton-Proton Collisions at 7 TeV with ATLAS*, *Eur. Phys. J.* **C72** (2012) 1844, [1108.5602]. 67, 79, 123

[133] ATLAS collaboration, *Performance of Missing Transverse Momentum Reconstruction in ATLAS studied in Proton-Proton Collisions recorded in 2012 at 8 TeV*, Tech. Rep. ATLAS-CONF-2013-082, CERN, Geneva, Aug, 2013. 67, 79

[134] ATLAS collaboration, *Expected performance of missing transverse momentum reconstruction for the ATLAS detector at* $\sqrt{s} = 13$ *TeV*, Tech. Rep. ATL-PHYS-PUB-2015-023, CERN, Geneva, Jul, 2015. 68

[135] ATLAS collaboration, *Performance of missing transverse momentum reconstruction for the ATLAS detector in the first proton-proton collisions at at* $\sqrt{s}$*= 13 TeV*, Tech. Rep. ATL-PHYS-PUB-2015-027, CERN, Geneva, Jul, 2015. 68

[136] DELPHI collaboration, J. Abdallah et al., *Measurement of the* $e^+e^- \to W^+W^-\gamma$ *cross-section and limits on anomalous quartic gauge couplings with DELPHI*, *Eur. Phys. J.* **C31** (2003) 139–147, [hep-ex/0311004]. 70

[137] L3 collaboration, P. Achard et al., *The* $e^+e^- \to Z\gamma\gamma \to q\bar{q}\gamma\gamma$ *reaction at LEP and constraints on anomalous quartic gauge boson couplings*, *Phys. Lett.* **B540** (2002) 43–51, [hep-ex/0206050]. 70

[138] L3 collaboration, P. Achard et al., *Study of the* $W^+W^-\gamma$ *process and limits on anomalous quartic gauge boson couplings at LEP*, *Phys. Lett.* **B527** (2002) 29–38, [hep-ex/0111029]. 70

[139] OPAL collaboration, G. Abbiendi et al., *Measurement of the* $W^+W^-\gamma$ *cross-section and first direct limits on anomalous electroweak quartic gauge couplings*, *Phys. Lett.* **B471** (1999) 293–307, [hep-ex/9910069]. 70

[140] OPAL collaboration, G. Abbiendi et al., *A Study of* $W^+W^-\gamma$ *events at LEP*, *Phys. Lett.* **B580** (2004) 17–36, [hep-ex/0309013]. 70

[141] OPAL collaboration, G. Abbiendi et al., *Constraints on anomalous quartic gauge boson couplings from nu anti-nu gamma gamma and q*

anti-q gamma gamma events at LEP-2, *Phys. Rev.* **D70** (2004) 032005, [hep-ex/0402021]. 70

[142] D0 collaboration, V. M. Abazov et al., *Search for anomalous quartic $WW\gamma\gamma$ couplings in dielectron and missing energy final states in $p\bar{p}$ collisions at $\sqrt{s}$ = 1.96 TeV*, *Phys. Rev.* **D88** (2013) 012005, [1305.1258]. 70

[143] CMS collaboration, S. Chatrchyan et al., *Study of exclusive two-photon production of W^+W^- in pp collisions at $\sqrt{s} = 7$ TeV and constraints on anomalous quartic gauge couplings*, *JHEP* **07** (2013) 116, [1305.5596]. 70

[144] CMS collaboration, S. Chatrchyan et al., *Search for $WW\gamma$ and $WZ\gamma$ production and constraints on anomalous quartic gauge couplings in pp collisions at $\sqrt{s} = 8$ TeV*, *Phys. Rev.* **D90** (2014) 032008, [1404.4619]. 70

[145] ATLAS collaboration, G. Aad et al., *Evidence of $W\gamma\gamma$ Production in pp Collisions at $\sqrt{s} = 8$ TeV and Limits on Anomalous Quartic Gauge Couplings with the ATLAS Detector*, *Phys. Rev. Lett.* **115** (2015) 031802, [1503.03243]. 70

[146] CMS collaboration, V. Khachatryan et al., *Study of vector boson scattering and search for new physics in events with two same-sign leptons and two jets*, *Phys. Rev. Lett.* **114** (2015) 051801, [1410.6315]. 70, 163

[147] ATLAS collaboration, G. Aad et al., *Evidence for Electroweak Production of $W^\pm W^\pm jj$ in pp Collisions at $\sqrt{s} = 8$ TeV with the ATLAS Detector*, *Phys. Rev. Lett.* **113** (2014) 141803, [1405.6241]. 70

[148] J. Butler, C. Diaconu, A. Di Simone, L. Helary, Y. Liu, B. A. Long et al., *Search for Triboson $W^\pm W^\mp W^\pm \to \ell^\pm\nu\ell^\mp\nu\ell^\pm\nu$ Production and Anomalous Quartic Gauge Couplings in 8 TeV ATLAS Data*, Tech. Rep. ATL-COM-PHYS-2015-601, CERN, Geneva, Jun, 2015. 70, 82, 87, 153

[149] T. Binoth, G. Ossola, C. G. Papadopoulos and R. Pittau, *NLO QCD corrections to tri-boson production*, *JHEP* **06** (2008) 082, [0804.0350]. 70, 73

[150] F. Campanario, V. Hankele, C. Oleari, S. Prestel and D. Zeppenfeld, *QCD corrections to charged triple vector boson production with leptonic decay*, *Phys. Rev.* **D78** (2008) 094012, [0809.0790]. 70, 73

[151] S. Yong-Bai, Z. Ren-You, M. Wen-Gan, L. Xiao-Zhou and G. Lei, *NLO QCD + EW corrections to WWW production with leptonic decays at the LHC*, 1605.00554. 70, 73

[152] ATLAS collaboration, M. Aaboud et al., *Luminosity determination in pp collisions at $\sqrt{s}$ = 8 TeV using the ATLAS detector at the LHC*, 1608.03953. 71, 124

[153] J. Alwall, M. Herquet, F. Maltoni, O. Mattelaer and T. Stelzer, *MadGraph 5 : Going Beyond*, *JHEP* **06** (2011) 128, [1106.0522]. 71, 73

[154] P. Nason, *A New method for combining NLO QCD with shower Monte Carlo algorithms*, *JHEP* **11** (2004) 040, [hep-ph/0409146]. 71

[155] S. Frixione, P. Nason and C. Oleari, *Matching NLO QCD computations with Parton Shower simulations: the POWHEG method*, *JHEP* **11** (2007) 070, [0709.2092]. 71

[156] S. Alioli, P. Nason, C. Oleari and E. Re, *A general framework for implementing NLO calculations in shower Monte Carlo programs: the POWHEG BOX*, *JHEP* **06** (2010) 043, [1002.2581]. 71

[157] T. Gleisberg, S. Hoeche, F. Krauss, M. Schonherr, S. Schumann, F. Siegert et al., *Event generation with SHERPA 1.1*, *JHEP* **02** (2009) 007, [0811.4622]. 71

[158] M. L. Mangano, M. Moretti, F. Piccinini, R. Pittau and A. D. Polosa, *ALPGEN, a generator for hard multiparton processes in hadronic collisions*, *JHEP* **07** (2003) 001, [hep-ph/0206293]. 71

[159] J. Alwall, R. Frederix, S. Frixione, V. Hirschi, F. Maltoni, O. Mattelaer et al., *The automated computation of tree-level and next-to-leading order differential cross sections, and their matching to parton shower simulations*, *JHEP* **07** (2014) 079, [1405.0301]. 72, 73

[160] B. P. Kersevan and E. Richter-Was, *The Monte Carlo event generator AcerMC versions 2.0 to 3.8 with interfaces to PYTHIA 6.4, HERWIG 6.5 and ARIADNE 4.1*, *Comput. Phys. Commun.* **184** (2013) 919–985, [hep-ph/0405247]. 72

[161] T. Sjostrand, S. Mrenna and P. Z. Skands, *A Brief Introduction to PYTHIA 8.1*, *Comput. Phys. Commun.* **178** (2008) 852–867, [0710.3820]. 72, 74

[162] G. Corcella, I. G. Knowles, G. Marchesini, S. Moretti, K. Odagiri, P. Richardson et al., *HERWIG 6: An Event generator for hadron emission reactions with interfering gluons (including supersymmetric processes)*, *JHEP* **01** (2001) 010, [hep-ph/0011363]. 72

[163] J. M. Butterworth, J. R. Forshaw and M. H. Seymour, *Multiparton interactions in photoproduction at HERA*, *Z. Phys.* **C72** (1996) 637–646, [hep-ph/9601371]. 72

[164] T. Binoth, N. Kauer and P. Mertsch, *Gluon-induced QCD corrections to $pp \to ZZ \to \ell\bar{\ell}\ell'\bar{\ell}'$*, in *Proceedings, 16th International Workshop on Deep Inelastic Scattering and Related Subjects (DIS 2008): London, UK, April 7-11, 2008*, p. 142, 2008. 0807.0024. DOI. 72

[165] T. Binoth, M. Ciccolini, N. Kauer and M. Kramer, *Gluon-induced W-boson pair production at the LHC*, *JHEP* **12** (2006) 046, [hep-ph/0611170]. 72

[166] M. Guzzi, P. Nadolsky, E. Berger, H.-L. Lai, F. Olness and C. P. Yuan, *CT10 parton distributions and other developments in the global QCD analysis*, 1101.0561. 72

[167] J. Pumplin, D. R. Stump, J. Huston, H. L. Lai, P. M. Nadolsky and W. K. Tung, *New generation of parton distributions with uncertainties from global QCD analysis*, *JHEP* **07** (2002) 012, [hep-ph/0201195]. 72

[168] ATLAS collaboration, *ATLAS tunes of PYTHIA 6 and Pythia 8 for MC11*, Tech. Rep. ATL-PHYS-PUB-2011-009, CERN, Geneva, July, 2011. 73

[169] ATLAS collaboration, *Summary of ATLAS Pythia 8 tunes*, Tech. Rep. ATL-PHYS-PUB-2012-003, CERN, Geneva, Aug, 2012. 73

[170] M. Beckingham, M. Duehrssen, E. Schmidt, M. Shapiro, M. Venturi, J. Virzi et al., *The simulation principle and performance of the ATLAS fast calorimeter simulation FastCaloSim*, Tech. Rep. ATL-PHYS-PUB-2010-013, CERN, Geneva, Oct, 2010. 73

[171] K. Arnold et al., *VBFNLO: A Parton level Monte Carlo for processes with electroweak bosons*, *Comput. Phys. Commun.* **180** (2009) 1661–1670, [0811.4559]. 73

[172] ATLAS collaboration, M. Aaboud et al., *Search for triboson $W^{\pm}W^{\pm}W^{\mp}$ production in pp collisions at $\sqrt{s} = 8$ TeV with the ATLAS detector*, *Eur. Phys. J.* **C77** (2017) 141, [1610.05088]. 74, 153

[173] C. Degrande, O. Eboli, B. Feigl, B. Jäger, W. Kilian, O. Mattelaer et al., *Monte Carlo tools for studies of non-standard electroweak gauge boson interactions in multi-boson processes: A Snowmass White Paper*, in *Proceedings, Community Summer Study 2013: Snowmass on the Mississippi (CSS2013): Minneapolis, MN, USA, July 29-August 6, 2013*, 2013. 1309.7890. 75

[174] W. Kilian, T. Ohl and J. Reuter, *WHIZARD: Simulating Multi-Particle Processes at LHC and ILC*, *Eur. Phys. J.* **C71** (2011) 1742, [0708.4233]. 75

[175] A. Alboteanu, W. Kilian and J. Reuter, *Resonances and Unitarity in Weak Boson Scattering at the LHC*, *JHEP* **11** (2008) 010, [0806.4145]. 75, 163

[176] A. C. Longhitano, *Low-energy impact of a heavy higgs boson sector*, *Nuclear Physics B* **188** (1981) 118 – 154. 75

[177] ATLAS collaboration, G. Aad et al., *Electron reconstruction and identification efficiency measurements with the ATLAS detector using the 2011 LHC proton-proton collision data*, *Eur. Phys. J.* **C74** (2014) 2941, [1404.2240]. 76, 122

[178] ATLAS collaboration, "ATLAS Twiki: ATLAS Muon Combined Performance Guidelines for Analyses of 2012 Data." https://twiki.cern.ch/twiki/bin/viewauth/AtlasProtected/MCPAnalysisGuidelinesData2012, 2016. 78, 174

[179] ATLAS collaboration, *Performance of Missing Transverse Momentum Reconstruction in ATLAS with 2011 Proton-Proton Collisions at sqrts = 7 TeV*, Tech. Rep. ATLAS-CONF-2012-101, CERN, Geneva, Jul, 2012. 79

[180] ATLAS collaboration, "ATLAS Twiki: Data Quality Checklist." https://twiki.cern.ch/twiki/bin/viewauth/Atlas/DataPreparationCheckListForPhysicsAnalysis, 2016. 81, 219

[181] ATLAS collaboration, "ATLAS Twiki: Jet Cleaning." https://twiki.cern.ch/twiki/bin/viewauth/AtlasProtected/HowToCleanJets2012, 2016. 81, 219

[182] A. Buckley, J. Butterworth, L. Lonnblad, D. Grellscheid, H. Hoeth, J. Monk et al., *Rivet user manual*, *Comput. Phys. Commun.* **184** (2013) 2803–2819, [1003.0694]. 84

[183] ATLAS collaboration, G. Aad et al., *Measurement of WZ production in proton-proton collisions at $\sqrt{s} = 7$ TeV with the ATLAS detector*, *Eur. Phys. J.* **C72** (2012) 2173, [1208.1390]. 87

[184] ATLAS collaboration, G. Aad et al., *Measurements of $W^{\pm}Z$ production cross sections in pp collisions at $\sqrt{s} = 8$ TeV with the ATLAS detector and limits on anomalous gauge boson self-couplings*, *Phys. Rev.* **D93** (2016) 092004, [1603.02151]. 87, 155, 163

[185] CMS collaboration, *Measurement of WZ production rate*, Tech. Rep. CMS-PAS-SMP-12-006, CERN, Geneva, 2013. 87

[186] M. Grazzini, S. Kallweit, D. Rathlev and M. Wiesemann, *$W^{\pm}Z$ production at hadron colliders in NNLO QCD*, 1604.08576. 87, 184

[187] ATLAS collaboration, G. Aad et al., *Measurements of $W\gamma$ and $Z\gamma$ production in pp collisions at $\sqrt{s}$=7 TeV with the ATLAS detector at the LHC*, *Phys. Rev.* **D87** (2013) 112003, [1302.1283]. 87, 88

[188] ATLAS collaboration, M. Aaboud et al., *Measurement of the $W^{\pm}Z$-boson production cross sections in pp collisions at $\sqrt{s} = 13$ TeV with the ATLAS Detector*, *Phys. Lett.* **B759** (2016) 601–621, [1606.04017]. 87

[189] F. Cascioli, T. Gehrmann, M. Grazzini, S. Kallweit, P. Maierhöfer, A. von Manteuffel et al., *ZZ production at hadron colliders in NNLO QCD*, *Phys. Lett.* **B735** (2014) 311–313, [1405.2219]. 88, 184

[190] J. Baglio, L. D. Ninh and M. M. Weber, *Massive gauge boson pair production at the LHC: a next-to-leading order story*, *Phys. Rev.* **D88** (2013) 113005, [1307.4331]. 88

[191] A. Bierweiler, T. Kasprzik and J. H. Kühn, *Vector-boson pair production at the LHC to $\mathcal{O}(\alpha^3)$ accuracy*, *JHEP* **12** (2013) 071, [1305.5402]. 88

[192] ATLAS collaboration, G. Aad et al., *Measurement of the ZZ Production Cross Section in pp Collisions at $\sqrt{s} = 13$ TeV with the ATLAS Detector*, *Phys. Rev. Lett.* **116** (2016) 101801, [1512.05314]. 88

[193] ATLAS collaboration, G. Aad et al., *Measurements of $Z\gamma$ and $Z\gamma\gamma$ production in pp collisions at $\sqrt{s} = 8$ TeV with the ATLAS detector*, *Phys. Rev.* **D93** (2016) 112002, [1604.05232]. 88

[194] J. M. Campbell and R. K. Ellis, *$t\bar{t}W^{\pm}$ production and decay at NLO*, *Journal of High Energy Physics* **2012** (2012) 1–12. 88, 180, 181

[195] M. V. Garzelli, A. Kardos, C. G. Papadopoulos and Z. Trocsanyi, *$t\bar{t}W^{\pm}$ and $t\bar{t}Z$ Hadroproduction at NLO accuracy in QCD with Parton Shower and Hadronization effects*, *JHEP* **11** (2012) 056, [1208.2665]. 88, 180, 181

[196] T. P. S. Gillam and C. Lester, *Identifying fake leptons in ATLAS while hunting SUSY in 8 TeV proton-proton collisions*. PhD thesis, Cambridge U., 2015. 95, 193

[197] T. P. S. Gillam and C. G. Lester, *Improving estimates of the number of 'fake' leptons and other mis-reconstructed objects in hadron collider events: Bob's your uncle*, *Journal of High Energy Physics* **2014** (2014) 1–21. 95, 193

[198] ATLAS collaboration, "ATLAS Twiki: MCTruthClassifier." https://twiki.cern.ch/twiki/bin/view/AtlasProtected/MCTruthClassifier, 2016. 106

[199] ATLAS collaboration, G. Aad et al., *Jet energy measurement and its systematic uncertainty in proton-proton collisions at $\sqrt{s} = 7$ TeV with the ATLAS detector*, *Eur. Phys. J.* **C75** (2015) 17, [1406.0076]. 122

[200] ATLAS collaboration, G. Aad et al., *Jet energy resolution in proton-proton collisions at $\sqrt{s} = 7$ TeV recorded in 2010 with the ATLAS detector*, *Eur. Phys. J.* **C73** (2013) 2306, [1210.6210]. 122

[201] ATLAS collaboration, *Calibration of b-tagging using dileptonic top pair events in a combinatorial likelihood approach with the ATLAS experiment*, Tech. Rep. ATLAS-CONF-2014-004, CERN, Geneva, Feb, 2014. 123

[202] ATLAS collaboration, *Measurement of the b-tag Efficiency in a Sample of Jets Containing Muons with 5 fb^{-1} of Data from the ATLAS Detector*, Tech. Rep. ATLAS-CONF-2012-043, CERN, Geneva, Mar, 2012. 123

[203] ATLAS collaboration, *Measurement of the Mistag Rate with 5 fb^{-1} of Data Collected by the ATLAS Detector*, Tech. Rep. ATLAS-CONF-2012-040, CERN, Geneva, Mar, 2012. 123

[204] ROOT collaboration, K. Cranmer, G. Lewis, L. Moneta, A. Shibata and W. Verkerke, *HistFactory: A tool for creating statistical models for use with RooFit and RooStats*, . 133

[205] L. Moneta, K. Cranmer, G. Schott and W. Verkerke, *The RooStats project*, p. 57, 2010. 1009.1003. 133

[206] W. Verkerke and D. Kirkby, *The RooFit toolkit for data modeling*, *ArXiv Physics e-prints* (June, 2003) , [physics/0306116]. 133

[207] F. James and M. Roos, *MINUIT: a system for function minimization and analysis of the parameter errors and corrections*, *Comput. Phys. Commun.* **10** (Jul, 1975) 343–367. 38 p. 134

[208] A. Wald, *Tests of Statistical Hypotheses Concerning Several Parameters When the Number of Observations is Large*, *Transactions of the American Mathematical Society* **54** (Nov., 1943) 426–482. 135, 145

[209] G. Cowan, K. Cranmer, E. Gross and O. Vitells, *Asymptotic formulae for likelihood-based tests of new physics*, *Eur. Phys. J.* **C71** (2011) 1554, [1007.1727]. 135, 142, 178, 205, 207

[210] I. Asimov, *Franchise*, *If: Worlds of Science Fiction* (1955) . 135

[211] S. S. Wilks, *The Large-Sample Distribution of the Likelihood Ratio for Testing Composite Hypotheses*, *Annals Math. Statist.* **9** (1938) 60–62. 142

[212] A. L. Read, *Presentation of search results: the CL_s technique*, *J. Phys.* **G28** (2002) 2693–2704. 144, 205

[213] J. Liu, L. Liu, M.-A. Pleier, J. Searcy, I. Siral, T. Xu et al., *Search for Triboson $W^{\pm}W^{\mp}W^{\pm} \to \ell^{\pm}\ell^{\pm}jj$ Production and Anomalous Quartic Gauge Couplings in 8 TeV ATLAS Data*, Tech. Rep. ATL-COM-PHYS-2015-500, CERN, Geneva, Jun, 2015. 153

[214] ATLAS collaboration, G. Aad et al., *Evidence for Electroweak Production of $W^{\pm}W^{\pm}jj$ in pp Collisions at $\sqrt{s} = 8$ TeV with the ATLAS Detector*, *Phys. Rev. Lett.* **113** (2014) 141803, [1405.6241]. 153, 163

[215] ATLAS collaboration, G. Aad et al., *Search for supersymmetry at $\sqrt{s}$=8 TeV in final states with jets and two same-sign leptons or three leptons with the ATLAS detector*, *JHEP* **06** (2014) 035, [1404.2500]. 165, 198

[216] N. Arkani-Hamed, P. Schuster, N. Toro, J. Thaler, L.-T. Wang, B. Knuteson et al., *MARMOSET: The Path from LHC Data to the New Standard Model via On-Shell Effective Theories*, hep-ph/0703088. 166

[217] J. Barnard and B. Farmer, *A simple technique for combining simplified models and its application to direct stop production*, *JHEP* **06** (2014) 132, [1402.3298]. 166

[218] LHC New Physics Working Group collaboration, D. Alves, *Simplified Models for LHC New Physics Searches*, *J. Phys.* **G39** (2012) 105005, [1105.2838]. 166

[219] ATLAS collaboration, "ATLAS Twiki: SUSY Feynman Diagrams." https://twiki.cern.ch/twiki/bin/viewauth/AtlasProtected/SUSYFeynmanDiagrams. 167, 169, 170

[220] A. H. Chamseddine, R. Arnowitt and P. Nath, *Locally supersymmetric grand unification*, *Phys. Rev. Lett.* **49** (Oct, 1982) 970–974. 170

[221] R. Barbieri, S. Ferrara and C. Savoy, *Gauge models with spontaneously broken local supersymmetry*, *Physics Letters B* **119** (1982) 343 – 347. 170

[222] L. Ibáñez, *Locally supersymmetric su(5) grand unification*, *Physics Letters B* **118** (1982) 73 – 78. 170

[223] L. Hall, J. Lykken and S. Weinberg, *Supergravity as the messenger of supersymmetry breaking*, *Phys. Rev. D* **27** (May, 1983) 2359–2378. 170

[224] N. Ohta, *Grand unified theories based on local supersymmetry*, *Progress of Theoretical Physics* **70** (1983) 542–549, [http://ptp.oxfordjournals.org/content/70/2/542.full.pdf+html]. 170

[225] G. L. Kane, C. F. Kolda, L. Roszkowski and J. D. Wells, *Study of constrained minimal supersymmetry*, *Phys. Rev.* **D49** (1994) 6173–6210, [hep-ph/9312272]. 170

[226] S. Roy and B. Mukhopadhyaya, *Some implications of a supersymmetric model with R-parity breaking bilinear interactions*, *Phys. Rev.* **D55** (1997) 7020–7029, [hep-ph/9612447]. 170

[227] M. Dine and W. Fischler, *A phenomenological model of particle physics based on supersymmetry*, *Physics Letters B* **110** (1982) 227 – 231. 170, 171

[228] L. Alvarez-Gaumé, M. Claudson and M. B. Wise, *Low-energy supersymmetry*, *Nuclear Physics B* **207** (1982) 96 – 110. 170, 171

[229] C. R. Nappi and B. A. Ovrut, *Supersymmetric extension of the $su(3)\times su(2)\times u(1)$ model*, *Physics Letters B* **113** (1982) 175 – 179. 170, 171

[230] M. Dine and A. E. Nelson, *Dynamical supersymmetry breaking at low energies*, *Phys. Rev. D* **48** (Aug, 1993) 1277–1287. 170, 171

[231] M. Dine, A. E. Nelson and Y. Shirman, *Low energy dynamical supersymmetry breaking simplified*, *Phys. Rev. D* **51** (Feb, 1995) 1362–1370. 170, 171

[232] M. Dine, A. E. Nelson, Y. Nir and Y. Shirman, *New tools for low energy dynamical supersymmetry breaking*, *Phys. Rev. D* **53** (Mar, 1996) 2658–2669. 170, 171

[233] H.-C. Cheng, K. T. Matchev and M. Schmaltz, *Bosonic supersymmetry? Getting fooled at the CERN LHC*, *Phys. Rev.* **D66** (2002) 056006, [hep-ph/0205314]. 170, 171

[234] H. Baer, V. Barger, P. Huang, D. Mickelson, A. Mustafayev and X. Tata, *Post-LHC7 fine-tuning in the minimal supergravity/CMSSM model with a 125 GeV Higgs boson*, *Phys. Rev.* **D87** (2013) 035017, [1210.3019]. 170

[235] D. F. Carvalho, M. E. Gómez and J. C. Romão, *Charged lepton flavor violation in supersymmetry with bilinear R-parity violation*, *Phys. Rev. D* **65** (May, 2002) 093013. 171

[236] Y. Grossman and S. Rakshit, *Neutrino masses in R-parity violating supersymmetric models*, *Phys. Rev. D* **69** (May, 2004) 093002. 171

[237] ATLAS collaboration, G. Aad et al., *Further search for supersymmetry at $\sqrt{s} = 7$ TeV in final states with jets, missing transverse momentum and isolated leptons with the ATLAS detector*, *Phys. Rev.* **D86** (2012) 092002, [1208.4688]. 171, 209, 212, 214

[238] ATLAS collaboration, G. Aad et al., *Search for events with large missing transverse momentum, jets, and at least two tau leptons in 7 TeV proton–proton collision data with the ATLAS detector*, *Phys. Lett.* **B714** (2012) 180–196, [1203.6580]. 171

[239] ATLAS collaboration, G. Aad et al., *Search for supersymmetry with jets, missing transverse momentum and at least one hadronically decaying τ lepton in proton-proton collisions at $\sqrt{s} = 7$ TeV with the ATLAS detector*, *Phys. Lett.* **B714** (2012) 197–214, [1204.3852]. 171

[240] ATLAS collaboration, G. Aad et al., *Improved luminosity determination in pp collisions at $\sqrt{s} = 7$ TeV using the ATLAS detector at the LHC*, *Eur. Phys. J.* **C73** (2013) 2518, [1302.4393]. 171, 201

[241] W. Beenakker, R. Hopker, M. Spira and P. M. Zerwas, *Squark and gluino production at hadron colliders*, *Nucl. Phys.* **B492** (1997) 51–103, [hep-ph/9610490]. 173

[242] A. Kulesza and L. Motyka, *Threshold resummation for squark-antisquark and gluino-pair production at the LHC*, *Phys. Rev. Lett.* **102** (2009) 111802, [0807.2405]. 173

[243] A. Kulesza and L. Motyka, *Soft gluon resummation for the production of gluino-gluino and squark-antisquark pairs at the LHC*, *Phys. Rev.* **D80** (2009) 095004, [0905.4749]. 173

[244] W. Beenakker, S. Brensing, M. Kramer, A. Kulesza, E. Laenen and I. Niessen, *Soft-gluon resummation for squark and gluino hadroproduction*, *JHEP* **12** (2009) 041, [0909.4418]. 173

[245] W. Beenakker, S. Brensing, M. n. Kramer, A. Kulesza, E. Laenen, L. Motyka et al., *Squark and Gluino Hadroproduction*, *Int. J. Mod. Phys.* **A26** (2011) 2637–2664, [1105.1110]. 173

[246] M. Kramer, A. Kulesza, R. van der Leeuw, M. Mangano, S. Padhi, T. Plehn et al., *Supersymmetry production cross sections in pp collisions at* $\sqrt{s} = 7$ *TeV*, 1206.2892. 173

[247] ATLAS collaboration, *Search for strongly produced superpartners in final states with two same sign leptons with the ATLAS detector using 21* fb^{-1} *of proton-proton collisions at* $\sqrt{s}$ *=8 TeV*, Tech. Rep. ATLAS-CONF-2013-007, CERN, Geneva, Mar, 2013. 177

[248] ATLAS collaboration, *Search for supersymmetry using events with three leptons, multiple jets, and missing transverse momentum in 13.0* fb^{-1} *of pp collisions with the ATLAS detector at* $\sqrt{s} = 8$ *TeV*, Tech. Rep. ATLAS-CONF-2012-151, CERN, Geneva, Nov, 2012. 177

[249] CMS collaboration, V. Khachatryan et al., *Observation of top quark pairs produced in association with a vector boson in pp collisions at* $\sqrt{s} = 8$ *TeV*, *JHEP* **01** (2016) 096, [1510.01131]. 180

[250] ATLAS collaboration, G. Aad et al., *Measurement of the* $t\bar{t}W$ *and* $t\bar{t}Z$ *production cross sections in pp collisions at* $\sqrt{s} = 8$ *TeV with the ATLAS detector*, *JHEP* **11** (2015) 172, [1509.05276]. 180

[251] J. Alwall, S. Höche, F. Krauss, N. Lavesson, L. Lönnblad, F. Maltoni et al., *Comparative study of various algorithms for the merging of parton showers and matrix elements in hadronic collisions*, *The European Physical Journal C* **53** (2008) 473–500. 180, 186

[252] J. Butterworth, E. Dobson, U. Klein, B. Mellado Garcia, T. Nunnemann, J. Qian et al., *Single Boson and Diboson Production Cross Sections in pp Collisions at* $\sqrt{s}$ *=7 TeV*, Tech. Rep. ATL-COM-PHYS-2010-695, CERN, Geneva, Aug, 2010. 184, 185

[253] J. M. Campbell, R. K. Ellis and C. Williams, *Vector boson pair production at the LHC*, *JHEP* **07** (2011) 018, [1105.0020]. 184, 185

[254] ATLAS collaboration, *Search for Supersymmetry in final states with two same-sign leptons, jets and missing transverse momentum with the ATLAS detector in pp collisions at $\sqrt{s}$ =8 TeV*, Tech. Rep. ATLAS-CONF-2012-105, CERN, Geneva, Aug, 2012. 192

[255] T. H. Kittelmann, V. Tsulaia, J. Boudreau and E. Moyse, *The virtual point 1 event display for the ATLAS experiment*, *J. Phys. Conf. Ser.* **219** (2010) 032012. 205, 227

[256] M. Baak, G. J. Besjes, D. Côté, A. Koutsman, J. Lorenz and D. Short, *HistFitter software framework for statistical data analysis*, *Eur. Phys. J.* **C75** (2015) 153, [1410.1280]. 205

[257] "The Durham HepData project." http://hepdata.cedar.ac.uk/reaction. 209

[258] ATLAS collaboration, G. Aad et al., *Search for squarks and gluinos with the ATLAS detector in final states with jets and missing transverse momentum using 4.7 fb^{-1} of $\sqrt{s} = 7$ TeV proton-proton collision data*, *Phys. Rev.* **D87** (2013) 012008, [1208.0949]. 209, 212

[259] ATLAS collaboration, G. Aad et al., *Search for supersymmetry in events with large missing transverse momentum, jets, and at least one τ lepton in 7 TeV proton-proton collision data with the ATLAS detector*, *Eur. Phys. J.* **C72** (2012) 2215, [1210.1314]. 209, 214

[260] ATLAS collaboration, G. Aad et al., *Search for top and bottom squarks from gluino pair production in final states with missing transverse energy and at least three b-jets with the ATLAS detector*, *Eur. Phys. J.* **C72** (2012) 2174, [1207.4686]. 209, 211

[261] ATLAS collaboration, G. Aad et al., *Search for new phenomena in final states with large jet multiplicities and missing transverse momentum at $\sqrt{s}$=8 TeV proton-proton collisions using the ATLAS experiment*, *JHEP* **10** (2013) 130, [1308.1841]. 209, 211, 212, 214

[262] ATLAS collaboration, "ATLAS Twiki: ATLAS Offline Activity Coordination Board." https://twiki.cern.ch/twiki/bin/view/AtlasProtected/OfflineActivityCoordinationBoard, 2017. 229

[263] ATLAS collaboration, "ATLAS Twiki: PhysValMonitoring." https://twiki.cern.ch/twiki/bin/view/AtlasProtected/PhysValMonitoring, 2017. 229

[264] "High Performance Computing Center North." http://www.hpc2n.umu.se/, 2017. 230

[265] "JIRA: Intel vs AMD Differences in Simulation." https://its.cern.ch/jira/browse/ATLASSIM-2295, 2017. 230

Acknowledgements

Within the ATLAS collaboration, any research project could not be accomplished without dedication and contribution of many people. Therefore, I would like to take this opportunity to express my thanks to those who helped me the most during the challenging and productive journey completed by this thesis.

First of all, I am deeply grateful to my supervisor Prof. Gregor Herten for his constant support throughout my studies in Freiburg. His encouragement and confidence motivated me to pursue two different analyses which helped me to enhance my knowledge in physics and broaden my research interests.

I would like to thank all the members of the *2SS/3L SUSY team* for very fruitful collaboration and useful discussions, particularly David Côté, Jean-François Arguin, Julien Maurer, Jan Eric Sundermann, Tobias Rave and Thibaut Müller. They taught me that all aspects of the analysis are important and need to fit together, like pieces of the puzzle, to perform a complete and meaningful search. I owe my special thanks to Tom Gillam for introducing me to the dynamic matrix method and for his willingness to share knowledge.

I would like to express my gratitude to all the members of the WWW *team*. It was my great pleasure to work with them and share this adventurous journey from the very beginning to the final publication. A particular thank goes to Louis Helary for his guidance, commitment and persistence. He gave an invaluable contribution to my work through discussions and advices. I would like to thank to Alex Long for very enjoyable cooperation and Prof. John Butler for providing me the opportunity to use the Tier2/3 machines at Boston University.

I owe my gratitude to many people from the *ATLAS Distributed Computing* group who warmly welcomed me and initiated me into the complexity and importance of the computing grid. I would particularly like to thank Simone Campana, Alessandro di Girolamo, Andrej Filipčič, David Cameron, Jaroslava Schovancová, Jose Enrique García Navarro and Andreu Pacheco for an amazing work environment, interesting topics and their encouragement.

I am thankful to the whole *group in Freiburg* and particularly Tomáš, Zuzka, Michael, Tobias, Jan Erik, Kim, Valerio, Simone, Manfredi, Fabio, Peter, Thorwald and Veronika for the friendly and supportive atmosphere. A special thank is due to Andrea di Simone who was always willing to discuss any topic related to the physics, helped me with many technical issues and reviewed this manuscript. As this work would have not been possible without the Tier2 site at Freiburg, I would like to thank also its admins for their permanent support.

Finally, and by no means least, I would like to express my deepest thanks to my friends and family who supported me, encouraged me and made me laugh over the past years. A very special thanks to my parents, my sister Dadka and my husband Tomáš for always being here for me, for believing in me, for their love and endless care. They have made this whole endeavour worthwhile.